Cavitation Assisted Hybrid Advanced Oxidation Processes for Degradation of Recalcitrant Pollutants

A
Thesis
Submitted in
Partial Fulfillment of the
Requirements for the degree of

DOCTOR OF PHILOSOPHY

By

Kuldeep Roy

Department of Chemical Engineering
Indian Institute of Technology Guwahati
Guwahati – 781039, Assam, India

March 2021

Dedicated

to

My Parents

And

My Mentor

INDIAN INSTITUTE OF TECHNOLOGY GUWAHATI

Department of Chemical Engineering

STATEMENT

I do hereby declare that the content embodied in this thesis entitled "**CAVITATION ASSISTED HYBRID ADVANCED OXIDATION PROCESSES FOR DEGRADATION OF RECALCITRANT POLLUTANTS**" is the result of investigations carried out by me in the Department of Chemical Engineering, Indian Institute of Technology Guwahati, Guwahati, India, under the guidance of Prof. Vijayanand S. Moholkar. In keeping with the general practice of reporting scientific observations, due acknowledgements have been made wherever the work described is based on the findings of other investigators.

March 2021

Kuldeep Roy

(Roll No.:156107033)

INDIAN INSTITUTE OF TECHNOLOGY GUWAHATI

Department of Chemical Engineering

CERTIFICATE

This is to certify that the work described in this thesis entitled "**CAVITATION ASSISTED HYBRID ADVANCED OXIDATION PROCESSES FOR DEGRADATION OF RECALCITRANT POLLUTANTS**" which is being submitted by **Mr. Kuldeep Roy (Roll No.: 156107033)** to the Indian Institute of Technology Guwahati, India, for the award of Doctor of Philosophy, is a record of bonafide research work carried out by him under my supervision. The work embodied in this thesis has not been submitted elsewhere for a degree.

March 2021

Prof. Vijayanand S. Moholkar
Department of Chemical Engineering
Indian Institute of Technology Guwahati
Guwahati -781 039, Assam, India

ACKNOWLEDGEMENTS

This thesis marks the end of my cherished memories as a research scholar at IITG. It gives me immense pleasure to express my deepest gratitude to each and everyone who made this thesis possible and constantly encouraged me during my research work.

The first and foremost appreciation goes to my supervisor **Prof. Vijayanand S. Moholkar** for encouragement, and relentless support throughout my research work. I would like to thank him for sharing his technical thoughts which has always motivated me to progress towards new aspects. I am fortunate that he took me under his wings and considered me working under his esteemed guidance. I have thoroughly enjoyed working with him and I strongly believe that he brought out the best in me in every aspect. His profound knowledge has helped me to understand the mechanistic features of cavitation.

I would like to acknowledge my sincere gratitude to my doctoral committee members, **Prof. Bishnupada Mandal**, **Prof. Pallab Ghosh** and **Prof. Ajay Kalamdhad** (Department of Civil Engineering) for their insightful advices and suggestions throughout the research that led to the successful completion of the thesis.

My sincere thanks go to the faculty members of Chemical Engineering Department for their continuous inspiration and valuable suggestions. The kind and constant help of the staff members of Department of Chemical Engineering is also acknowledged. The advanced analytical facilities from Central Instruments Facility (CIF) of Indian Institute of Technology Guwahati is duly acknowledged.

I am immensely thankful to my seniors Dr. Pritam K. Dixit, Dr. Maneesh Poddar, Dr, Debarshi Mallick, Dr. Arup J. Borah, Dr. Shyamali Sarma, Dr. Ritesh S. Malani, Dr. Binota Thokchom and research group members, Neha, Niharika, Dr. Belachew Z. Tizazu, Philip, Bhaskar, Kajal, Udangshree, Chandrodai, Chiranjeevi, Pushpita, Karan, Aradhana, Rishiraj, Kaustubh, Saptarshi, Komal, Umesh and Dr. Lopa Pattanaik. I am highly thankful to my friends, Barnali, Bitang, Pyarimohan, Ritesh and Rupam for their love and support.

I would like to thanks my parents (**Amma and Papa**) and my sweet sister (**Deepshikha Roy**) for showering their endless love, care and support throughout my life. I owe my gratitude to all of them.

Last but not the least, I express my deepest gratitude to **Almighty GOD** for blessing me and giving the strength to complete this research work.

March 2021 Kuldeep Roy

ABSTRACT

This thesis has demonstrated the efficacy of the cavitation (both ultrasonic and hydrodynamic) based hybrid advanced oxidation processes for enhanced degradation of organic pollutants, and has also brought forth the mechanistic features of these processes in terms of the synergistic interactions. We have dealt with the pollutants from pharmaceuticals and pesticide industries such as sulfadiazine (SDZ), carbamazepine (CBZ) and p-nitrophenol (PNP). SDZ degradation was studied with hybrid AOP coupling hydrodynamic cavitation and heterogeneous Fenton + persulfate. Two solid Fenton catalysts (α-Fe_2O_3 and Fe_3O_4) in the form of nanoparticles were synthesized. Optimization of degradation process resulted in the highest degradation of 81%. A kinetic model for SDZ degradation was proposed based on homogeneous Fenton/persulfate system, and experimental degradation profiles were analyzed vis-à-vis simulated profiles. Kinetic model analysis showed the closest match between experimental and simulated profiles for $[Fe^{2+}]/[H_2O_2]$ initial ratio = 4. This indicated efficient catalytic activity of α-Fe_2O_3 nanoparticles – close to that of homogeneous catalyst. This is a consequence of high rate of leaching at surface of α-Fe_2O_3 particles due to intense turbulence and shear generated in cavitating flow. The synergy between hydrodynamic cavitation and other AOPs is mostly of physical nature, i.e. enhanced leaching at the catalyst surface. Next, optimization of hybrid HC+Fenton/persulfate system for degradation of SDZ was carried out. In hydrodynamic cavitation, the flow geometry essentially influences the total pressure head loss and turbulent pressure fluctuation frequency, which in turn determines the cavitational yield. Results of this study also gives an insight into the inter-relation or inter-dependence among various design and operational parameters of hydrodynamic cavitation reactor. This study has also revealed synergistic interactions among different AOPs in the hybrid system of HC+Fenton/persulfate. Enhanced leaching of Fe^{2+} ions from surface of solid Fenton catalysts due to intense turbulence and shear generated in cavitating flow results in faster degradation of SDZ. Hybrid AOPs based on ultrasonic cavitation for degrading SDZ were also attempted. The Fenton reagent (Fe^{2+} + H_2O_2) was added in the form of yolk-shell nanoparticles Fe_3O_4@hollow@mSiO_2. The highest degradation of 93.14% was achieved at optimized conditions. A kinetic model for SDZ degradation was formulated using reactions of Fenton-persulfate system. Concurrent analysis of experiments and simulations revealed faster leaching of Fe^{2+}/Fe^{3+} ions from

the metal core of Fe_3O_4@hollow@$mSiO_2$ nanoparticles due to micro-convection generated by sonication, which enhanced SDZ degradation four times. The hollow space between metal core and silica shell of the particles acted as "micro-reactors" with far enhanced interactions between $^{\bullet}OH$ radicals and the SDZ molecules. Inhibition effect of inorganic anions (Cl^-, NO_3^-, CO_3^{2-}, SO_4^{2-}) on SDZ degradation was also studied with experiments and an extended kinetic model. CO_3^{2-} and SO_4^{2-} had the strongest inhibition effect due to both metal ion complexation and radical scavenging. The degradation of yet another pollutant, p-nitrophenol was studied with combination of hydrodynamic cavitation and the heterogeneous Fenton process. Spherical Fe_3O_4 magnetic nanoparticles were used as heterogeneous Fenton reagent. Experimental results showed that 78% PNP degradation could be achieved under optimized operating conditions. The experimental results were explained with three approaches: (1) hydrodynamic model for the cavitating flow, (2) kinetic model for PNP degradation and (3) DFT simulations for identification of the intermediates of the PNP degradation and possible pathways. Two distinct pathways for PNP degradation were identified, viz. $^{\bullet}OH$ addition and H-abstraction. For the former route, the *ortho*-C of benzene ring was the most favourable site, while H atom of phenolic hydroxyl group was more susceptible (or more reactive) for H-atom abstraction route. Lastly, investigations on degradation of carbamazepine have been presented using hydrodynamic cavitation-based hybrid advanced oxidation systems. Hydrodynamic cavitation has been coupled with persulfate system ($Na_2S_2O_8$) and photocatalytic system employing ZnO/$ZnFe_2O_4$ particles. Among several binary, ternary and quaternary hybrid AOPs, the binary system of HC and persulfate (HC+$Na_2S_2O_8$) seemed most effective in boosting the CBZ degradation. Seven intermediates of degradation with m/z values 237, 283, 267, 253, 224, 196, 180, 149 were detected. The analysis of the CBZ molecule using DFT simulations helped in identification of several vulnerable sites for the attack of $^{\bullet}OH$ and $SO_4^{\bullet-}$ radicals. The ionization of CBZ molecule through carbon atoms in heterocyclic and bilateral benzene rings is the key step in the degradation pathway. An empirical correlation relating degradation to the operational parameters revealed inverse relationship with pH and initial concentration. The inlet pressure of hydrodynamic cavitation was the most effective parameter governing the degradation.

CONTENTS

LIST OF TABLES

CHAPTER 1

CHAPTER 2

CHAPTER 3

CHAPTER 4

CHAPTER 1

CHAPTER 2

CHAPTER 3

CHAPTER 4

CHAPTER 5

CHAPTER 6

ACRONYMS

ANOVA	Analysis of variance
AOP	Advanced oxidation processes
BA	Benzoic acid
BET	Brunauer– Emmett –Teller
BJH	Barrett–Joyner–Halanda
CBZ	Carbamazepine
CCD	Central composite design
CFD	Computational fluid dynamics
DFT	Density functional theory
EDX	Energy-dispersive X-ray spectroscopy
FE-SEM	Field emission scanning electron microscopy
FE-TEM	Field emission transmission electron microscope
HC	Hydrodynamic cavitation
HPLC	High-performance liquid chromatography
IRC	Intrinsic reaction coordinate
LC-MS	Liquid chromatography–mass spectrometry
MNPs	Magnetic nanoparticles
PNP	4–Nitrophenol
PS	Persulfate
ROS	Reactive oxygen species
SAED	Selected area electron diffraction
SDZ	Sulfadiazine
SIMPLEC	Semi-Implicit Method for Pressure Linked Equations-Consistent
TS	Transitions state
US	Ultrasound
VFD	Variable frequency drive
VSM	Vibrating sample magnetometer
VVF	Vapour Volume Fraction
XRD	X-ray diffraction

PARAMETRIC SYMBOL

I_o	Average photonic light intensity per volume of UV
B3LYP	Becke's three-parameter Lee–Yang–Parr
$P_B(t)$	Bubble pressure
R_b	Bubble radius
C_v	Cavitation number
R_c	Condensation rate
Y_M	Contribution of the fluctuating dilatation in compressible turbulence to the overall dissipation rate
d_h	Diameter of each hole
F	Empirical calibration coefficient
A_o	Empirical constant
R_e	Evaporation rate
$f_{[CBZ]}$	Fraction of UV irradiation absorbed CBZ
G_b	Generation of turbulence kinetic energy due to buoyancy
G_k	Generation of turbulence kinetic energy due to the mean velocity gradients
k	Kinetic constants
ν_L	Liquid kinematic viscosity
$\bar{v}_m$	Mass average velocity
ρ_m	Mixture density
R	Net phase change rate
N_h	Number of holes
b	Optical path length
z	Path length of quartz cuvette
P_2	Recovered downstream pressure
$P_\infty(t)$	The instantaneous bulk pressure in the liquid
k	Turbulent kinetic energy
P_v	Vapor pressure of the liquid
ν_o	Velocity at the throat of the cavitator

GREEK SYMBOL

μ_m	Dynamic viscosity of the mixture
ε_{CBZ}	Molar extinction coefficient of CBZ
$\varepsilon_{oxidant}$	Molar extinction coefficient of the oxidant
$\phi_{[CBZ]}$	Quantum yield of CBZ
ε	Rate of dissipation of turbulent kinetic energy
β_o	Ratio of total area of holes to the cross–sectional area of pipe
α	Ratio of total perimeter of the holes to total area of opening
η	Removal percentage
σ_ε	Turbulent Prandtl numbers for ε
σ_k	Turbulent Prandtl numbers for k
λ	Wavelength of UV light

CHAPTER 1

Introduction and Literature Review

CHAPTER 1

INTRODUCTION AND LITERATURE REVIEW

1.1 INTRODUCTION

In recent decades, water pollution has been a daunting environmental issue globally, especially due to the presence of biorefractory pollutants contributed by wastewater streams emerging from industrial discharges and other sources like agricultural run-offs. The biorefractory pollutants in water also pose a severe danger to aquatic life. Unregulated discharge of polluted water from process industries into natural water bodies like rivers and lakes has led to diffuse contamination with aliphatic and aromatic compounds, endocrine-disrupting chemicals, organic dyes, agro–chemicals, nitrogen and sulphur containing compounds (Richardson and Ternes, 2011; Bokare and Choi, 2014). A sustainable reuse and recycle of this polluted water are a possible solution to both environmental pollution and the conservation of natural resources. For the treatment of biorefractory pollutants, various new techniques are being adopted, as these pollutants are hardly degradable by the conventional process. Conventional wastewater treatment using biological and physicochemical processes (chlorination, flocculation and ozonation), eventually followed by adsorption and filtration-based separations, are efficient to degrade a majority of anthropogenically–polluted water resources. Chan et al. (2009) have shown that an integrated bioreactor with stacked configuration is highly efficient for the treatment of high strength industrial wastewaters due to minimal space

requirements, low capital cost and excellent COD removal efficiencies (in excess of 83%). Physicochemical techniques like adsorption, coagulation-flocculation, membrane and reverse osmosis (RO) require additional secondary treatments to avoid the secondary sludge disposal (Tyagi and Lo, 2011).

The prominent technique for effective and efficient degradation of the biorecalcitrant pollutants is Advanced Oxidation Processes (AOPs) or the Advanced Oxidation Techniques (AOTs), or *in-situ* chemical oxidation (ISCO), which are based on production of highly oxidizing radicals in the system, with bulk conditions at nearly ambient temperature and pressure. Reactive radicals attack on random molecular positions of the pollutant and oxidize/mineralize the pollutant molecule into intermediates, CO_2 and H_2O (Brillas et al., 2009; Chakma and Moholkar, 2013a; He et al., 2016a). AOPs (or AOTs) are environmentally friendly chemical oxidation methods as they involve *in-situ* production of reactive radicals such as hydroxyl radical ($^{\bullet}OH$, oxidation potential = 2.8 eV) and sulfate radicals ($SO_4^{\bullet-}$, oxidation potential = 2.6 eV). AOPs are categorized according to the reactive phase (homogeneous and heterogeneous) and generation methods (chemical, electro–chemical, photo–chemical, cavitation–chemical and solar–chemical), as shown in Table 1.1.

Among the various AOPs that have been explored for biorecalcitrant pollutants, cavitation is recognized as highly effective and efficient, and also integrable with other AOPs. It can be applied either individually or in a hybrid manner (combining with other techniques) for the degradation of biorefractory pollutants (Gogate, 2002; Adewuyi, 2005a; Adewuyi, 2005b; Mahamuni and Adewuyi, 2010; Chakma and Moholkar, 2013b; Bagal and Gogate, 2014b; Rajoriya et al., 2016; Gągol et al., 2018;).

Table 1.1: Classification of advanced oxidation processes (AOPs)

Phase	Generation method	Individual and Hybrid AOPs
Homogeneous	Chemical oxidation	O_3, H_2O_2, Persulfate ($S_2O_8^{2-}$), Peroxymono-sulfate (HSO_5^-), Fenton ($H_2O_2 + Fe^{2+}$)
	Electrochemical oxidation	Electro–Fenton ($Fe^{3+}/H_2O_2/e^-$), Photo–Electro–Fenton ($UV/Fe^{3+}/H_2O_2/e^-$), Sono–Electro–Fenton ($US/Fe^{3+}/H_2O_2/e^-$)
	Photochemical oxidation	UV/O_3, UV/H_2O_2, $UV/O_3/H_2O_2$, Photo–Fenton ($UV/Fe^{2+}/H_2O_2$)
	Cavitation (US or HC) chemical oxidation	US or HC/H_2O_2, US or HC/O_3, US or $HC/H_2O_2/O_3$, US or $HC/UV/S_2O_8^{2-}$, US or HC–Fenton (US or $HC/Fe^{2+}/H_2O_2$)
	Solar chemical oxidation	Solar–Fenton ($h\nu/Fe^{2+}/H_2O_2$), Solar Photo–Fenton ($h\nu/UV/Fe^{2+}/H_2O_2$), Solar–Photo–Electro–Fenton ($h\nu/UV/Fe^{3+}/H_2O_2/e^-$)
Heterogeneous	Chemical oxidation	Fenton like: H_2O_2 + solid ($Fe^0/Fe/Fe^{3+}$), Solid Photo catalysts: UV + TiO_2/ZnO/CdS/ $ZnFe_2O_4$/$CuFe_2O_4$/$NiFe_2O_4$, different solid nanoparticles with AOPs

By definition, cavitation is sequential nucleation, growth, and rapid collapse of tiny gas or vapour micro-bubbles driven by bulk pressure variation in the liquid medium. The transient collapse of cavitation bubbles leads to generation of high temperature ~ 5000 K and pressure ~ 500 bar within small time interval (in few microseconds) (Suslick, 1990; Balaji et al., 2011). The generated high temperature and pressure during bubble collapse provide the activation energy which required for the bond cleavage. The thermal dissociation/pyrolysis of entrapped solvent/pollutant molecules generates an oxidative environment due to the generation of reactive oxygen species (ROS) including hydroxyl radical ($^{\bullet}OH$), hydroperoxyl radical ($HO_2^{\bullet}$), superoxide anion ($O_2^{-\bullet}$), hydrogen ($^{\bullet}H$) and singlet oxygen ($^1O_2$). Non-selective reactivity of $^{\bullet}OH$ radical with rate constant of 10^8 – 10^{10} M^{-1} s^{-1} is primarily responsible for fast and efficient degradation of recalcitrant

compounds (Buxton et al., 1988). Figure 1.1 shows the physicochemical effects of cavitation, i.e. mechanical, physical and chemical effects, which mainly contribute to process intensification.

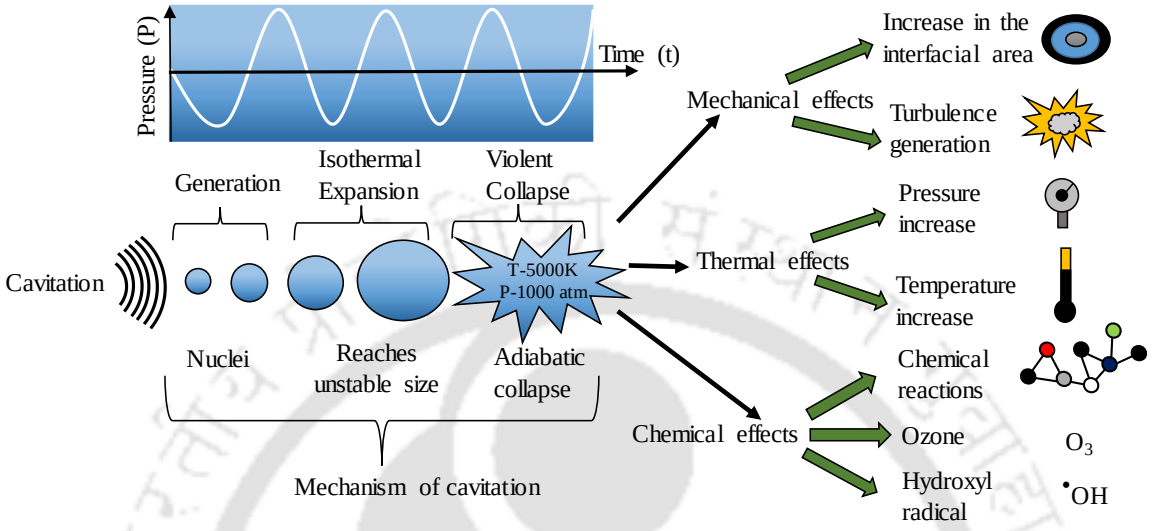

Figure 1.1: Physicochemical effects of the cavitation process

Several studies have also attempted a sequential or simultaneous use of different AOPs (a hybrid AOPs configurations) for wastewater treatment. A few combinations of individual AOPs for devising a hybrid AOPs are presented in Table 1.1. These Hybrid AOPs have been found more effective for degradation/mineralization of recalcitrant pollutants as compared to the individual oxidation process. The major advantage of the hybrid AOPs is the synergistic interaction among their individual mechanisms that lead to enhancement in kinetics and yields as a result of *in-situ* chemical oxidation reactions. The literature reports various hybrid AOPs through combinations of individual AOPs, but the exact mechanism of these hybrid AOPs (or the synergy between individual AOPs) is not fully established yet. Identification of the underlying mechanism, which could serve as a basic guideline, is rather important and crucial for the efficient design of large–scale commercial processes employing these hybrid AOPs.

Recently, cavitation-based hybrid techniques, in which cavitation process is combined with conventional other AOPs such as UV, persulfate, Fenton, Fenton like, photo-Fenton and various nanomaterials etc., have been used for effective and efficient degradation/mineralization of biorefractory pollutants. Based on the mode of generation, cavitation can be classified into four types, viz. acoustic, hydrodynamic, optic and particle. Among all, acoustic and hydrodynamic cavitation have been adopted in academic and industrial research due to its simplicity, ease of operation and efficacy for achieving desirable results (Moholkar et al., 1999; Gogate et al., 2001; Gogate and Pandit, 2004; Saharan et al., 2011a). Hydrodynamic cavitation assisted hybrid AOPs can degrade a wide range of pollutants like dyes (Saharan et al., 2011a; Cai et al., 2016a; Cai et al., 2016b; Innocenzi et al. 2019; Askarniya et al., 2020; Li et al., 2020), phenolic compounds (Chakinala et al., 2008a; Bagal and Gogate, 2013), pharmaceutical wastes (Patil and Gogate, 2012; Raut Jadhav et al., 2013; Patil et al., 2014; Angaji and Ghiaee, 2015) and industrial wastewater (Chakinala et al., 2008b; Chakinala et al., 2009; Boczkaj et al., 2018; Gągol et al., 2019). Similarly, ultrasound–assisted hybrid AOPs can degrade pollutants like dyes (Chakma and Moholkar, 2013b; Chakma et al., 2015; Li et al., 2015; Wang et al., 2019; Dhanke and Wagh, 2020), phenolic compounds (Huang et al., 2012; ElMetwally et al., 2019; Wang et al., 2019; Eshaq et al., 2020), pharmaceutical compounds (Madhavan et al., 2010; Patil et al., 2014; Zhang et al., 2020) and industrial waste (Monteagudo et al., 2014; Alfonso Muniozguren et al., 2020).

Cavitation activity depends on the deformities present in the liquid medium, which could result in the formation of microbubbles or cavities. The presence of additives in the system, in either homogeneous or heterogeneous form, could assist the process of generation of the cavitational events at multiple locations inside the reactor. Recently, numerous studies have been described the beneficial use of heterogeneous catalysts (solid

nanoparticles) in wastewater treatment by virtue of their physicochemical characteristics like reusability, long-term stability, relatively smaller requirement of external chemical inputs and integration from small to modular systems (Bethi et al., 2016; Hodgeset al., 2018). These nanoparticles introduce surface inhomogeneity into the liquid medium, in addition to entrapped gas pockets on their surfaces, both of which can act as additional nuclei for the cavitation bubbles. It is important to note that leaching of solid surface primary enable homogeneous process though dissolved metal ions. (Atchley and Prosperetti, 1989; Borkent et al., 2009; Gogate and Katekhaye, 2012)

In the last two decades, significant research in the world has been dedicated to degradation/mineralization of biorecalcitrant pollutants using cavitation-based hybrid AOPs. More recently, the use of novel nanocatalysts along with the AOPs has also been attempted by several authors. Despite these efforts, the exact physical and chemical mechanism of the hybrid AOPs has not been explored in depth. The synergistic interactions among different individual AOPs and also the catalyst (if applied) have not been identified. This is a crucial aspect of all AOPs – especially from the viewpoint of optimization and scale – up. The principal aim of this thesis is to fulfill this knowledge gap through a dual approach of experiments and mathematical modelling. As a prologue to this thesis, basic mechanisms of the well-known individual AOPs have been described in the next section.

1.2 CAVITATION BASED ADVANCED OXIDATION PROCESSES AND LITERATURE REVIEW

Cavitation reactors have been recognized as a new generation multiphase reactors, which are adequate to generate *in-situ* oxidation conditions from local “hot spots” or transient cavitation events, which result in the generation of highly reactive radicals in the liquid

medium. Cavitation reactors have the potential for degradation/ mineralization of toxic and complex organic pollutants. In this section, the fundamental chemistry and mechanism of individual AOPs has been described to get the mechanistic insight of the processes. Moreover, the hybrid AOPs in combination with either acoustic or hydrodynamic cavitation have also been discussed and described.

1.2.1 Ultrasonic Cavitation

Sonolysis or ultrasound cavitation (US) assisted degradation/ mineralization has been extensively investigated in both individual (or standalone) form and as a hybrid system. As noted earlier, the physicochemical effects of sonolysis are generated due to transient cavitation events induced due to pressure fluctuation in the liquid medium as the ultrasound wave propagates through it. The cavitation bubble initially expands in the rarefaction half cycle of ultrasound with the evaporation of water at gas-liquid interface. These vapour molecules enter in the bubble and later diffuse back to the interface and condense at the interface during the compression phase. Adiabatic compression of the bubble during transient collapse is capable to generating extreme conditions of high temperature and pressure. With the fragmentation of the bubble, highly reactive radicals are released into the bulk liquid medium, where they induce various oxidation reactions. Three distinct chemical mechanisms, i.e. hydroxylation in the bulk liquid medium, pyrolysis inside the bubble and thermal decomposition in the supercritical zone at the bubble interface, have been proposed for the sonochemical degradation of organic pollutants. The main reaction chain that occurs during the collapse of a bubble is shown below (Adewuyi, 2005a; Adewuyi, 2005b; Kidak and Ince, 2006):

$$H_2O \xrightarrow{)))} {}^{\bullet}OH + {}^{\bullet}H$$

$${}^{\bullet}OH + {}^{\bullet}OH \longrightarrow H_2O + O^{\bullet}$$

$$^{\bullet}OH + {}^{\bullet}H \longrightarrow H_2O$$

$$^{\bullet}H + {}^{\bullet}H \longrightarrow H_2$$

$$^{\bullet}OH + {}^{\bullet}OH \longrightarrow H_2O_2$$

$$^{\bullet}OH + H_2O \longrightarrow H_2O_2 + H^{\bullet}$$

The most common gas bubble is an air bubble comprising nitrogen and oxygen. Moreover, some dissolved oxygen generally present in the liquid medium may also diffuse inside the bubble. Several other reactions may also be induced by nitrogen and oxygen, which are listed below (Chakma and Moholkar, 2013a):

$$O_2 + {}^{\bullet}H \longrightarrow HO_2^{\bullet}$$

$$^{\bullet}O + HO_2^{\bullet} \longrightarrow {}^{\bullet}OH + O_2$$

$$^{\bullet}O + H_2O \longrightarrow {}^{\bullet}OH + {}^{\bullet}OH$$

$$HO_2^{\bullet} + HO_2^{\bullet} \longrightarrow H_2O_2 + O_2$$

$$N_2 + {}^{\bullet}OH \longrightarrow N_2H + O^{\bullet}$$

$$N_2 + {}^{\bullet}OH \longrightarrow N_2O + H^{\bullet}$$

$$N_2 + {}^{\bullet}OH \longrightarrow NH + NO$$

$$NH + {}^{\bullet}OH \longrightarrow NH_2 + O^{\bullet}$$

$$NO + O_2 \longrightarrow NO_2 + O^{\bullet}$$

$$O^{\bullet} + O_2 \longrightarrow O_3$$

1.2.2 Hydrodynamic Cavitation

Hydrodynamic cavitation (HC) has been established as an alternative to ultrasonic or acoustic cavitation for all types of processes, viz. physical, chemical and biological – including as an advanced oxidation technique for degradation/mineralization of organic

pollutants. Hydrodynamic cavitation reactors are energy efficient and can operate at large capacity. Such reactors are very easy to design, and thus, easy to scale up.

In hydrodynamic cavitation, cavitation bubbles can be generated by passing the fluid through the in–line constriction/geometry such as orifice, venturi, throttling valve etc. When the liquid passes through the constriction, reduction in the cross-sectional area increases the velocity head at the expense of the local pressure head. Flow separation occurs at vena – contracta resulting in the generation of large eddies in the downstream section. This results in a significant loss of pressure head in the downstream region where pressure recovery occurs. Reduction of pressure in the flow at vena – contracta results in the release of dissolved gas. In situations where the pressure falls below vapour pressure of the liquid at prevalent temperature, partial vaporization of the liquid may also occur, resulting in the generation of vapour bubbles. The gas and vapour bubbles undergo oscillation and transient collapse with the recovery of pressure downstream of the flow constriction. The cavitation intensity depends on the magnitude of the pressure drop, which in turn depends on the flow geometry and upstream pressure (Moholkar et al., 1999; Gogate et al., 2001; Arrojo and Benito, 2008). The cavitation inception and degree of cavitation (in terms of magnitude and intensity) in the flowing medium is defined by the dimensionless number termed as "cavitation number (C_v)" (Shah et al., 1999). It is defined as $C_v = \left(P_2 - P_v\right) \Big/ \left(\rho v^2 / 2\right)$ where P_2 is the fully recovered downstream pressure, P_v = vapour pressure of the liquid, v = velocity at the throat of cavitational reactor, ρ = density of flowing medium.

In principle, vaporous cavitation commences at $C_v \leq 1$; however, in practice, cavitation is seen to occur at condition $C_v > 1$ due to the presence of dissolved gas and generation of gas bubbles. C_v at which initiation of the cavitation process occurs is called

cavitation inception number (C_{vi}) (Yan and Thorpe, 1990). Yan and Thorpe (1990) investigated the behaviour of C_{vi} to analyze the cavitation zone for different types of orifice plates. They observed that C_{vi} does not change with the fluid velocity, and it remains constant for a given orifice plate. However, C_{vi} increases linearly with the diameter ratio of the orifice diameter (d) to the pipe diameter (D).

In spite of the difference in generation methods, an analogy is well established between ultrasonic (or acoustic) cavitation and hydrodynamic cavitation on the basis of bubble dynamics or bubble behaviour as a function of design and operating parameters (Moholkar et al. 1999; Moholkar and Pandit, 2001; Arrojo and Benito, 2008), cavitational yield (Saharan et al., 2011a; Gogate and Bhosale, 2013), energy efficiency and scalable feasibility (Moholkar et al., 1999; Gogate et al., 2001; Gogate, 2002; Benito et al., 2005; Bagal and Gogate, 2014; Gągol et al. 2018; Saxena et al., 2018; Gągol et al., 2019; Rajoriya et al., 2019;).

As an example of the comparison between ultrasonic and hydrodynamic cavitation, given below is a summary of the study of Saharan et al. (2011b), who quantified the cavitational yield (moles of pollutant degraded/ the total energy input) for the degradation of Acid Red 88 dye using hydrodynamic cavitation and sonication (ultrasonic cavitation). They observed that cavitation yield for hydrodynamic cavitation (8.97×10^{-10} gmol/J) was 13× higher than ultrasonic cavitation (0.682×10^{-10} gmol/J).

1.3 CONVENTIONAL ADVANCED OXIDATION PROCESSES

1.3.1 Persulfate System

In recent years, sulfate radical ($SO_4^{\bullet-}$) assisted *in-situ* chemical oxidation (ISCO) have been received great attention as an alternative to $^{\bullet}OH$ radical assisted AOPs due to its

high capability for the degradation of biorefractory contaminants. $SO_4^{\bullet-}$ radicals have advantages over $^{\bullet}OH$ radicals because of its comparable oxidation potential, reduced selectivity and wider pH range. Table 1.2 shows the physiochemical properties of different types of oxidants, which are frequently used for degradation. In literature, various methods have been used to activate the persulfate (PS), viz peroxydisulfate (PDS, $S_2O_8^{2-}$) or peroxymonosulfate (PMS, HSO_5^-) ions for generation of the $SO_4^{\bullet-}$ radicals, such as thermal, ultraviolet light, alkaline, electrolysis, carbonaceous materials, transition metals (homogenous and heterogeneous) etc. Table 1.3 shows the detailed summary with key reaction pathways for the activation of persulfate ions. Persulfate activation can also be achieved through transient cavitation. Cavitation-activated persulfate oxidation has dual advantage, i.e. generation of persulfate radicals by homolysis of the peroxide bond and direct $^{\bullet}OH$ radical generation through the transient collapse of cavitation bubbles. This synergy in cavitation – assisted persulfate oxidation enhances the extent of degradation of organic compounds (Gogate and Bhosale, 2013; Wang and Zhou, 2016; Wang and Wang, 2018; Yang et al., 2019). Wang and Zhou (2016) degraded carbamazepine using ultrasound (40 kHz, 50 W) activated persulfate process. Here, 1.2%, 25.7% and 43.8% of degradation were obtained with ultrasound alone, persulfate alone and persulfate combined with ultrasound, respectively. Their study clearly shows a synergistic effect between the individual AOPs of persulfate and cavitation in the hybrid system.

On the other hand, the physical effects of ultrasound and hydrodynamic cavitation, viz. microstreaming, microturbulence and acoustic waves, are especially beneficial in heterogeneous reaction systems (solid/liquid, liquid/liquid or solid/liquid/gas etc.). Particularly, in catalytic degradation processes, sonication can

reduce mass transfer barriers, provide high surface area through fragmentation of catalyst, and reduce catalyst poisoning by renewing the catalytic surface. Moreover, the addition of heterogeneous transition metals (shown in Table 1.3) in cavitation-assisted persulfate system enhances the synergy of persulfate activation and nucleation for cavitation (Matzek and Carter, 2016; Roy and Moholkar 2020a; Roy et al., 2020b). Zou et al. (2014) degraded sulfadiazine in an ultrasound-assisted heterogeneous Fe^0/persulfate system. The degradation achieved with US alone, US+Fe^0 and US+PS was 9.7%, 9.8% and 13.7%, respectively. However, due to the synergetic interactions 95.7% degradation was achieved in the US/Fe^0/PS system. This study shows the evidence that ultrasound generates intense microturbulence in an aqueous medium, which enhances the mass transfer at solid–liquid interface, which is manifested in terms of enhanced oxidation into the reaction mixture.

Table 1.2: Characteristics of oxidants used for *in–situ* oxidation (Olmez-Hanci and Arslan-Alaton, 2013; Devi et al., 2016; Ghanbari and Moradi, 2017; Wacławek et al., 2017)

Oxidant	O–O bond dissociation energy (kJ/mol)	Average lifetime in groundwater	Reactive Species	Oxidation potential (eV)
H_2O_2	213	hours to day	$^{\bullet}OH$, $O_2^{\bullet-}$, $HO_2^{\bullet}$	1.8
O_3	364	< 1 h	$^{\bullet}OH$, O_3	2.1
PDS ($S_2O_8^{2-}$)	92	> 5 months	$SO_4^{\bullet-}$, $S_2O_8^{2-}$	2.1
PMS (HSO_5^-)	377	hours to days	$SO_4^{\bullet-}$, $SO_5^{\bullet-}$, $^{\bullet}OH$	1.82
$^{\bullet}OH$	–	10^{-3} µs (half-life)		2.8
$SO_4^{\bullet-}$	–	30–40 µs (half-life)		2.5–3.1

1.3.2 Fenton Process

The Fenton process is perhaps the first-ever advanced oxidation process based on the production of $^{\bullet}OH$ radicals. It still remains one of the leading and most applied AOP for

degradation of numerous organic pollutants. The Fenton process uses ferrous ions (Fe^{2+}) and hydrogen peroxide (H_2O_2) (classical Fenton process:

$Fe^{2+} + H_2O_2 \longrightarrow Fe^{3+} + {}^{\bullet}OH + OH^{-}$) for the generation of $^{\bullet}OH$ radicals in aqueous solution at preferably acidic pH (Fenton, 1894). *In–situ* generated $^{\bullet}OH$ radicals can produce following reactions for dissociation of biorefractory pollutants which includes: redox reaction ($RX + {}^{\bullet}OH \longrightarrow RX^{+\bullet} + OH^{-}$), dehydrogenation reaction (hydrogen abstraction) ($RH + {}^{\bullet}OH \longrightarrow R^{\bullet} + H_2O$), and electrophilic addition to π systems (hydroxylation reaction) ($RHX + {}^{\bullet}OH \longrightarrow RHX(OH)$) (Oturan, 2000; Nidheesh, 2015). Huang et al. (1993) have made a comparative evaluation of various AOPs, and emphasized on the potential of Fenton process for the treatment of wastewaters.

Based on the phase in which the Fe^{2+} ions are added into the system, Fenton process can be categorized as: (1) Homogeneous Fenton and (2) Heterogeneous Fenton. The homogeneous Fenton process, in which the Fe^{2+} ions are added in the form of salt (mostly $FeSO_4 \cdot 7H_2O$) has been widely used because of its simplicity, negligible mass transfer limitations, probability of using conventional processes at ambient temperature and pressure. However, there are certain limitations encountered by the process: (1) loss of iron oxides, (2) recovery of iron oxides before the discharging, (3) higher H_2O_2 consumption, (4) narrow pH range, (5) formation of Fe^{3+} complexes, and (6) costs associated with subsequent neutralization after treatment. Therefore, heterogeneous Fenton process, in which iron metal particles are added as a source of Fe^{2+} ions. The leaching at the surface of metal particles releases Fe^{2+} ions in the medium. Thus, heterogeneous Fenton process can circumvent the shortcoming of homogeneous Fenton system (Pouran et al., 2014; Kuan et al., 2015; He et al., 2016a; Mirzaei et al., 2017).

Table 1.3: Persulfate activation mechanism (Yuan et al., 2013; Yuan et al., 2014; Oh et al., 2016; Matzek and Carter, 2016; Wacławek et al., 2017; Wang and Wang, 2018; Zhou et al., 2019)

Method	Mechanism	Key reaction pathways	Highlights
Heat	Homolysis / homolytic fission of peroxide bond (O–O)	$S_2O_8^{2-} + \text{heat} \longrightarrow 2SO_4^{\bullet-}$ $SO_4^{\bullet-} + H_2O \longrightarrow SO_4^{2-} + {}^{\bullet}OH + H^+$	activation temperature ≥ 40 °C
UV radiation	Homolysis of peroxide bond (O–O)	$S_2O_8^{2-} + UV \longrightarrow 2SO_4^{\bullet-}$ $H_2O \longrightarrow {}^{\bullet}OH + H^{\bullet}$ $S_2O_8^{2-} + H^{\bullet} \longrightarrow SO_4^{\bullet-} + SO_4^{2-} + H^+$	Often used λ = 254 nm, Quantum yield = 1
Alkaline pH	Hydrolysis of PDS to form HO_2^-, later one-electron transfer	$S_2O_8^{2-} + H_2O \xrightarrow{OH^-} 2SO_4^{2-} + HO_2^- + H^+$ $2S_2O_8^{2-} + 2HO_2^- \xrightarrow{OH^-} 3SO_4^{2-} + SO_4^{\bullet-} + O_2^{\bullet-} + 4H^+$ $SO_4^{\bullet-} + OH^- \longrightarrow SO_4^{2-} + {}^{\bullet}OH$	Often pH > 10
Electrolysis	Fe^{2+} generated in electrochemical and chemical anodic corrosion of iron	$S_2O_8^{2-} + e^- \xrightarrow{OH^-} SO_4^{2-} + SO_4^{\bullet-}$ $Fe \longrightarrow Fe^{2+} + 2e^-$ $Fe^{3+} + e^- \longrightarrow Fe^{2+}$	Fe^{3+} reduction on the cathode
Cavitation	Homolysis of peroxide bond (O–O)	$S_2O_8^{2-} + \text{Cavitation} \longrightarrow 2SO_4^{\bullet-}$ $H_2O \xrightarrow{)))))} {}^{\bullet}OH + H^{\bullet}$	Intense micro-turbulence and micro-mixing in the medium
Carbonaceous materials	surface moieties with delocalized π-electrons	$CX-OOH + S_2O_8^{2-} \longrightarrow SO_4^{\bullet-} + CX-OO^{\bullet} + HSO_4^-$ $CX-OH + S_2O_8^{2-} \longrightarrow SO_4^{\bullet-} + CX-O^{\bullet} + HSO_4^-$	O–O bond of PDS is debilitated on the defective edges of carbocatalysts
Transition metals Homogenous Heterogeneous	One electron transfer	$S_2O_8^{2-} + M^{n+} \longrightarrow M^{n+1} + SO_4^{\bullet-} + SO_4^{2-}$ $SO_4^{\bullet-} + M^{n+} \longrightarrow M^{n+1} + SO_4^{2-}$ where M = Ni^{2+}, Fe^{3+}, Fe^0, Mn^{2+}, V^{3+}, Ce^{3+}, Fe^{2+}, Ru^{3+}, Co^{2+}	Homogenous: Often requires low pH, difficult to recover. Heterogeneous: Mass transfer limitation, easy to recover

CX = carbonaceous materials surface

The heterogeneous Fenton reaction operates efficiently over wider range of operating pH and also reduces the limitations associated with the recovery of iron oxides after the treatment. Because of limited leaching of Fe^{3+} from the heterogeneous catalytic surface, the ferric hydroxide precipitation is restrained with the lesser formation of iron sludge with facile recycle of catalyst. However, in heterogeneous Fenton system, the bulk concentration of Fe^{2+} is relatively small (due to limited leaching at the metal surface) which results in relatively slower degradation. To overcome this issue, new types of heterogeneous nanomaterials/nanoparticles with the higher surface area have been developed in recent years that enhance surface leaching and also increase the long–term stability and activity of the catalyst particles (Hermosilla et al., 2009; Bae et al., 2013).

The homogeneous Fenton process depends on the chemical reaction between the radicals and contaminants, but the heterogeneous Fenton process depends on the physical process (on the catalytic surface) and chemical reaction (in bulk). In the heterogeneous Fenton, three reaction mechanisms are possible: (i) chemisorption of pollutant on the catalyst surface, (ii) reaction of H_2O_2 with pre–leached Fe^{2+} ions in the bulk medium to generate $^{\bullet}OH$, and (iii) surface reaction of H_2O_2 with iron metal particles to generate $^{\bullet}OH$. All of these mechanisms involve both mass transfer and reaction kinetics (Soon and Hameed, 2011; Tisa et al., 2014; Kuan et al., 2015; Pouran et al., 2014; Mirzaei et al., 2017). Fig. 1.2 describes the three mechanisms (with possible reactions) for the generation of reactive radicals (He et al., 2016a).

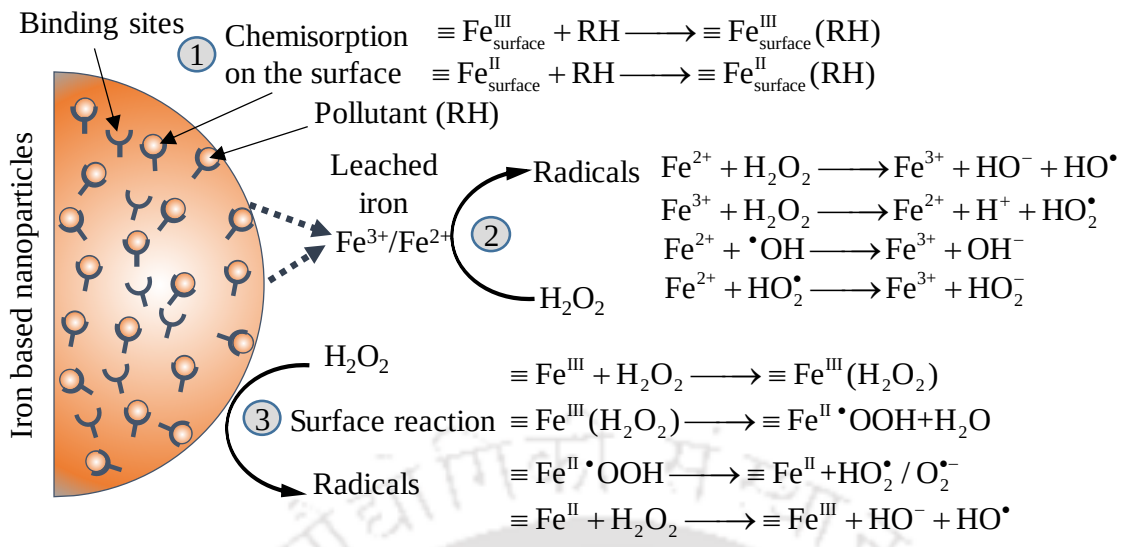

Figure 1.2: Interfacial mechanisms for heterogeneous Fenton like system in iron–based nanoparticles

On the other hand, a few studies also described a non–radical mechanism in heterogeneous Fenton oxidation process (Andreozzi et al., 2002; Garrido-Ramírez et al., 2010). Andreozzi et al. (2002) studied the non–radical mechanism for the oxidation of 3,4-dihydroxybenzoic acid (3,4-DHB) in the reaction mixture of H_2O_2 + goethite slurry (α-Fe – OOH, surface–active site: $\equiv Fe(III) - OH$) and suggested the following reactions:

$$\equiv Fe(III) - OH + H^+ \rightleftharpoons \equiv Fe(III) - OH_2^+$$

$$\equiv Fe(III) - OH \rightleftharpoons \equiv Fe(III) - O^- + H^+$$

$$H_2O_2 + (*) \underset{K_h}{\rightleftharpoons} H_2O_2^*$$

$$S + (*) \xrightarrow{k_1} S^*$$

$$H_2O_2^* + S^* \xrightarrow{k_2} \text{product} + 2(*)$$

where $K_h = \dfrac{[H_2O_2^*]}{[H_2O_2] \cdot C_L}$, $*$ = free catalytic active sites, C_L = concentration (mol/dm^3)

Generally, the catalytic characteristics such as pore volume, porosity, surface area and distribution are taken into consideration in the synthesis of nanomaterials. The catalyst surface can be modified based on the process efficacy to obtain higher catalytic performance and stability (Soon and Hameed, 2011).

Variants of the Fenton processes, i.e. Fenton process combined with other AOPs such as sono–Fenton, electro–Fenton, photo–Fenton, HC–Fenton, sono–photo–Fenton, HC–photo–Fenton and sono–electro–Fenton processes (in both homogeneous and heterogenous phases) have been studied for efficient degradation of wide range of biorefractory pollutants, as depicted in Table 1.1. A summary of published literature on the degradation of biorecalcitrant pollutants using hybrid Fenton processes (in both homogenous and heterogenous form) coupled with cavitation-based AOPs using both hydrodynamic cavitation and acoustic cavitation are given separately in Table 1.4, 1.5, 1.6 and 1.7.

1.3.3 Photo–Fenton Process

Photo–Fenton process is the combination of Fenton reagent and ultraviolet (UV) or solar or visible light irradiation to enhance the overall production of $^{\bullet}OH$ through (i) photo–reduction of Fe^{3+} to Fe^{2+} ($Fe^{3+} + H_2O_2 + h\nu \longrightarrow Fe^{2+} + {}^{\bullet}OH + H^+$), and (ii) direct photolysis of H_2O_2 ($H_2O_2 + h\nu \longrightarrow 2HO^{\bullet}$). The photochemical oxidation process accelerates the degradation induced by Fenton process through additional generation of radicals, which reduces the iron requirement and sludge generation in the system. The rate of photochemical oxidation depends on the quantum yield (Φ) (ratio of the molar flux of reacting molecules to the flux of photons absorbed by the molecule) and local volumetric rate of photon absorption of the molecule (Loubière et al., 2016; Bloh, 2019).

Many studies have demonstrated that heterogenous iron oxide (Fe_2O_3, Fe–OOH), iron–immobilized materials and iron composites ($ZnFe_2O_4$, $ZnO/ZnFe_2O_4$, $CuFe_2O_4$) can behave as photocatalyst through a very efficient hole-electron recombination. The exact mechanism of heterogeneous photo-Fenton oxidation is scant, and the authors usually have assumed that this mechanism is essentially a replica of homogenous system but involving iron surface species. In literature, a 2–step mechanism has been proposed for photocatalytic degradation, which includes: (1) generation of photo–excited electron/hole pairs by absorption of photon energy by the surface of photocatalyst, (2) either recombination of electron/hole pair and release of energy as heat, or (3) occurrence of surface for redox reaction with electron reducing Fe^{3+} to Fe^{2+}, and the hole transferring its charge to an organic substrate (Ruales-Lonfat et al., 2015; Rauf and Ashraf, 2019). The sequence of redox processes for the degradation of organic compounds in an aqueous solution is described as:

$$Fe_2O_3 + h\nu \longrightarrow Fe_2O_3(e^- + h^+)$$

$$e^-_{cb} + O_2 \longrightarrow O_2^{\bullet -}$$

$$h^+_{vb} + O_2^{\bullet -} \longrightarrow {}^1O_2$$

$$e^-_{cb} + Fe^{3+} \longrightarrow Fe^{2+}$$

$$h^+_{vb} + RX \longrightarrow RX$$

Cai et al. (2016) proposed the mechanism for the visible light/$ZnFe_2O_4$/persulfate system for the degradation of azo dyes, as illustrated in Figure 1.3. It suggests that light irradiation promotes the conversion from $\equiv Fe^{III}_{surface}$ to $\equiv Fe^{II}_{surface}$ and activation of persulfate ions, which accelerate the generation of $^{\bullet}OH$ and $SO_4^{\bullet -}$ for the degradation.

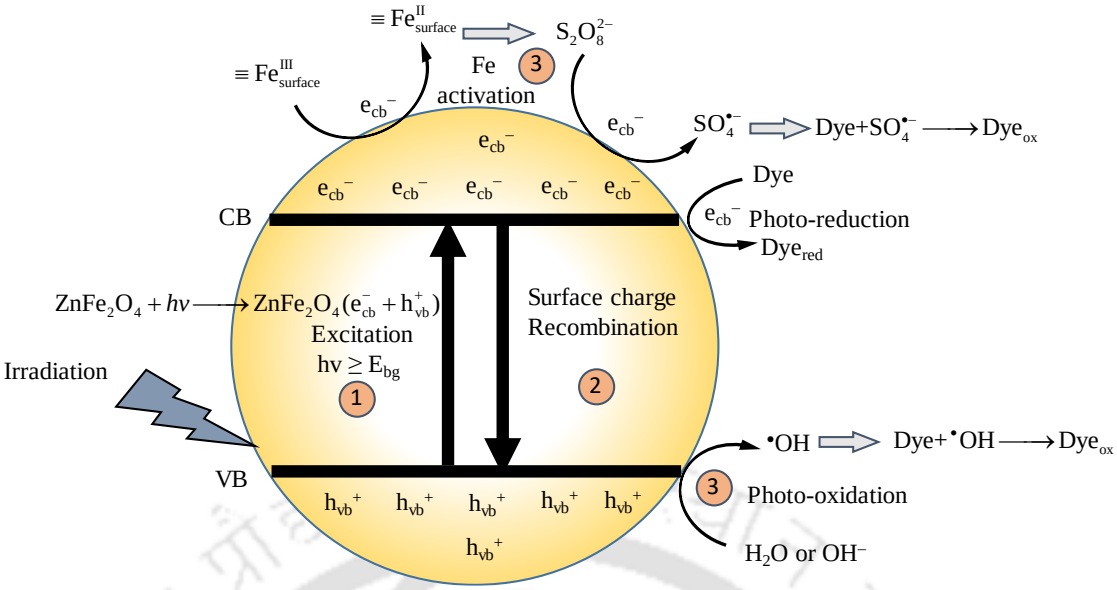

Figure 1.3: Possible mechanism of visible light assisted heterogenous $ZnFe_2O_4$/PS system

As a prologue to the thesis, the next section presents summaries of the published literature in four tables as: Table 1.4– Hydrodynamic cavitation assisted heterogeneous and homogeneous Fenton process, Table 1.5– Hydrodynamic cavitation assisted other hybrid AOPs, Table 1.6– Ultrasound–assisted heterogeneous and homogeneous Fenton process, Table 1.7– Ultrasound–assisted other hybrid AOPs.

Table 1.4: Literature survey on hydrodynamic cavitation (HC) assisted heterogeneous and homogeneous Fenton techniques

Hydrodynamic cavitation assisted heterogeneous Fenton process							
Pollutant	**Types of HC reactor**	**Heterogeneous Catalysts/ Hybrid AOPs**	**Experimental conditions**	**Highlights of work**			**References**
Rhodamine B (RhB)	Venturi	TiO_2 and Fe^{3+} doped TiO_2	Inlet pressure = 3.0 bar, $[RhB]_o$ = 10 mg/L, T = 40°C, Fe^{3+} – doped TiO_2 = 0.05:1.00 M ratio, t = 150 min.	HC alone = 58.32% degradation HC + Fe^{3+} – doped TiO_2 = 91.11% degradation			Li et al. (2020)
Orange G (OG)	Orifice	Zero valent iron (ZVI), H_2O_2	Volume = 1.25 L, $[OG]_o$ = 20 mg/L, pH = 3.0, fluid flow = 0.55 L/s, H_2O_2 = 0.5 g/L, ZVI = 0.5 g/L	HC alone = 25.6% degradation HC + H_2O_2 = 99.5% HC +ZVI + H_2O_2 = 99.8%			Cai et al. (2016b)
Unsymme-trical dimethyl hydrazine (UDMH)	Multiple hole orifice	Zero-valent iron in the form of iron metal blades (IMB)	$[UDMH]_o$ = 5 mg/L, volume = 150 L, pH = 3, recirculation time = 120 min, inlet pressure = 5.5 bar, downstream pressure = 1 bar	HC alone = 37% degradation HC + IMB = 71%			Angaji and Ghiaee (2015)
Imida-cloprid	Orifice and Venturi	H_2O_2, Fenton, (H_2O_2:$FeSO_4$), advanced Fenton (H_2O_2: Fe), $FeSO_4$:$Na_2S_2O_8$	$[Imidacloprid]_o$ = 20 ppm, inlet pressure = 4 bar, T = 34°C, pH = 3, H_2O_2 = 1:3, Fenton (H_2O_2:$FeSO_4$) = 2:1, advanced Fenton (H_2O_2:Fe Powder) = 2:1, $FeSO_4$:$Na_2S_2O_8$ = 1:4	Process	orifice	venturi	Patil et al. (2014)
				HC	23.85	27.93	
				HC+ H_2O_2	95.13	99.28	
				HC+Fenton	98.40	100	
				HC+Adv Fenton	99.41	100	
				HC+$FeSO_4$:$Na_2S_2O_8$	98.90	100	

Rhodamine B (RhB)	Multiple-hole orifice	Scrap iron sheets	pH = 3, inlet pressure = 5.8 bar, orifice plate = A (Number of holes = 32 and diameter = 1 mm), $[RhB]_o$ = 5 mg/L	HC + iron sheet = 71.1% degradation	Parsa and Zonouzian (2013)
2,4-dinitro phenol (DNP)	Orifice	H_2O_2, Fenton ($FeSO_4$:H_2O_2), Advanced Fenton (Fe:H_2O_2), CuO, $Na_2S_2O_8$,	$[DNP]_o$ = 20 ppm, pH = 4, T = 35°C, inlet pressure = 4 bar, t = 120 min, volume = 4 L, $[DNP]_o$:H_2O_2 = 1:5, $FeSO_4$:H_2O_2 = 1:0.5, Fe:H_2O_2 = 1:0.66, H_2O_2:CuO = 1:6, $FeSO_4$:$Na_2S_2O_8$ = 1:2	HC alone = 12.4% degradation HC+ H_2O_2 = 21.30% HC+Fenton = 100% HC+ Fe:H_2O_2 = 54.1% HC+CuO: H_2O_2 = 29.80% HC+ $FeSO_4$:$Na_2S_2O_8$ = 55.30%	Bagal and Gogate (2013)
Acid Red 88 (AR88)	Venturi	H_2O_2, Fenton like (Fe–TiO_2)	$[AR88]_o$ = 100 µM; inlet pressure = 5 bar, pH = 2, H_2O_2 = 100µM, volume = 4 L, Fe–TiO_2 = 1.8g/L	HC alone = 3.24 x 10^{-2} min^{-1} HC + H_2O_2 = 5.42 x 10^{-2} min^{-1} HC + Fenton like =8.75 x 10^{-2} min^{-1}	Saharan et al. (2011b)
Industrial wastewater treatment	Orifice	Fenton like (zero valent iron pieces:150 g)	pH = 2.5, volume = 8 L, iron pieces = 100, dilution factor = 25 times, H_2O_2 = 1900 mg/L, T = 30 ± 5°C, pressure = 1500 psi	HC + iron pieces = 60% TOC reduction HC + Copper winded iron pieces = 40% of TOC reduction	Chakinala et al. (2009)
Phenol	liquid whistle reactor	Fenton like (zero valent iron pieces: 80 g)	pH = 2.5, $[phenol]_o$ = 2.5 mM, H_2O_2 = 2000 mg/L, iron pieces = 50 pieces, inlet pressure = 1500 psi	HC + Fenton =50–60% TOC reduction in 105 min	Chakinala et al. (2008a)
Industrial wastewater effluents (E_1 and E_2)	liquid whistle reactor	Fenton like (zero valent iron pieces: 80 g)	dilution ratio = 50, pressure = 1500 psi, H_2O_2 = 1900 ppm, volume = 4L, E_1: COD= 42000mg/L, TOC = 14000 mg/L and E_2– COD= 17000 mg/L, TOC =6000 mg/L	HC + Fenton = 60% TOC removal and 85% COD removal (E_1) HC + Fenton = 70% TOC removal 85% COD removal (E_2)	Chakinala et al. (2008b)

Hydrodynamic cavitation assisted homogeneous Fenton process					
Pollutant	**Types of HC reactors**	**Catalysts/Hybrid AOPs**	**Experimental Condition**	**Highlights of work**	**Reference**
Congo red	Orifice	Fenton process (H_2O_2 and $FeSO_4$)	pH = 3, H_2O_2 = 1000 mg/L and $FeSO_4$ = 25 mg/L	HC = 6×10^{-4} mg/kJ yield efficiency Fenton = 2.9×10^{-3} mg/kJ HC + Fenton = 8.3×10^{-3} mg/kJ	Askarniya et al. (2020)
Methyl orange (MO)	Venturi	Iron and nickel ions	Inlet pressure = 4 bar, H_2O_2 = 0.005% v/v, $[MO]_o$ = 5 ppm, Fe = 20 mg/L, Ni = 10 mg/L, T = 20°C	HC alone = 31.57% degradation HC+H_2O_2 = 53.11% HC+H_2O_2+Fe+Ni = 90.15%	Innocenzi et al. (2019)
Methyl orange (MO)	Venturi	Iron and nickel ions	$[MO]_o$ = 5 ppm, Inlet pressure = 0.6 MPa, T = 20°C, Fe = 20 mg/L, Ni = 10 mg/L	HC alone = 22.51 % degradation HC + Fe+ Ni = 75%	Innocenzi et al. (2018)
Atrazine (ATZ)	Venturi	H_2O_2, $FeSO_4$, UV, sodium persulfate (SPS)	$[ATZ]_o$ = 20 ppm, inlet pressure = 3 bar, pH = 3, [ATZ]: H_2O_2 = 1:5, ATZ:SPS: $FeSO_4$ = 1:2:15	HC alone = 25.62 % degradation UV alone = 20.11 % HC +H_2O_2 = 42.15% HC + SPS+ $FeSO_4$ = 99.9% HC + UV = 44.44%	Jawale et al. (2018)
Ternary commercial dyes	Orifice	H_2O_2, TiO_2, $FeSO_4.7H_2O$	Inlet pressure = 6 bar, pH = 3, dye: H_2O_2 = 1:40, $FeSO_4.7H_2O$: H_2O_2 = 1:10, TiO_2 = 200 mg/L	HC alone = 8.53% TOC removal HC + H_2O_2 = 16.95% HC + Fenton = 38.42 % HC+UV+Fenton = 41.28%	Kumar et al. (2018)

Methomyl	Venturi	H_2O_2, Fenton reagent, O_3	$[Methomyl]_o$ = 25 ppm, volume = 5 lit, pH = 2.5, inlet pressure = 5 bar, $[Methomyl]_o$:H_2O_2 = 1:30, , $FeSO_4$:H_2O_2 = 1:20, O_3 = 2 gm/h	HC alone = 5.45 % TOC removal O_3 alone = 5.96% Fenton alone = 9.57% HC + H_2O_2 = 15.4 % HC + Fenton = 35.79% HC + O_3 = 70.79%	Raut-Jadhav et al. (2016)
Triazophos	Orifice	Fenton, O_3	Inlet pressure = 5 bar, pH = 3, $[Triazophos]_o$: $FeSO_4$: H_2O_2 = 1:4:4, O_3 = 1.95 gm/h	HC only: 49.7% degradation HC+Fenton = 83.12% O_3 alone = 70.41 % HC+O_3 in tank = 89.16%	Gogate and Patil (2015)
Imidaclo-prid	Venturi	Photolytic, Fenton, photo-Fenton, photo-catalytic (Nb_2O_5)	$[imidacloprid]_o$ = 25 ppm, inlet pressure = 15 bar, pH = 2.7, $[imidacloprid]_o$: H_2O_2 = 1:40, $FeSO_4.7H_2O$: H_2O_2 = 1:40, Nb_2O_5 = 200 mg/L	HC alone = 9.89% TOC removal HC + Fenton = 48.25% HC+UV+Fenton =48.96% HC + UV = 13.34 % HC+ UV+ Nb_2O_5 = 19.78%	Raut-Jadhav et al. (2013)
Methyl parathion (MP)	Orifice	H_2O_2, CCl_4, Fenton	$[MP]_o$ = 20 ppm Inlet pressure = 4 bar, pH = 3, H_2O_2 = 200 mg/L, CCl_4 = 5g/L, H_2O_2:$FeSO_4$ = 1:4	HC alone = 44.40% degradation HC+ H_2O_2 = 99.8% HC+CCl_4 = 81.60% HC+Fenton = 93.8%	Patil and Gogate (2012)

Dichlorvos	Orifice	H_2O_2, CCl_4, Fenton	Inlet pressure = 5 bar; temp. = 31°C; pH = 3, $[dichlorvos]_o$:H_2O_2 = 1:0.8, $FeSO_4$:H_2O_2 = 3:1, CCl_4 = 3 mg/L	HC alone = 16% HC+H_2O_2 = 17% HC+CCl_4 = 26.8% HC/Fenton = 91.5%	Joshi and Gogate (2012)
Rhodamine B (RhB)	Orifice and venturi	H_2O_2, Fenton reagent, CCl_4	$[RhB]_o$ = 10 ppm, inlet pressure= 4.84 atm, pH = 2.5, T = 40 °C, H_2O_2 = 200 mg/L, Fenton ($FeSO_4$:H_2O_2) = 1:5, CCl_4 =1 g/L	HC (venturi) alone = 59.3% degradation HC/H_2O_2 = 99.9% HC/Fenton = 99.9% HC/CCl_4 = 82%	Mishra & Gogate (2010)

Table 1.5: Literature survey on hydrodynamic cavitation (HC) assisted other AOPs Techniques

Pollutant	Types of HC reactor	Catalysts /Hybrid AOPs	Experimental Condition	Highlights of work	Reference
Acid RED-18 (AR-18)	Orifice (HC–O), venturi (HC–V), US	H_2O_2, UV, TiO_2,	$[AR\text{-}18]_o$ = 15 ppm, pH = 3, T = 35 °C H_2O_2 = 300 mg/L, TiO_2 = 300 mg/L,	HC–O, HC–V, US = 80%, 66% and 50% degradation respectively. HC–O + TiO_2 = 88.1% degradation HC–V + TiO_2 = 70.4% US + TiO_2 = 64.8%	Dhanke and Wagh (2020)
Benz[a]anthracene (B[a]A)	Orifice	Chlorine dioxide (ClO_2)	C_v = 0.05, inlet pressure = 4 bar, T = 34 °C, ClO_2 = 25 mg/L,	HC alone = 41.7% ClO_2 alone = 90.5% HC + ClO_2 (20 mg/L) = 98.9%	Wang et al. (2020)
Dicofol	Liquid whistle HC reactor	H_2O_2, Sodium bicarbonate	$[Dicofol]_o$ = 50 mg/L, inlet pressure = 7 bar, pH = 3, H_2O_2 = 50 mg/L, $NaHCO_3$ = 5 g/L	HC alone = 94 % degradation HC + H_2O_2 = 100% HC + $NaHCO_3$ = 80%	Panda and Manickam (2019)

Potassium thiocyante (KSCN)	Venturi	TiO_2, ZnO, CuO, O_3	Inlet pressure = 4 bar, pH = 2, $[KSCN]_o$: H_2O_2 = 1:1, O_3 = 400 mg/h, CuO = 0.15g/L	HC alone = 52.8% degradation HC + O_3 + CuO = 86.5% HC + H_2O_2 + CuO = 88% HC + H_2O_2 + O_3 = 95.6% HC + H_2O_2 + O_3 +CuO = 100% removal	Jawale and Gogate (2019)
Rhodamine B (RhB)	Multiple orifice	H_2O_2 or ClO_2	$[RhB]_o$ = 4 mg/L, Inlet pressure = 4 bar, pH = 2, $[RhB]_o$: H_2O_2 = 1:105.64, $[RhB]_o$: ClO_2 = 1:105.64	HC alone: 27.4% degradation H_2O_2 alone: 25.5% ClO_2 alone = 36.3 % HC + H_2O_2 = 80.6 % HC + ClO_2 = 95.3 %	Wang et al. (2019)
Effluents (S^{2-}: 2000 mg/L)	Venturi	H_2O_2, US (power = 173 W/L), O_3, Peroxone (O_3 + H_2O_2)	Reaction time = 30 min, O_3 and peroxone processes = 2.4 g/dm^3·h, H_2O_2 and peroxone processes = 12 g/dm^3·h	Process / HC / US Alone / 41.8% / 40.2% HC + O_3 / 100% / 99.8% HC + H_2O_2 / 100% / 100% HC + peroxone / 100% / 100%	Gągol et al. (2019)
2,4,6-trichlorophenol (2,4,6-TCP)	Venturi	H_2O_2, O_3	Inlet pressure = 4 bar, pH = 5, TCP:H_2O_2 = 1:5, O_3 = 400 mg/h	HC H_2O_2 and O_3 alone = 24.34% 17.4% and 85.85% degradation respectively HC + H_2O_2 = 62.07% degradation HC + O_3 = 97.11% HC + O_3 + H_2O_2 = 99.99%	Barik and Gogate (2018)

Carbamazepine (CBZ)	Venturi	UV, O_3	Inlet pressure = 4 bar, pH = 4, UV = 16 W, $[CBZ]_o$: H_2O_2 = 1: 5, O_3 = 400 mg/L,	HC, UV, H_2O_2 and O_3 alone = 38.7%, 18%, 29.4%, 49.1% degradation, respectively HC + UV = 52.9% HC + O_3 = 91.4% HC + H_2O_2+O_3 = 100%		Thanekar et al. (2018)
Effluents	Venturi	H_2O_2, O_3, Peroxone (O_3 + H_2O_2)	t = 360 min, inlet pressure = 8 bar, O_3 = 9.41 g/h, H_2O_2 = 1.0 mL/min) (Effluents: COD: 20,000 mg O_2/ L, BOD: 6000 mg O_2/ L, S^{2-}: 2000 mg/L)		COD (%)	BOD_5 (%)	Boczkaj et al. (2018)
				HC alone	13	17.5	
				O_3 alone	20.1	34.7	
				H_2O_2 alone	6.8	17.4	
				HC + H_2O_2	19.7	49.8	
				HC + O_3	39.7	50.1	
				O_3+ H_2O_2	37.0	41.4	
				HC + O_3+ H_2O_2	24.8	31.9	
Tetracycline	Venturi	UV (254 nm), TiO_2	$[Tetracycline]_o$ = 30 mg/L, TiO_2 = 100 mg/L, t = 90 min	HC alone = 12.2% degradation UV+TiO_2 = 28.1% HC + UV+TiO_2 = 78.2%			Wang et al. (2017)
Methylene blue (MB)	Venturi	Bismuth-TiO_2 (Bi-TiO_2)	Inlet pressure = 5 bar, pH = 2, $[MB]_o$: H_2O_2 = 1:20, t = 60 min, Bi-TiO_2 = 200 mg/L	HC alone: 9.46 % TOC removal HC + H_2O_2 = 18.41% HC + Bi-TiO_2 = 12.68 %			Kumar et al. (2017)
Crystal violet (CV)	Venturi	UV (125 W), Pure TiO_2, Fe–TiO_2, Ce–TiO_2	$[CV]_o$ = 50 mg/L, temp. = 35 °C, pressure = 5 bar pH = 6.5, Solid catalysts = 0.6 g/L, Fe and Ce loading = 0.8 & 1.6 %	UV alone = 0.0029 min^{-1} rate UV + TiO_2 = 0.0048 min^{-1} rate HC alone = 0.003 min^{-1} rate HC + TiO_2 + 0.8% Fe: 0.0332 min^{-1} rate HC + TiO_2 + 1.6% Ce: 0.0302 min^{-1} rate			Bethi et al. (2016)

Polyacryla-mide (PAM)	Venturi	H_2O_2, O_3, UV (λ= 254 nm)	Inlet pressure = 3 bar, UV = 8W, O_3 = 400 mg/h, H_2O_2 = 0.2%	H_2O_2 = 18.15 % depolymerization HC = 35.38% UV = 40.83% O_3 = 50.34% HC+UV+O_3 = 89.06% HC+UV+H_2O_2 =97.27%	Prajapat and Gogate (2016)
Methyl orange (MO)	Orifice	zero-valent copper (Cu^0)	Volume = 5 L, $[MO]_o$ = 10 ppm, Pressure = 0.4 MPa, pH = 3, Cu^0 = 40 mg/L	HC alone: 6.8% degradation Cu^0 alone = 20% HC + Cu^0 = 83%	Li et al. (2015)
Acid Orange 7 (AO-7)	Orifice	Two electrodes (stainless and graphite), H_2O_2	$[AO\text{-}7]_o$ = 10 mg/L, Inlet pressure = 3.9 kgf/cm^2, pH = 3.0, applied voltage = 37.7 V	C-HC system: 15.42% degradation C-HC + H_2O_2 system: 39.5% M-HC system: 22.06% M-HC + H_2O_2 system: 51% EFM-HC, EFM-HC, EFM-HC+ H_2O_2 system = 100%	Jung et al. (2015)
Diclofenac sodium	Venturi	UV lamp (250 W), TiO_2, H_2O_2	Inlet pressure = 3 bar, pH = 4, volume = 5 L, t = 120 min; TiO_2 = 0.2 g/L, H_2O_2 = 0.2 g/L	HC alone = 26.85% degradation, UV alone = 49.75% HC+UV = 65.53% HC+TiO_2 = 30.37% HC+UV+TiO_2 = 79.38% HC+UV+TiO_2+H_2O_2 = 94.78%	Bagal and Gogate (2014)

Orange acid-II (OA-II) and brilliant green (BG)	Orifice	Ultrasonic horn, H_2O_2, $Na_2S_2O_8$	$[OA\text{-}II]_o$ = 20 mg/L, [BG] = 20 mg/L, T = 20°C, pH = 3, Power = 80 W, Inlet pressure = 5 bar	Process	OA-II	BG	Gogate and Bhosale (2013)
				US	49.5%	68%	
				HC	34.2%		
				US +H_2O_2	75% (95 mg/L)	81% (571 mg/L)	
				HC + H_2O_2	96% (571 mg/L)	86% (244 mg/L)	
				US + $Na_2S_2O_8$	70% (1607 mg/L)	82% (23 mg/L)	
				HC + $Na_2S_2O_8$	100% (535 mg/L)		
Imida-cloprid	Venturi	H_2O_2	Inlet pressure = 15 bar, pH = 2.7, $[Imidacloprid]_o$ = 25 mg/L, $[Imidacloprid]_o$: H_2O_2 = 1:40	HC alone = 11.4% degradation H_2O_2 alone = 11.2% HC+ H_2O_2 = 100%			Raut-Jadhav et al. (2013)
Microcystis aeruginosa (Ma)	Orifice (D = 5, 10 and 12 mm)	O_3 with 4-tandem gas-wash cylinders	$[Ma]_o$ = 30 µg/L, volume = 1.75 L, D = 12 mm, T = 20°C, O_3 = 1.9 mg/min, t = 10 min	HC alone = 15% removal O_3 = 35% HC + O_3 = 99%			Wu et al. (2012)
Reactive Red 120 (RR120)	Venturi	H_2O_2	$[RR120]_o$ = 34 µM, pH = 2.0, inlet pressure: 5 bar, H_2O_2 = 2040 µM, volume = 6 L	HC alone = 60% decolorization HC + H_2O_2 = 100%			Saharan et al. (2011a)

Table 1.6: Literature survey on ultrasound (US) assisted heterogeneous and homogeneous Fenton techniques

Ultrasound assisted heterogeneous Fenton process					
Pollutant	**Types of HC reactor**	**Catalysts /Hybrid AOPs**	**Experimental Condition**	**Highlights of work**	**Reference**
Chloramphenicol (CAP)	Ultrasonic cleaner (f = 20, 40 and 60 kHz).	nZVI, persulfate (PS), [Fe(II)], [Fe(III)]	$[CAP]_o$ = 5 mg/L, nZVI = 0.5 g/L, PS = 1.0 mM, power = 0.36 W/mL, f = 40 kHz, [Fe(II)] & [Fe(III)]=1.0 mM	nZVI + PS = 62.7% degradation US + nZVI + PS = 98.1% US + Fe(II) + PS = 75.5% US + Fe(III) + PS = 52.0%	Zhang et al. (2020)
4-nitro-phenol (4-NP)	Sonicator with titanium probe (f=20kHz), UV	$FeVO_4@CeO_2$, H_2O_2	$[4\text{-NP}]_o$ = 20 ppm, pH = 7, Fenton : $FeVO_4@CeO_2$ = 0.1 g/L and H_2O_2 = 10 mM	US alone = 16% degradation UV alone = 27% US + H_2O_2 (20 mM) = 38% US + Fenton = 85% UV + Fenton = 94% US + UV+ Fenton = 100% (30 min)	Eshaq et al. (2020a)
p-nitro-phenol (PNP)	Sonicator with titanium probe (f=20kHz), UV	$FeVO_4@BiOCl$, H_2O_2	$[PNP]_o$ = 20 ppm, $FeVO_4@BiOCl$ = 0.1 g/L, H_2O_2 = 10 Mm, pH = 7	Sonophotocatalysis > photocatalysis > sonocatalysis.	Eshaq et al. (2020b)
Methylparaben (MP)	US (20 kHz)	Co-Fe carbon xerogel (CX/CoFe)	CX/CoFe = 25 mg/L, $[MP]_o$ = 1 mg/L, t = 60 min, US_1 = 25 W/L US_2 = 52 W/L	US_1 alone = 10% degradation US_2 alone = 64% US_1 + CX/CoFe = 54.6% US_2 + CX/CoFe = 100%	Zanias et al. (2020)

Alachlor	Ultrasonic horn (20 kHz max. P = 100 W), Bath (400 kHz, P = 80 W)	H_2O_2, CCl_4, $FeSO_4$, Fe power (100 mesh size)	$[Alachlor]_o$ = 20 ppm, pH = 3, Alachlor: H_2O_2 = 1:3.5, Alachlor : CCl_4 = 1:50, $FeSO_4$:H_2O_2 = 1:2, Fe: H_2O_2 = 1:3.5,		Horn	Bath	Bagal and Gogate (2012)
				US alone	55.8 %	3.5 %	
				US + H_2O_2	88.4 %	8.6 %	
				US + CCl_4	87.2%	32.2%	
				US + Fenton	100%	96.4%	
				US + advanced Fenton	100%	100%	
Nitro-benzene (NB)	US probe (f = 20 kHz, P = 125 W)	FeOCl (I), CuOCl (II), ZnOCl (III) and BiOCl (IV), UV (λ = 254 nm)	$[NB]_o$ = 20 ppm, pH = 7, catalyst = 0.1 g/L, H_2O_2 = 5 mM, T= 25 °C	Sonophotocatalytic > photocatalytic > sonocatalytic with (I) > (II) > (IV) > (III) solid catalyst			ElMetwally et al. (2019)
Orange II (O-II)	US probe (f = 20 kHz)	Fe–Co/SBA-15, Peroxymonosulfate (PMS)	$[O\text{-}II]_o$ = 0.30 mM, PMS = 3.2 mM, catalyst = 1.0 g/L, P = 104.8 W/L, T = 20°C, pH = 6	US alone = 3% degradation PMS + catalyst = 25.2% US + catalyst + PMS = 95.5%			Cai et al. (2016)
Diclofenac (DF)	US (f = 213 kHz,), Xenon UV lamp (λ = 320, 420 nm)	TiO_2, Fe–ZnO	$[DF]_o$ = 0.07 mM, TiO_2 & Fe–ZnO = 1 g/L)	US alone = 15.2×10^{-7} M min^{-1} US + TiO_2 = 11.5×10^{-7} M min^{-1} UV + TiO_2 = 36.8×10^{-7} M min^{-1} US + UV + TiO_2 = 64.4×10^{-7} M min^{-1} US + Fe–ZnO= 14.3×10^{-7} M min^{-1} US + vis + Fe–ZnO = 15.3×10^{-7} M min^{-1}			Madhavan et al. (2010)
Bisphenol A (BPA)	US (f = 40 kHz, 100 W)	Fe_3O_4, H_2O_2	T = 35°C, $[BPA]_o$ = 20 mg/L, H_2O_2 = 160 mmol/L, Fe_3O_4 = 585 mg/L	US alone = negligible US + Fe_3O_4 + H_2O_2 = 100% (pH 3) US + Fe_3O_4 + H_2O_2 = 98.1% (pH 7) US + Fe_3O_4 + H_2O_2 = 95.1% (pH 9)			Huang et al. (2012)

Imida-cloprid	US horn (f = 20 kHz, P= 240 W), US bath (f = 25 kHz, P = 1 kW)	UV (λ = 350, 450, 365 nm), H_2O_2, CuO, advanced Fenton reagent (AFP) (Fe:H_2O_2)	$[imidacloprid]_o$ = 20 ppm, pH = 5, H_2O_2 = 35 ppm, CuO = 2 g/l, Fe = 1g/L		US horn	US bath	Patil et al. (2014)
				US	66.8	26.1	
				US + H_2O_2	92.7	78.7	
				US + CuO	77.7	57.5	
				US + AFP	96.5	89.3	
				US + UV	75.5	32.8	
				US+ UV+ H_2O_2	98.5	83.2	
C.I. Acid Orange 7	US bath (P = 100 W, f =20 kHz)	Fe_2O_3/SBA-15, UV (4 W, λ = 254 nm)	C_0 = 100 mg/L, H_2O_2 = 8 mmol/L, P = 80 W, pH= 2; Fe_2O_3/SBA-15 = 0.3 g/L	US + H_2O_2 = 12.6% degradation UV + US + H_2O_2 = 20.0% UV + catalyst + H_2O_2 = 26% US + catalyst + H_2O_2 = 57% US + UV + catalyst + H_2O_2 = 84.9%			Zhong et al. (2011)

Ultrasound assisted homogeneous Fenton process

Pollutant	Types of HC reactor	Catalysts /Hybrid AOPs	Experimental Condition	Highlights of work	Reference
amoxicillin (AMX)	US (40 kHz)	UV (365 nm), Fenton	$[AMX]_o$ = 10 ppm, Fe^{2+} = 30 mg/l, H_2O_2 = 375 mg/L, pH = 3,	100 % degradation = Photo-Fenton (3.5 min) > Sono-Photo-Fenton (6.0 min) > Solar photo-Fenton (9 min) > Fenton (12 min) > Sono-Fenton (20 min)	Verma and Haritash, (2019)
Direct Red 81 (DR81)	US probe (f = 120 kHz, 60 W)	Fenton	$[DR81]_o$ =50 mg/L, pH = 3.0, Fe^{2+} = 0.2 g/l, H_2O_2 = 5.1 mM	US = 20 % degradation US + Fenton = 99%	Harichan-dran and Prasad, (2016)

Polycyclic aromatic hydrocarbons (PAHs)	US probe (f = 20 kHz)	Fenton, H_2O_2	t = 60 min, ultrasonic density = 1.80 w/cm^3, H_2O_2 = 140 mmol/L, Fe^{2+} = 140 mmol/L, pH = 3	16 PAHs degradation efficiency = Sono–Fenton (73.0%) > Fenton (70.3%) > ultrasound (41.4%)		Lin et al. (2016)
Dichlorvos	US bath (P = 150 W, f = 36 kHz)	H_2O_2, TiO_2, solar, Fenton & O_3	$[Dichlorvos]_o$ = 20 mg/L, pH = 3, $[Dichlorvos]_o$:H_2O_2 = 1:25, TiO_2 = 0.1, H_2O_2:$FeSO_4$ = 4:4	US, Fenton & O_3 alone: 6.4%, 33.2% & 100 % degradation respectively US + H_2O_2, US + Fenton = 20%, 81% degradation respectively US + solar + TiO_2 = 83.12% US + ozone = 100%		Patil and Gogate (2015)
Methylene Blue (MB), Acid Red B (ARB)	US bath (f = 40 kHz, P = 200 W)	UV, Fenton like (Fe^{3+} + H_2O_2), ferrioxalate (FeOX)	$[ARB]_o$ = 0.04 mM, [MB] = 0.063 mM, Fe^{3+} = 0.2 mM, $C_2O_4^{2-}$ = 0.6 mM, H_2O_2 = 5 mM, pH = 3, T = 298 K			Chakma et al. (2015)
					ARB	MB
				US alone	14.76	6.84
				US + Fenton like	68.94	99.65
				US + Fenton like + FeO_X + UVA	85.87	96.39
Pharmaceutical waste-water	US horn (f=24 kHz, 200 W)	Fenton, UV (150 W, λ = 190–280 nm)	T = 30 °C, pH = 7, $[TOC]_o$ = 125 ppm, Fe^{2+} = 0 ppm	US alone = 6% TOC removal UV + H_2O_2 = 71% US + UV+H_2O_2 = 100%		Monteagudo et al. (2014a)

Reactive Blue 4 (RB4)	US horn (f=24 kHz, 200 W	Fenton, UV (15 W, λ = 254 nm)	$[RB4]_o$ = 30 mg/L, pH = 3, t = 60 min, amplitude = 60%, pulse length = 1, H_2O_2 = 500 mg/L, Fe^{2+} =5 mg/L	UV & US alone = 5% TOC removal UV + H_2O_2 = 33% UV + Fenton = 82% US + UV + Fenton = 94%	Monteagudo et al. (2014b)
Reactive Blue 19 (RB 19)	US probe (20 kHz, 200 W)	Fenton	$[RB19]_o$ = 25 mg/L, H_2O_2 = 0.5 mM, $FeSO_4$ = 3 mg/L, pH = 3.5, P = 8 W/cm^2	US, H_2O_2, $FeSO_4$ alone: < 5% degradation Fenton = 50% US + Fenton = 78%	Siddique et al. (2014)
Bisphenol A	US bath (f = 40 kHz, P = 200 W)	Fenton	$[BPA]_o$ = 10 ppm, Fe^{2+} = 0.36 mM, H_2O_2 = 7.85 Mm, pH = 2	US = 19.9% degradation US + Fenton = 98.7 % degradation	Chakma and Moholkar (2014)
Antipyrine (ANP)	US horn (f = 24 kHz, P = 200 W)	UV (P = 150 W, λ = 190 – 280 nm), Fenton	pH = 2.7, H_2O_2 = 1500 ppm, Fe(II) = 12 ppm, pulse length (cycles) = 0.3 (during 15 min) and 1 later, $[ANP]_o$ = 50 mg/L	US + UV + Fenton = 92% TOC removal	Durán et al. (2013)
Acid Red B (ARB) and Blue HE2R (BLH)	US bath (f = 40 kHz, P = 200 W)	Fenton	$[Dye]_o$ = 10 ppm $FeSO_4.7H_2O$ = 2.5 mg, H_2O_2 = 27µL, P = 101.3 kPa, time = 60 min	ARB: US = 14.04%; US + H_2O_2 = 13.35%; US + Fenton = 91.81% BLH: US = 11.43%; US + H_2O_2 = 38.59%; US + Fenton = 100.0%	Chakma and Moholkar (2013)
Reactive black 5 (RB5)	US probe, UV (λ = 365 nm)	Fenton, H_2O_2, ligands	Fe^{3+} = 0.5 mM, ligand = 1.0 mM, $[RB5]_o$ = 20 mg /L, ligands- Oxa, Cit, Tar, Suc, NTA and EDTA	$k_{\bullet OH}$ = US/Fe(III)–Oxa < UV/Fe^{3+} < US/Fe^{3+} < UV/Fe(III)-Oxa ≈ US/UV/Fe^{3+} < US/UV/Fe(III)-Oxa	Zhou et al. (2011)
Carbofuran	US probe (f = 20 kHz, P = 300 W)	Fenton, H_2O_2	$[Carbofuran]_o$ = 50 mg/L, pH = 3, Fe^{2+} = 10 mg/L & H_2O_2 = 100 mg/L	Ultrasound + Fenton = 100% degradation	Shih et al. (2010)

Table 1.7: Literature survey on ultrasound cavitation (US) assisted other AOPs Techniques

Pollutant	Types of HC reactor	Catalysts /Hybrid AOPs	Experimental Condition	Highlights of work	Reference
Industrial wastewater	US horn (f = 20 kHz, P = 120 W)	UV (P = 125 W), O_3, TiO_2, CuO	pH = 2, T = 31 °C, P = 100 W, O_3 = 400 mg/h	US alone = 51.52% COD removal US + H_2O_2 = 57.14 US + UV + CuO = 78.5% US + UV + TiO_2 = 85.5% US + UV + CuO + O_3 = 91.67% US + UV + TiO_2 + O_3 = 94.44%	Ayare and Gogate (2020)
Abattoir wastewater (COD = 242 mg O_2/L BOD = 53 mg O_2/L)	US (f = 44, 300 & 1000 kHz, P = 40 W)	O_3 (71 mg/L)	f = 300 kHz, t = 60 min	US: COD 18%, BOD 50% O_3: COD 33%, BOD 74% US + O_3: COD 44%, BOD 78%	Alfonso-Muniozguren et al. (2020)
Rhodamine B (RhB)	Ultrasound Bath (40 kHz or 59 kHz)	ZnO (Desert Roses, Multipods, Microwires, Nanoparticles, Nanowires), sun-light	Volume = 10 ml, pH = 5.8, $[RhB]_o$ = 2.5 ppm, ZnO = 0.5 mg/mL	US + ZnO (Desert Roses) = 100% degradation US + ZnO (Multipods) = 86% US + ZnO (Microwires) = 62% US + ZnO (Nanoparticles) = 69% US + ZnO (Nanowires) = 66% Sunlight + ZnO (DRs) = 76% US + Sunlight + ZnO (Desert Roses) = 100%	Lops et al. (2019)

Rhodamine B (RhB)	US (P= 120 W, f = 33 kHz)	$ZnSnO_3$, benzoquinone (BQ), EDTA	$[RhB]_o = 4.7 \times 10^{-6}$ M, $ZnSnO_3$ = 25 mg	US + $ZnSnO_3$ = 4.5×10^{-2} min^{-1} US + $ZnSnO_3$ + BQ = 2.0×10^{-2} min^{-1} US + $ZnSnO_3$ + EDTA = 4.6×10^{-3} min^{-1}	Biswas et al. (2019)
4-Acetamido-phenol (4-AMP)	US (f = 20 kHz, P = 750 W)	UV (280 – 400 nm), Sm-doped TiO_2, N-doped TiO_2, HC (P_{inlet}= 5 bar),	$[4\text{-AMP}]_o$ = 50 ppm, catalyst =2 g/L, pH = 6.8	US alone: 7.0 % degradation US + UV = 9.4 % US + UV + N-TiO_2 = 86.6% HC alone = 8.3% HC + UV = 14.6% HC + UV + N-TiO_2 = 90.8%	Rajoriya et al. (2019)
Eosin B	US (f = 20 kHz P: 50–250 W)	ZnO	P = 250 W, t = 70 min, [dye] = 5.08 mg/L, ZnO = 2.17 g/l	US + ZnO = 93.46% degradation	Mahdavi and Talesh (2019)
Rhodamine B (RB)	US bath (P= 300W)	Stirrer (0 – 900 r/min)	Stirring speed = 700 r/min, RB = 10 mg/L, f = 40 kHz	98% degradation in three-necked bottle	Zhang et al. (2019)
Bisphenol AF (BPAF)	US (P = 120 W, f = 20 kHz)	Zero-valent copper (ZVC), persulfate (PS)	$[BPAF]_o$ = 20 µM, ZVC = 0.5 g/L, PS = 1 mM, T = 20 °C, pH = 4	ZVC or PS alone = negligible US = 13.7% degradation US + ZVC = 16.7% PS + US = 31.7% PS + ZVC = 59.8% PS+ ZVC + US = 97.0%	Wang et al. (2019)
Lovastatin	US (f = 35 kHz, P = 95W)	g-C_3N_4, H_2O_2, UV	H_2O_2 = 4 mM, g-C_3N_4 = 0.050 g/L, $[Lovastatin]_o$ = 30 mg/L, pH = 6.8	US alone = 18.49% degradation US + UV = 38.71 % US + H_2O_2 = 41.64 % US +g-C_3N_4+H_2O_2 + UV = 93.25%	Dinesh and Chakma (2019)

Acid Orange 7 (AO7)	US (100 W, f = 20 kHz)	ZnO–GAC, persulfate (PS)	$[AO7]_o$ = 50 mg/L, Catalyst = 0.5 g /L, PS = 0.5 g/L, P = 60 W, T = 30°C, pH = 3	US and PS alone = negligible US + PS = 20.7% degradation US + ZnO–GAC = 56.7% ZnO–GAC + PS = 68.7% US + ZnO–GAC + PS = 91.2%			Liu et al. (2018)
2,4-dichlorophenol (2,4-DCP)	US bath (f = 36 kHz, P = 150 W)	O_3, CuO, ZnO	$[2,4\text{-DCP}]_o$ = 20 ppm, T = 34°C, pH = 5, ZnO = 0.15 g/L, CuO = 0.08 g/L, CuO =0.08 g/L, O_3 = 400 mg/h	US alone = 15.7% degradation O_3 alone = 81% US + ZnO = 38.9% US + CuO = 40.36% US + O_3 + ZnO = 95.66% US + O_3 + CuO = 97.03%			Barik and Gogate (2017)
Ibuprofen & sulfamethoxazole	US (f = 1000 kHz, P = 180 ± 3 W)	Single walled carbon nanotubes (SWNTs).	T = 15 °C, pH = 7, SWNTs = 45 mg/L, PhACs = 10 µM, t = 60 min		IBP (min^{-1})	SMX (min^{-1})	Hamadani et al. (2017)
				US only	1.85×10^{-2}	1.35×10^{-2}	
				SWNTs	0.99×10^{-2}	1.03×10^{-2}	
				US + SWNTs	3.25×10^{-2}	2.68×10^{-2}	
4-chloro 2-aminophenol (4C2AP)	Ultrasonic horn (20 kHz) and bath (36 kHz)	UV (254 nm), O_3	pH = 4, T = 30°C, horn power = 120 W, $[4C2AP]_o$ = 20 ppm		Horn	Bath	Barik and Gogate (2016)
				US	24.17	15.46	
				O_3	40.24	39.6	
				UV	80.8	69.91	
				US + O_3	50.05	53.29	
				US + UV	88.42	74.96	
				US + UV + O_3	99.27	89.9	

Methyl orange (MO)	US (f = 40 kHz, P = 80–200 W)	Bi_2WO_6	$[MO]_o$ = 10 mg/L, Bi_2WO_6 = 1.00 g/L, pH = 7	US = 16% degradation US + Bi_2WO_6 = 84%			He et al. (2016b)
Acid Orange 7 (AO7)	US probe (f = 20 kHz, P = 100 – 500 W)	Zero-valent aluminum (ZVAl)	$[AO7]_o$ = 20 mg/L, ZVAl = 2 g/L, pH = 2.5, P = 400 W	US and ZVAl alone = negligible degradation US+ ZVAI = 96.5% degradation			Wang et al. (2014)
Acetaminophen (AAP) and naproxen (NPX)	US (f = 28 and 1000 kHz, P= 180 W)	Single-walled carbon nanotubes (SWNTs)	pH = 6, T = 15°C, SWNT = 45 mg, AAP = 5 µM and $[NPX]_o$ = 5 µM		AAP ($\times 10^{-2}$ min^{-1})	NPX ($\times 10^{-2}$ min^{-1})	Im et al. (2013)
				US (28 kHz)	0.36	1.18	
				US (1000 kHz)	2.35	6.53	
				SWNTs	0.87	2.23	
				US (28 kHz) + SWNTs	1.51	4.27	
				US (1000 kHz) + SWNTs	3.57	7.17	
Phenol	US (f = 850 kHz, P =170 W)	Two stainless steel electrodes	$[Phenol]_o$ = 1 mmol/L, H_2SO_4= 0.36 g/L, voltage = 10 V, t = 1 h	US = 16% degradation EC = 32% US + EC = 75%			Ren et al. (2013)

Amoxicillin	US probe (f = 20 kHz, 200 W)	Oxone, $Co(NO_3)_2$,	$[amoxicillin]_o$ = 0.095 mmol/L, oxone= 5 mmol/L, cobalt solution = 0.025 mmol/L	Oxone alone = 22% COD removal Oxone + Co^{2+} = 51% Oxone + US = 63% Oxone + Co^{2+} + US = 85%	Su et al. (2012)
ARB, RR2, DB6	US probe (f = 20 kHz, P = 500 W)	TiO_2, SDS	TiO_2 = 50 mg, SDS = 0.5 mM, $[dye]_o$ = 10 ppm ARB - Acid Red B, RR2 - Reactive Red 2, DB6- Direct Blue 6	See nested table below	Balaji et al. (2011)

	ARB	RR2	DB6
US	26.3	20.4	22.8
US + TiO_2	45.7	24.7	33.1
US + TiO_2 + SDS	8.1	3	17.7

1.4 AIM, APPROACH AND SCOPE OF THE PRESENT THESIS

In the previous sections, an introduction was given about different advanced oxidation processes (AOPs) along with their chemistry. An extensive literature review on hybrid systems combining different AOPs has also been presented. One single conclusion that can be drawn from the literature review is that hybrid AOPs achieve much faster and higher degradation/mineralization of the organic pollutants as compared to single conventional AOPs. This result is true irrespective of the type of organic pollutant and its physical/chemical properties. This is an encouraging result that opens opportunities for design and application on large scale systems. However, most of the studies in previous literature are of black–box kind in which the functionality of the system is tested without peering into its internal structures and workings –or– in simpler words, the basic underlying physical/ chemical mechanism.

Effective scale-up of technology requires thorough knowledge of the basic mechanisms of the physical, chemical, mechanical or biological processes and transformations that occur in the system. In the present context of hybrid AOPs, a thorough knowledge of the synergistic (both positive and negative) interactions among the individual AOPs is essential that leads to higher and faster degradation. The present thesis is aimed at fulfilling this knowledge gap. This thesis comprises of the studies on degradation / mineralization of a variety of pollutants from petrochemical and pharmaceutical industries using hybrid cavitation based AOPs. Both ultrasonic and hydrodynamic cavitation have been coupled with other AOPs like persulfate, heterogeneous Fenton and photolysis. Novel catalysts have been synthesized for the heterogeneous Fenton system. For deducing the mechanism of the hybrid AOPs, the new approach of analyzing experimental results on the basis of a mathematical (or physical) model has been adopted.

The results of the mathematical model have been compared against the experimental results. Such analysis has brought forth very interesting aspects of the basic mechanism of the process.

An outline of the thesis contents is given herewith:

Chapter 1 (the present chapter) starts with an introduction to the topic and theme of the thesis. Initially, a background on the technique of cavitation based advanced oxidation processes (AOPs) and the other conventional processes has been given. Following this, an extensive literature review on hybrid advanced oxidation processes has been given for the degradation of biorecalcitrant pollutants appearing in wastewater. On the basis of this literature review, the objectives and approach of the thesis have been described.

Chapter 2 describes the degradation of sulfadiazine (SDZ) in the hybrid hydrodynamic cavitation/heterogeneous Fenton/persulfate hybrid system. Two types of iron oxides, viz. Fe_3O_4 and α–Fe_2O_3 were synthesized using solvothermal and hydrothermal techniques as the solid catalyst of heterogeneous Fenton like system. In hybrid system, HC accelerates the *in-situ* oxidation of SDZ via activation of persulfate (to produce $SO_4^{\bullet-}$ radicals), and also reduces mass transfer limitation in the system for the solid catalyst (to produce additional $^{\bullet}OH$ radicals). The effect of operating parameters as initial SDZ concentration, inlet pressure, pH, H_2O_2, $Na_2S_2O_8$, Fe_3O_4 and α–Fe_2O_3 loading on the degradation of SDZ have been investigated. A kinetic model for SDZ degradation has been proposed on the basis of homogeneous Fenton/persulfate system, and experimental degradation profiles were analyzed vis-à-vis the simulated profiles of SDZ degradation.

Chapter 3 presents results on the degradation of SDZ in hybrid hydrodynamic cavitation/ heterogeneous Fenton/ persulfate system. The effects of following parameters on the SDZ degradation was analyzed: (1) inlet pressure, (2) cavitation number, (3) α (total perimeter

of the holes/total area of opening), and (4) β (total flow area/cross-sectional area of the pipe). The intermediates and by-products of degradation were identified using LC-MS analysis and a possible degradation pathway was proposed on that basis. A kinetic model for SDZ degradation was extended for different orifice plates and compared with experimental degradation profiles.

Chapter 4 presents the mechanistic investigation of sono – heterogenous Fenton – persulfate oxidation process using SDZ as model pollutant. Yolk shell structure magnetic nanoparticle with the typical structure of Fe_3O_4@hollow@$mSiO_2$ was synthesized by adopting Stöber sol-gel method and ultrasonic etching followed by extraction method. The operating parameters viz. ultrasound power, pH, H_2O_2, Fe_3O_4@hollow@$mSiO_2$, $Na_2S_2O_8$ loading were optimized for maximum degradation. Inhibition effect of inorganic anions like Cl^-, NO_3^-, CO_3^{2-}, SO_4^{2-} was also studied on SDZ degradation. An extended kinetic model for anions on the SDZ degradation was concurrently analyzed with experiment data.

Chapter 5 describes the study of degradation of 4-nitrophenol (PNP) degradation with hydrodynamic cavitation assisted heterogeneous Fenton-like catalyst. Spherical shaped Fe_3O_4 nanoparticles were synthesized using solvothermal method with higher saturation magnetization. The optimization of operating parameters such as inlet pressure, initial concentration, H_2O_2, Fenton and pH was done. Computational study of the hydrodynamic cavitation reactor (orifice plate) was performed to quantify and characterize the low-pressure region in the downstream section. The degradation profiles of PNP in the heterogeneous Fenton like system were modelled on the basis of homogenous Fenton systems.

Chapter 6 deals with the degradation of carbamazepine (CBZ) using hydrodynamic cavitation-assisted photo-Fenton system. Bimetallic $ZnO/ZnFe_2O_4$ magnetic nanoparticles were synthesised in a Teflon-lined autoclave. The operational parameters as inlet pressure, pH, CBZ concentration, UV power, $ZnO/ZnFe_2O_4$, and $Na_2S_2O_8$ was optimized. An empirical model was developed through non-linear regression analysis varying range of operating parameters. A kinetic model for CBZ degradation was proposed based on homogeneous photo-Fenton/ persulfate system, and experimental degradation profiles were analyzed vis-à-vis simulated profiles.

Chapter 7 presents a summary and overview of all studies in the thesis using hybrid AOPs coupled with either ultrasonic or hydrodynamic cavitation. Different synergistic interactions among the physical/ chemical effects of ultrasonic and hydrodynamic cavitation and the mechanism of the coupling AOP have been identified and compared on the basis of characteristics of cavitation bubble dynamics in two types of cavitation reactors. A discussion is also presented as how the mechanistic insights obtained in different studies of the thesis using different kinds of pollutants could form general guidelines for optimization and scale-up of the novel reactors employing combination of AOPs or the hybrid AOPs.

REFERENCES

Adewuyi, Y.G., Sonochemistry in environmental remediation. 1. Combinative and hybrid sonophotochemical oxidation processes for the treatment of pollutants in water, *Environ. Sci. Technol.* 39(10) (2005a) 3409-3420.

Adewuyi, Y.G., Sonochemistry in environmental remediation. 2. Heterogeneous sonophotocatalytic oxidation processes for the treatment of pollutants in water. *Environ. Sci. Technol.* 39(22) (2005b) 8557-8570.

Alfonso-Muniozguren, P., Bohari, M.H., Sicilia, A., Avignone-Rossa, C., Bussemaker, M., Saroj, D., Lee, J., Tertiary treatment of real abattoir wastewater using combined acoustic cavitation and ozonation. *Ultrason. Sonochem.* 64 (2020) 104986.

Al-Hamadani, Y.A., Jung, C., Im, J.K., Boateng, L.K., Flora, J.R., Jang, M., Heo, J., Park, C.M., Yoon, Y., Sonocatalytic degradation coupled with single-walled carbon nanotubes for removal of ibuprofen and sulfamethoxazole. *Chem. Eng. Sci.* 162 (2017) 300-308.

Andreozzi, R., Caprio, V., Marotta, R., Oxidation of 3, 4-dihydroxybenzoic acid by means of hydrogen peroxide in aqueous goethite slurry. *Water Res.* 36(11) (2002) 2761-2768.

Angaji, M.T., Ghiaee, R., Decontamination of unsymmetrical dimethylhydrazine wastewater by hydrodynamic cavitation-induced advanced Fenton process. *Ultrason. Sonochem.* 23 (2015) 257-265.

Askarniya, Z., Sadeghi, M.T., Baradaran, S., Decolorization of Congo red via hydrodynamic cavitation in combination with Fenton's reagent. *Chem. Eng. Process. Process Intensif.* (2020) 107874.

Atchley, A.A., Prosperetti, A., The crevice model of bubble nucleation. *J. Acoust. Soc. Am.* 86(3) (1989) 1065-1084.

Ayare, S.D., Gogate, P.R., Sonophotocatalytic oxidation based treatment of phthalocyanine pigment containing industrial wastewater intensified using oxidising agents. *Sep. Purif. Technol.* 233 (2020) 115979.

Bae, S., Kim, D., Lee, W., Degradation of diclofenac by pyrite catalyzed Fenton oxidation. *Appl. Catal., B Environ.* 134 (2013) 93-102.

Bagal, M.V., Gogate, P.R., Degradation of 2, 4-dinitrophenol using a combination of hydrodynamic cavitation, chemical and advanced oxidation processes. *Ultrason. Sonochem.* 20(5) (2013) 1226-1235.

Bagal, M.V., Gogate, P.R., Degradation of diclofenac sodium using combined processes based on hydrodynamic cavitation and heterogeneous photocatalysis. *Ultrason. Sonochem.* 21(3) (2014a) 1035-1043.

Bagal, M.V., Gogate, P.R., Sonochemical degradation of alachlor in the presence of process intensifying additives. *Sep. Purif. Technol.* 90 (2012) 92-100.

Bagal, M.V., Gogate, P.R., Wastewater treatment using hybrid treatment schemes based on cavitation and Fenton chemistry: a review. *Ultrason. Sonochem.* 21(1) (2014b) 1-14.

Balaji, C., Moholkar, V.S., Pandit, A.B., Ashokkumar, M., Mechanistic investigations on sonophotocatalytic degradation of textile dyes with surface active solutes. *Ind. Eng. Chem. Res.* 50(20) (2011)11485-11494.

Barik, A.J., Gogate, P.R., Degradation of 2, 4-dichlorophenol using combined approach based on ultrasound, ozone and catalyst. *Ultrason. Sonochem.* 36 (2017) 517-526.

Barik, A.J., Gogate, P.R., Degradation of 4-chloro 2-aminophenol using combined strategies based on ultrasound, photolysis and ozone. *Ultrason. Sonochem.* 28 (2016) 90-99.

Barik, A.J., Gogate, P.R., Hybrid treatment strategies for 2, 4, 6-trichlorophenol degradation based on combination of hydrodynamic cavitation and AOPs. *Ultrason. Sonochem.* 40 (2018) 383-394.

Benito, Y., Arrojo, S., Hauke, G., Vidal, P., Hydrodynamic cavitation as a low-cost AOP for wastewater treatment: preliminary results and a new design approach. *WIT Trans. Ecol. Environ.* 80 (2005).

Bethi, B., Sonawane, S.H., Rohit, G.S., Holkar, C.R., Pinjari, D.V., Bhanvase, B.A., Pandit, A.B., Investigation of TiO_2 photocatalyst performance for decolorization in the presence of hydrodynamic cavitation as hybrid AOP. *Ultrason. Sonochem.* 28 (2016) 150-160.

Biswas, A., Saha, S., Jana, N.R., $ZnSnO_3$ nanoparticle-based piezocatalysts for ultrasound-assisted degradation of organic pollutants. *ACS Appl. Nano Mater.* 2(2) (2019) 1120-1128.

Bloh, J.Z., A holistic approach to model the kinetics of photocatalytic reactions. *Front. Chem.* 7 (2019) 128.

Boczkaj, G., Gągol, M., Klein, M., Przyjazny, A., Effective method of treatment of effluents from production of bitumens under basic pH conditions using hydrodynamic cavitation aided by external oxidants. *Ultrason. Sonochem.* 40 (2018) 969-979.

Bokare, A. D., Choi, W., Review of iron-free Fenton-like systems for activating H_2O_2 in advanced oxidation processes. *J. Hazard. Mater.* 275 (2014) 121-135.

Borkent, B.M., Gekle, S., Prosperetti, A., Lohse, D., Nucleation threshold and deactivation mechanisms of nanoscopic cavitation nuclei. *Phys. Fluids* 21(10) (2009) 102003.

Brillas, E., Sirés, I., Oturan, M.A., Electro-Fenton process and related electrochemical technologies based on Fenton's reaction chemistry. *Chem. Rev.* 109(12) (2009) 6570-6631.

Buxton, G.V., Greenstock, C.L., Helman, W.P., Ross, A.B., Critical review of rate constants for reactions of hydrated electrons, hydrogen atoms and hydroxyl radicals ($^{\bullet}OH/^{\bullet}O^{-}$) in aqueous solution. *J. Phys. Chem. Ref. Data* 17(2) (1988) 513-886.

Cai, C., Liu, J., Zhang, Z., Zheng, Y., Zhang, H., Visible light enhanced heterogeneous photo-degradation of Orange II by zinc ferrite ($ZnFe_2O_4$) catalyst with the assistance of persulfate. *Sep. Purif. Technol.* 165 (2016a) 42-52.

Cai, M., Su, J., Zhu, Y., Wei, X., Jin, M., Zhang, H., Dong, C., Wei, Z., Decolorization of azo dyes Orange G using hydrodynamic cavitation coupled with heterogeneous Fenton process. *Ultrason. Sonochem.* 28 (2016b) 302-310.

Chakinala, A.G., Bremner, D.H., Gogate, P.R., Namkung, K.C., Burgess, A.E., Multivariate analysis of phenol mineralisation by combined hydrodynamic cavitation and heterogeneous advanced Fenton processing. *Appl. Catal., B Environ.* 78(1-2) (2008a) 11-18.

Chakinala, A.G., Gogate, P.R., Burgess, A.E., Bremner, D.H., Industrial wastewater treatment using hydrodynamic cavitation and heterogeneous advanced Fenton processing. *Chem. Eng. J.* 152(2-3) (2009) 498-502.

Chakinala, A.G., Gogate, P.R., Burgess, A.E., Bremner, D.H., Treatment of industrial wastewater effluents using hydrodynamic cavitation and the advanced Fenton process. *Ultrason. Sonochem.* 15(1) (2008b) 49-54.

Chakma, S., Das, L., Moholkar, V.S., Dye decolorization with hybrid advanced oxidation processes comprising sonolysis/Fenton-like/photo-ferrioxalate systems: a mechanistic investigation. *Sep. Purif. Technol.* 156 (2015) 596-607.

Chakma, S., Moholkar, V.S., Investigations in synergism of hybrid advanced oxidation processes with combinations of sonolysis+ fenton process+ UV for degradation of bisphenol A. *Ind. Eng. Chem. Res.* 53(16) (2014) 6855-6865.

Chakma, S., Moholkar, V.S., Numerical simulation and investigation of system parameters of sonochemical process. *Chin. J. Eng.* ID362682 (2013a) 1-14.

Chakma, S., Moholkar, V.S., Physical mechanism of sono-Fenton process. *AIChE J.* 59(11) (2013b) 4303-4313.

Chan, Y.J., Chong, M.F., Law, C.L., Hassell, D.G., A review on anaerobic–aerobic treatment of industrial and municipal wastewater. *Chem. Eng. J.* 155(1) (2009). 1-18.

Dhanke, P.B., Wagh, S.M., Intensification of the degradation of Acid RED-18 using hydrodynamic cavitation. *Emerging Contaminants* 6 (2020) 20-32.

Dinesh, G.K., Chakma, S., Degradation kinetic study of cholesterol lowering statin drug using sono-hybrid techniques initiated by metal-free polymeric catalyst. *J. Taiwan Inst. Chem. Eng.* 100 (2019) 95-104.

Durán, A., Monteagudo, J.M., Sanmartín, I., García-Díaz, A., Sonophotocatalytic mineralization of antipyrine in aqueous solution. *Appl. Catal., B Environ.* 138 (2013) 318-325.

ElMetwally, A.E., Eshaq, G.H., Al-Sabagh, A.M., Yehia, F.Z., Philip, C.A., Moussa, N.A. ElShafei, G.M., Insight into heterogeneous Fenton-sonophotocatalytic degradation of nitrobenzene using metal oxychlorides. *Sep. Purif. Technol.* 210 (2019) 452-462.

Eshaq, G., Wang, S., Sun, H., Sillanpaa, M., Core/shell $FeVO_4$@BiOCl heterojunction as a durable heterogeneous Fenton catalyst for the efficient sonophotocatalytic degradation of p-nitrophenol. *Sep. Purif. Technol.* 231 (2020b) 115915.

Eshaq, G., Wang, S., Sun, H., Sillanpaa, M., Superior performance of $FeVO_4$@CeO_2 uniform core-shell nanostructures in heterogeneous Fenton-sonophotocatalytic degradation of 4-nitrophenol. *J. Hazard. Mater.* 382 (2020a) 121059.

Fenton, H.J.H., LXXIII.—Oxidation of tartaric acid in presence of iron. *J. Chem. Soc., Transactions*, 65 (1894) 899-910.

Gągol, M., Przyjazny, A., Boczkaj, G., Wastewater treatment by means of advanced oxidation processes based on cavitation–a review. *Chem. Eng. J.* 338 (2018) 599-627.

Gągol, M., Soltani, R.D.C., Przyjazny, A., Boczkaj, G., Effective degradation of sulfide ions and organic sulfides in cavitation-based advanced oxidation processes (AOPs). *Ultrason. Sonochem.* 58 (2019) 104610.

Garrido-Ramírez, E.G., Theng, B.K.G. and Mora, M.L., Clays and oxide minerals as catalysts and nanocatalysts in Fenton-like reactions—a review. *Appl. Clay Sci.* 47(3-4) (2010) 182-192.

Gogate, P.R., Bhosale, G.S., Comparison of effectiveness of acoustic and hydrodynamic cavitation in combined treatment schemes for degradation of dye wastewaters. *Chem. Eng. Process. Process Intensif.* 71 (2013) 59-69.

Gogate, P.R., Cavitation: an auxiliary technique in wastewater treatment schemes. *Adv. Environ. Res.* 6(3) (2002) 335-358.

Gogate, P.R., Katekhaye, S.N., A comparison of the degree of intensification due to the use of additives in ultrasonic horn and ultrasonic bath. *Chem. Eng. Process. Process Intensif.* 61 (2012) 23-29.

Gogate, P.R., Pandit, A.B., A review of imperative technologies for wastewater treatment I: oxidation technologies at ambient conditions. *Adv. Environ. Res.* 8(3-4) (2004) 501-551.

Gogate, P.R., Patil, P.N., Combined treatment technology based on synergism between hydrodynamic cavitation and advanced oxidation processes. *Ultrason. Sonochem.* 25 (2015) 60-69.

Gogate, P.R., Shirgaonkar, I.Z., Sivakumar, M., Senthilkumar, P., Vichare, N.P., Pandit, A.B., Cavitation reactors: efficiency assessment using a model reaction. *AIChE J.* 47(11) (2001) 2526-2538.

Gogate, P.R., Tayal, R.K., Pandit, A.B., Cavitation: a technology on the horizon. *Current Sci.* 91(1) (2006) 35-46.

Harichandran, G., Prasad, S., SonoFenton degradation of an azo dye, Direct Red. *Ultrason. Sonochem.* 29 (2016) 178-185.

He, J., Yang, X., Men, B., Wang, D., Interfacial mechanisms of heterogeneous Fenton reactions catalyzed by iron-based materials: A review. *J. Environ. Sci.* 39 (2016a) 97-109.

He, L.L., Liu, X.P., Wang, Y.X., Wang, Z.X., Yang, Y.J., Gao, Y.P., Liu, B., Wang, X., Sonochemical degradation of methyl orange in the presence of Bi_2WO_6: Effect of operating parameters and the generated reactive oxygen species. *Ultrason. Sonochem.* 33 (2016b) 90-98.

Hermosilla, D., Cortijo, M., Huang, C.P., Optimizing the treatment of landfill leachate by conventional Fenton and photo-Fenton processes. *Sci. Total Environ.* 407(11) (2009) 3473-3481.

Hodges, B.C., Cates, E.L., Kim, J.H., Challenges and prospects of advanced oxidation water treatment processes using catalytic nanomaterials. *Nat. Nanotechnol.* 13(8) (2018) 642-650.

Huang, C.P., Dong, C., Tang, Z., Advanced chemical oxidation: its present role and potential future in hazardous waste treatment. *Waste Manage.*13(5-7) (1993) 361-377.

Huang, R., Fang, Z., Yan, X., Cheng, W., Heterogeneous sono-Fenton catalytic degradation of bisphenol A by Fe_3O_4 magnetic nanoparticles under neutral condition. *Chem. Eng. J.* 197 (2012) 242-249.

Im, J.K., Heo, J., Boateng, L.K., Her, N., Flora, J.R., Yoon, J., Zoh, K.D., Yoon, Y., Ultrasonic degradation of acetaminophen and naproxen in the presence of single-walled carbon nanotubes. *J. Hazard. Mater.* 254 (2013) 284-292.

Innocenzi, V., Prisciandaro, M., Centofanti, M., Vegliò, F., Comparison of performances of hydrodynamic cavitation in combined treatments based on hybrid induced advanced Fenton process for degradation of azo-dyes. *J. Environ. Chem. Eng.* 7(3) (2019) 103171.

Innocenzi, V., Prisciandaro, M., Tortora, F., Vegliò, F., Optimization of hydrodynamic cavitation process of azo dye reduction in the presence of metal ions. *J. Environ. Chem. Eng.* 6(6) (2018) 6787-6796.

Jawale, R.H., Dapurkar, O., Gogate, P.R., Treatment of atrazine containing wastewater using cavitation based hybrid treatment approaches. *Chem. Eng. Process. Process Intensif.* 130 (2018) 275-283.

Jawale, R.H., Gogate, P.R., Novel approaches based on hydrodynamic cavitation for treatment of wastewater containing potassium thiocyanate. *Ultrason. Sonochem.* 52 (2019) 214-223.

Joshi, R.K., Gogate, P.R., Degradation of dichlorvos using hydrodynamic cavitation based treatment strategies. *Ultrason. Sonochem.* 19(3) (2012) 532-539.

Jung, K.W., Park, D.S., Hwang, M.J., Ahn, K.H., Decolorization of Acid Orange 7 by an electric field-assisted modified orifice plate hydrodynamic cavitation system: Optimization of operational parameters. *Ultrason. Sonochem.* 26 (2015) 22-29.

Kidak, R., Ince, N.H., Ultrasonic destruction of phenol and substituted phenols: A review of current research. *Ultrason. Sonochem.* 13(3) (2006)195-199.

Kuan, C.C., Chang, S.Y., Schroeder, S.L., Fenton-like oxidation of 4-chlorophenol: homogeneous or heterogeneous?. *Ind. Eng. Chem. Res.* 54(33) (2015) 8122-8129.

Kumar, M.S., Sonawane, S.H., Bhanvase, B.A., Bethi, B., Treatment of ternary dye wastewater by hydrodynamic cavitation combined with other advanced oxidation processes (AOP's). *J. Water Process Eng.* 23 (2018) 250-256.

Kumar, M.S., Sonawane, S.H., Pandit, A.B., Degradation of methylene blue dye in aqueous solution using hydrodynamic cavitation based hybrid advanced oxidation processes. *Chem. Eng. Process. Process Intensif.* 122 (2017) 288-295.

Li, G., Yi, L., Wang, J., Song, Y., Hydrodynamic cavitation degradation of Rhodamine B assisted by Fe^{3+}-doped TiO_2: Mechanisms, geometric and operation parameters. *Ultrason. Sonochem.* 60 (2020) 104806.

Li, P., Song, Y., Wang, S., Tao, Z., Yu, S., Liu, Y., Enhanced decolorization of methyl orange using zero-valent copper nanoparticles under assistance of hydrodynamic cavitation. *Ultrason. Sonochem.* 22 (2015) 132-138.

Liu, F., Yi, P., Wang, X., Gao, H., Zhang, H., Degradation of Acid Orange 7 by an ultrasound/ZnO-GAC/persulfate process. *Sep. Purif. Technol.* 194 (2018) 181-187.

Loubiere, K., Oelgemoeller, M., Aillet, T., Dechy-Cabaret, O., Prat, L., Continuous-flow photochemistry: A need for chemical engineering. *Chem. Eng. Process. Process Intensif.* 104 (2016) 120-132.

Madhavan, J., Kumar, P.S.S., Anandan, S., Zhou, M., Grieser, F., Ashokkumar, M., Ultrasound assisted photocatalytic degradation of diclofenac in an aqueous environment. *Chemosphere* 80(7) (2010) 747-752.

Mahamuni, N.N., Adewuyi, Y.G., Advanced oxidation processes (AOPs) involving ultrasound for waste water treatment: a review with emphasis on cost estimation. *Ultrason. Sonochem.* 17(6) (2010) 990-1003.

Mahdavi, R., Talesh, S.S.A., Enhancement of ultrasound-assisted degradation of Eosin B in the presence of nanoparticles of ZnO as sonocatalyst. *Ultrason. Sonochem.* 51 (2019) 230-240.

Matzek, L.W., Carter, K.E., Activated persulfate for organic chemical degradation: a review. *Chemosphere* 151 (2016) 178-188.

Mirzaei, A., Chen, Z., Haghighat, F., Yerushalmi, L., Removal of pharmaceuticals from water by homo/heterogonous Fenton-type processes–A review. *Chemosphere* 174 (2017) 665-688.

Mishra, K.P., Gogate, P.R., Intensification of degradation of Rhodamine B using hydrodynamic cavitation in the presence of additives. *Sep. Purif. Technol.* 75(3) (2010) 385-391.

Moholkar, V.S., Kumar, P.S., Pandit, A.B., Hydrodynamic cavitation for sonochemical effects. *Ultrason. Sonochem.* 6(1-2) (1999) 53-65.

Moholkar, V.S., Pandit, A.B., Modeling of hydrodynamic cavitation reactors: a unified approach. *Chem. Eng. Sci.* 56(21-22) (2001) 6295-6302.

Monteagudo, J.M., Durán, A., San Martín, I., García, S., Ultrasound-assisted homogeneous photocatalytic degradation of Reactive Blue 4 in aqueous solution. *Appl. Catal., B Environ.* 152 (2014b) 59-67.

Monteagudo, J.M., Durán, A., San Martín, I., Mineralization of wastewater from the pharmaceutical industry containing chloride ions by UV photolysis of H_2O_2/Fe (II) and ultrasonic irradiation. *J. Environ. Manage.* 141 (2014a) 61-69.

Nidheesh, P.V., Heterogeneous Fenton catalysts for the abatement of organic pollutants from aqueous solution: a review. *RSC Adv.* 5(51) (2015) 40552-40577.

Oh, W.D., Dong, Z., Lim, T.T., Generation of sulfate radical through heterogeneous catalysis for organic contaminants removal: current development, challenges and prospects. *Appl. Catal., B Environ.* 194 (2016) 169-201.

Olmez-Hanci, T., Arslan-Alaton, I., Comparison of sulfate and hydroxyl radical based advanced oxidation of phenol. *Chem. Eng. J.* 224 (2013) 10-16.

Oturan, M.A., An ecologically effective water treatment technique using electrochemically generated hydroxyl radicals for in situ destruction of organic pollutants: application to herbicide 2, 4-D. *J. Appl. Electrochem.* 30(4) (2000) 475-482.

Panda, D., Manickam, S., Hydrodynamic cavitation assisted degradation of persistent endocrine-disrupting organochlorine pesticide Dicofol: Optimization of operating parameters and investigations on the mechanism of intensification. *Ultrason. Sonochem.* 51 (2019) 526-532.

Parsa, J.B., Zonouzian, S.A.E., Optimization of a heterogeneous catalytic hydrodynamic cavitation reactor performance in decolorization of Rhodamine B: Application of scrap iron sheets. *Ultrason. Sonochem.* 20(6) (2013) 1442-1449.

Patil, A.L., Patil, P.N., Gogate, P.R., Degradation of imidacloprid containing wastewaters using ultrasound based treatment strategies. *Ultrason. Sonochem.* 21(5) (2014) 1778-1786.

Patil, P.N., Bote, S.D., Gogate, P.R., Degradation of imidacloprid using combined advanced oxidation processes based on hydrodynamic cavitation. *Ultrason. Sonochem.* 21(5) (2014) 1770-1777.

Patil, P.N., Gogate, P.R., Degradation of dichlorvos using hybrid advanced oxidation processes based on ultrasound. *J. Water Process Eng.* 8 (2015) 58-65.

Patil, P.N., Gogate, P.R., Degradation of methyl parathion using hydrodynamic cavitation: effect of operating parameters and intensification using additives. *Sep. Purif. Technol.* 95 (2012) 172-179.

Pouran, S.R., Raman, A.A.A., Daud, W.M.A.W., Review on the application of modified iron oxides as heterogeneous catalysts in Fenton reactions. *J. Cleaner Prod.* 64 (2014) 24-35.

Prajapat, A.L., Gogate, P.R., Intensified depolymerization of aqueous polyacrylamide solution using combined processes based on hydrodynamic cavitation, ozone, ultraviolet light and hydrogen peroxide. *Ultrason. Sonochem.* 31 (2016) 371-382.

Rajoriya, S., Bargole, S., George, S., Saharan, V.K., Gogate, P.R., Pandit, A.B., Synthesis and characterization of samarium and nitrogen doped TiO_2 photocatalysts for photo-degradation of 4-acetamidophenol in combination with hydrodynamic and acoustic cavitation. *Sep. Purif. Technol.* 209 (2019) 254-269.

Rajoriya, S., Carpenter, J., Saharan, V.K., Pandit, A.B., Hydrodynamic cavitation: an advanced oxidation process for the degradation of bio-refractory pollutants. *Rev. Chem. Eng.* 32(4) (2016) 379-411.

Rauf, M.A., Ashraf, S.S., Fundamental principles and application of heterogeneous photocatalytic degradation of dyes in solution. *Chem. Eng. J.* 151(1-3) (2009) 10-18.

Raut-Jadhav, S., Saharan, V.K., Pinjari, D., Sonawane, S., Saini, D., Pandit, A.B., Synergetic effect of combination of AOP's (hydrodynamic cavitation and H_2O_2) on the degradation of neonicotinoid class of insecticide. *J. Hazard. Mater.* 261 (2013) 139-147.

Raut-Jadhav, S., Saharan, V.K., Pinjari, D.V., Saini, D.R., Sonawane, S.H., Pandit, A.B., Intensification of degradation of imidacloprid in aqueous solutions by combination of hydrodynamic cavitation with various advanced oxidation processes (AOPs). *J. Environ. Chem. Eng.* 1(4) (2013) 850-857.

Raut-Jadhav, S., Saini, D., Sonawane, S., Pandit, A.B., Effect of process intensifying parameters on the hydrodynamic cavitation based degradation of commercial

pesticide (methomyl) in the aqueous solution. *Ultrason. Sonochem.* 28 (2016) 283-293.

Ren, Y.Z., Wu, Z.L., Franke, M., Braeutigam, P., Ondruschka, B., Comeskey, D.J., King, P.M., Sonoelectrochemical degradation of phenol in aqueous solutions. *Ultrason. Sonochem.* 20(2) (2013) 715-721.

Richardson, S.D., Ternes, T.A. Water analysis: emerging contaminants and current issues. *Anal. Chem.* 83(12) (2011) 4614-4648.

Roy, K., Moholkar, V.S., Sulfadiazine degradation using hybrid AOP of heterogeneous fenton/persulfate system coupled with hydrodynamic cavitation. *Chem. Eng. J.* 386 (2020a) 121294.

Roy, K., Agarkoti, C., Malani, R.S., Thokchom, B. and Moholkar, V.S., Mechanistic study of sulfadiazine degradation by ultrasound-assisted Fenton-persulfate system using yolk-shell Fe_3O_4@hollow@mSiO_2 nanoparticles. *Chem. Eng. Sci.* 217 (2020b) 115522.

Ruales-Lonfat, C., Barona, J.F., Sienkiewicz, A., Bensimon, M., Vélez-Colmenares, J., Benítez, N., Pulgarín, C., Iron oxides semiconductors are efficients for solar water disinfection: a comparison with photo-Fenton processes at neutral pH. *Appl. Catal., B Environ.* 166 (2015) 497-508.

Saharan, V. K., Badve, M. P., Pandit, A. B., Degradation of Reactive Red 120 dye using hydrodynamic cavitation. *Chem. Eng. J.* 178 (2011a) 100-107.

Saharan, V.K., Pandit, A.B. Satish Kumar, P.S., Anandan, S., Hydrodynamic cavitation as an advanced oxidation technique for the degradation of acid red 88 dye. *Ind. Eng. Chem. Res.* 51(4) (2011b) 1981-1989.

Saxena, S., Rajoriya, S., Saharan, V.K., George, S., An advanced pretreatment strategy involving hydrodynamic and acoustic cavitation along with alum coagulation for the mineralization and biodegradability enhancement of tannery waste effluent. *Ultrason. Sonochem.* 44 (2018) 299-309.

Shah, Y.T., Pandit, A.B., Moholkar, V.S., *Cavitation Reaction Engineering*, New York: Plenum Press/Kluwer Academic (1999).

Siddique, M., Farooq, R., Price, G.J., Synergistic effects of combining ultrasound with the Fenton process in the degradation of Reactive Blue 19. *Ultrason. Sonochem.* 21(3) (2014) 1206-1212.

Su, S., Guo, W., Yi, C., Leng, Y., Ma, Z., Degradation of amoxicillin in aqueous solution using sulphate radicals under ultrasound irradiation. *Ultrason. Sonochem.* 19(3) (2012) 469-474.

Suslick, K.S., Sonochemistry. *Science* 247(4949) (1990) 1439-1445.

Tang, S.Y., Sivakumar, M., A novel and facile liquid whistle hydrodynamic cavitation reactor to produce submicron multiple emulsions. *AIChE J.* 59(1) (2013) 155-167.

Thanekar, P., Panda, M., Gogate, P.R., Degradation of carbamazepine using hydrodynamic cavitation combined with advanced oxidation processes. *Ultrason. Sonochem.* 40 (2018) 567-576.

Tyagi, V.L., Lo, S.L., Application of physico-chemical pretreatment methods to enhance the sludge disintegration and subsequent anaerobic digestion: an up to date review, *Rev. Environ. Sci. Biotechnol.* 10 (2011) 215–242.

Verma, M., Haritash, A.K., Degradation of amoxicillin by Fenton and Fenton-integrated hybrid oxidation processes. *J. Environ. Chem. Eng.* 7(1) (2019) 102886.

Wacławek, S., Lutze, H.V., Grübel, K., Padil, V.V., Černík, M., Dionysiou, D.D., Chemistry of persulfates in water and wastewater treatment: a review. *Chem. Eng. J.* 330 (2017) 44-62.

Wang, A., Guo, W., Hao, F., Yue, X., Leng, Y., Degradation of Acid Orange 7 in aqueous solution by zero-valent aluminum under ultrasonic irradiation. *Ultrason. Sonochem.* 21(2) (2014) 572-575.

Wang, C., Jin, R., He, Z., Qiao, Y., Wang, Y., Wang, K., Lu, Y., Wang, X., Liu, D., A new water treatment technology for degradation of B [a] A by hydrodynamic cavitation and chlorine dioxide oxidation. *Ultrason. Sonochem.* 61 (2020) 104834.

Wang, J., Wang, S., Activation of persulfate (PS) and peroxymonosulfate (PMS) and application for the degradation of emerging contaminants. *Chem. Eng. J.* 334 (2018) 1502-1517.

Wang, K., Jin, R.Y., Qiao, Y.N., He, Z.D., Wang, Y., Wang, X.J., The removal of Rhodamine B by H_2O_2 or ClO_2 combined with hydrodynamic cavitation. *Water Sci. Technol.* 80 (8) (2019) 1571–1580.

Wang, Q., Cao, Y., Zeng, H., Liang, Y., Ma, J., Lu, X., Ultrasound-enhanced zero-valent copper activation of persulfate for the degradation of bisphenol AF. *Chem. Eng. J.* 378 (2019) 122143.

Wang, S., Zhou, N., Removal of carbamazepine from aqueous solution using sono-activated persulfate process. *Ultrason. Sonochem.* 29 (2016) 156-162.

Wang, X., Jia, J., Wang, Y., Combination of photocatalysis with hydrodynamic cavitation for degradation of tetracycline. *Chem. Eng. J.* 315 (2017) 274-282.

Wu, Z., Shen, H., Ondruschka, B., Zhang, Y., Wang, W., Bremner, D.H., Removal of blue-green algae using the hybrid method of hydrodynamic cavitation and ozonation. *J. Hazard. Mater.* 235 (2012) 152-158.

Yan, Y., Thorpe, R.B., Flow regime transitions due to cavitation in the flow through an orifice. *Int. J. Multiphase Flow* 16(6) (1990) 1023-1045.

Yang, L., Xue, J., He, L., Wu, L., Ma, Y., Chen, H., Li, H., Peng, P., Zhang, Z., Review on ultrasound assisted persulfate degradation of organic contaminants in wastewater: influences, mechanisms and prospective.*Chem. Eng. J.* (2019) 122146.

Yuan, S., Liao, P., Alshawabkeh, A.N., Electrolytic manipulation of persulfate reactivity by iron electrodes for trichloroethylene degradation in groundwater. *Environ. Sci. Technol.* 48(1) (2014) 656-663.

Yuan, S., Liao, P., Alshawabkeh, A.N., Electrolytic manipulation of persulfate reactivity by iron electrodes for trichloroethylene degradation in groundwater. *Environ. Sci. Technol.* 48(1) (2014) 656-663.

Zanias, A., Frontistis, Z., Vakros, J., Arvaniti, O.S., Ribeiro, R.S., Silva, A.M., Faria, J.L., Gomes, H.T., Mantzavinos, D., Degradation of methylparaben by sonocatalysis using a Co–Fe magnetic carbon xerogel. *Ultrason. Sonochem.* (2020) 105045.

Zhang, X., Hao, C., Ma, C., Shen, Z., Guo, J., Sun, R., Studied on sonocatalytic degradation of Rhodamine B in aqueous solution. *Ultrason. Sonochem.* 58 (2019) 104691.

Zhong, X., Royer, S., Zhang, H., Huang, Q., Xiang, L., Valange, S., Barrault, J., Mesoporous silica iron-doped as stable and efficient heterogeneous catalyst for the degradation of CI Acid Orange 7 using sono–photo-Fenton process. *Sep. Purif. Technol.* 80(1) (2011) 163-171.

Zhou, Z., Liu, X., Sun, K., Lin, C., Ma, J., He, M., Ouyang, W., Persulfate-based advanced oxidation processes (AOPs) for organic-contaminated soil remediation: A review. *Chem. Eng. J.* 372 (2019) 836-851.

CHAPTER 2

Sulfadiazine Degradation Using Hydrodynamic Cavitation Assisted Fenton/ Persulfate System

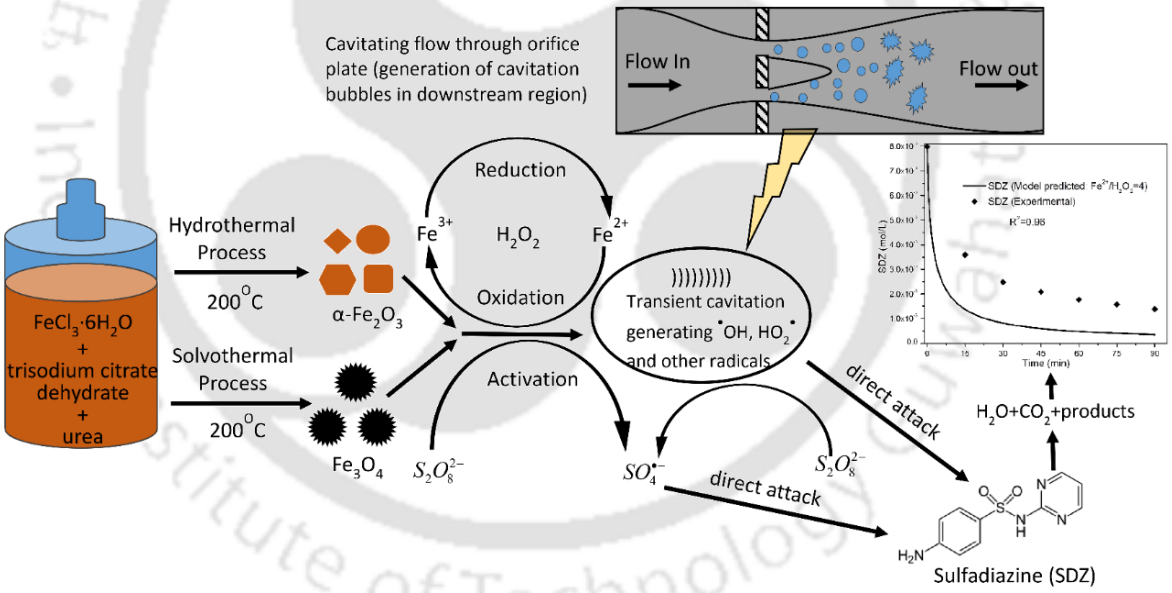

CHAPTER 2

SULFADIAZINE DEGRADATION USING HYDRODYNAMIC CAVITATION ASSISTED FENTON/ PERSULFATE SYSTEM

2.1 INTRODUCTION

Antibiotics appearing in water discharge from domestic and agricultural sectors (especially animal husbandries), and also the discharges from pharmaceutical industries are the new class of pollutants of both surface and groundwater. Several antibiotics are highly stable and persistent in the environment and can interact with soil components. If water contaminated with these pollutants is used for irrigation of crops, these antibiotics can enter the food chain through contaminated soil and cause significant harm to human health. Many of these antibiotics are biorecalcitrant, and hence, special techniques based on advanced oxidation processes (AOP) have been developed for the effective degradation of these antibiotics. A prominent class of antibiotics that appears in sewage water and water discharges from animal husbandries are sulfonamides or sulfa drugs. Among the sulfa drugs family, sulfadiazine (SDZ) is a potential antibiotic widely used in veterinary and human medicines. Degradation of sulfadiazine with AOP has been attempted by several previous authors.

Lastre-Acosta et al. (2015) have studied the degradation of SDZ in aqueous solution using high frequency (580, 862 and 1142 kHz) ultrasound at initial concentrations of 25, 50 and 70 mg/L. The highest SDZ degradation was achieved at the lowest frequency of 580 kHz and acidic pH of 5.5. The addition of Fenton reagent along with sonication boosted

the degradation rate. Zou et al. (2014) and Zhou et al. (2016) have studied SDZ degradation in heterogeneous ultrasound enhanced Fe^0/persulfate system. The synergistic role of ultrasound in US/Fe^0/persulfate system was in terms of enhancement in heterogeneous iron corrosion reactions and acceleration of bulk radical reactions. Oxidation induced by $SO_4^{\bullet-}$ radicals was revealed to be the main degradation pathway. Zhou et al. (2016) have shown that SDZ degradation can be inhibited by SO_4^{2-}, NO_3^-, HCO_3^-/CO_3^{2-} and $H_2PO_4^-$ ions. The chelating agents like oxalic acid and EDTA enhanced SDZ degradation at appropriate dosages. The inorganic anions reacted with $SO_4^{\bullet-}$ to yield species with reduced oxidation potential, while chelating agents like oxalic acid and EDTA enhanced dissociation of Fe^0, and production of additional oxidants of H_2O_2 and $[Fe^{IV}O]^{2+}$ through electron transfer reactions. Feng et al. (2016) have reported SDZ degradation using peroxymonosulfate (PMS) activated using $CuFeO_2$ rhombocrystals. For 0.1 g/L $CuFeO_2$ rhombocrystals and 33.0 μM PMS, nearly complete degradation of SDZ occurred in just 24 min. Authors have reported synergistic effects between Cu(I) and Fe(III), probably due to accelerated reduction of Fe(III). With solid Cu(I) as catalyst, two activation stages existed that produced •OH radicals followed by $SO_4^{\bullet-}$ radicals.

Most of the AOP are based on the production of •OH radicals, which have the highest oxidation potential of 2.80 eV. However, major operational issue for the •OH radical-based AOP is high instability of •OH radicals that restrict its utilization for the degradation of pollutants. An alternative for the treatment of the bio-recalcitrant pollutants is persulfate ($S_2O_8^{2-}$) based oxidative degradation. Persulfate ions have high solubility and stability, and can be activated through various means (thermal, UV, ultrasound and transition metal ions) to produce persulfate radicals, $SO_4^{\bullet-}$. Persulfate

radicals, although have slightly lesser oxidation potential (2.6 eV), have nonselective reactivity over wide range of pH. A popular technique for activation of persulfate ions is the reaction with Fe^{2+} (viz. $S_2O_8^{2-} + Fe^{2+} \longrightarrow Fe^{3+} + SO_4^{2-} + SO_4^{\bullet -}$). However, relatively large dosages of Fe^{2+} are required, which ultimately end up as precipitates of iron hydroxides. Zero valent iron (Fe^0) has been proposed as an alternative to Fe^{2+}, and Fe^0/persulfate system has been applied for degradation of variety of recalcitrant organic pollutants. The limiting factor in this case is corrosive leaching of Fe^{2+} ions into the solution with typical reactions ($Fe^0 \longrightarrow Fe^{2+} + 2e^-$; $Fe^0 + H_2O_2 + 1/2O_2 \longrightarrow Fe^{2+} + OH^-$; $Fe^0 + H_2O \longrightarrow Fe^{2+} + 2OH^-$). Thus, the reactive mass transfer of solid-liquid interface is an important factor governing the kinetics of these systems. Precipitation and re-deposition of flocs of Fe^{2+}/Fe^{3+} hydroxo-complexes on the surface of solids is an operational problem that hinders Fe^{2+} generating reactions at the solid-liquid interface. The generation of high shear in the medium can remove passivated hydroxide films from solid surface of catalysts, which exposes fresh solid surface and enhances mass transfer.

In the present study, we have reported SDZ degradation using two systems, viz. hydrodynamic cavitation/α-Fe_2O_3/persulfate and hydrodynamic cavitation/Fe_3O_4/ persulfate. Instead of zero-valent iron as Fenton catalyst, we have used two iron oxides (in the form of nanoparticles for the high surface area) as catalysts, viz. α-Fe_2O_3 and Fe_3O_4. The rationale underlying use of iron oxide nanoparticles instead of zero valent iron is higher stability of oxides for prolonged treatment. Zero valent iron is rather unstable and is quickly oxidized in the presence of air and water. Hydrodynamic cavitation (HC) is a relatively new technique of generating transient cavitation. Conventionally, ultrasound irradiation or sonication has been employed for the generation of cavitation. In HC, transient cavitation events are produced through bulk pressure variation induced by flow geometries such as orifice plate or venturi. Throttling

of discharge of a pump through flow constriction such as orifice plate results in a rise in velocity head at the expense of reduction in pressure head in the downstream region. This results in the generation of gas/vapour bubbles in the flow through release of dissolved gas and partial vaporization of liquid. These gas and vapour bubbles can undergo transient collapse with recovery of pressure in expanding flow in downstream region giving rise to radicals. The specific objectives of the present study are: (1) synthesis of iron oxides (α-Fe_2O_3 and Fe_3O_4) nanoparticles through hydrothermal and solvothermal techniques; (2) study of SDZ degradation with HC alone, and HC combined with persulfate and iron oxides nanoparticles (either α-Fe_2O_3 or Fe_3O_4); and (3) determination of kinetics of SDZ degradation using a mathematical model based on reaction system.

2.2 MATERIALS AND METHODS

2.2.1 Materials

The following chemicals were procured from Himedia (India): ferric chloride hexahydrate (> 99%, ACS grade), ethylene glycol (99%, LR grade), urea (> 99%, ACS grade), hydrogen peroxide (30%, w/v, extra pure), sodium persulfate (99%). The following chemicals were procured from Sigma-Aldrich (India): sodium citrate tribasic dihydrate (≥ 99% ACS grade), sulfadiazine (≥ 99%, AR Grade), acetonitrile (≥ 99%, HPLC grade), benzoic acid (≥ 99% ACS grade), sodium hydroxide (≥ 97% ACS grade). Absolute ethanol (≥ 99%, AR Grade) was purchased from Changshu Yangyuan Chemicals, China. All chemicals were used as received without any pre-treatment.

2.2.2 Experimental Setup

Fig. 2.1 (A) shows the schematic diagram of the experimental setup. The HC reactor consisted of a closed-loop circuit incorporating a feed tank, a main line, a bypass line and

a reciprocating pump with power rating of 1.1 kW. Three control valves (V_1, V_2, V_3) were provided at appropriate locations in the reactor: V_1 – in the bypass line connecting pump outlet to the tank input, V_2 – in the mainline to control the flow rate of process liquid, and V_3 – at reactor drain for collecting the samples. The motor of the pump was controlled using a VFD (Variable Frequency Drive) that varied the frequency (motor speed) and voltage of the power supplied to the motor – which ultimately controlled the motor speed. The motor speed governs the number of piston strokes of the pump per unit time, which in turn regulated the generated flow rate. The by-pass line which was a short circuit of pump discharge into the tank, was provided to control the flow rate through the mainline in case of breakdown of VFD. Pressure gauges were provided to measure the inlet pressure (P_1) in the mainline and the fully recovered downstream pressure (P_2) which was equal to 1 atm. The mainline was fitted with a cavitation device in the form of orifice plate for generating transient cavitation bubbles. A water-cooling jacket was provided around the feed tank for regulation of the temperature (30 ± 5 °C) of flow. The inner diameter of both mainline and bypass line was 21 mm and holding tank was having the maximum capacity of 30 L. The design of the orifice plate as cavitation generating device was based on our previous computational and experimental studies (Kuldeep and Saharan, 2016; Bashir et al., 2011; Sivakumar and Pandit, 2002). The orifice plate with diameter of 98 mm and thickness of 2 mm was fabricated using stainless steel SS-316, and comprised of 2 holes of dia. 4 mm. The schematic of the orifice plate is shown in Fig. 2.1 (B). 5 L solution was taken for the degradation of SDZ in each experiment for 90 min of treatment.

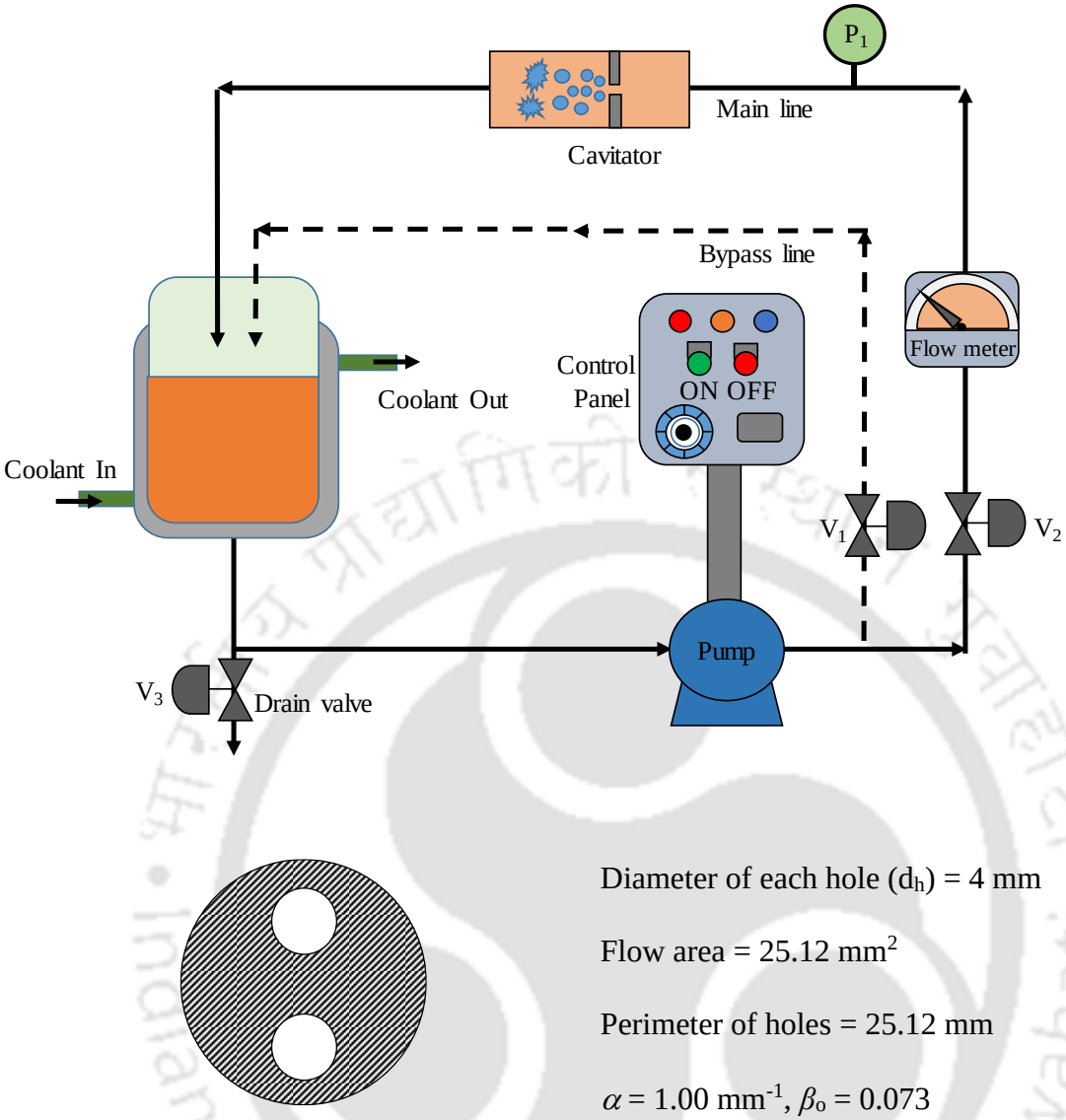

Figure 2.1: (A) Schematic of hydrodynamic cavitation reactor; (B) Geometric specifications of orifice plate used as a cavitator

2.2.3 Synthesis of Fe_3O_4 and α-Fe_2O_3 Nanoparticles

***Fe_3O_4 nanoparticles*:** The super-magnetic Fe_3O_4 nanoparticles were prepared using solvothermal method. Briefly, 3.2 g of $FeCl_3 \cdot 6H_2O$, 0.15 g of sodium citrate tribasic dihydrate and 4.8 g of urea were dissolved in 80 mL of ethylene glycol. The mixture was stirred at 400 rpm for 1 h at room temperature. Resulting homogeneous brown solution was transferred in a sealed Teflon-lined stainless-steel autoclave (100 mL) and was

heated at 200°C for 12 h, and then allowed to cool to room temperature. The resultant black Fe_3O_4 nanoparticles were washed with deionized water several times until a neutral pH was attained, followed by 3-times wash with ethanol. A magnet was used to separate the nanoparticles from solution. These nanoparticles were dried under vacuum at 60°C.

***α-Fe₂O₃ nanoparticles*:** α-Fe_2O_3 nanoparticles were synthesized using the hydrothermal method. Deionized water was used as a solvent for the synthesis of α-Fe_2O_3 in the above mentioned solvothermal method. The resultant reddish-brown α-Fe_2O_3 nanoparticles were washed with deionized water several times until a neutral pH was attained, followed by 3-times wash with ethanol. A centrifuge was used to separate the nanoparticles from the solution. These nanoparticles were dried under vacuum at 60°C overnight.

***Characterization of magnetic nanoparticles*:** Crystal structures of both iron oxides were obtained from powder X-ray diffraction (XRD) patterns (Rigaku RINT 2500 TTRAX-III) using Cu Kα radiation (λ = 1.5406 Å). The diffraction patterns were recorded over a 2θ range from 10° to 80° with a step width of 0.03° and a sampling time of 4°/min at 50 kV/100 mA. Phase identification was done by comparing the XRD patterns with the standard JCPDS database. The surface structures and morphologies of the nanoparticles were analysed from FE-SEM micrographs (Make: Zeiss, Model: Sigma 300). Brunauer Emmett Teller (BET) surface area of the iron oxides was quantified by N_2 adsorption/desorption pattern using surface area analyzer (Make: M/s Micromeritics, USA) at 77.3 K. Before the analysis, the iron oxides samples were degassed under vacuum condition at 423 K. The pore volume and pore size distribution were obtained from the desorption profiles of the nitrogen based on the Barrett–Joyner–Halanda (BJH) method. Vibrating sample magnetometer (VSM) (Make: Lakeshore, Model: 7410 series) was used to study magnetization at 300 K under applied field ranging from –15 kOe to 15 kOe.

2.2.4 Experiments for SDZ Degradation

Experiments for SDZ degradation in the HC reactor were performed in two categories, viz. preliminary experiments and main experiments:

The preliminary experiments were aimed at assessing the effect of initial SDZ concentration (varied as 20, 30 and 40 ppm at pH 6.2) and effect of pH (varied as pH 4, 7 and 10 at initial SDZ concn. = 20 ppm) on extent of SDZ degradation in HC reactor in absence of catalyst. These experiments were conducted at inlet pressure of 10 atm. In these experiments, the SDZ degradation occurred only through the •OH radicals generated from transient cavitation bubbles. The results of these experiments are shown in Fig. 2.2 and Fig. 2.3 respectively. Interestingly, although percentage SDZ degradation was reduced with initial SDZ concentration, the absolute SDZ degradation was independent of the initial concentration. Moreover, the highest SDZ degradation was obtained at pH 4. A plausible explanation for this result can be given as follows: the pKa value of SDZ is 6.28 and it exists in un-dissociated molecular form at acidic pH of 4, and in ionized form at neutral and basic pH. Boriani et al. (2013) have reported octanol-water distribution coefficient for SDZ as ~ 0.58, which represents strong hydrophobic character of SDZ in molecular (or undissociated) form. Under these conditions, SDZ is likely to partition at the liquid interface of cavitation bubbles, which enhances the probability of interaction between SDZ molecules and •OH radicals resulting in faster degradation of SDZ. At neutral and basic pH, SDZ undergoes ionization with an increase in hydrophilicity. At these conditions, SDZ molecules prefer to stay in bulk liquid medium, which reduces their interactions with •OH radicals generated during transient collapse of cavitation bubbles. Similar trends in degradation kinetics of SDZ with pH have also been reported by Lastre-Acosta et al. (2015) for the ultrasonic degradation of SDZ in aqueous

solutions. In view of these results, the initial SDZ concentration and pH in main experiments were fixed as 20 ppm and pH 4.

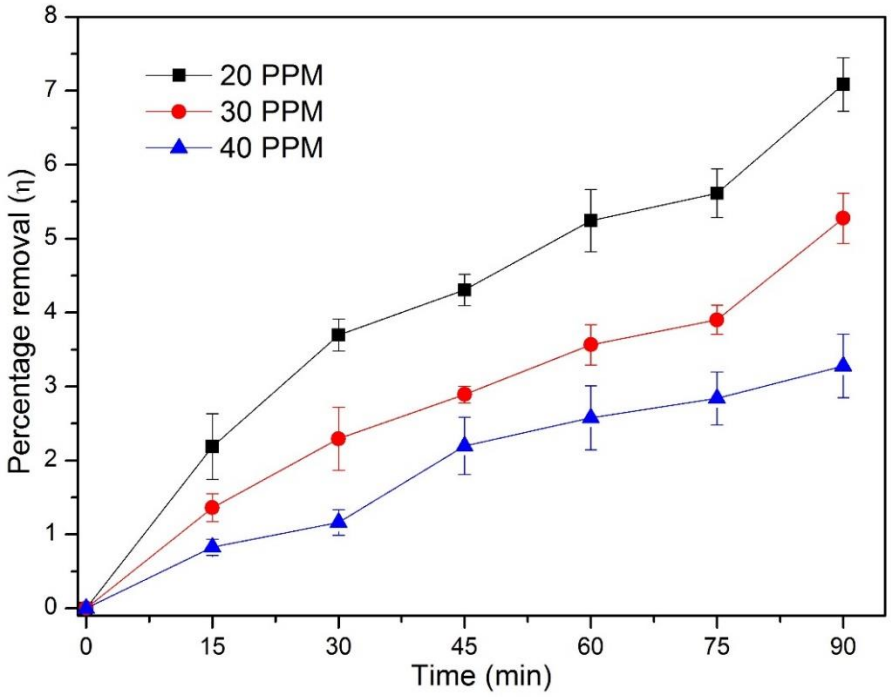

Figure 2.2: Effect of initial concentration on the degradation of SDZ (Experimental conditions: inlet pressure – 10 atm; pH – 6.2)

The main experiments were planned as follows:

1. Variation in inlet pressure of pump = 4, 6, 8 and 10 atm in the presence of a heterogeneous Fenton catalyst. Other additives (with pre-optimized quantities using statistical techniques) in the reaction solution were as follows: Set 1: H_2O_2 = 0.95 mL/L, $Na_2S_2O_8$ = 348.5 mg/L, α-Fe_2O_3 = 181.8 mg/L; Set 2: H_2O_2 = 0.91 mL/L, $Na_2S_2O_8$ = 343.5 mg/L, Fe_3O_4 = 203 mg/L. In this category of experiments, SDZ degradation achieved with both $^{\bullet}OH$ and $SO_4^{\bullet-}$ radicals. It may be noted that the sources of $^{\bullet}OH$ radicals were both transient cavitation bubbles and Fenton reactions.
2. Determination of kinetic constants of SDZ degradation by $^{\bullet}OH$ and $SO_4^{\bullet-}$ radicals using relative rate technique of Xie et al. (2015) with benzoic acid (BA) as reference

compound (or pollutant). These experiments were conducted at optimized conditions for SDZ degradation. Reactions were performed in two sets with the equal initial concentration of BA and SDZ. Set 1 (degradation by •OH radicals) reaction mixture: H_2O_2 = 0.95 mL/L, α-Fe_2O_3 = 181.8 mg/L, BA = 20 ppm, SDZ = 20 ppm, pH = 4. Set 2 (degradation by $SO_4^{\bullet-}$ radicals) reaction mixture: $Na_2S_2O_8$ = 348.49 mg/L, BA = 20 ppm, SDZ = 20 ppm, pH = 4. In the second set, the activation of persulfate is achieved through •OH radicals generated through transient cavitation and high shear generated by cavitation flow.

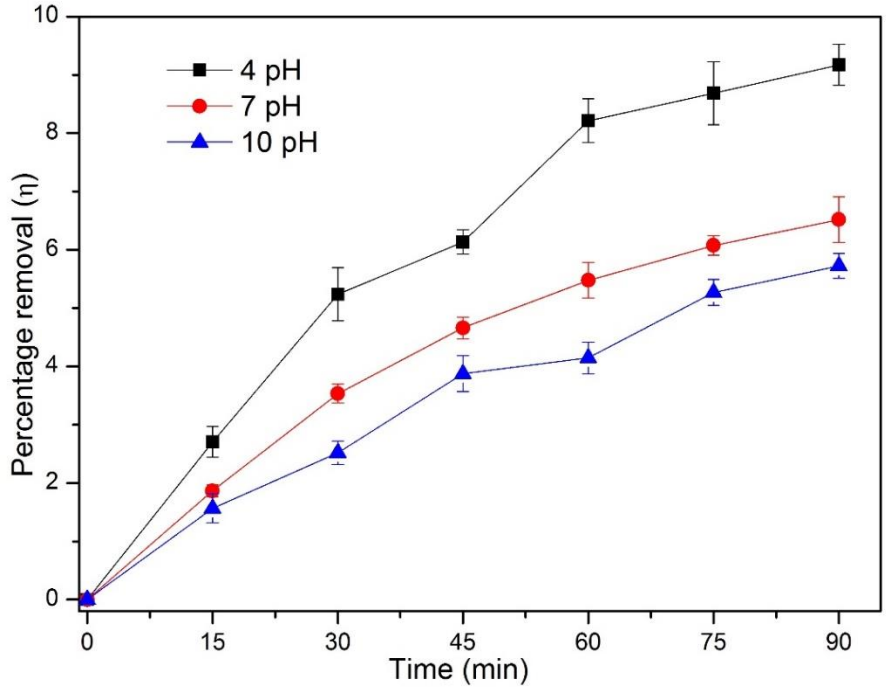

Figure 2.3: Effect of pH on degradation of SDZ
(Experimental conditions: SDZ initial concn. 20 ppm, inlet pressure 10 atm)

The total volume of the reaction solution was 5 L and the treatment period (or flow circulation time) was 90 min in all experiments. Aliquots of reaction mixture were withdrawn at intervals of 15 min for analysis of residual SDZ concentration. The inlet

pressures were adjusted by controlling the VFD while closing the bypass line completely. All experiments were conducted in triplicate to assess the reproducibility of the results.

2.2.5 Analysis

The residual concertation of SDZ in the aliquots of the reaction mixture was analysed using HPLC (Shimadzu, Model: SPD 20A), which was equipped with C-18 reverse phase column (250 mm × 4.6 mm, 5 µm) and UV detector with an autosampler (Shimadzu, Model: SIL-20AC-HT). The mobile phase was a mixture of acetonitrile (25%) and sodium acetate (75%, 0.02 mol/L, pH 4.75) with an isocratic flow rate of 0.8 mL/min. The detection wavelength and temperature were set at 275 nm and 30^{o}C, respectively. The concentration of the reference pollutant benzoic acid (BA) was also analysed with HPLC. UV detector was set at 227 nm with mobile phase of methanol (50%) and phosphoric acid (50%, 10 mM) at a flow rate of 1.0 mL/min.

***Leached iron measurement*:** Concentrations of total iron (Fe^{t}) and Fe^{2+} ions in reaction solution was determined by colorimetric method using a UV–Vis spectrophotometer (Shimadzu, Model No: UV-2600) as specified in a standard method (3500-Fe B, Phenanthroline method) (American Public Health Association, 1998). Iron concentration was identified by the reaction of Fe^{t} with 1,10-phenanthroline giving orange-red complex with absorbance at λ_{max} = 510 nm under acidic conditions. To estimate the degree of oxidation of Fe^{2+} to Fe^{3+} or vice versa, the concentrations of total iron ($[Fe^{t}] = [Fe^{2+}] + [Fe^{3+}]$) and ferrous ions ($Fe^{2+}$) in aqueous solution were determined using phenanthroline method. To measure the concentration of total iron in 5 mL sample withdrawn from the reaction mixture, 50 mL deionized water, 2 mL of conc. HCl and 1 mL of hydroxylamine (1.45 M) were mixed with the sample, and the solution was boiled to reduce to 15-20 mL. This was followed by the addition of 4 mL of phenanthroline solution (5 mM) and 10 mL

of ammonium acetate buffer to the solution and the final volume was diluted to 100 mL. After thorough mixing, the absorbance of the solution at 510 nm was measured. The concentration of Fe^{2+} in the reaction mixture was determined at site by acidifying a separate 5 mL sample with 2 mL conc. HCl. Immediately thereafter, 20 mL of phenanthroline solution and 10 mL of ammonium acetate buffer solution were added to the mixture and the final volume was diluted to 100 mL with thorough mixing. The absorbance of this solution was measured at 510 nm.

2.2.6 Kinetic Model for SDZ Degradation

***Determination of kinetic constants of SDZ degradation using reference compound method*:** Aschmann et al. (2011) have proposed a method of reference compound for determination of kinetic constant of $^{\bullet}OH$ radical induced degradation of 3-methoxy 3-methyl 1-butanol. This method has also been used by Xie et al. (2015) for the determination of kinetic constants of degradation of 2-methylisoborneol (2-MIB) and geosmin by $^{\bullet}OH$ and $SO_4^{\bullet-}$ radicals in UV/persulfate system. In the present study, we have adopted this technique to determine the kinetic constants of SDZ degradation by $^{\bullet}OH$ and $SO_4^{\bullet-}$ radicals, viz. k_{11} and k_{12}, produced by hybrid HC/α-Fe_2O_3/H_2O_2/persulfate system. Benzoic acid was used as the model or reference compound in the reaction mixture along with the main pollutant of SDZ. The kinetic constants of degradation of benzoic acid by $^{\bullet}OH$ and $SO_4^{\bullet-}$ radicals have been reported by Buxton et al. (1988) and Neta et al. (1988) as 5.9×10^9 and 1.2×10^9 $M^{-1} \cdot s^{-1}$, respectively. On the basis of these known kinetic constants, the kinetic constants of SDZ degradation by $SO_4^{\bullet-}$ or $^{\bullet}OH$ radicals are obtained as follows:

Under assumption that the target compound (SDZ) and the reference compound (BA) were degraded only by either reactive radicals (viz. $SO_4^{\bullet-}$ or $^{\bullet}OH$), the relation between their degradation profiles and the kinetic constants of degradation is given as:

$$\ln\left(\frac{[SDZ]_0}{[SDZ]_t}\right) = \frac{k_{SDZ}}{k_{BA}} \ln\left(\frac{[BA]_0}{[BA]_t}\right) \quad (2.1)$$

$[SDZ]_0$ and $[BA]_0$ are the initial concentrations of SDZ and reference compound BA, respectively. $[SDZ]_t$ and $[BA]_t$ are instantaneous concentrations of SDZ and reference compound BA at sampling time *t*. k_{SDZ} and k_{BA} are the kinetic constants of degradation of SDZ and BA. A plot of $\ln([SDZ]_0/[SDZ]_t)$ vs. $\ln([BA]_0/[BA]_t)$ yields a straight line with slope k_{SDZ}/k_{BA} and zero intercept. From the literature value of k_{BA} and the numerical value of slope, k_{SDZ} can be determined. To distinguish between individual degradation of 2-MIB and geosmin by $^{\bullet}OH$ and $SO_4^{\bullet-}$ radicals, Xie et al. (2015) have used radical scavengers, viz. *t*-butyl alcohol and methanol. However, in the present study, we have conducted independent experiments of SDZ degradation with only Fenton reagents and $Na_2S_2O_8$, as noted previously in the experimental section. The model was validated by comparing the simulated and experimental profiles of SDZ, as discussed in greater detail subsequently.

Simulation of degradation profile of SDZ in homogeneous Fe^{2+}/H_2O_2/persulfate system: A kinetic model was proposed for SDZ degradation based on a reaction network for homogeneous Fe^{2+}/H_2O_2/persulfate system, as depicted in Table 2.1. The kinetic model is based on the hypothesis that SDZ degradation occurs via both $^{\bullet}OH$ and $SO_4^{\bullet-}$ radicals. $^{\bullet}OH$ radicals in the reaction medium are generated through the Fenton reactions as well as the transient collapse of the cavitation bubbles generated at the orifice plate in HC reactor. Activation of persulfate occurs via both Fe^{2+} and $^{\bullet}OH$ radicals. For the

simplicity, the Fenton reaction system has been categorized into three sets of reactions, viz. chain initiation, oxidation and chain termination, while the persulfate reaction system has been categorized into two reaction sets, viz. chemical activation and oxidation.

Table 2.1: The proposed reactions mechanism and rate constants used in kinetic modelling of SDZ degradation

Reaction	Reactions	k (M^{-1} s^{-1})	References
	Fenton reactions[#]		
R1	$Fe^{2+} + H_2O_2 \longrightarrow Fe^{3+} + {}^{\bullet}OH + OH^-$	70	Wu et al. (2010)
R2	${}^{\bullet}OH + H_2O_2 \longrightarrow H_2O + HO_2^{\bullet}$	3.3×10^7	Wu et al. (2010)
R3	$H_2O_2 + Fe^{3+} \longrightarrow Fe^{2+} + HO_2^{\bullet} + H^+$	0.01	Wu et al. (2010)
R4	$Fe^{3+} + HO_2^{\bullet} \longrightarrow Fe^{2+} + O_2 + H^+$	1.2×10^6	Wu et al. (2010)
R5	$Fe^{2+} + HO_2^{\bullet} \longrightarrow Fe^{3+} + OH^-$	1.3×10^6	Wu et al. (2010)
R6	${}^{\bullet}OH + Fe^{2+} \longrightarrow Fe^{3+} + OH^-$	3.2×10^8	Wu et al. (2010)
	Persulfate reactions[*]		
R7	$S_2O_8^{2-} + Fe^{2+} \longrightarrow Fe^{3+} + SO_4^{2-} + SO_4^{\bullet-}$	27	Xu and Li (2010)
R8	$S_2O_8^{2-} + {}^{\bullet}OH \longrightarrow S_2O_8^{\bullet-} + OH^-$	1.4×10^7	Xie et al. (2015)
R9	$Fe^{2+} + SO_4^{\bullet-} \longrightarrow Fe^{3+} + SO_4^{2-}$	3×10^8	Xu and Li (2010)
R10	$Fe^{3+} + SO_4^{\bullet-} \longrightarrow Fe^{2+} + SO_4^{2-}$	4.6×10^9	Ghauch et al. (2013)
	Gross degradation reactions		
R11	$SDZ + {}^{\bullet}OH \longrightarrow H_2O + CO_2 + products$	5.2×10^9	This study
R12	$SDZ + SO_4^{\bullet-} \longrightarrow H_2O + CO_2 + products$	1.8×10^9	This study
	Gross degradation reactions in presence of BA		
R13	$BA + {}^{\bullet}OH \longrightarrow H_2O + CO_2 + products$	5.9×10^9	Buxton et al. (1988)
R14	$BA + SO_4^{\bullet-} \longrightarrow H_2O + CO_2 + products$	1.2×10^9	Neta et al. (1988)

Fenton reactions: Chain initiation = R1, Oxidation reaction = R2, R3, R4, Chain termination = R5, R6.
*Persulfate reactions: Chemical activation = R7, R8, Oxidation reaction = R9, R10.

The mass balances for all species involved in the reaction system are given below. These mass balances are based on two assumptions: (1) all reactions are 1st order with respect to the species involved in it, and (2) both radicals ($SO_4^{\bullet-}$ or ${}^{\bullet}OH$) are produced in the reaction medium in large excess so that rates of oxidative degradation of one of the

pollutants (either main pollutant SDZ or reference pollutant BA) is not influenced by the other.

$$\frac{d\left[SO_4^{\bullet-}\right]}{dt} = k_7\left[S_2O_8^{2-}\right]\left[Fe^{2+}\right] - k_9\left[Fe^{2+}\right]\left[SO_4^{\bullet-}\right] - k_{10}\left[Fe^{3+}\right]\left[SO_4^{\bullet-}\right] - k_{12}\left[SDZ\right]\left[SO_4^{\bullet-}\right] \quad (2.2)$$

$$\frac{d\left[S_2O_8^{2-}\right]}{dt} = -k_7\left[S_2O_8^{2-}\right]\left[Fe^{2+}\right] - k_8\left[S_2O_8^{2-}\right]\left[^{\bullet}OH\right] \quad (2.3)$$

$$\frac{d\left[^{\bullet}OH\right]}{dt} = k_1\left[Fe^{2+}\right]\left[H_2O_2\right] - k_2\left[^{\bullet}OH\right]\left[H_2O_2\right] - k_6\left[^{\bullet}OH\right]\left[Fe^{2+}\right] - k_8\left[S_2O_8^{2-}\right]\left[^{\bullet}OH\right] - k_{11}\left[SDZ\right]\left[^{\bullet}OH\right] \quad (2.4)$$

$$\frac{d\left[HO_2^{\bullet}\right]}{dt} = k_2\left[^{\bullet}OH\right]\left[H_2O_2\right] + k_3\left[Fe^{3+}\right]\left[H_2O_2\right] - k_4\left[Fe^{3+}\right]\left[HO_2^{\bullet}\right] - k_5\left[Fe^{2+}\right]\left[HO_2^{\bullet}\right] \quad (2.5)$$

$$\frac{d\left[H_2O_2\right]}{dt} = -k_1\left[Fe^{2+}\right]\left[H_2O_2\right] - k_2\left[^{\bullet}OH\right]\left[H_2O_2\right] - k_3\left[Fe^{3+}\right]\left[H_2O_2\right] \quad (2.6)$$

$$\frac{d\left[Fe^{2+}\right]}{dt} = -k_1\left[Fe^{2+}\right]\left[H_2O_2\right] + k_3\left[H_2O_2\right]\left[Fe^{3+}\right] + k_4\left[Fe^{3+}\right]\left[HO_2^{\bullet}\right] - k_5\left[Fe^{2+}\right]\left[HO_2^{\bullet}\right] - k_6\left[^{\bullet}OH\right]\left[Fe^{2+}\right] - k_7\left[S_2O_8^{2-}\right]\left[Fe^{2+}\right] - k_9\left[Fe^{2+}\right]\left[SO_4^{\bullet-}\right] + k_{10}\left[Fe^{3+}\right]\left[SO_4^{\bullet-}\right] \quad (2.7)$$

$$\frac{d\left[Fe^{3+}\right]}{dt} = k_1\left[Fe^{2+}\right]\left[H_2O_2\right] - k_3\left[H_2O_2\right]\left[Fe^{3+}\right] - k_4\left[Fe^{3+}\right]\left[HO_2^{\bullet}\right] + k_5\left[Fe^{2+}\right]\left[HO_2^{\bullet}\right] + k_6\left[^{\bullet}OH\right]\left[Fe^{2+}\right] + k_7\left[S_2O_8^{2-}\right]\left[Fe^{2+}\right] + k_9\left[Fe^{2+}\right]\left[SO_4^{\bullet-}\right] - k_{10}\left[Fe^{3+}\right]\left[SO_4^{\bullet-}\right] \quad (2.8)$$

An analytical solution of eq. 2.3 for the concentration of persulfate ions is obtained as:

$$\left[S_2O_8^{2-}\right] = e^{-\left(k_7\left[Fe^{2+}\right] + k_8\left[^{\bullet}OH\right]\right)t} \quad (2.9)$$

The three-radical species in the reaction system, $SO_4^{\bullet -}$, $OH^{\bullet}$ and $HO_2^{\bullet}$ are extremely reactive and unstable. Moreover, these are continuously produced in the reaction medium through different reactions listed in Table 2.1, and also through the transient cavitation occurring in HC reactor. In view of this, we have assumed pseudo-steady state for these species – in which their net concentration in the reaction medium remains constant. Thus equating LHS of equations 2.2, 2.4 and 2.5 and solving for $[SO_4^{\bullet -}]$, $[^{\bullet}OH]$ and $[HO_2^{\bullet}]$ yields the pseudo steady-state concentration of these species as:

$$\left[SO_4^{\bullet -}\right] = \frac{k_7\left[S_2O_8^{2-}\right]\left[Fe^{2+}\right]}{k_9\left[Fe^{2+}\right] + k_{10}\left[Fe^{3+}\right] + k_{12}\left[SDZ\right]} \tag{2.10}$$

$$\left[^{\bullet}OH\right] = \frac{k_1\left[Fe^{2+}\right]\left[H_2O_2\right]}{k_2\left[H_2O_2\right] + k_6\left[Fe^{2+}\right] + k_8\left[S_2O_8^{2-}\right] + k_{11}\left[SDZ\right]} \tag{2.11}$$

$$\left[HO_2^{\bullet}\right] = \frac{k_2\left[^{\bullet}OH\right]\left[H_2O_2\right]}{k_4\left[Fe^{3+}\right] + k_5\left[Fe^{2+}\right]} \tag{2.12}$$

The concentration profile of SDZ is obtained as:

$$-\frac{d\left[SDZ\right]}{dt} = k_{11}\left[SDZ\right]\left[^{\bullet}OH\right] + k_{12}\left[SDZ\right]\left[SO_4^{\bullet -}\right] \tag{2.13}$$

The ordinary differential eqs. for four species, viz. SDZ, Fe^{2+}, Fe^{3+} and H_2O_2 were solved after substitution of pseudo-steady state expressions for radical species (eqs. 2.10 – 2.12) and an analytical expression for persulfate ions, viz. eq. 2.13. Runge–Kutta 4th order – 5th order method (adaptive step size) (Press et al., 1992) was employed for numerical solution. The values of kinetic constants k_1 to k_{10} were borrowed from literature and are listed in Table 2.1.

2.3 RESULT AND DISCUSSION

2.3.1 Characterization of Iron Oxide Catalysts

The surface structure and morphology of the magnetic nanoparticles synthesized using solvothermal and hydrothermal methods was characterized FE-SEM micrographs shown in Fig. 2.4. It could be seen from Fig. 2.4(A) that uniform spherical shaped magnetite (Fe_3O_4) nanoparticles with an average size of 250 nm were obtained in the ethylene glycol assisted solvothermal system. Fig. 2.4(B) shows α-Fe_2O_3 particles with non-uniform size and rhombic like irregular shapes formed in hydrothermal system. The average diameter of the individual particle is approx. 90 nm. However, the micrograph clearly shows strong agglomeration between the nanoparticles.

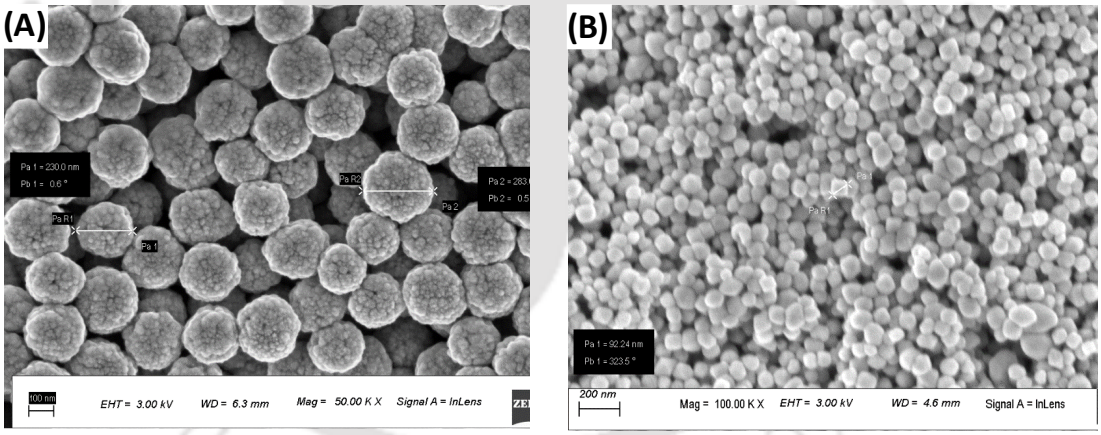

Figure 2.4: FE-SEM micrographs of (A) Fe_3O_4, and (B) Fe_2O_3

Phase composition and structure of as-synthesized Fe_3O_4 and α-Fe_2O_3 nanoparticles were identified by X-ray diffractograms. As shown in Fig. 2.5, XRD patterns of the iron oxide nanoparticles exhibit existence of pure α-Fe_2O_3 (hematite) and Fe_3O_4 (magnetite) phases. The XRD peaks correspond to expected rhombohedral structure of pure α-Fe_2O_3 with lattice constants of a = b = 5.038 Å, and c = 13.7619 Å, which are consistent with the values reported in JCPDS database (no. 24-0072). The patterns of iron oxide

nanoparticles synthesized hydrothermally show a series of diffraction peaks at (0 1 2), (1 0 4), (1 1 0), (1 1 3), (2 0 2), (0 2 4), (1 1 6), (1 2 2), (2 1 4), (3 0 0), (2 0 8), (1 0 1 0), (2 2 0) and (3 0 6) planes, which are in well accordance with the hexagonal structure of α-Fe_2O_3 phase (space group: R3). In the XRD patterns of solvothermally synthesized Fe_3O_4 nanoparticles, the diffraction peaks corresponding to (1 1 1), (2 2 0), (3 1 1), (2 2 2) (4 0 0), (4 2 2), (5 1 1), (4 4 0), (6 2 0) and (5 3 3) planes represent clear evidence of presence of inverse spinel cubic structure (space group: Fd3m) with lattice constant of a = 0.8393 Å. This confirms both crystallinity of the nanoparticles and the existence of the magnetite phase (as per JCPDS standard no. 19-0629). The narrow sharp peaks in XRD patterns of both nanoparticles indicate high crystallinity of hematite.

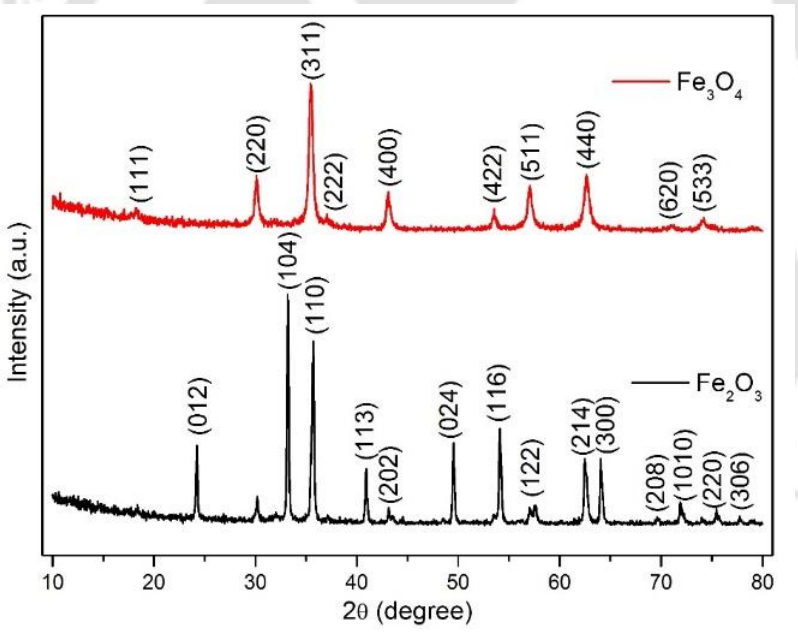

Figure 2.5: XRD patterns of Fe_3O_4 and α-Fe_2O_3 synthesized with solvo- and hydrothermal methods

Vibrating sample magnetometer (VSM) was used to characterize the magnetic behaviour of as-synthesized iron oxide nanoparticles. Fig. 2.6 (A) shows the hysteresis loop (M-H curves) of as-synthesized Fe_3O_4 (magnetite) nanoparticles. These nanoparticles exhibit

typical ferromagnetic behaviour with saturation magnetization (Ms), remnant magnetization (Mr) and coercive force of 78.48 emu/g, 1.90 emu/g, and 33.30 Oe, respectively. On the other hand, magnetic properties of α-Fe_2O_3 nanoparticles were saturation magnetization (Ms) = 0.84 emu/g, remnant magnetization (Mr) = 0.18 emu/g, and coercive force = 251.10 Oe, as evident from Fig. 2.6 (B). The magnetic properties of the iron oxide nanoparticles are relevant from the viewpoint of separation and recycle of these particles. Fe_3O_4 nanoparticles, by virtue of their higher saturation magnetization, are easily separable by application of magnetic field. For the α-Fe_2O_3 nanoparticles, separation through magnetic fields may not be effective, and thus may require the application of techniques of nanofiltration or centrifugation.

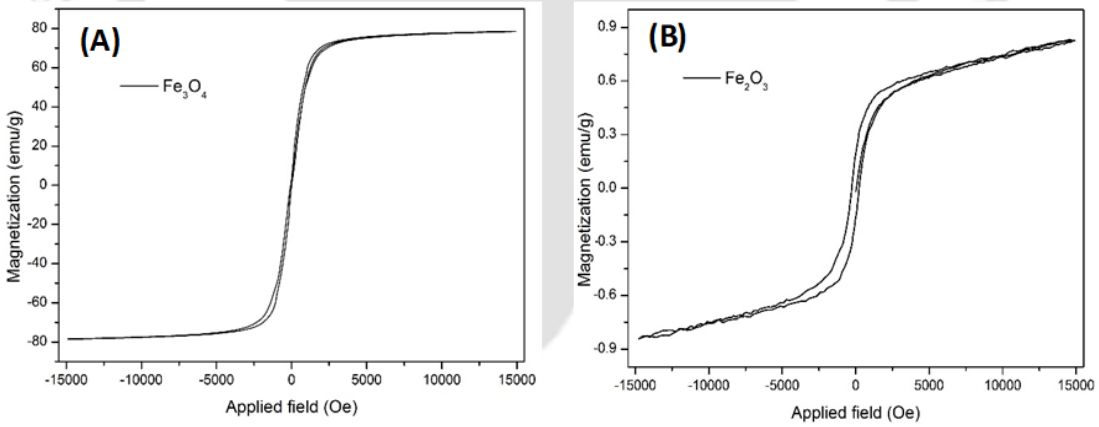

Figure 2.6: Magnetization curves of nanoparticles of (A) Fe_3O_4 and (B) α-Fe_2O_3

The Brunauer–Emmett–Teller (BET) surface area of iron oxide nanoparticles was determined with N_2 adsorption–desorption analysis at 77 K. Fig. 2.7 shows the adsorption-desorption isotherms of Fe_3O_4 and α-Fe_2O_3, which were characterized as type II and type III for Fe_3O_4 and α-Fe_2O_3, respectively. According to IUPAC, the isotherms of both Fe_3O_4 and α-Fe_2O_3 could be classified as type H_3 hysteresis loop, which indicated slit shaped mesoporous morphology of iron oxide nanoparticles (Sing et al., 1985). The

hysteresis loop of Fe_3O_4 nanoparticles revealed lesser uniformity of pore diameters among the particles, as compared to the pore diameters of α-Fe_2O_3 nanoparticles. During desorption, smaller pores which still contain condensed N_2, would interrupt the capillary evaporation from inner parts of the pores, and the inter-connectivity of these pores could be a probable reason for wider hysteresis loop of Fe_3O_4. FE-SEM micrographs of Fe_3O_4 reveal cracks on surface which may contribute to higher pore volume (V_{pore} = 0.0434 cm^3/g). On the other hand, micrographs of α-Fe_2O_3 show rather dense and agglomerated structure leading to relatively lesser pore volume (V_{pore} = 0.0247 cm^3/g). The BET surface area of Fe_3O_4 and α-Fe_2O_3 nanoparticles was determined as 32.36 and 20.22 m^2/g, respectively. The smaller BET surface area of α-Fe_2O_3 nanoparticles (as compared to Fe_3O_4 nanoparticles) despite much smaller size is essentially a consequence of strong agglomeration between the particles, as noted earlier.

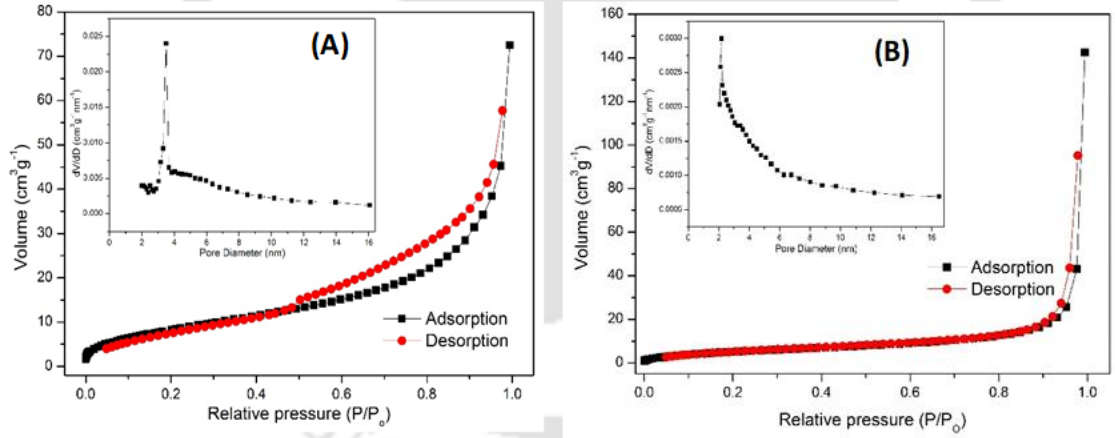

Figure 2.7: BET analysis - N_2 adsorption–desorption isotherms of nanoparticles of (A) Fe_3O_4 and (B) α-Fe_2O_3

2.3.2 Experimental Results of Sulfadiazine Degradation

2.3.2.1 Hydraulic Characteristic of Orifice Plates

Prior to main experiments on SDZ degradation, hydraulic characteristics of orifice plate were studied by measuring the flow rate through the mainline and calculating cavitation

number with varying inlet pressure to the orifice plate (or the discharge pressure of the pump, P_1) from 4 to 10 atm. The dimensionless cavitation number can be used to characterize the flow conditions in the mainline. The cavitation number is defined as: $C_v = (P_2 - P_v)/(\rho v_o^2/2)$, where P_2 is the fully recovered downstream pressure, P_v is the vapor pressure of the liquid, v_o is the net flow velocity at vena–contracta in the downstream region of orifice plate, which can be determined by ratio of flow rate through orifice plate and open area of orifice. Flow characteristics of the orifice plate are depicted in Fig. 2.8 (A), which shows the effect of inlet pressure on C_v and volumetric flow rate through the mainline. The number density of cavitation bubbles generated in the downstream region of orifice increases with reduction in cavitation number. This essentially enhances the quantum of total intensity of transient cavitation in the flow, and hence, the cavitational yield.

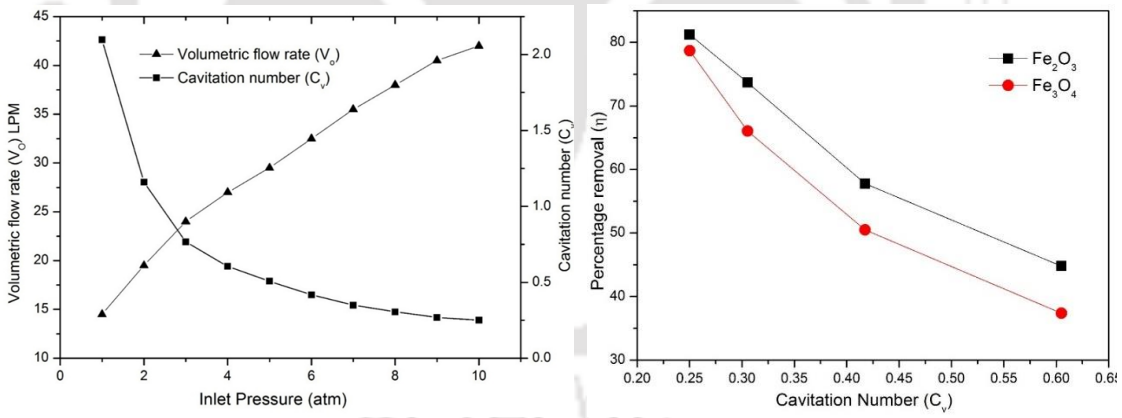

(A) (B)

Figure 2.8: (A) Effect of inlet pressure on the main line flow rate (V_o) and cavitation number (C_v) (B) Effect of Cavitation number (C_v) for degradation of SDZ (d_h = 4 mm and number of holes in orifice plate = 2). (Experimental conditions: Initial concentration – 20 ppm, pH – 4. For Fe_3O_4 as catalyst: Fe_3O_4= 203 mg/L, $Na_2S_2O_8$ = 343.5 mg/L, H_2O_2= 0.91 mL/L. For α-Fe_2O_3 as catalyst: α-Fe_2O_3 = 181.8 mg/L, $Na_2S_2O_8$ = 348.5 mg/L, H_2O_2 = 0.95 mL/L)

2.3.2.2 Comparative Evaluation of Two Iron Oxides as Fenton Reagents

Performance of the two iron oxide nanoparticles as Fenton reagents was evaluated using a statistical design of experiments for inlet pressure = 10 atm, pH = 4 and initial SDZ concn. = 20 ppm. The optimization variables in the 3-factor, 3-level statistical design were: (1) loading of the solid catalyst (either Fe_3O_4 or α-Fe_2O_3) denoted as X_1, (2) concn. of $Na_2S_2O_8$ denoted as X_2, and (3) concn. of H_2O_2 denoted as X_3. This design not only gave comparative evaluation of degradation efficiency of the two catalysts, but also the optimum composition of reaction mixture. It may be noted that in these experiments, the SDZ degradation was facilitated by the combined action of $SO_4^{\bullet-}$ and $^{\bullet}OH$ radicals. The details of the levels and factors for optimization, the complete central composite design (CCD) of experiments with response variable (% SDZ degradation) and ANOVA analysis of the quadratic model fitted to the experimental data are summarized in Table: 2.2, 2.3 and 2.4.

Table 2.2: Factors and levels of statistical experimental design for optimization of SDZ degradation

Experimental factors	Notation	Actual and coded values of optimization variables		
		Low (-1)	Middle (0)	High (+1)
α-Fe_2O_3/Fe_3O_4 (mg/L)	X_1	0	150	300
$Na_2S_2O_8$ (mg/L)	X_2	0	250	500
H_2O_2 (mL/L)	X_3	0	1	2

Table 2.3: Central composite design (CCD) of experiments for SDZ degradation along with response variables (Initial concentration of SDZ = 20 mg/L, pH = 4 and inlet pressure = 10 atm)

Run	Fenton catalyst (α-Fe_2O_3/ Fe_3O_4) nanoparticles (mg/L)	$Na_2S_2O_8$ (mg/L)	H_2O_2 (mL/L)	Response variable for Fenton catalyst (percentage SDZ degradation)	
				Fe_3O_4 nanoparticles	α-Fe_2O_3 nanoparticles
1	0	500	0	59.86±0.67	59.86±1.31
2	300	500	0	62.45±0.93	63.25±1.13
3	150	250	1	77.56±1.99	80.36±0.84
4	300	500	2	46.56±2.08	49.45±1.87
5	150	250	1	78.12±1.99	80.45±1.50
6	150	250	2	61.45±1.07	66.60±0.86
7	300	0	0	15.31±1.15	16.58±2.30
8	0	0	0	8.26±1.10	8.26±0.66
9	150	250	1	77.26±3.20	80.83±1.22
10	150	500	1	70.46±3.18	75.56±0.79
11	0	250	1	74.56±1.36	72.56±2.77
12	150	250	0	61.52±3.44	63.46±3.81
13	0	0	2	27.06±1.47	27.96±1.09
14	300	0	2	29.10±0.93	36.11±2.85
15	0	500	2	47.74±0.76	47.20±3.43
16	150	250	1	78.12±0.20	80.15±2.78
17	150	250	1	76.46±0.20	80.56±0.77
18	300	250	1	76.83±0.60	77.93±2.10
19	150	250	1	77.16±0.35	80.45±1.91
20	150	0	1	37.56±0.31	42.88±0.99

Table 2.4: Analysis of variance (ANOVA) for the quadratic model fitted to CCD experimental design

Source	Degrees of freedom	Fe_3O_4 nanoparticles		α-Fe_2O_3 nanoparticles	
		F-value	*p*-value	F-value	*p*-value
Regression	9	2884.54	0.00	29289.40	0.00
Linear	3	2554.18	0.00	24324.77	0.00
Square	3	5680.26	0.00	58685.24	0.00
Interaction	3	419.17	0.00	4858.18	0.00
Residual Error	10	-	-	-	-
Lack-of-Fit	5	0.88	0.55	0.51	0.763
Pure Error	5	-	-	-	-
Total	19	9831.76	-	10025.3	-

The final quadratic expressions for the response variable for the two catalysts are reproduced below:

Fe_3O_4 catalyst:
$$\%\ \text{Degradation} = 77.338 + 1.277X_1 + 16.978X_2 + 0.451X_3 - 1.48X_1^2 - 23.166X_2^2 - 15.69X_3^2 - 0.96X_1 \cdot X_2 - 1.098X_1 \cdot X_3 - 7.575X_2 \cdot X_3$$

(Optimum values of parameters: X_1 = 203.1 mg/L, X_2 = 343.4 mg/L, X_3 = 0.91 mL/L, percentage degradation of SDZ (experimental) = 78.70 ± 1.16%).

α-Fe_2O_3 catalyst:
$$\%\ \text{Degradation} = 80.468 + 2.748X_1 + 16.353X_2 + 1.597X_3 - 5.225X_1^2 - 21.25X_2^2 - 15.41X_3^2 - 1.354X_1 \cdot X_2 - 0.164X_1 \cdot X_3 - 8.211X_2 \cdot X_3$$

(Optimum values of parameters: X_1 = 181.8 mg/L, X_2 = 348.5 mg/L, X_3 = 0.95 mL/L, percentage degradation of SDZ (experimental) = 81.25 ± 1.43%).

Although the percentage SDZ degradation at optimum conditions for both iron oxide catalysts is almost similar, the optimum loading for α-Fe_2O_3 is marginally smaller, despite significantly smaller BET surface area as depicted in Table 2.5. Moreover, the porosity of the nanoparticles does not seem to be a governing factor influencing extent of degradation. Relatively smaller loading required for α-Fe_2O_3 nanoparticles could be a consequence of greater surface corrosion of the particles leading to larger generation of Fe^{2+} ions. This, in turn, could possibly be an effect of increased surface area of α-Fe_2O_3 particles due to de-agglomeration caused by high shear produced in cavitating flow through orifice, and also the shock waves produced by transient cavitation events. Similar results of enhancement in the degradation of antibiotic with cavitation-assisted hybrid heterogeneous Fenton like system have been reported in previous literature (Zhou et al., 2013; Zhou et al., 2014; Zhou et al., 2017). Zhou et al. (2013 & 2014) have studied the degradation of sulfamethazine in heterogeneous sonophotochemical magnetite-catalyzed Fenton-like (US/UV/Fe_3O_4/oxalate) system and sonophotocatalytic goethite/oxalate

Fenton-like system. More recently, Zhou et al. (2017) have also reported the degradation of norfloxacin in sonochemical Fe^0/tetraphosphate Fenton-like system. In all of these systems, the synergistic effect of ultrasound in promotion of degradation of antibiotic was identified in terms of reduction in mass transfer barriers, additional generation of radicals through cavitation bubbles and enhanced iron corrosion at solid-liquid interface. Zhou et al. (2013, 2014, 2017) have quantified the synergistic interactions among different degradation systems on the basis of ratios of pseudo 1st order kinetic constants for hybrid systems and individual systems. The typical synergy factor for the degradation of two antibiotics in different hybrid systems was ~ 2.

Table 2.5: Physical characteristics of magnetic nanoparticles

Nanoparticles	Colour	Particle type	S_{BET} (m^2/g)	V_{pore} (pore volume) (cc/g)	Average particle size (nm)
Fe_3O_4	Dark black	3D pinecone-like porous nanoparticles	32.36	0.0434	250
α-Fe_2O_3	Reddish-brown	Irregular submicron particles and rhomb like nanoparticles	20.22	0.0247	90

Separation of the iron oxide nanoparticles after treatment for recycle and reuse also gave interesting results. After the first 90 min of treatment, the solid catalyst was separated from the reaction mixture. Fe_3O_4 nanoparticles could be separated with a magnet, while α-Fe_2O_3 nanoparticles were separated using centrifugation. These particles were washed several times with water to removed adsorbed chemical species and other deposits. Three consecutive cycles of degradation experiments with recycled nanoparticles of both iron oxides resulted in almost consistent degradation. α-Fe_2O_3 nanoparticles gave percentage degradations of 80 ± 1.30, 79 ± 1.80, 79 ± 2.10 in three consecutive experiments at

optimum operating conditions noted earlier. Fe_3O_4 nanoparticles gave percentage degradations of 76.7 ± 1.20, 75.6 ± 1.40, 74.8 ± 2.60 in three consecutive experiments at optimum operating conditions.

2.3.2.3 Effect of Inlet Pressure

An important operational parameter for HC reactor is the inlet pressure of the flow entering the cavitation device (the orifice plate in present study). This factor not only governs the intensity of transient cavitation produced in the flow but also affects the net power consumption of the pump (and hence the operating cost). The degradation profiles of SDZ for different inlet pressures of HC reactor, viz. 4, 6, 8 and 10 atm, are shown in Fig. 2.9 (A) and (B) for solid catalysts of α-Fe_2O_3 and Fe_3O_4, respectively. The other operating conditions were at their optimum, as noted in the previous section (also listed in the figure captions). These degradation profiles were fitted to pseudo 1st order kinetics. The final percentage of degradation and the corresponding kinetic constants are listed in Table 2.6. It could be seen that the extent of degradation and kinetics of degradation varied proportionately with inlet pressure. The highest inlet pressure of 10 atm gave maximum degradation of 81.24 ± 2.32% (with the highest $k_{SDZ} = 41.50 \times 10^{-3}$ min^{-1}) and 78.69 ± 1.63% (again with the highest $k_{SDZ} = 32.81 \times 10^{-3}$ min^{-1}) for α-Fe_2O_3 and Fe_3O_4 nanoparticles, respectively. For all inlet pressures, higher and faster degradation was seen for α-Fe_2O_3 nanoparticles as compared to Fe_3O_4 nanoparticles. The plausible reasons underlying this result have already been discussed in the previous section. The local energy dissipation rate and the shear (or turbulence) in cavitating flow are proportional to inlet pressure. Numerous previous authors have demonstrated that the intensity of transient collapse of cavitation bubbles and the extent of production of oxidizing radicals ($^{\bullet}OH$ and $HO_2^{\bullet}$) increases with inlet pressure (Rajoriya et al., 2017a; Rajoriya et al.,

2017b; Pawar et al. 2017; Saharan et al., 2011). It may be noted that in these experiments, persulfate was also present in the reaction mixture (at cocn. of 348.5 mg/L and 343.5 mg/L for α-Fe_2O_3 and Fe_3O_4, respectively). Thus, both $^{\bullet}OH$ and $SO_4^{\bullet-}$ radicals contributed to the degradation of SDZ. The trend of higher and faster degradation with increasing inlet pressure essentially points towards dominant role of $^{\bullet}OH$ radicals in the SDZ degradation. This inference will be further confirmed with the result of the kinetic model for SDZ degradation.

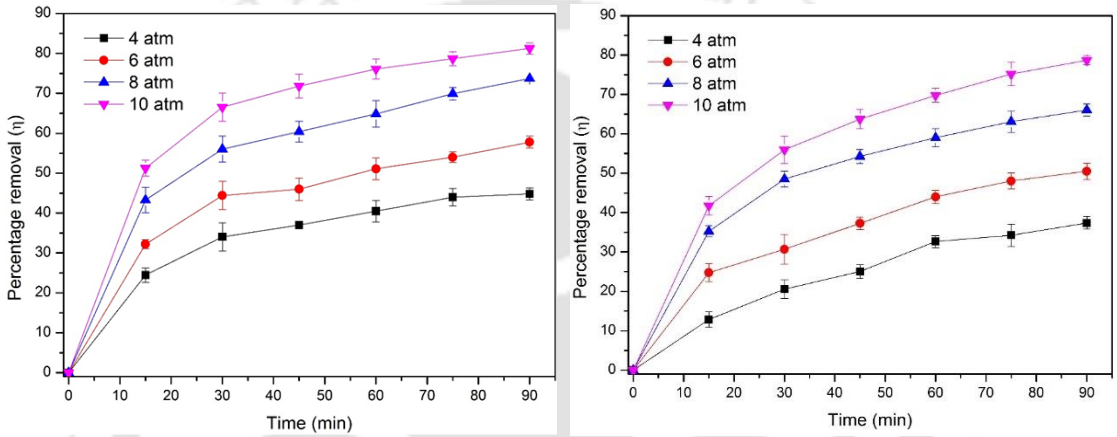

Figure 2.9: Effect of inlet pressure for degradation of SDZ (d_h = 4 mm and number of holes in orifice plate = 2) (Experimental conditions: Initial concentration – 20 ppm, pH – 4. (A) Degradation with α-Fe_2O_3 as catalyst: α-Fe_2O_3 = 181.8 mg/L, $Na_2S_2O_8$ = 348.5 mg/L, H_2O_2 = 0.95 mL/L; and (B) Degradation with Fe_3O_4 as catalyst: Fe_3O_4 = 203 mg/L, $Na_2S_2O_8$ = 343.5 mg/L, H_2O_2= 0.91 mL/L)

Table 2.6: Percentage degradation (η) and pseudo 1st order kinetic rate constant of SDZ degradation at different operating pressures

Inlet Pressure	α-Fe_2O_3		Fe_3O_4	
	η	k (min^{-1})#	η	k (min^{-1})#
4	44.80±2.10	15.50×10^{-3}	37.39±1.80	9.27×10^{-3}
6	57.78±1.26	22.10×10^{-3}	50.51±2.89	13.62×10^{-3}
8	73.69±1.89	28.40×10^{-3}	66.05±2.21	22.13×10^{-3}
10	81.24±2.32	41.50×10^{-3}	78.69±1.63	32.81×10^{-3}

- The pseudo 1st order profiles are shown in Figs. 2.10 and 2.11.

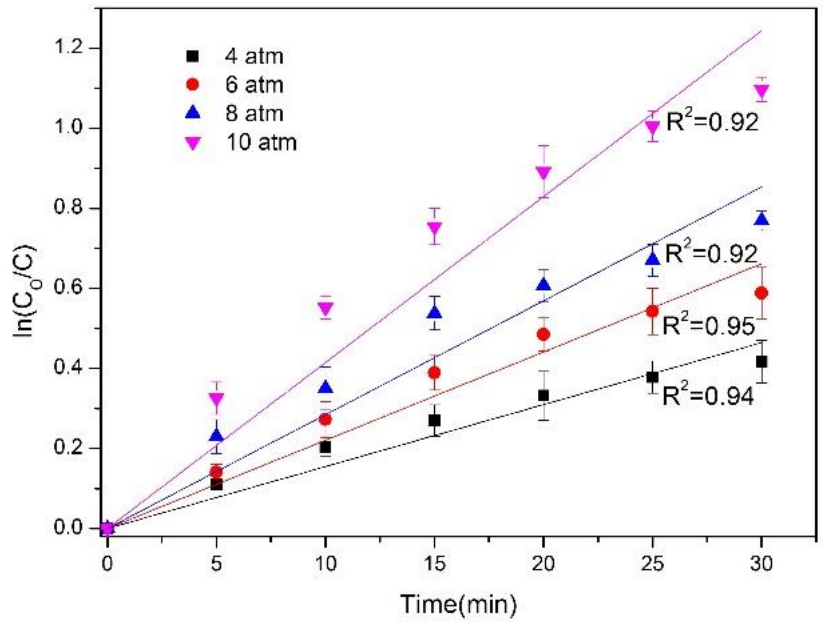

Figure 2.10: Determination of pseudo 1st order kinetic constant. (d_h = 4 mm and number of holes in orifice plate = 2) (Experimental conditions: Initial concentration – 20 ppm, pH – 4, α-Fe_2O_3 = 181.8 mg/L, $Na_2S_2O_8$ = 348.5 mg/L, H_2O_2= 0.95 mL/L)

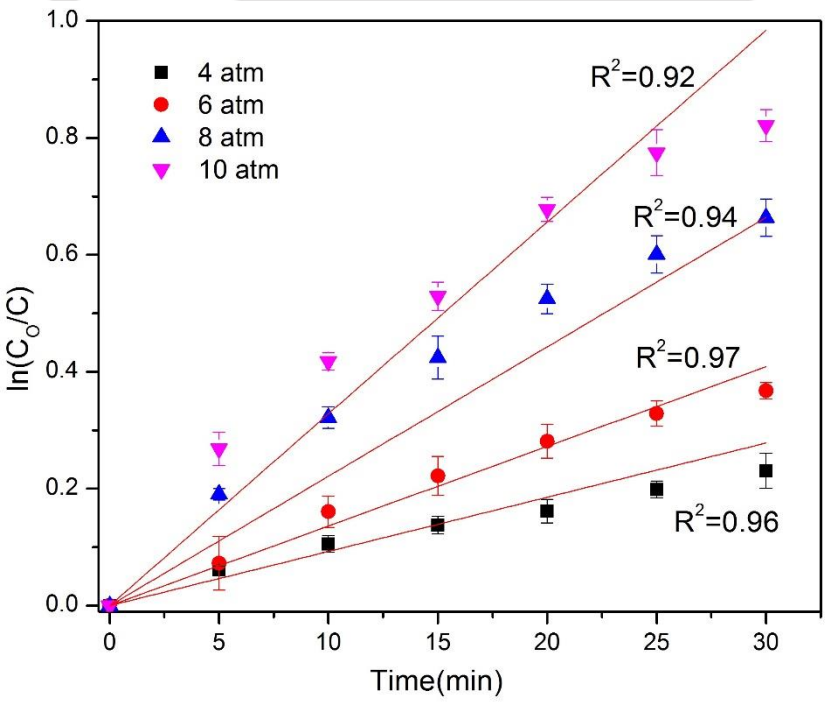

Figure 2.11: Determination of pseudo 1st order kinetic constant. (d_h = 4 mm and number of holes in orifice plate = 2) (Experimental conditions: Initial concentration – 20 ppm, pH – 4, Fe_3O_4 = 203 mg/L, $Na_2S_2O_8$ = 343.5 mg/L, H_2O_2= 0.91 mL/L)

2.3.2.4 Trends in SDZ Degradation with Cavitation Number (C_v)

Fig. 2.8 (B) shows the effect of cavitation number on the degradation of SDZ in the presence of both catalysts. For both α-Fe_2O_3 and Fe_3O_4 the extent of SDZ degradation shows continuous rise with reduction in cavitation number. Maximum SDZ degradation for both catalysts was achieved at C_v = 0.25 for the maximum operating pressure of 10 atm. Simultaneous reduction in C_v with increase in the inlet pressure augments generation of active cavitation bubbles in the downstream region of orifice. Transient oscillation and collapse of these cavitation bubbles augments the production of oxidizing (•OH or $HO_2^{\bullet}$) radicals, which also stimulates the production of persulfate radicals. The ultimate manifestation of these effects is rise in extent of SDZ degradation.

2.3.2.5 Validation of the New Kinetic Model

Fig. 2.12 (A) depicts the plot of $\ln(C_0/C)_{SDZ}$ vs. $\ln(C_0/C)_{BA}$ for determination of kinetic constant of SDZ degradation by •OH and $SO_4^{\bullet-}$ radicals (refer to experimental category 4, as described in section 2.2.4). The slopes of the plots (which are the ratio of kinetic constants k_{SDZ} /k_{BA}, as per eq. 2.1) are 0.88 and 1.49, for •OH and $SO_4^{\bullet-}$ radicals mediated degradation, respectively. Using these values of slopes and the values of $k_{BA} = 5.9 \times 10^9$ M^{-1} s^{-1} for •OH radicals (Buxton et al., 1988) and $k_{BA} = 1.2 \times 10^9$ M^{-1} s^{-1} for $SO_4^{\bullet-}$ radicals (Neta et al., 1988), the values of k_{SDZ} are determined as: $k_{SDZ} = 5.2 \times 10^9$ M^{-1} s^{-1} for •OH radicals and $k_{SDZ} = 1.8 \times 10^9$ M^{-1} s^{-1} for $SO_4^{\bullet-}$ radicals. These kinetic constants indicate that contribution of •OH radicals towards SDZ degradation is higher than $SO_4^{\bullet-}$ radicals.

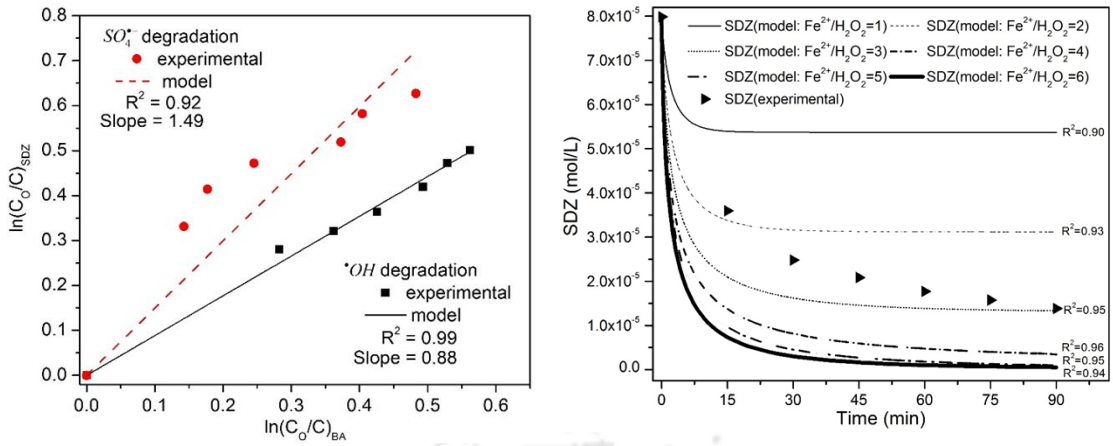

(A) (B)

Figure 2.12: (A) Determination of kinetic constants of SDZ degradation by $^{\bullet}OH$ and $SO_4^{\bullet-}$ radicals using technique of reference compound, viz. benzoic acid (BA). (B) Experimental profile of SDZ degradation for hybrid AOP of HC/α-Fe_2O_3/H_2O_2/persulfate vis-à-vis simulated profiles of SDZ degradation for homogenous Fenton/persulfate system for different initial ratios of Fe^{2+}/H_2O_2.
[Other experimental conditions for SDZ degradation: inlet pressure = 10 atm, SDZ initial concn. = 20 ppm (0.0799 mM) pH = 4, $Na_2S_2O_8$ = 348.5 mg/L (1.464 mM), α-Fe_2O_3 loading = 181.8 mg/L (1.138 mM), H_2O_2 = 0.95 mL/L (0.0279 mM)].

In order to assess the efficiency of hybrid AOP of heterogeneous Fenton (α-Fe_2O_3/H_2O_2) coupled with persulfate and HC vis-à-vis the conventional AOP of homogeneous Fenton/persulfate system ($Fe^{2+}/H_2O_2/S_2O_8^{2-}$), simulated profiles of SDZ degradation were obtained the kinetic model described in section 2.2.6. The principal difference between the two AOP systems is that SDZ degradation in homogeneous system commences with the highest concentration of Fe^{2+}, while in the present AOP with heterogeneous Fenton, Fe^{2+} ions are continuously generated in the system through leaching at surface of α-Fe_2O_3 nanoparticles.

Fig. 2.12 (B) compares the simulated degradation profiles of SDZ for different initial ratios of $[Fe^{2+}]/[H_2O_2]$ against the experimental profile of degradation at optimum set of parameters (listed in figure caption). It could be seen that the best match between experimental and simulated profiles (R^2 = 0.96) is obtained for initial $[Fe^{2+}]/[H_2O_2]$ ratio

of 4. This result is essentially an indication of high Fe^{2+} concentration prevalent in the reaction medium throughout 90 min treatment. This is attributed to high rate of leaching at the surface of α-Fe_2O_3 nanoparticles. The enhanced leaching is a possible consequence of high intensity turbulence and shear generated in cavitating flow that augments the solid-liquid mass transfer at surface of α-Fe_2O_3 nanoparticles.

A plausible explanation for this result can be given on the basis of kinetic constants of reactions R9, R10 and R12 listed in Table 2.1. Fe^{2+} ions generated through leaching at surface of α-Fe_2O_3 nanoparticles are oxidized to Fe^{3+} through reactions R1 and R6. Both Fe^{2+} and Fe^{3+} compete with SDZ for reaction with $SO_4^{\bullet-}$ radicals due to high kinetic constants of reactions R9 and R10 (3×10^8 and 4.6×10^9 M^{-1} s^{-1}, respectively), which are comparable to the degradation kinetic constant k_{SDZ} for $SO_4^{\bullet-}$ radicals (1.8×10^9 M^{-1} s^{-1}). This reduces the net utility of $SO_4^{\bullet-}$ radicals for SDZ degradation. On the other hand, •OH radicals produced in the medium through reaction R1 and transient collapse of cavitation bubbles are preferentially consumed by SDZ as the kinetic constant of reaction between SDZ and •OH (5.2×10^9 M^{-1} s^{-1}) is at least one order of magnitude higher than other competitive reactions of •OH radicals, viz. R2 ($k_2 = 3.3 \times 10^7$ M^{-1} s^{-1}), R6 ($k_6 = 3.2 \times 10^8$ M^{-1} s^{-1}) and R8 ($k_8 = 1.4 \times 10^7$ M^{-1} s^{-1}).

2.4 CONCLUSIONS

The present study has investigated degradation of sulfadiazine with the novel AOP of heterogeneous Fenton/persulfate coupled with hydrodynamic cavitation. Two types of iron oxides, viz. α-Fe_2O_3 and Fe_3O_4, in the form of nanoparticles were used as solid Fenton catalyst. The composition of reaction mixture was optimized using statistical

experimental design, and the influence of other experimental parameters on SDZ degradation was studied. The highest and fastest SDZ degradation was obtained at acidic pH 4, pump inlet pressure = 10 atm for α-Fe_2O_3 as Fenton catalyst at loading of 181.8 mg/L. Analysis of experimental degradation profiles of SDZ vis-à-vis kinetic model for homogeneous Fenton/persulfate system revealed high concentration of Fe^{2+} in reaction mixture. This was attributed to the high rate of leaching of Fe^{2+} ions from surface of solid Fenton catalyst due to intense turbulence and shear generated in cavitating flow. The kinetic constants of SDZ degradation by $^{\bullet}OH$ and $SO_4^{\bullet-}$ radicals indicated faster degradation due to $^{\bullet}OH$ radicals. In summary, the results of this study have demonstrated the application of hydrodynamic cavitation in augmenting the efficacy of heterogeneous Fenton/persulfate system for degradation of SDZ.

REFERENCES

American Public Health Association, Standard Methods for the Examination of Water and wastewater Treatment, 20th ed., American Public Health Association, Washington, DC, USA, 1998.

Aschmann, S.M., Arey, J., Atkinson, R., Kinetics and products of the reaction of $^{\bullet}OH$ radicals with 3-methoxy-3-methyl-1-butanol, *Environ. Sci. Technol.* 45(16) (2011) 6896-6901.

Bashir, T.A., Soni, A.G., Mahulkar, A.V., Pandit, A.B., The CFD driven optimisation of a modified venturi for cavitational activity, *Can. J. Chem. Eng.* 89 (2011) 1366-1375.

Boriani, E., Benfenati, E., Baderna, D., Thomsen, M., Application of ERICA index to evaluation of soil ecosystem health according to sustainability threshold for chemical impact, *Sci. Total Environ.* 443 (2013) 134-142.

Buxton, G.V., Greenstock, C.L., Helman, W.P., Ross, A.B., Critical review of rate constants for reactions of hydrated electrons, hydrogen atoms and hydroxyl

radicals ($^{\bullet}OH/^{\bullet}O^{-}$) in aqueous solution, *J. Phys. Chem. Ref. Data* 17(2) (1988) 513-886.

Feng, Y., Wu, D., Deng, Y., Zhang, T., Shih, K., Sulfate radical-mediated degradation of sulfadiazine by $CuFeO_2$ rhombohedral crystal-catalyzed peroxymonosulfate: synergistic effects and mechanisms, *Environ. Sci. Technol.* 50 (2016) 3119-3127.

Ghauch, A., Ayoub, G., Naim, S., Degradation of sulfamethoxazole by persulfate assisted micrometric Fe^0 in aqueous solution, *Chem. Eng. J.* 228 (2013) 1168-1181.

Kuldeep, Saharan, V.K., Computational study of different venturi and orifice type hydrodynamic cavitating devices, *J. Hydrodyn.* 28(2) (2016) 293-305.

Lastre-Acosta, A.M., Cruz-González, G., Nuevas-Paz, L., Jáuregui-Haza, U.J., Teixeira, A.C.S.C., Ultrasonic degradation of sulfadiazine in aqueous solutions, *Environ. Sci. Pollut. Res.* 22(2) (2015) 918-925.

Neta, P., Huie, R.E., Ross, A.B., Rate constants for reactions of inorganic radicals in aqueous solution, *J. Phys. Chem. Ref. Data* 17(3) (1988) 1027-1284.

Pawar, S.K., Mahulkar, A.V., Pandit, A.B., Roy, K., Moholkar, V.S., Sonochemical effect induced by hydrodynamic cavitation: Comparison of venturi/orifice flow geometries, *AIChE J.* 63 (2017) 4705-4716.

Press, W.H., Teukolsky, S.A., Flannery, B.P., Vetterling, W.T., Numerical Recipes. New York: Cambridge University Press, 1992.

Rajoriya, S., Bargole, S., Saharan, V.K., Degradation of a cationic dye (Rhodamine 6G) using hydrodynamic cavitation coupled with other oxidative agents: reaction mechanism and pathway, *Ultrason. Sonochem.* 34 (2017a) 183-194.

Rajoriya, S., Bargole, S., Saharan, V.K., Degradation of reactive blue 13 using hydrodynamic cavitation: Effect of geometrical parameters and different oxidizing additives, *Ultrason. Sonochem.* 37 (2017b) 192-202.

Saharan, V.K., Badve, M.P., Pandit, A.B., Degradation of Reactive Red 120 dye using hydrodynamic cavitation, *Chem. Eng. J.* 178 (2011) 100-107.

Sing, K.S., Everett, D.H., Haul, R.A.W., Moscou, L., Pierotti, R.A., Rouquerol, J., Siemieniewska, T., Reporting physisorption data for gas/solid systems with special reference to the determination of surface area and porosity (Recommendations 1984), *Pure. Appl. Chem.* 57(4) (1985) 603-619.

Sivakumar, M., Pandit, A.B., Wastewater treatment: a novel energy efficient hydrodynamic cavitational technique, *Ultrason. Sonochem.* 9(3) (2002) 123-131.

Wu, Y., Zhou, S., Qin, F., Zheng, K., Ye, X., Modeling the oxidation kinetics of Fenton's process on the degradation of humic acid, *J. Hazard. Mater.* 179 (2010) 533-539.

Xie, P., Ma, J., Liu, W., Zou, J., Yue, S., Li, X., Wiesner, M.R., Fang, J., Removal of 2-MIB and geosmin using UV/persulfate: contributions of hydroxyl and sulfate radicals, *Water Res.* 69 (2015) 223-233.

Xu, X.R., Li, X.Z., Degradation of azo dye Orange G in aqueous solutions by persulfate with ferrous ion, *Sep. Purif. Technol.* 72(1) (2010) 105-111.

Zhou, T., Wu, X., Mao, J., Zhang, Y., Lim, T.T., Rapid degradation of sulfonamides in a novel heterogeneous sonophotochemical magnetite-catalyzed Fenton-like (US/UV/Fe_3O_4/oxalate) system, *Appl. Catal. B.* 160 (2014) 325-334.

Zhou, T., Wu, X., Zhang, Y., Li, J., Lim, T.T., Synergistic catalytic degradation of antibiotic sulfamethazine in a heterogeneous sonophotolytic goethite/oxalate Fenton-like system. *Appl. Catal., B.* 136 (2013) 294-301.

Zhou, T., Zou, X., Mao, J., Wu, X., Decomposition of sulfadiazine in a sonochemical Fe^0-catalyzed persulfate system: parameters optimizing and interferences of wastewater matrix, *Appl. Catal. B.* 185 (2016) 31-41.

Zhou, T., Zou, X., Wu, X., Mao, J., Wang, J., Wang Synergistic degradation of antibiotic norfloxacin in a novel heterogeneous sonochemical Fe^0/tetraphosphate Fenton-like system. *Ultrason. Sonochem.* 37 (2017) 320-327.

Zou, X., Zhou, T., Mao, J., Wu, X., Synergistic degradation of antibiotic sulfadiazine in a heterogeneous ultrasound-enhanced Fe^0/persulfate Fenton-like system, *Chem. Eng. J.* 257 (2014) 36-44.

CHAPTER 3

Optimization of Hydrodynamic Cavitation Rector for Sulfadiazine Degradation

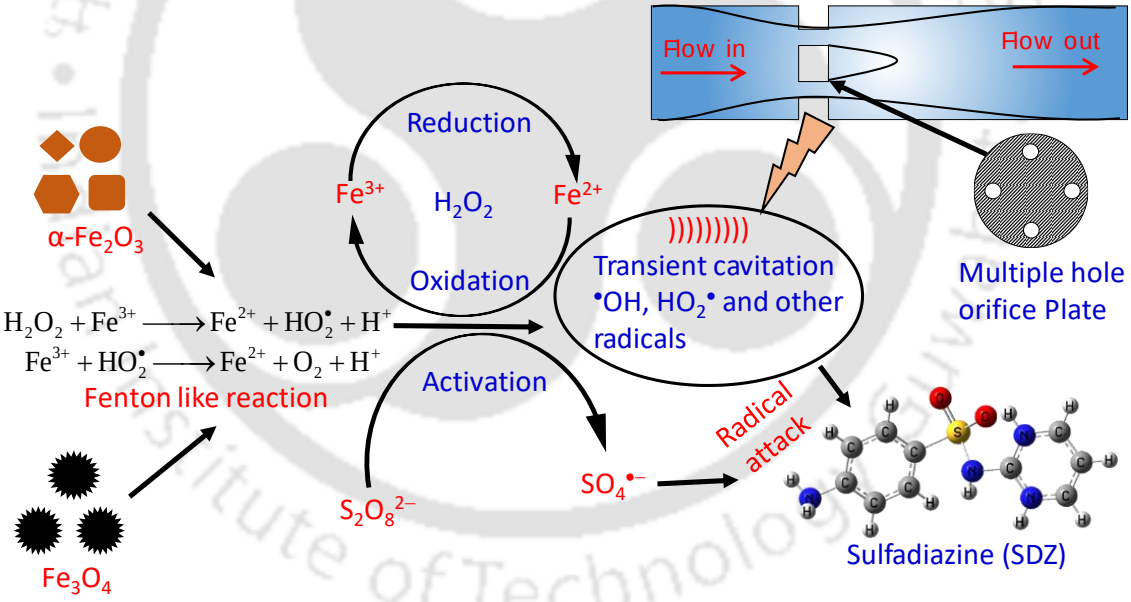

CHAPTER 3

OPTIMIZATION OF HYDRODYNAMIC CAVITATION REACTOR FOR SULFADIAZINE DEGRADATION

3.1 INTRODUCTION

In the previous chapter, the study on degradation of sulfadiazine (SDZ) with the novel AOP of heterogeneous Fenton/persulfate coupled with hydrodynamic cavitation was presented. A solid Fenton catalyst, in the form of nanoparticles of two iron oxides, α-Fe_2O_3 and Fe_3O_4, was employed. The experimental profiles of SDZ degradation were analyzed vis-à-vis kinetic model for homogeneous Fenton/persulfate system. This analysis revealed the enhanced leaching of Fe^{2+} ions from the surface of solid Fenton catalyst leading to a high concentration of Fe^{2+} in the reaction mixture. Intense turbulence and shear generated in cavitating flow was the probable cause leading to this effect. The results of the previous chapter indeed showed the efficacy of hydrodynamic cavitation in enhancing the degradation of SDZ through a heterogeneous Fenton/persulfate system. However, in order to achieve maximum synergy between hydrodynamic cavitation and Fenton/persulfate system, a thorough optimization study is needed that addresses various process and design issues of hydrodynamic cavitation. In this chapter, we take ahead the theme of oxidative degradation of SDZ through hybrid AOP of heterogeneous Fenton/persulfate coupled with hydrodynamic cavitation.

3.2 MATERIALS AND METHODS

3.2.1 Experimental setup

The HC setup used for the degradation of SDZ has been described in the previous chapter. As noted in the previous chapter, the orifice plates used for the generation of cavitating flow which were designed on the basis of previous computational and experimental studies (Bashir et al., 2011; Kuldeep and Saharan, 2016; Rajoriya et al., 2017, Vichare et al., 2000). In the previous chapter, we had used a single type of orifice plate with specifications: diameter of hole = 4 mm, number of holes =2, orifice plate diameter = 98 mm, orifice plate thickness = 2 mm, material = stainless steel (SS–316). In this chapter, we have tried to optimize the orifice plate design. Three orifice plates with different numbers of holes and sizes (i.e. diameters) have been used – the schematic of orifice plate is shown in Fig. 3.1. The specifications of the three orifice plates are given in Table 3.1.

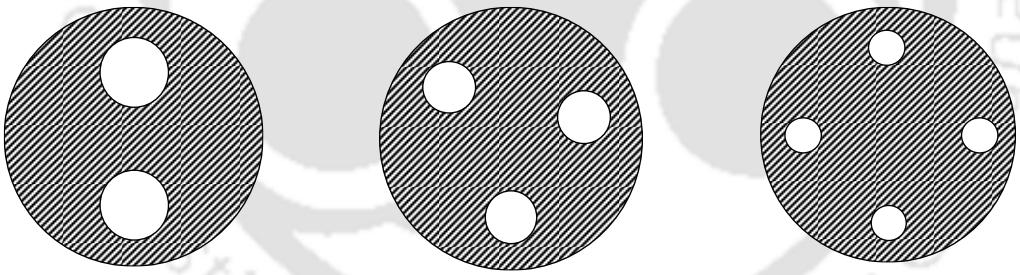

Plate – 1 Plate – 2 Plate – 3

Figure 3.1: Schematic of the orifice plates used in hydrodynamic cavitation reactor

Table 3.1: Flow geometry of orifice plates

Plate Number	Diameter of each hole (d_h) (mm)	Number of hole (N_h)	Flow area (mm^2)	α (mm^{-1})	β_0	Total perimeter of holes (mm)
Plate–1	4	2	25.12	1.00	0.073	25.12
Plate–2	3	3	21.20	1.33	0.061	28.26
Plate–3	2	4	12.56	2.00	0.036	25.12

3.2.2 Synthesis and Characterization of iron oxides i.e. Fe_3O_4 and α–Fe_2O_3

In this study, two iron oxides as: Fe_3O_4 and α–Fe_2O_3 were used as heterogeneous Fenton reagent. The synthesis and characterization of these iron oxide nanoparticles have been described in the previous chapter.

3.2.3 Analysis

The analytical procedure followed in this chapter is very much similar to the previous chapter. The degradation profile of SDZ (i.e. residual concentration of SDZ in the reaction mixture) was determined using HPLC (Shimadzu, Model: SPD 20A). A C–18 reverse phase column (250 mm × 4.6 mm, 5 µm) and UV detector with an auto sampler (Shimadzu, Model: SIL–20AC–HT) was used. A mixture of acetonitrile (25%) and sodium acetate (75%, 0.02 mol/L, pH 4.75) was used as mobile phase. The detection wavelength and temperature were set at 275 nm and 30 °C, respectively. The degradation profile of the reference pollutant benzoic acid (BA) was also determined using HPLC. In this case, UV detector was set at 227 nm with the mobile phase being mixture of methanol and phosphoric acid (1:1 v/v, 10 mM) at a flow rate of 1.0 mL/min.

The Mass spectrometric analysis was performed using Q-Tof Premier Mass Spectrometer (Make: Waters, LC-MS/MS) equipped with Electro Spray ionization (ESI)/Time of flight (Tof) source in MS mode without any purification to identify the intermediate products. The ESI–MS was performed in selected ion monitoring modes with positive electrospray ionization (ESI+) ion source with a full scan. Other parameters were as follows: capillary voltage: 3 eV, Source temperature: 100°C, ionization energy: 1 eV, collision energy: 5 eV, desolvation temperature: 250°C. MS data were recorded by scanning from 90 to 270 m/z. 1% formic acid was used to enhance the ionization.

3.2.4 Computational details

Molecular calculations were performed for the discernment of chemical mechanism and pathway of SDZ degradation by HC assisted heterogeneous Fenton/persulfate process. The model reactions for the computational study were possible reactions between the substrate SDZ molecule and the two oxidizing radicals, viz. $^{\bullet}OH$ and $SO_4^{\bullet-}$. The computational study was aimed at the identification of the reaction sites on the SDZ molecule leading to the formation of certain intermediates that are detected by LC-MS/MS analysis. The density functional theory (DFT) methods used to calculate the exact electron density, molecular properties and energies of possible reaction sites (or chemical bonds). The geometry optimizations of the SDZ molecule were performed. The DFT calculations were carried out as implemented in Gaussian 09 program, using the exchange–correlation functional B3LYP (Becke's three-parameter Lee–Yang–Parr) in combination with the 6-311 + g (d, p) basis set. Vibrational frequencies were calculated for the determination of the structures as stationary points and true minima on the potential energy surfaces. The optimization calculations were performed at standard gradient techniques with default convergence criteria using un-restricted polarization.

3.3 KINETIC MODEL FOR SDZ DEGRADATION

3.3.1 Determination of kinetic constant of reactions of SDZ with radicals

The same strategy of reference compound (as described in the previous chapter) has been followed to determine kinetic constants of SDZ degradation by $^{\bullet}OH$ and $SO_4^{\bullet-}$ radicals (Aschmann et al., 2011). Benzoic acid (BA) has been chosen as the reference compound. The kinetic constants of benzoic acid degradation by $^{\bullet}OH$ and $SO_4^{\bullet-}$ radicals have been deduced as 5.9×10^9 (Buxton et al., 1988) and 1.2×10^9 $M^{-1}{\cdot}s^{-1}$ (Neta et al., 1988)), respectively, (Table 3.2B). The kinetic constants of SDZ and BA degradation (k_{SDZ} and

k_{BA}) by any of the radicals are related as: $(C_0/C)_{SDZ} = (C_0/C)_{BA}^{(k_{SDZ}/k_{BA})}$. In other words, the kinetic constants of SDZ degradation can be determined from the slope of the plot of $\ln(C_0/C)_{SDZ}$ versus $\ln(C_0/C)_{BA}$.

As noted earlier, the degradation profiles of SDZ in all reaction systems have been determined using a kinetic model, which is based on a particular set of reactions for each system. These profiles have been compared with the experimental profiles of SDZ in that reaction system. The basic reaction system for oxidative degradation of SDZ is Fenton + persulfate in the presence of hydrodynamic cavitation. The basic 14 chemical reactions of Fenton + persulfate system involving eight species, as mentioned in the previous chapter, are listed below, with the inclusion of some new reactions (Table 3.2A).

Table 3.2 (A): The reactions and rate constants used in kinetic modelling for SDZ degradation

A.1	Fenton reaction system	k ($M^{-1}\cdot s^{-1}$)
R1	$Fe^{2+} + H_2O_2 \longrightarrow Fe^{3+} + {}^{\bullet}OH + OH^-$	70
R2	$Fe^{3+} + H_2O_2 \longrightarrow Fe^{2+} + HO_2^{\bullet} + H^+$	0.01
R3	$Fe^{3+} + HO_2^{\bullet} \longrightarrow Fe^{2+} + O_2 + H^+$	1.2×10^6
R4	$Fe^{2+} + HO_2^{\bullet} \longrightarrow Fe^{3+} + OH^-$	1.3×10^6
R5	$Fe^{2+} + {}^{\bullet}OH \longrightarrow Fe^{3+} + OH^-$	3.2×10^8
R6	${}^{\bullet}OH + H_2O_2 \longrightarrow H_2O + HO_2^{\bullet}$	3.3×10^7
R7[1]	$HO_2^{\bullet} + {}^{\bullet}OH \longrightarrow H_2O + O_2$	0.71×10^{10}
R8[2]	${}^{\bullet}OH + {}^{\bullet}OH \longrightarrow H_2O_2$	5.3×10^9
R9[2]	$HO_2^{\bullet} + HO_2^{\bullet} \longrightarrow H_2O_2 + O_2$	8.5×10^5
A.2	Fenton + Persulfate reaction system	k ($M^{-1}\cdot s^{-1}$)
R10	$S_2O_8^{2-} + Fe^{2+} \longrightarrow Fe^{3+} + SO_4^{2-} + SO_4^{\bullet-}$	27
R11	$S_2O_8^{2-} + {}^{\bullet}OH \longrightarrow S_2O_8^{\bullet-} + OH^-$	1.4×10^7
R12	$Fe^{2+} + SO_4^{\bullet-} \longrightarrow Fe^{3+} + SO_4^{2-}$	3×10^8
R13	$Fe^{3+} + SO_4^{\bullet-} \longrightarrow Fe^{2+} + SO_4^{2-}$	4.6×10^9
R14[3]	$SO_4^{\bullet-} + {}^{\bullet}OH \longrightarrow HSO_5^-$	1×10^{10}

[1]Gallard and Laat (2000), [2]Burbano et al. (2005), [3]Xie et al. (2015)

Table 3.2 (B): Kinetic constants of simultaneous degradation of SDZ and BA (reference compound method)

B	Degradation reactions	k ($M^{-1}\cdot s^{-1}$)
R15	$SDZ + {}^{\bullet}OH \longrightarrow H_2O + CO_2 + products$	Expt[#]
R16	$SDZ + SO_4^{\bullet-} \longrightarrow H_2O + CO_2 + products$	Expt[#]
R17	$BA + {}^{\bullet}OH \longrightarrow H_2O + CO_2 + products$	5.9×10^9
R18	$BA + SO_4^{\bullet-} \longrightarrow H_2O + CO_2 + products$	1.2×10^9

[#] described in Table 3.7

The mass balances for other species are based on two assumptions: (1) all reactions are 1st order with respect to all species involved, and (2) concentration of both ${}^{\bullet}OH$ and $SO_4^{\bullet-}$ radicals in the reaction medium in large excess so that rates of oxidative degradation of one of the pollutants (either main pollutant SDZ or reference pollutant BA) is not influenced by the other.

$$-\frac{d[SDZ]}{dt} = k_{15}[SDZ][{}^{\bullet}OH] + k_{16}[SDZ][SO_4^{\bullet-}] \tag{3.1}$$

$$\frac{d[{}^{\bullet}OH]}{dt} = k_1[Fe^{2+}][H_2O_2] - k_5[{}^{\bullet}OH][Fe^{2+}] - k_6[{}^{\bullet}OH][H_2O_2] - k_7[HO_2^{\bullet}][{}^{\bullet}OH] - k_8[{}^{\bullet}OH][{}^{\bullet}OH] - k_{11}[S_2O_8^{2-}][{}^{\bullet}OH] - k_{14}[SO_4^{\bullet-}][{}^{\bullet}OH] - k_{15}[SDZ][{}^{\bullet}OH] \tag{3.2}$$

$$\frac{d[HO_2^{\bullet}]}{dt} = k_2[Fe^{3+}][H_2O_2] - k_3[Fe^{3+}][HO_2^{\bullet}] - k_4[Fe^{2+}][HO_2^{\bullet}] + k_6[{}^{\bullet}OH][H_2O_2] - k_7[HO_2^{\bullet}][{}^{\bullet}OH] - k_9[HO_2^{\bullet}][HO_2^{\bullet}] \tag{3.3}$$

$$\frac{d[SO_4^{\bullet-}]}{dt} = k_{10}[S_2O_8^{2-}][Fe^{2+}] - k_{12}[Fe^{2+}][SO_4^{\bullet-}] - k_{13}[Fe^{3+}][SO_4^{\bullet-}] - k_{14}[SO_4^{\bullet-}][{}^{\bullet}OH] - k_{16}[SDZ][SO_4^{\bullet-}] \tag{3.4}$$

$$\frac{d[H_2O_2]}{dt} = -k_1[Fe^{2+}][H_2O_2] - k_2[Fe^{3+}][H_2O_2] - k_6[{}^{\bullet}OH][H_2O_2] + k_8[{}^{\bullet}OH][{}^{\bullet}OH] + k_9[HO_2^{\bullet}][HO_2^{\bullet}] \tag{3.5}$$

$$\frac{d\left[S_2O_8^{2-}\right]}{dt} = -k_{10}\left[S_2O_8^{2-}\right]\left[Fe^{2+}\right] - k_{11}\left[S_2O_8^{2-}\right]\left[^{\bullet}OH\right] \tag{3.6}$$

$$\begin{aligned}\frac{d\left[Fe^{2+}\right]}{dt} &= -k_1\left[Fe^{2+}\right]\left[H_2O_2\right] + k_2\left[Fe^{3+}\right]\left[H_2O_2\right] + k_3\left[Fe^{3+}\right]\left[HO_2^{\bullet}\right] \\ &-k_4\left[Fe^{2+}\right]\left[HO_2^{\bullet}\right] - k_5\left[Fe^{2+}\right]\left[^{\bullet}OH\right] - k_{10}\left[Fe^{2+}\right]\left[S_2O_8^{2-}\right] - k_{12}\left[Fe^{2+}\right]\left[SO_4^{\bullet-}\right] \\ &+k_{13}\left[Fe^{3+}\right]\left[SO_4^{\bullet-}\right]\end{aligned} \tag{3.7}$$

$$\begin{aligned}\frac{d\left[Fe^{3+}\right]}{dt} &= k_1\left[Fe^{2+}\right]\left[H_2O_2\right] - k_2\left[Fe^{3+}\right]\left[H_2O_2\right] - k_3\left[Fe^{3+}\right]\left[HO_2^{\bullet}\right] \\ &+k_4\left[Fe^{2+}\right]\left[HO_2^{\bullet}\right] + k_5\left[Fe^{2+}\right]\left[^{\bullet}OH\right] + k_{10}\left[Fe^{2+}\right]\left[S_2O_8^{2-}\right] + k_{12}\left[Fe^{2+}\right]\left[SO_4^{\bullet-}\right] \\ &-k_{13}\left[Fe^{3+}\right]\left[SO_4^{\bullet-}\right]\end{aligned} \tag{3.8}$$

For the mass balances of radical species, viz. [$^{\bullet}$OH], [$HO_2^{\bullet}$] and [$SO_4^{\bullet-}$] assumption of pseudo steady–state has been made – for the reasons mentioned in the previous chapter. Thus solving equation 3.2, 3.3 and 3.4 for [$^{\bullet}$OH], [$HO_2^{\bullet}$] and [$SO_4^{\bullet-}$] yields the pseudo steady-state concentration of these species as:

$$\begin{aligned}\left[^{\bullet}OH\right] = \frac{k_1\left[Fe^{2+}\right]\left[H_2O_2\right]}{k_5\left[Fe^{2+}\right] + k_6\left[H_2O_2\right] + k_7\left[HO_2^{\bullet}\right] + k_8\left[^{\bullet}OH\right] + k_{11}\left[S_2O_8^{2-}\right]} \\ +k_{14}\left[SO_4^{\bullet-}\right] + k_{15}\left[SDZ\right]\end{aligned} \tag{3.9}$$

$$\left[HO_2^{\bullet}\right] = \frac{k_2\left[Fe^{3+}\right]\left[H_2O_2\right] + k_6\left[^{\bullet}OH\right]\left[H_2O_2\right]}{k_3\left[Fe^{3+}\right] + k_4\left[Fe^{2+}\right] + k_7\left[^{\bullet}OH\right] + k_9\left[HO_2^{\bullet}\right]} \tag{3.10}$$

$$\left[SO_4^{\bullet-}\right] = \frac{k_{10}\left[S_2O_8^{2-}\right]\left[Fe^{2+}\right]}{k_{12}\left[Fe^{2+}\right] + k_{13}\left[Fe^{3+}\right] + k_{14}\left[^{\bullet}OH\right] + k_{16}\left[SDZ\right]} \tag{3.11}$$

The ordinary differential eqs. for five species, viz. SDZ, Fe^{2+}, Fe^{3+}, H_2O_2 and $S_2O_8^{2-}$ were solved after substitution of pseudo-steady state expressions for radical species. Runge–Kutta 4th order – 5th order method (adaptive step size) method was used for the numerical

solution. The kinetic constants k_1 to k_{14} were borrowed from literature as listed in Table 3.2.

3.4 EXPERIMENTAL RESULTS OF SULFADIAZINE DEGRADATION

3.4.1 Hydraulic characteristic of multiple hole orifice plates

Hydraulic characteristics of orifice plate with variable flow area have been studied by measuring the flow rate through the mainline and calculating cavitation number with varying inlet pressure (P_1) from 4 to 10 bar. Dimensionless cavitation number can be used to characterize the flow conditions in mainline. The cavitation number is defined as:

$$C_v = P_2 - P_v \Big/ \left(\rho v_0^{\,2} / 2 \right)$$

where, P_2 is the fully recovered downstream pressure, P_v is the vapor pressure of the liquid, v_o is the velocity at the throat of the cavitator. Velocity at vena contracta (the "throat" of the cavitating flow downstream of the orifice) can be calculated by dividing the volumetric flow rate by cross-sectional area of holes on orifice plate. Flow characteristics of the orifice plates with different total flow area are tabulated in Table 3.3, which gives the effect of inlet pressure on C_v, volumetric flow rate and number of passes through the mainline. The liquid flow rate through mainline is enhanced with the inlet pressure, which in turn increases the velocity at the throat of orifice. The enhancement of the throat velocity head decreases the cavitation number. The number density of cavitation bubbles generated in the flow increases with reduction in downstream pressure – which is indicated by lowering of cavitation number. This essentially results in rise in the cavitation intensity in the flow – i.e. the extreme conditions of temperature and pressure reached in the cavitation zone, which in turn influences the cavitational yield. It has been reported in the literature that at very high

inlet pressures, the population of cavitation bubbles generated in the downstream region is very high, which fills up the entire downstream volume of the venturi. Coalescence of cavitation bubbles leads to the formation of "bubble clouds" which decreases the extremes of temperature and pressure reached during the transient collapse, and hence, the cavitational intensity. This phenomenon of *choked cavitation* has also been observed in the present work.

Table 3.3: Flow characteristics of multiple hole orifice plates

Inlet pressure	Plate 1			Plate 2			Plate 3		
	Flow rate (LPM)	C_v	No. of passes	Flow rate (LPM)	C_v	No. of passes	Flow rate (LPM)	C_v	No. of passes
2	19.5	1.16	351	19.5	0.81	356	12.0	0.74	220
4	27.0	0.61	486	25.0	0.50	450	16.0	0.43	288
6	32.5	0.42	585	31.5	0.31	572	19.5	0.30	347
8	38.0	0.31	684	36.5	0.24	657	22.0	0.23	396
10	42.0	0.25	756	42.5	0.17	765	26.5	0.16	477

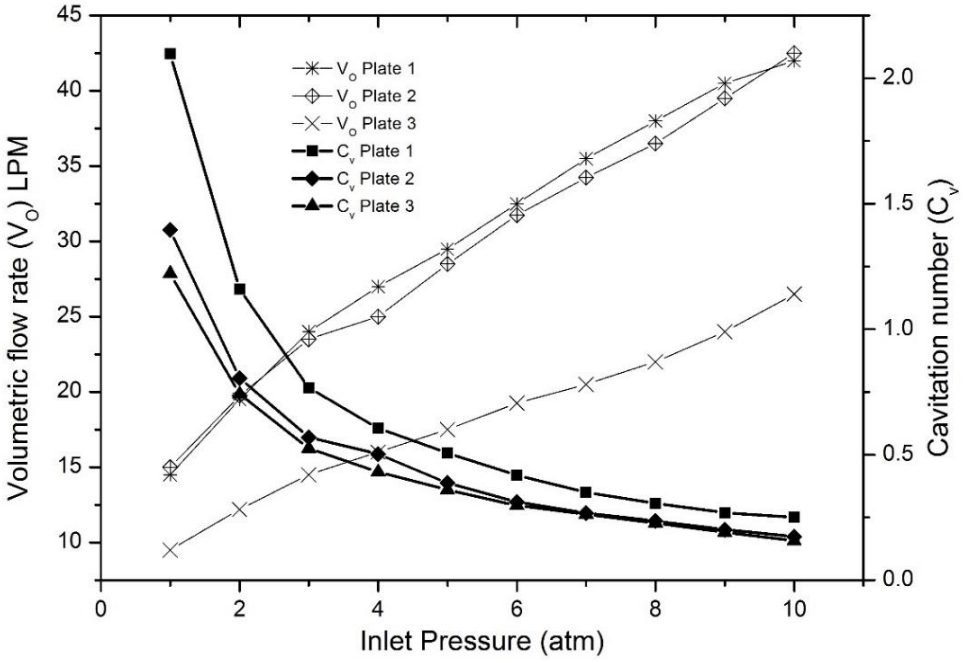

Figure 3.2: Effect of inlet pressure on the mainline flow rate and cavitation number

3.4.2 Effect of geometry of orifice plates on SDZ degradation for α-Fe_2O_3 and Fe_3O_4 nanoparticles

The extent of degradation has been found to be different for different plates, which can be attributed to the variation in cavitation intensity produced in the flow – as a result of flow patterns produced by different orifice plates by virtue of the configuration of holes (i.e. the number and diameters of the holes). To quantify the effects of flow geometry on cavitating flow and cavitation intensity, a characteristic parameter α is defined as:

$$\alpha = \frac{\text{Total perimeter of the holes}}{\text{Total area of opening}} = \frac{n \cdot \pi d_h}{n \cdot \pi \left(d_h / 2 \right)^2}$$

where d_h is the diameter of the hole on the orifice plate, and n is the number of holes. The value of α ranges from 1, 1.33 and 2 mm^{-1}. It has been observed that the extent of SDZ degradation increases with an increase in the value of α (Fig. 3.3). To give a quantitative idea, the rate constant for plate 3 has been found to be 43.38×10^{-3} min^{-1} as against 41.42×10^{-3} min^{-1} for plate 1. This can be explained on the basis of the peak conditions of temperature and pressure reached at the transient collapse of cavitation bubbles (Sivakumar and Pandit, 2002). It should be noted that the cavitation intensity (or the magnitudes of peak temperature and pressure conditions required for SDZ degradation) produced by orifice plate 3 with total flow area of 12.56 mm^2 was the highest.

If the plates having the same total perimeters of holes (plates 1 and 3) are compared, then SDZ degradation obtained with plate 3 having a larger value of α was higher than plate 1. Also, the plates having a smaller flow area produce better extent of degradation than the higher flowing area. A plausible explanation for this result can be given as follows: the relatively lower (~ 2×) flow area for plate 3 results in higher orifice velocity and reduced cavitation number, which in turn enhances the cavitational activity produced by flow in each hole. Thus, if a given open flow area is to be arranged on an

orifice plate, large number of holes with the smaller diameter would be the preferred configuration.

Table 3.4: Effect of geometry of orifice plates on SDZ degradation

Sr. No.	Plate–1 (α = 1.00)		Plate–2 (α = 1.33)		Plate–3 (α = 2.00)	
	α–Fe_2O_3	Fe_3O_4	α–Fe_2O_3	Fe_3O_4	α–Fe_2O_3	Fe_3O_4
η (%)	81.25±1.42	78.69±1.15	84.03±1.8	79.92±1.24	92.11±1.2	90.66±1.42
Rate	41.42×10^{-3}	32.81×10^{-3}	42.60×10^{-3}	33.15×10^{-3}	43.38×10^{-3}	42.74×10^{-3}

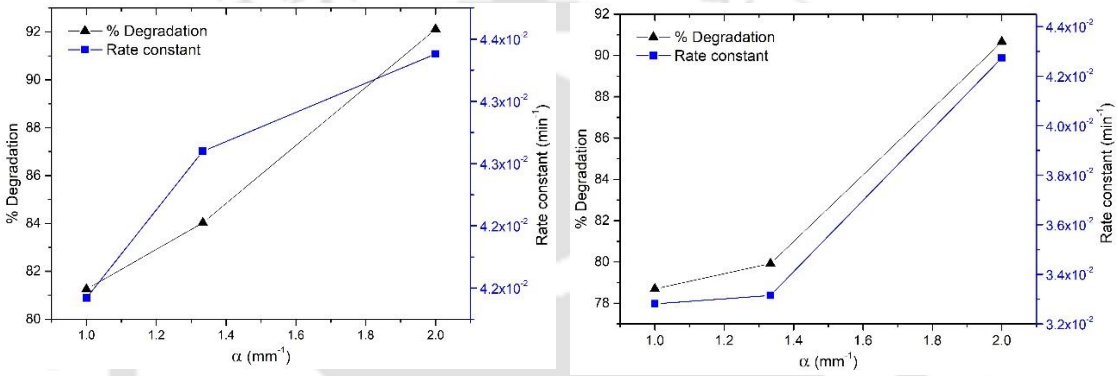

Figure 3.3: Effect of α on the SDZ degradation (A) α–Fe_2O_3 and (B) Fe_3O_4

Another parameter that can be used as performance yardstick of the orifice plates is β_0, defined as ratio of total area of holes to the cross–sectional area of pipe, i.e. the fractional open area of the plates.

$$\beta_0 = \frac{\text{Total flow area}}{\text{Cross-sectional area of the pipe}} = \frac{n \times \pi \left(d_h / 2\right)^2}{\pi \left(d_p / 2\right)^2}$$

where d_h is the diameter of the hole opening, and d_p is the diameter of pipe. The range of β_0 for the present study is 0.073–0.036 (Table 3.1). The effect of β_0 on the rate constant for the degradation of SDZ has been depicted in Fig. 3.4. It can be seen from this figure that the extent of degradation or the rate constant is inversely proportional to β_0.

The combined effect of α and total perimeter again comes into the picture for explaining these observations. It is known that the magnitude of cavitation intensity and the resultant

cavitational yield increases with reduction in flow area offered for the liquid medium and is proportional to the magnitude of collapse pressure generated (Moholkar and Pandit, 1997; Sivakumar and Pandit, 2002; Vichare et al., 2000). The decrease in β_0 from 0.073 to 0.036 boosts the chemical effects of cavitating flow significantly. A decrease in β_0 enhances both the intensity and frequency of turbulent velocity fluctuations. Because of the higher intensity of turbulent fluctuations, bubble expansion is increased. Thus, the amount of water vapor diffusing inside it increases. Moreover, the higher frequency of turbulent fluctuations decreases the time scale of compression, thus decreasing the extent of heat and mass transfer during this phase. This results in higher water vapor entrapment and higher temperatures and pressures during the collapse. Krishnan et al. (2006) has given detailed explanation of the effect of β_0 on the cavitation intensity produced by orifice plates.

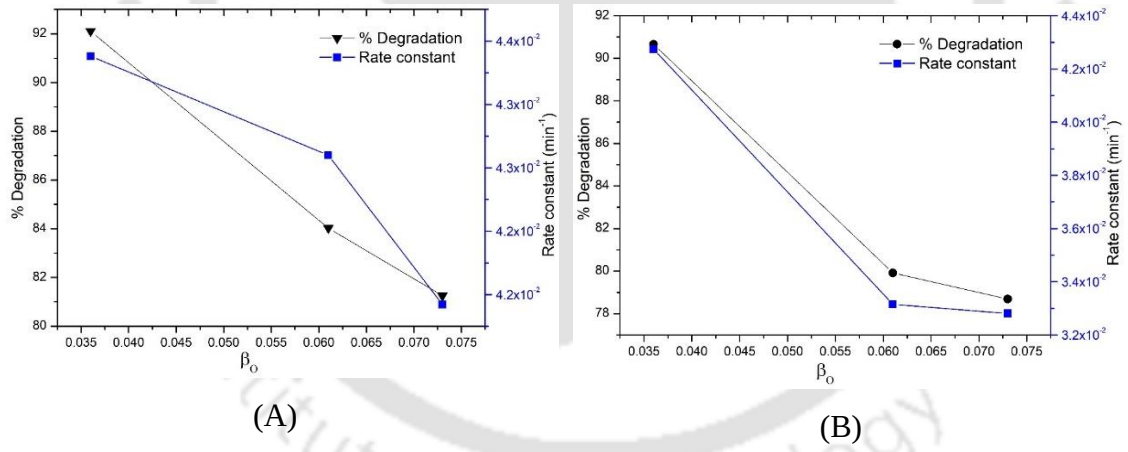

Figure 3.4: Effect of β_0 on the SDZ degradation (A) α–Fe_2O_3 and (B) Fe_3O_4

3.4.3 Effect of Inlet pressure and cavitation number (C_v)

Inlet fluid pressure is the most important parameter the governs the performance of hydrodynamic cavitation reactor for oxidative degradation of organic pollutants. The cavitation intensity in the "cavitation zone" in the downstream region of the orifice is mainly governed by the inlet fluid pressure. As per the definition of cavitation number, for the theoretical cavitation number = 1, the liquid velocity at the orifice plate (or

vena–contracta) is proportional to the inlet pressure. The overall pressure head loss in the downstream region and the intensity of turbulence generated in the flow also varies proportionately with inlet pressure. Stronger turbulence pressure fluctuations help in higher growth of the bubbles, which in turn undergo stronger collapse producing higher quantities of the radicals (Suslick et al., 1997; Moholkar and Pandit, 2001; Kumar et al., 2000).

Herewith, the results of studies on the degradation of SDZ at different inlet pressures using orifice plates with multiple holes are presented. The flow configuration of orifice plates, i.e. number of holes, the diameter of each hole and the total open area for flow, influences the cavitation intensity generated in the flow. We herewith compare the three orifice plates in term of maximum degradation of SDZ. Figs. 3.5 and 3.6 show that liquid flow through orifice plates with multiple holes of smaller diameter achieve higher rate of degradation, as compared to degradation for orifice plate with larger hole diameter. This result is consistent for both α-Fe_2O_3 and Fe_3O_4 nanoparticles as Fenton reagents. A probable reason underlying this result is that flow through multiple hole orifice plates produces significantly large number of cavitation bubbles which collapse with greater intensity.

Maximum SDZ degradation using α–Fe_2O_3 nanoparticles for both plate 1 (81.24±2.32%) and plate 2 (84.02±1.25%) was obtained for inlet pressure of 10 atm, whereas for plate 3, maximum degradation of 93.07±1.67% was seen for 8 atm inlet pressure (Table 3.5). For Fe_3O_4 nanoparticles (Table 3.6), the highest SDZ degradation was obtained at inlet pressure of 10 atm for all plates, viz. plate 1 = 78.69±1.63%, plate 2 = 79.92±1.24%, and plate 3 = 90.66 ± 1.18%. The intensity of turbulence and the local energy dissipation rate increases with the inlet pressure. This is manifested in terms of rise in intensity of transient collapse of the cavitation bubbles leading to generation of

large number of free radicals. The reduction in degradation rate beyond 8 bar (43.70×10^{-3} min^{-1}) inlet pressure can be attributed to the condition of choked cavitation in case of plate 3 for α–Fe_2O_3. Beyond a particular optimum pressure, the generation of large number of cavitation bubbles results in the formation of bubble clouds, thereby decreasing the intensity of the transient cavitation collapse events and hence the extent of the degradation.

Table 3.5: Rate constants and % degradation at different operating pressures for α–Fe_2O_3

Inlet pressure (atm)	Plate 1 (d_h = 4 mm & N_h = 2)		Plate 2 (d_h = 3 mm & N_h = 3)		Plate 3 (d_h = 2 mm & N_h = 4)	
	η	$k \times 10^3$ (min^{-1})	η	$k \times 10^3$ (min^{-1})	η	$k \times 10^3$ (min^{-1})
4	44.80±2.10	15.50	56.83±0.89	19.70	64.76±2.80	24.60
6	57.78±1.26	22.10	69.77±1.24	27.40	79.48±2.23	34.90
8	73.69±1.89	28.40	78.13±2.12	36.50	93.07±1.67	43.70
10	81.24±2.32	41.50	84.02±1.25	42.90	92.11±1.41	40.60

Plate	Removal percentage (η)	Rate kinetics
1	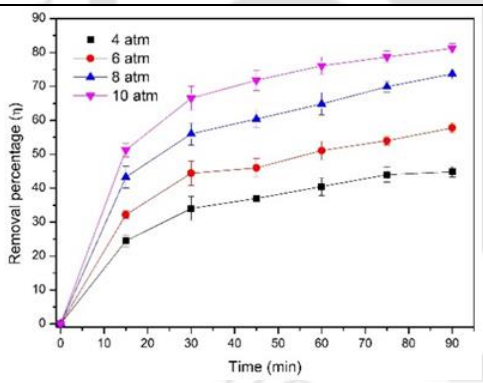	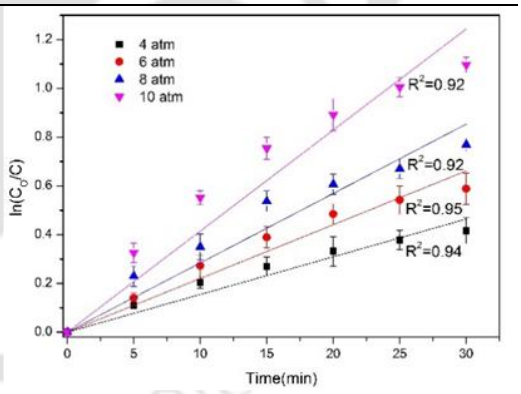
2	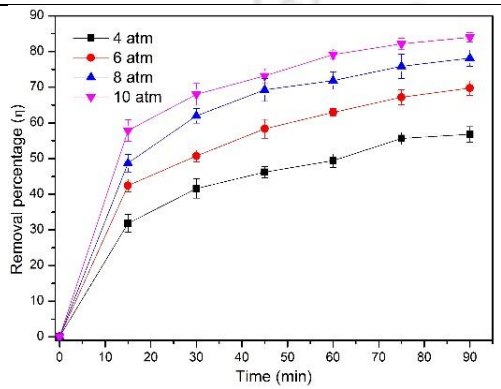	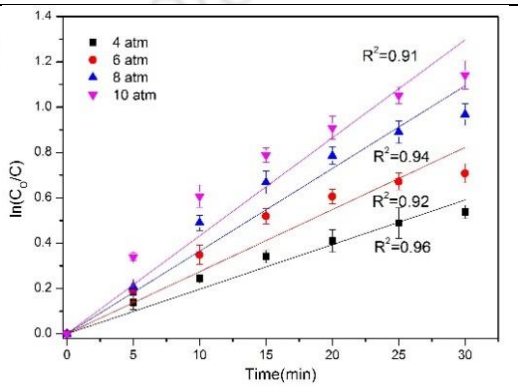

3

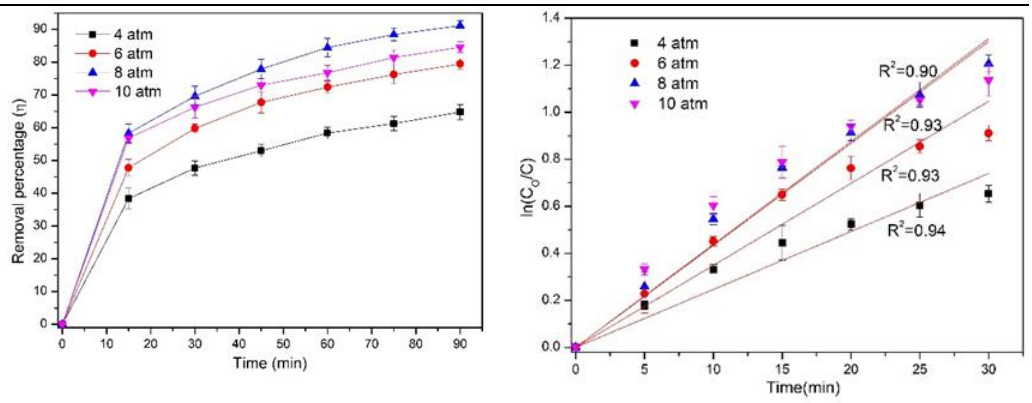

Figure 3.5: SDZ degradation profiles with α–Fe_2O_3 and their kinetic analysis: Effect of inlet pressure (Experimental conditions: Fenton reagent = Fe_2O_3 nanoparticles, Initial concentration = 20 ppm, pH = 4, α–Fe_2O_3 = 181.8 mg/L, $Na_2S_2O_8$ = 348.5 mg/L, H_2O_2 = 0.95 mL/L)

Table 3.6: Kinetic rate constants and % degradation at different operating pressures for Fe_3O_4

Inlet Pressure	Plate 1 (d_h = 4 mm & N_h =2)		Plate 2 (d_h = 3 mm & N_h = 3)		Plate 3 (d_h = 2 mm & N_h = 4)	
	η	$k \times 10^3$ (min^{-1})	η	$k \times 10^3$ (min^{-1})	η	$k \times 10^3$ (min^{-1})
4	37.39±1.80	9.27	51.84±1.41	15.70	61.36±1.87	19.90
6	50.51±2.89	13.62	65.18±2.05	22.80	74.71±1.54	27.40
8	66.05±2.21	22.13	73.79±1.18	29.00	89.07±2.14	39.30
10	78.69±1.63	32.81	79.92±1.24	33.10	90.66±1.18	42.70

Plate	Removal perseantage (η)	Rate kinetics
1	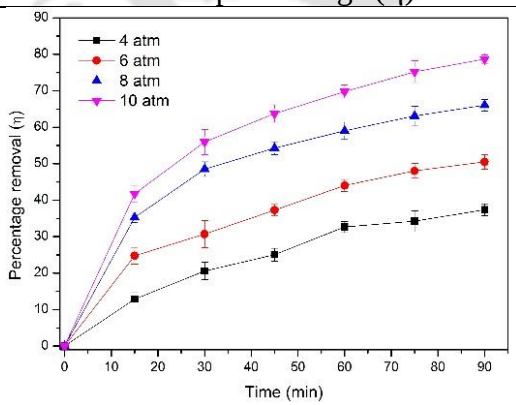	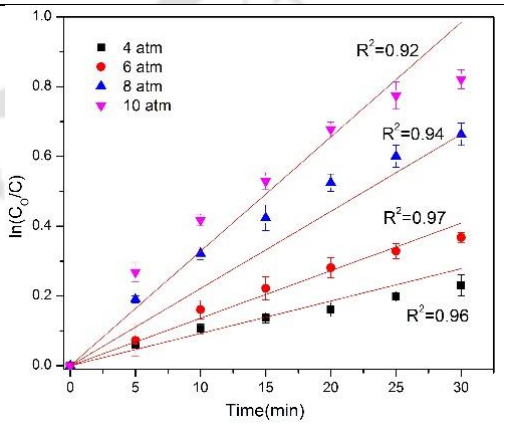

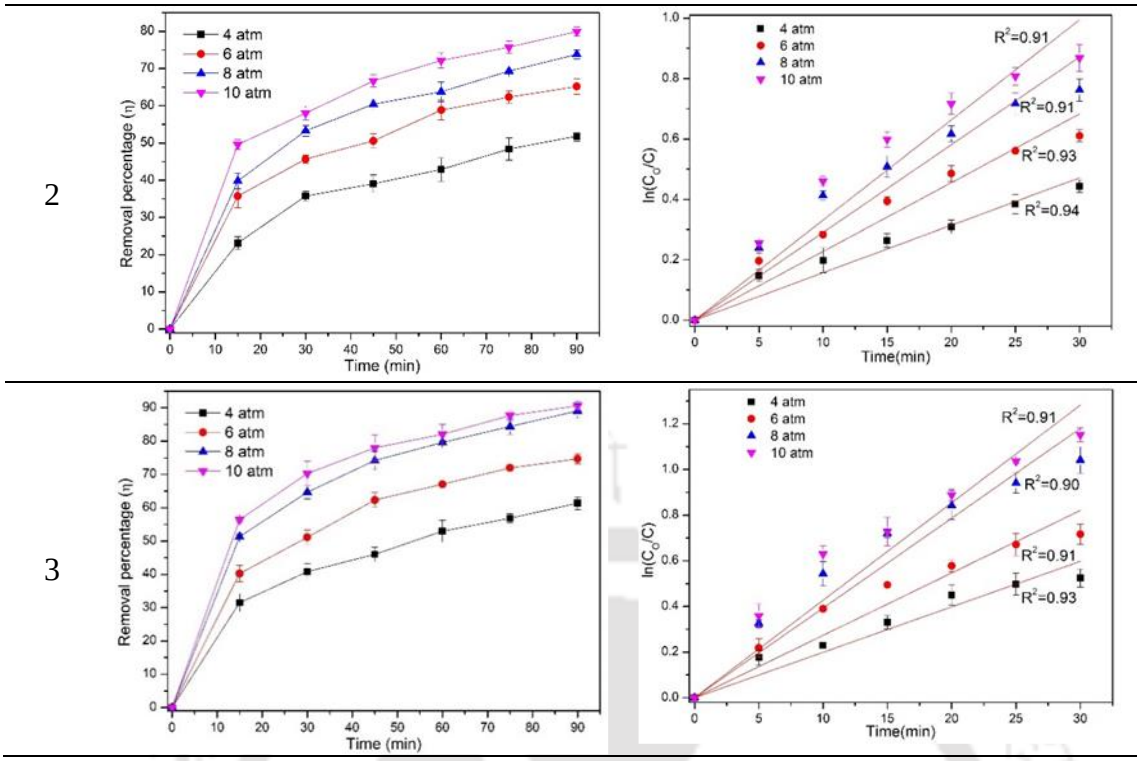

Figure 3.6: SDZ degradation profiles with Fe_3O_4 and their kinetic analysis: Effect of inlet pressure. Experimental conditions: Initial concentration = 20 ppm, pH = 4, Fe_3O_4 = 203 mg/L, $Na_2S_2O_8$ = 343.5 mg/L, H_2O_2= 0.91 mL/L

3.4.4 Determination and validation of kinetic modelling for all three plates

Fig. 3.7(A) depicts the plot of $\ln(C_0/C)_{SDZ}$ vs. $\ln(C_0/C)_{BA}$ for determination of kinetic constant of SDZ degradation by •OH and $SO_4^{\bullet-}$ radicals. The slopes of the plots (which are the ratio of kinetic constants k_{SDZ}/k_{BA}) are 0.88 and 1.49, for •OH and $SO_4^{\bullet-}$ radicals mediated degradation, respectively. Using these values of slopes and values of k_{BA} = 5.9 × 10^9 M^{-1} s^{-1} for •OH radicals (Buxton et al., 1988) and k_{BA} = 1.2 × 10^9 M^{-1} s^{-1} for $SO_4^{\bullet-}$ radicals (Neta et al., 1988), the values of k_{SDZ} are determined as: k_{SDZ} = 5.2 × 10^9 $M^{-1}s^{-1}$ for •OH radicals and k_{SDZ} = 1.8 × 10^9 M^{-1} s^{-1} for $SO_4^{\bullet-}$ radicals. These kinetic constants indicate that contribution of •OH radicals towards SDZ degradation is higher than $SO_4^{\bullet-}$ radicals. Similarly, rate constant was calculated for all three orifice plates from Figs.

3.8(A) and 3.9(A) for plate 2 and 3, respectively. Rate kinetic values were used in kinetic modelling concurrently to analyse the degradation profile.

Fig. 3.7(B) compares the simulated degradation profiles of SDZ for different initial ratios of $[Fe^{2+}]/[H_2O_2]$ against the experimental profile of degradation at optimum set of parameters (listed in figure caption). It could be seen that the best match between experimental and simulated profiles (R^2 = 0.96) is obtained for initial $[Fe^{2+}]/[H_2O_2]$ ratio of 4. This result is essentially an indication of high Fe^{2+} concentration prevalent in the reaction medium throughout 90 min treatment. This is attributed to high rate of leaching at the surface of α–Fe_2O_3 nanoparticles. The enhanced leaching is a possible consequence of high intensity turbulence and shear generated in cavitating flow that augments the solid–liquid mass transfer at surface of α–Fe_2O_3 nanoparticles. Similarly, initial $[Fe^{2+}]/[H_2O_2]$ ratio of 4, 4.5 and 5 was found the best fit with SDZ degradation profiles for plate 1, 2 and 3, respectively as shown in Table 3.7.

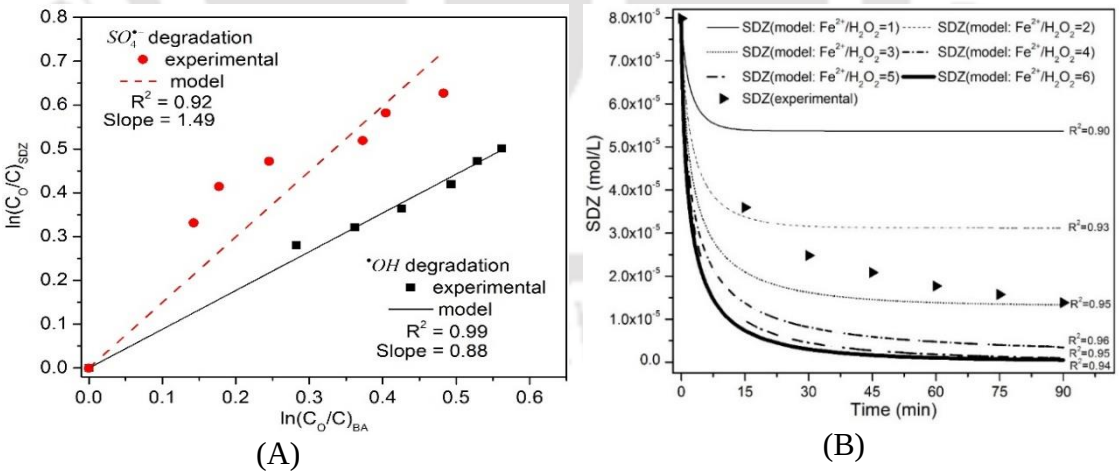

(A) (B)

Figure 3.7: Determination of kinetic constants of SDZ degradation by •OH and $SO_4^{\bullet-}$ radicals and experimental and simulated profile for plate 1 (d_h = 4 mm & N_h = 2)

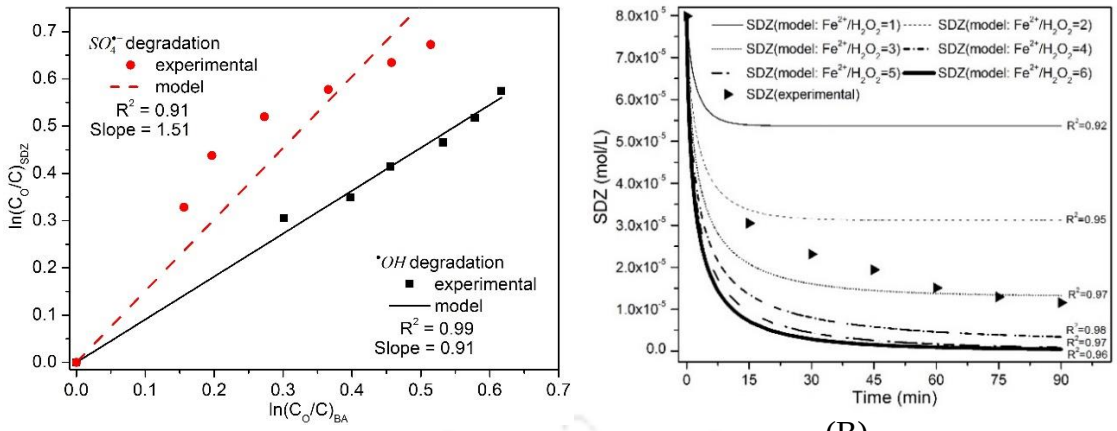

(A) (B)

Figure 3.8: Determination of kinetic constants of SDZ degradation by •OH and $SO_4^{\bullet-}$ radicals and experimental and simulated profile for plate 2 (d_h = 3 mm & N_h = 3)

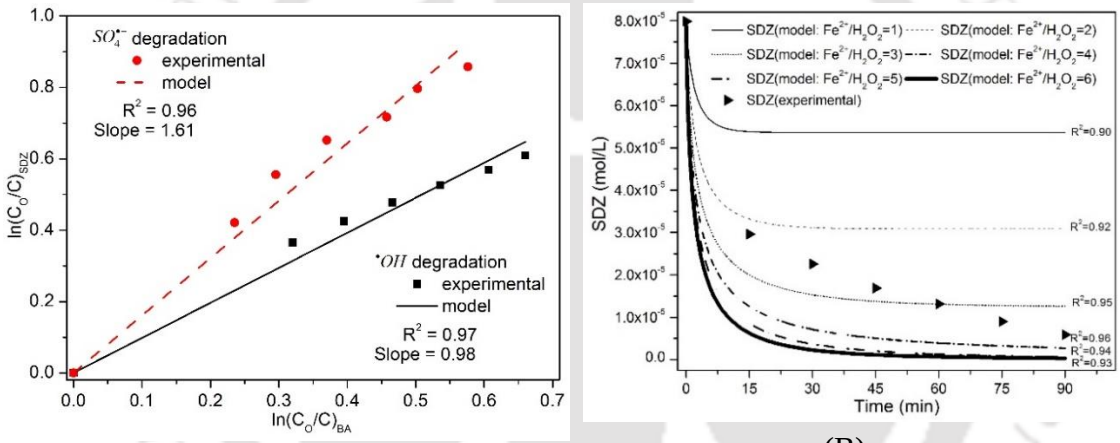

(A) (B)

Figure 3.9: Determination of kinetic constants of SDZ degradation by •OH and $SO_4^{\bullet-}$ radicals and experimental and simulated profiles for plate 3 (d_h = 2 mm & N_h = 4)

Table 3.7: Comparison of model with experimental results for α–Fe_2O_3

	Plate–1	**Plate–2**	**Plate–3**
$k_{15,}$ (•OH) ($M^{-1}\cdot s^{-1}$)	5.2×10^9	5.4×10^9	5.8×10^9
k_{16}, ($SO_4^{\bullet-}$) ($M^{-1}\cdot s^{-1}$)	1.8×10^9	1.81×10^9	1.9×10^9
η_{exp}	81.24 ± 2.32	84.02±1.25	92.11±1.41
η_{model}	95.70	97.1	99.2
Fe^{2+}/H_2O_2	4 (R^2 = 0.96)	4.5 (R^2 = 0.97)	5 (R^2 = 0.96)

3.4.5 Concentration of Fe^{2+}, Fe^{3+} and total iron of α–Fe_2O_3 nanoparticles

As aforementioned in the previous section, the leached concentration of Fe^{2+} was the determining factor for the heterogeneous Fenton like system. The concentration of Fe^{2+}, Fe^{3+} and total iron were determined for HC assisted α–Fe_2O_3/persulfate system using Phenanthroline method. Fig. 3.10 shows the concentration profile of iron oxides. The leached Fe^{2+} concentration increased at initial phase of reaction (solution colour changed from colourless to yellow–green and brown) upto 30 min reaction, and then get saturated. The plausible explanation is that the cavitation enhanced faster rate of leaching (corrosion for the surface of α–Fe_2O_3 nanoparticles) of Fe^{3+} and Fe^{2+} at the beginning and further leached iron oxides lead to generate various iron oxides or precipitates. The generated iron oxide or precipitates form α–Fe_2O_3 surface inhibited iron ions generation. Enhanced leaching of Fe^{2+} ions also lead to higher rate of SDZ degradation at the beginning of reaction (> 60% SDZ degradation in 30 min of treatment) as shown in Fig. 3.5, where reaction system more likely as a homogeneous system. Obtained SDZ degradation also corroborate that higher leaching of Fe^{2+} simultaneously accelerated the degradation.

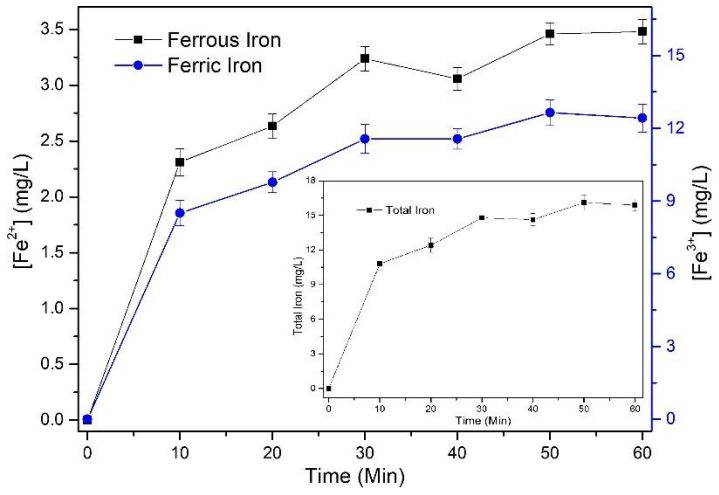

Figure 3.10: Concentration of Fe^{2+} and Fe^{3+} ions and inserted figure showed total concentration of iron leached from the surface of α–Fe_2O_3 nanoparticles, (Experimental condition: inlet pressure = 10 atm, $[SDZ]_0$ = 20 ppm, pH = 4, $Na_2S_2O_8$ = 348.5 mg/L, α-Fe_2O_3 loading = 181.8 mg/L, H_2O_2 = 0.95 mL/L

3.4.6 Analysis of degradation pathway of SDZ

Density functional theory (DFT) calculations: DFT calculations were performed to predict the vulnerable sites of SDZ molecules for reactions with either $^{\bullet}OH$ or $SO_4^{\bullet-}$ radicals and the probable intermediates resulting from the reactions. The optimized structure of model pollutant as SDZ molecule is shown in Fig. 3.12. The charge distribution and bond length on various atoms of SDZ molecule are given in Table 3.8 and 3.9, respectively. The bonds connecting atoms with negative charges on them are possible sites for reaction. However, another parameter that also influences the vulnerability of the site is the bond length. As per molecular simulations, the lengths of different bonds of negatively charged atoms are: S(16)–N(26) = 1.716 Å, C(2)–S(16) = 1.777 Å, C(5)–N(11) = 1.383 Å, C(20)–N(24) = 1.333 Å, C(18)–N(25) = 1.331 Å, N(11)–H(13) = 1.008 Å. The larger the bond length, more vulnerable it is for the reaction with radicals. According to the charge distribution of optimized structure of SDZ molecules, the atoms 14(O), 15(O), 24(N), 25(N), 26(N) and 11(N) had relatively larger negative charge. However, the N(11)–H(13) bond is relatively less susceptible due to very short bond length. Correspondingly, 3 sites, viz. α, β and γ (as shown in Fig. 3.11) could be potential cleavage sites of SDZ molecules with the generation of different intermediates.

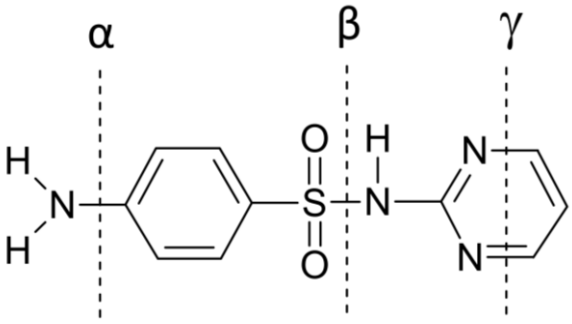

Figure 3.11: Degradation sites SDZ molecule during oxidation

Table 3.8: Charge of atoms in the optimized structure of SDZ molecule

Atom	Charges	Atom	Charges	Atom	Charges	Atom	Charges
1C	-0.566	8H	0.159	15O	-0.165	22H	0.141
2C	0.173	9H	0.113	16S	0.875	23H	0.134
3C	-0.115	10H	0.112	17C	-0.203	24N	-0.139
4C	-0.008	11N	-0.357	18C	0.027	25N	-0.112
5C	-0.232	12H	0.236	19C	-0.167	26N	-0.559
6C	-0.153	13H	0.236	20C	0.086	27H	0.350
7H	0.168	14O	-0.169	21H	0.136		

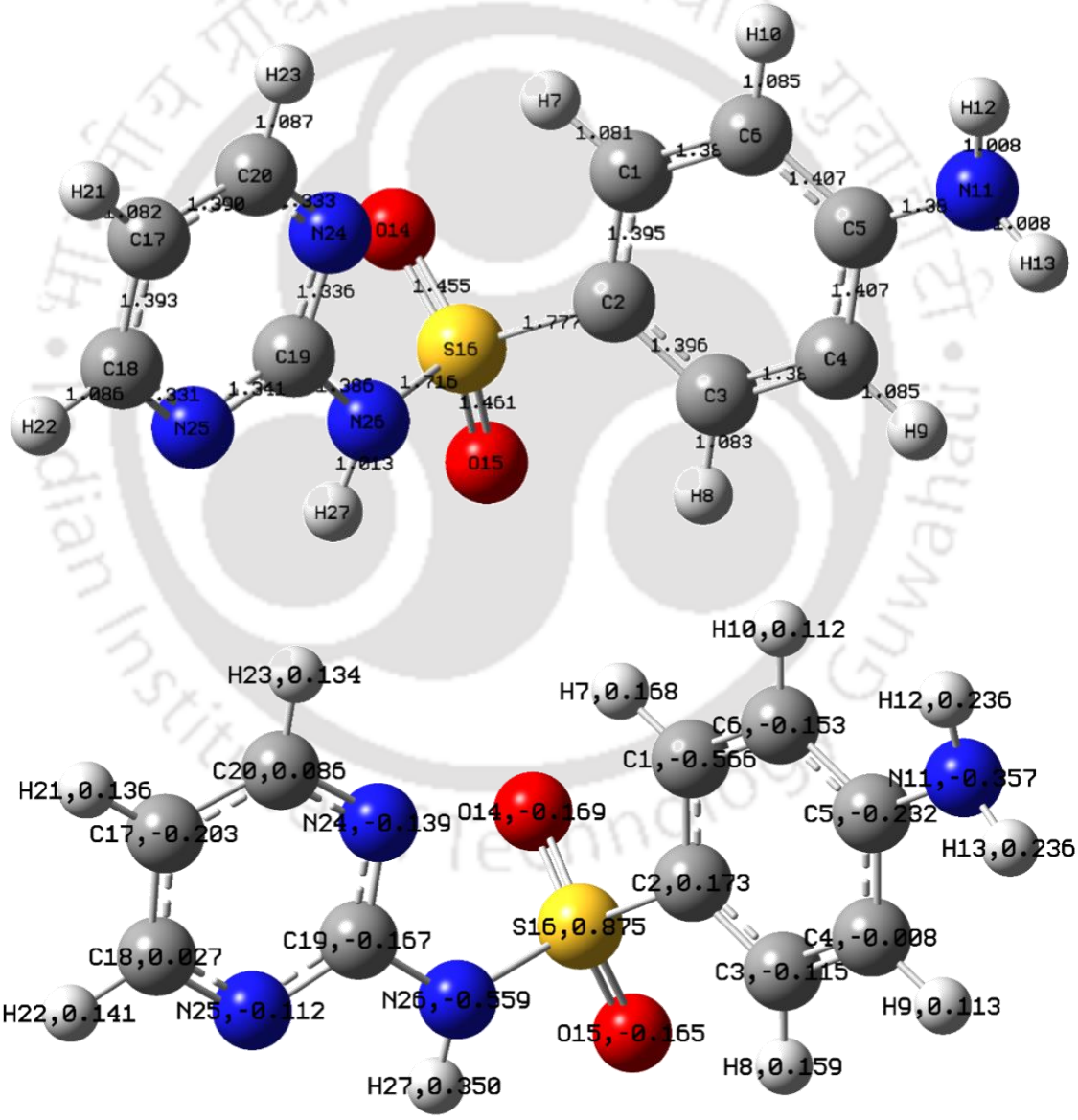

Figure 3.12: (A) Optimized structure with bond length (B) Mullikan atomic charge distribution of SDZ molecule

Table 3.9: Bond lengths (Å) between atoms in the optimized structure of SDZ molecule

Bond	Length	Bond	Length	Bond	Length
C1–C2	1.395	C6-H10	1.085	N25-C18	1.331
C2–C3	1.396	N11–H13	1.008	C18-H22	1.086
C3–C4	1.385	N11–H12	1.008	C18-C17	1.393
C4–C5	1.407	C2-S16	1.777	C17-H21	1.082
C5–C6	1.407	S16-O14	1.455	C17-C20	1.390
C6–C1	1.386	S16-O15	1.461	C20-H23	1.087
C1-H7	1.081	S16-N26	1.716	C20-N24	1.333
C3-H8	1.083	N26-H27	1.013	N24-C19	1.336
C4-H9	1.085	N26-C19	1.386		
C5-N11	1.383	C19-N25	1.341		

Identification of Intermediates: Intermediates and products formed during degradation were identified using LC–MS/MS in full scan mode. A typical LC-MS/MS spectrum is shown in Fig. 3.13. The degradation intermediates of SDZ molecules were identified from comparison of this spectra vis–à–vis the spectra reported in published literature (Guo et al., 2012; Zou et al., 2014; Rong et al., 2014; Feng et al., 2016a; Feng et al., 2016b; Zhou et al., 2016; Yang et al., 2018; Zheng et al., 2020). As many as 8 intermediates of SDZ degradation were detected with this analysis. Identification of chemical moities corresponding to these fragmented m/z ratios can help determine chemical pathways of the oxidative degradation of SDZ originating from α, β, γ sites, as shown in Fig. 3.11.

The first degradation pathway involves the direct cleavage of C–N bond (α site) via $SO_4^{\bullet-}$ attack to get intermediate of m/z = 233. Further S–N bond cleavage was seen to result in two intermediates, viz. benzene sulphonic acid (m/z = 158) and 2–aminopyrimidine (m/z = 96). Both of these intermediates undergo further oxidation induced by $^{\bullet}OH$ radicals to intermediates of 4–aminophenol (m/z = 109) and phenol (m/z = 95), followed by ring opening into small molecular weight products like CO_2, H_2O,

H_2SO_4, HCOOH etc. Second path of SDZ oxidation starts at the α–amine group through $SO_4^{\bullet-}$ attack to produce intermediate of m/z = 267. Attack of radicals on the γ–position results in intermediate of m/z = 219 and further reactions will result in ring opening (Guo et al., 2012, Zou et al., 2014, Zhou et al., 2016).

Another degradation path is SO_2 extrusion (*β* site) leading to formation of 4–[2–imino–pyrimidine–1(2H)–yl] aniline (m/z = 187). C–N bond cleavage occurs through direct attack of $SO_4^{\bullet-}$ to degrade SDZ into aniline and 2–aminopyrimidine (m/z = 96). Second degradation pathway is attack of $^{\bullet}$OH radical to oxidize SDZ molecule into 4–hydroxyl–sulfadiazine (m/z = 267) after the protonation of SDZ in accordance of formula $C_{10}H_{10}N_4O_2S$ (M = 250.3). However, the structure of this compound still deserves further confirmation, although the hydroxylation of sulfanilamide has been widely reported (Wang et al. 2011, Feng et al. 2016b). Hydroxyl radicals act as electrophiles and react preferably with nucleophiles groups/compounds possessing high negative charge. $^{\bullet}$OH radical will attack directly on the S-N bond to produce 4–hydroxyl–sulfadiazine or 5–hydroxyl–sulfadiazine. These compounds corresponded to the intermediates with m/z 267. Further breakage of S-N bond (*β* sites) will form 2–aminopyrimidine (m/z = 96) and 4-Aminophenol (m/z = 109), which is followed by ring opening and dissociation into small molecular weight species. Scheme-1 summarizes the degradation pathways of SDZ deduced with concurrent analysis of LC-MS/MS results and DFT simulations.

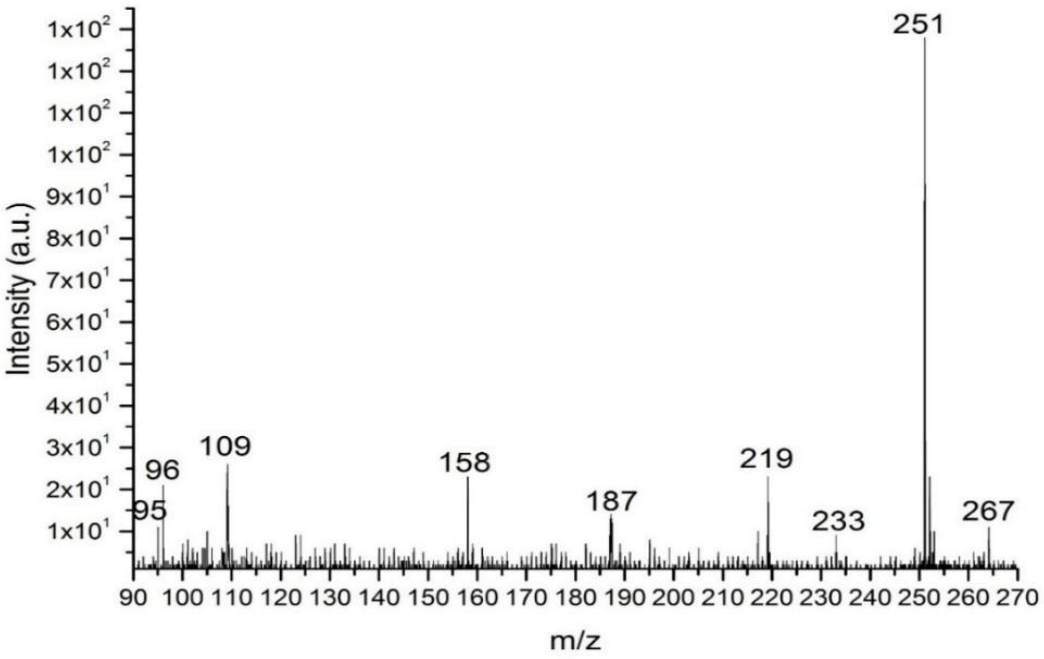

Figure 3.13: LC–MS/MS spectra of SDZ degradation

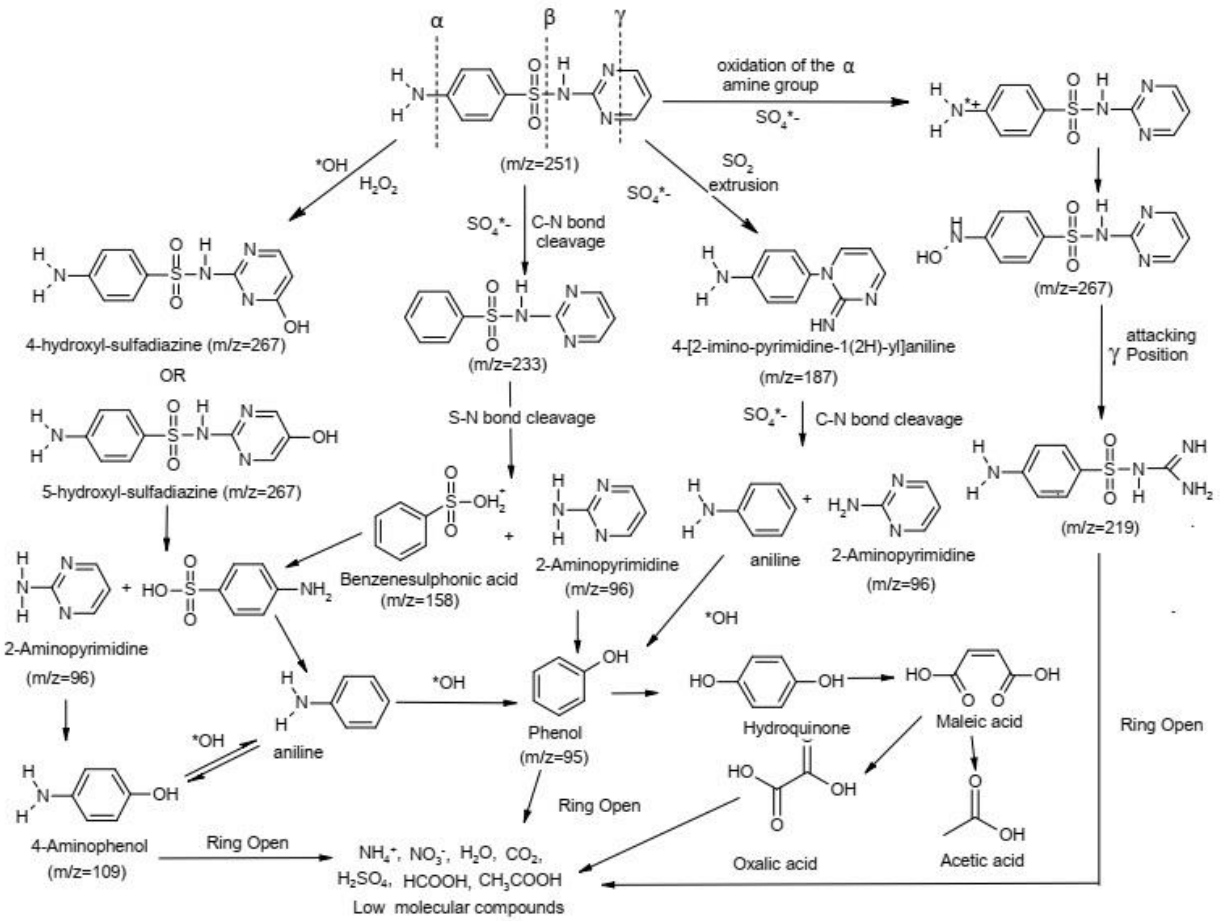

Scheme 1: The proposed degradation pathway of SDZ

3.5 CONCLUSIONS

This chapter has presented the optimization studies for hybrid HC+Fenton/persulfate system for degradation of SDZ. In hydrodynamic cavitation, the flow geometry essentially influences the total pressure head loss and turbulent pressure fluctuation frequency, which in turn determines the cavitational yield. It has been observed that for the plates having the same flow area, it is advisable to use a plate with a smaller hole size (and thus greater number of holes) in order to achieve a larger area of the shear layer. The smaller size of orifice plate hole results in higher pressure head loss and higher turbulent pressure fluctuation frequency leading to a more efficient collapse. Results of this study also gives an insight into the inter-relation or inter-dependence among various design and operational parameters of hydrodynamic cavitation reactor. Thus, in the optimization of hydrodynamic cavitation reactor with multiple hole orifice plates, all parameters should be considered simultaneously. Moreover, this study has also revealed synergistic interactions among different AOPs in the hybrid system of HC+Fenton/persulfate. Enhanced leaching of Fe^{2+} ions from surface of solid Fenton catalysts due to intense turbulence and shear generated in cavitating flow results in faster degradation of SDZ. The kinetic constants of SDZ degradation by $^{\bullet}OH$ and $SO_4^{\bullet-}$ radicals indicated faster degradation due to $^{\bullet}OH$. In summary, the results of this study provide mechanistic guidelines for optimization of hydrodynamic cavitation reactors from viewpoint of design parameters and process (or operational) conditions.

REFERENCES

Aschmann, S.M., Arey, J., Atkinson, R., Kinetics and products of the reaction of •OH radicals with 3–methoxy–3–methyl–1–butanol. *Environ. Sci. Technol.* 45 (2011) 6896–6901.

Bashir, T.A., Soni, A.G., Mahulkar, A.V., Pandit, A.B., The CFD driven optimisation of a modified venturi for cavitational activity. *Can. J. Chem. Eng.* 89(6) (2011) 1366–1375.

Buxton, G.V., Greenstock, C.L., Helman, W.P., Ross, A.B., Critical review of rate constants for reactions of hydrated electrons, hydrogen atoms and hydroxyl radicals (•OH/•O^- in aqueous solution). *J. Phys. Chem. Ref. Data* 17 (1988) 513–886.

Feng, Y., Wu, D., Deng, Y., Zhang, T., Shih, K., Sulfate radical-mediated degradation of sulfadiazine by $CuFeO_2$ rhombohedral crystal-catalyzed peroxymonosulfate: synergistic effects and mechanisms. *Environ. Sci. Technol.* 50(6) (2016a) 3119-3127.

Feng, Y., Wu, D., Liao, C., Deng, Y., Zhang, T., Shih, K., Red mud powders as low-cost and efficient catalysts for persulfate activation: pathways and reusability of mineralizing sulfadiazine. *Sep. Purif. Technol.* 167 (2016b) 136-145.

Guo, Z., Zhou, F., Zhao, Y., Zhang, C., Liu, F., Bao, C., Lin, M., Gamma irradiation-induced sulfadiazine degradation and its removal mechanisms. *Chem. Eng. J.* 191 (2012) 256-262.

Krishnan, J.S., Dwivedi, P., Moholkar, V.S., Numerical investigation into the chemistry induced by hydrodynamic cavitation. *Ind. Eng. Chem. Res.* 45(4) (2006) 1493–1504.

Kuldeep, Saharan, V.K., Computational study of different venturi and orifice type hydrodynamic cavitating devices. *J. Hydrodyn. Ser. B 28*(2) (2016) 293–305.

Kumar, P.S., Kumar, M.S., Pandit, A.B., Experimental quantification of chemical effects of hydrodynamic cavitation. *Chem. Eng. Sci.* 55(9) (2000) 1633–1639.

Moholkar, V.S., Pandit, A.B., Bubble behavior in hydrodynamic cavitation: effect of turbulence. *AIChE Journal* 43(6) (1997) 1641–1648.

Moholkar, V.S., Pandit, A.B., Modeling of hydrodynamic cavitation reactors: a unified approach. *Chem. Eng. Sci.* 56 (21–22) (2001) 6295–6302.

Neta, P., Huie, R.E., Ross, A.B., Rate constants for reactions of inorganic radicals in aqueous solution. *J. Phys. Chem. Ref. Data* 17 (1988) 1027–1284.

Rajoriya, S., Bargole, S., Saharan, V.K., Degradation of reactive blue 13 using hydrodynamic cavitation: Effect of geometrical parameters and different oxidizing additives. *Ultrason. Sonochem.* 37 (2017) 192-202.

Rong, S.P., Sun, Y.B., Zhao, Z.H., Degradation of sulfadiazine antibiotics by water falling film dielectric barrier discharge. *Chin. Chem. Lett.* 25(1) 2014 187-192.

Sivakumar, M., Pandit, A.B., Wastewater treatment: a novel energy efficient hydrodynamic cavitational technique. *Ultrason. Sonochem.* 9 (3) (2002) 123–131.

Suslick, K.S., Mdleleni, M.M., Ries, J.T., Chemistry induced by hydrodynamic cavitation. *J. Am. Chem. Soc.* 119(39) (1997) 9303–9304.

Vichare, N.P., Gogate, P.R., Pandit, A.B., Optimization of hydrodynamic cavitation using a model reaction. *Chem. Eng. & Tech.: Ind. Chem. Plant Equip. Process Eng. Biotechnol.* 23(8) (2000) 683–690.

Yang, X.L., Zhang, S., Li H., Zhang, L.M., Song, H.L., Wang, Y.W., Effects of voltage on sulfadiazine degradation and the response of sul genes and microbial communities in biofilm-electrode reactors. *Ecotoxicol. Environ. Saf.* 151 (2018) 272-278.

Zheng, J., Wang, S., Zhou, A., Zhao, B., Dong, J., Zhao, X., Li, P., Yue, X., Efficient elimination of sulfadiazine in an anaerobic denitrifying circumstance: Biodegradation characteristics, biotoxicity removal and microbial community analysis. *Chemosphere* 252 (2020) 126472.

Zhou, T., Zou, X., Mao, J., Wu, X., Decomposition of sulfadiazine in a sonochemical Fe^0-catalyzed persulfate system: parameters optimizing and interferences of wastewater matrix. *Appl. Catal. B Env.* 185 (2016) 31-41.

Zou, X., Zhou, T., Mao, J., Wu, X., Synergistic degradation of antibiotic sulfadiazine in a heterogeneous ultrasound-enhanced Fe^0/persulfate Fenton-like system. *Chem. Eng. J.* 257 (2014) 36-44.

CHAPTER 4

Sulfadiazine Degradation by Ultrasound-Assisted Fenton-Persulfate System

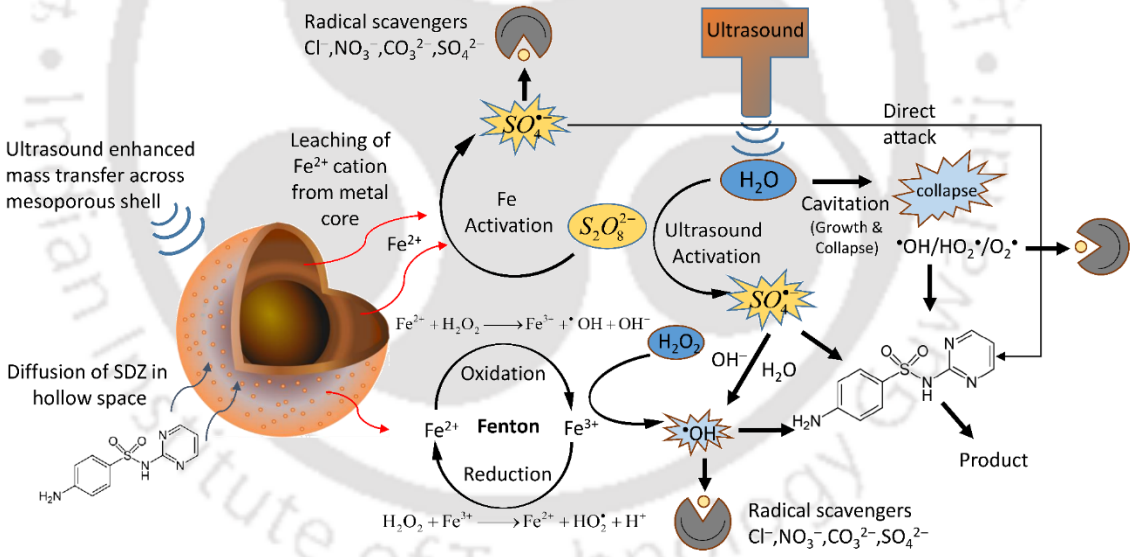

CHAPTER 4

SULFADIAZINE DEGRADATION BY ULTRASOUND-ASSISTED FENTON-PERSULFATE SYSTEM

4.1 INTRODUCTION

Wastewater discharges from pharmaceutical industries and animal husbandries contain antibiotics which have the potential of polluting both aqueous and terrestrial ecosystems. One of the ubiquitous antibiotic pollutants that appear in wastewater discharges from animal husbandries is sulfadiazine (SDZ). Traces of SDZ are often detected in soil and water bodies, which demonstrate its stable nature in the environment. Being biorecalcitrant, SDZ needs to be degraded with advanced oxidation processes (AOPs).

A popular AOP for oxidative degradation of biorecalcitrant pollutants is the Fenton process. This process produces $^{\bullet}OH$ radicals with the highest oxidation potential of 2.8 eV, which induces effective oxidative degradation of pollutants. More recently, hybrid AOPs that combine Fenton and persulfate systems have been applied. Persulfate radicals (oxidation potential 2.6 eV) are produced through activation of persulfate anion ($S_2O_8^{2-}$) by Fe^{2+} ions (Feng et al., 2016) or $^{\bullet}OH$ radicals produced by cavitation bubbles (Balaji et al., 2011; Grčić et al., 2012). This hybrid system has proven to be more effective than the sole Fenton process due to high solubility and stability of persulfate anions ($S_2O_8^{2-}$), in addition to non-selective reactivity of sulfate radical ($SO_4^{\bullet-}$) over a wide range of pH (Zou et al., 2014; Zhou et al., 2016). This system, however, has issues of the

generation of iron hydroxide precipitates, and thus, heterogeneous Fenton systems involving solid particles of zero-valent iron (Fe^0) or iron oxides have been used as an alternative.

Sonication (or ultrasound irradiation) is a relatively new AOP. Sonication of aqueous medium produces $^{\bullet}OH$ and other oxidizing radicals (such as $HO_2^{\bullet}$, $H^{\bullet}$, $O^{\bullet}$ or $O_2^{\bullet-}$) through thermal dissociation of water vapour inside cavitation bubble during transient collapse (Sivasankar et al., 2007; Balaji et al., 2011; Shah et al., 2012; Chakma and Moholkar, 2013). Sonication also produces intense micromixing and microturbulence in the medium, which helps in the enhancement of mass transfer. Coupling of hybrid AOP of Fenton + persulfate to sonication further enhances the efficiency of SDZ degradation (Moholkar et al., 2000; Kusic et al., 2011; Chakma et al., 2017; Bokare and Choi, 2014). In the present study, we have addressed the matter of oxidative degradation of SDZ using hybrid heterogeneous Fenton + persulfate + sonication system from a mechanistic perspective. A notable and novel feature of this study is the addition of Fenton reagent (Fe^{2+}) in heterogeneous phase in the form of yolk-shell structured nanoparticles with the typical structure of core (Fe_3O_4@hollow@shell). The yolk-shell structured particles have improved properties than bare Fe_3O_4 particles such as high stability, low agglomeration, easy separation, and recyclability (Purbia and Paria, 2015). The shell surrounding the core particle can also enhance adsorption of pollutant and accessibility to catalyst core. The hollow space (or void) between core and shell essentially functions as "nanoreactor," which brings about intimate contact of pollutant molecules and radicals produced at the surface of catalyst core (Qiu et al., 2015).

Finally, this study has also analyzed the influence of other inorganic anions present ubiquitously in wastewater streams on the degradation of SDZ by Fenton + persulfate system coupled with sonication. As reported in previous literature, inorganic

anions retard SDZ degradation through scavenging of radicals and other chemical species involved in the chemistry of degradation. We have analyzed the influence of four common anions on degradation profiles of SDZ (viz. Cl^-, NO_3^-, CO_3^{2-}, SO_4^{2-}) on the basis of a rigorous chemical kinetics model. The approach in the present study is 2-fold, viz. simulations of SDZ degradation (using differential mass balance based on set of reactions for a particular reaction system) and experiments of SDZ degradation by Fenton + persulfate + sonication system, in the presence of different concentrations of inorganic anions. Concurrent analysis of the simulations and experiments has been done to get mechanistic insights of SDZ degradation and relative influences of competing for physical phenomena occurring in the system.

Grčić et al. (2012) have reported the degradation of two reactive dyes, viz. C.I. Reactive Violet 2 (azo dye) and C.I. Reactive Blue 7 (phthalocyanine dye) with AOPs of peroxymonosulfate, persulfate, and a combination of both. Inorganic ions species present in wastewater such as Cl^-, CO_3^{2-} and HCO_3^- act as a scavenger of $^{\bullet}OH$ and $SO_4^{\bullet-}$ radicals and retard kinetics of degradation. A similar effect has also been reported by Luo et al. (2015) in the degradation of atrazine by hybrid AOPs of UV/H_2O_2, UV/HSO_5^- and $UV/S_2O_8^{2-}$. Luo et al. (2015) found that HCO_3^-/CO_3^{2-} had a prominent scavenging effect on $^{\bullet}OH$ than $SO_4^{\bullet-}$; while Cl^- selectively scavenged the $SO_4^{\bullet-}$ radicals. Zhou et al. (2016) have demonstrated the inhibition effect of numerous anions, viz. SO_4^{2-}, NO_3^-, HCO_3^-/CO_3^{2-} and $H_2PO_4^-$ on the decomposition of antibiotic sulfadiazine in Fe^0 catalyzed persulfate (or Fenton like) system. Inhibition effect of bicarbonate ions on both $^{\bullet}OH$ and $SO_4^{\bullet-}$ radicals has been reported by Xie et al. (2015) for degradation of 2-MIB and geosmin using UV/persulfate system. Wang et al. (2018) have reported scavenging of

both $^{\bullet}OH$ and $SO_4^{\bullet-}$ radicals by HPO_4^{2-} and OH^- ions during degradation of dibutyl phthalate in UV/persulfate system. Scavenging of the radicals by the ions reduces their utility towards the degradation of pollutants and retards the kinetics of degradation.

4.2 MATERIALS AND METHODS

4.2.1 Materials

The following chemicals have been used in this study: ferric chloride hexahydrate ($FeCl_3 \cdot 6H_2O$), ethylene glycol (99%), sodium acetate anhydrous (NaAc), concn. ammonia solution (30%, NH_4OH), hydrogen peroxide (30% w/v), sodium persulfate ($Na_2S_2O_8$), sodium carbonate (Na_2CO_3), sodium chloride (NaCl), sodium nitrate ($NaNO_3$), sodium sulphate (Na_2SO_4) procured from Himedia (India) with AR/ACS grade. Moreover, ACS grade trisodium citrate dihydrate ($Na_3Cit \cdot 2H_2O$), tetraethyl orthosilicate (TEOS), cetyl trimethyl ammonium bromide (CTAB), sulfadiazine (SDZ), and acetonitrile (HPLC grade) were obtained from Sigma-Aldrich. Absolute ethanol (≥ 99%, AR Grade) was purchased from Changshu Yangyuan Chemicals, China. All chemicals were used as received without any pre-treatment.

4.2.2 Preparation of Yolk-Shell Nanoparticles of Fe_3O_4

As noted earlier, the Fenton reagent was added in heterogeneous phase in the form of yolk-shell nanoparticles. The core of these particles comprised of nanoparticles of iron oxide (Fe_3O_4). The material chosen for the shell of the particles was mesoporous silica due to its distinct merits such as inert and non-toxic nature, transparency towards the magnetic field, and steric repulsion to avoid agglomeration. Besides, the high porosity of the mesoporous silica shell facilitates easy accessibility of active metal core inside the

hollow shell to reactants. The protocol for the synthesis of Fe_3O_4@hollow@$mSiO_2$ particles is illustrated in scheme 1.

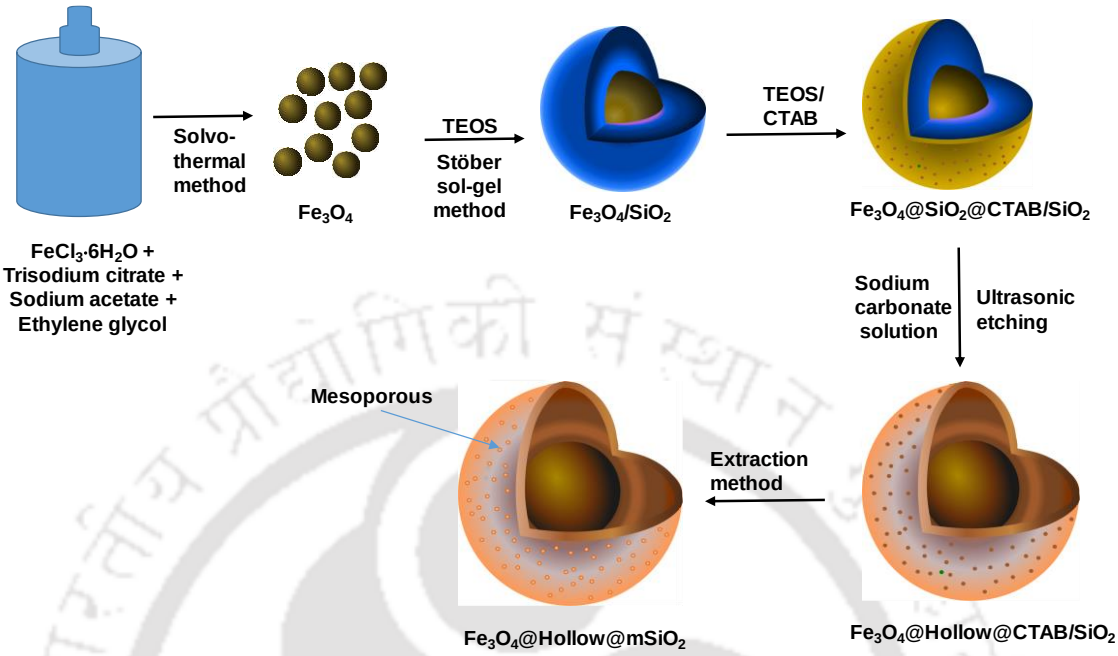

Scheme 1: Schematic of the synthesis protocol of Fe_3O_4@hollow@$mSiO_2$ (adopted from Qiu et al., 2015, Wang et al., 2015, Deng et al., 2008)

***Synthesis of Fe_3O_4 nanoparticles* (*Qiu et al., 2015*)**: Fe_3O_4 nanoparticles were synthesized using a solvothermal method (Qiu et al., 2015). Briefly, $FeCl_3 \cdot 6H_2O$ (2.6 g), $Na_3Cit \cdot 2H_2O$ (0.85 g) and NaAc (4.8 g) were dissolved in 80 mL of ethylene glycol with stirring @ 800 rpm for 1 h at room temperature to obtain a homogeneous brown solution. This solution was transferred to a Teflon-lined SS autoclave (100 mL) and heated at 200°C for 10 h, followed by cooling to room temperature. The resulting precipitate was washed with deionized water several times until a neutral pH of wash-water was attained. Further, the precipitate was also washed 3× with ethanol. Following washing with water and ethanol, the Fe_3O_4 particles were separated using a magnet. These particles were further dried overnight under vacuum at 60°C.

***Synthesis of Fe_3O_4@nanosphere silica ($nSiO_2$) nanoparticles* (*Wang et al., 2015*):** The core-shell Fe_3O_4@SiO_2 microspheres were synthesized using the Stöber method (Wang et al., 2015). 0.15 g of as-prepared Fe_3O_4 nanoparticles were dispersed using sonication (40 kHz, 200 W) in the mixture of anhydrous ethanol (270 mL), Millipore water (70 mL) and concn. ammonia solution (5 mL, 30% v/v). Next, 10 mL anhydrous ethanol containing 4.0 mL of TEOS was added dropwise into dark brown homogeneous solution, and the reaction was allowed to proceed for ten h at room temperature under continuous mechanical stirring (300 rpm). The resultant solid product (identified as Fe_3O_4@SiO_2) was separated with a magnet followed by washing with deionized water and ethanol.

***Synthesis of Fe_3O_4@$nSiO_2$@CTAB/*mesoporous silica (*$mSiO_2$*) *nanoparticles* (*Qiu et al., 2015*):** The mesoporous silica ($mSiO_2$) shell was coated uniformly on the surface of Fe_3O_4@$nSiO_2$ nanoparticles via the soft template method (Qiu et al., 2015). The core-shell Fe_3O_4@SiO_2 nanoparticles were added in 250 mL round bottom flask containing H_2O (25 mL), ethanol (10 mL), ammonia solution (0.30 mL) and CTAB (75 mg) as a surfactant. The mixture was sonicated in an ultrasound bath (40 kHz, 200 W) for 30 min. Subsequently, 5 mL anhydrous ethanol containing 0.15 mL of TEOS was added dropwise, and the reaction was carried out for six h at room temperature under continuous stirring at 300 rpm. The resultant solid particles were washed with deionized water and ethanol three times, and solid microspheres (designated as Fe_3O_4@$nSiO_2$@CTAB/ $mSiO_2$) were produced for further processing.

***Synthesis of yolk-shell Fe_3O_4@hollow@CTAB/$mSiO_2$ nanoparticles* (*Qiu et al., 2015*)**

The yolk-shell or nano-rattles structure of nanospheres was attained in sodium carbonate solution using an ultrasound-assisted cationic surfactant aided selective etching method. Typically, as-prepared Fe_3O_4@$nSiO_2$@CTAB/$mSiO_2$ nanoparticles were added into a mixture of 40 mL water and 212 mg sodium carbonate in a 250 mL round bottom flask

and placed in an ultrasound bath (37 kHz, 100 W) for six h. The temperature of the bath was maintained at 25 °C using water reflux. The resultant product was collected by a magnet and washed with Millipore water and ethanol several times to remove the template. The resultant solid particles were designated as: Fe_3O_4@hollow@CTAB/$mSiO_2$.

***Synthesis of yolk-shell Fe_3O_4@hollow@$mSiO_2$ nanoparticles* (*Deng et al., 2008*)**

CTAB from the solid product of the previous step (designated as Fe_3O_4@hollow@CTAB/$mSiO_2$) was removed by the soxhlet extraction process. The solvent for soxhlet extraction was acetone, which was refluxed at 60°C for 48 h. The extraction was repeated twice to achieve the maximum possible removal of surfactant CTAB. The resultant particles were thoroughly washed with Millipore water and ethanol and dried in an oven at 60°C for six h. Complete removal of CTAB from particles was ensured using FTIR (i.e., absence of a peak at 2348 and 2325 cm^{-1}). The resultant particles were designated as Fe_3O_4@hollow@$mSiO_2$.

The hollow portion between metal oxide core and structured mesoporous silica shell was achieved by limited etching off of the inner Fe_3O_4 core. For this purpose, the yolk-shell structured magnetic mesoporous silica particles from the previous step (designated as Fe_3O_4@hollow@$mSiO_2$) were dissolved in 10 mL HCl (0.1 mol L^{-1}) and subjected to sonication for two h. The solid particles were washed with H_2O and ethanol several times and dried in an oven at 60°C for six h. These particles were designated as rattle type magnetic nanoparticles with core/shell structures (designated as Fe_3O_4@hollow@$mSiO_2$) and were characterized with standard techniques as explained below.

4.2.3 Characterization of Fe_3O_4@hollow@$mSiO_2$ Nano-particles

XRD analysis of the nanoparticles was carried out at room temperature with X-Ray Diffractometer (Rigaku RINT 2500 TTRAX-III) equipped with Cu–Kα radiation (λ =

1.5406 Å) with nickel filter. Scans were recorded in the 2θ ranging from 10°–80° using a 0.03° step rate and a counting time of 5°/min at 50 kV/100 mA. Surface and structural morphology of the nanocomposites was assessed with the transmission electron microscope (TEM, Make: JEOL, Model: JEM 2100) and field emission scanning electron microscope (FE–SEM, Make: Zeiss, Model: Sigma). Brunauer-Emmett-Teller surface areas of the nanoparticle were obtained from nitrogen adsorption isotherms using a surface area and porosity analyzer (BET, Make: Quantachrome, Model: Autosorb-IQ MP). Vibrating sample magnetometer (VSM) (Make: Lakeshore, Model:7410 series) was used to study the hysteresis loops and the magnetic properties of the nanoparticles at 300 K under applied field ranging from –15 kOe to 15 kOe.

4.2.4 Experiments of SDZ Degradation

***Test experiments* (*with sonication*):** A microprocessor-controlled ultrasound probe (Sonics and Materials Inc., Model: VCX 500) with an operating frequency of 20 kHz and a maximum power of 500 W was used for sonication. Fig. 4.1 shows the schematic diagram of the experimental setup. The actual power dissipation was quantified separately by the calorimetric method using millipore water into the same reactor system where the experiments were conducted. Fig. 4.2 (A) shows the efficiency of actual power applied to system for the maximum percentage of SDZ degradation. Table 4.1 gives the calculated values of actual dissipated power into the reaction system with the corresponding efficiency at its applied intensity (20–40%). Fig. 4.2 (B) shows the time profile of SDZ degradation at various level of theoretical power viz. 100, 150, and 200 W. The ultrasound probe was operated at optimized power as 40% of maximum power (acoustic intensity = 74548 W/m^2, pressure amplitude = 470 kPa or 4.7 bar) for the rest experiments.

Experiments of sonocatalytic degradation of SDZ were carried out in glass beaker with a reaction volume of 100 mL. Total time of sonication of the reaction mixture was 1 h in all experiments. The temperature of the reaction mixture in the beaker was maintained at 25°C using a circulating water bath. The protocol for SDZ degradation was as follows: Based on our previous study (Roy and Moholkar, 2020), the initial concentration of SDZ in all experiments was fixed as 20 mg/L (or 20 ppm). The initial pH of the solution during degradation was optimized in preliminary experiments (in the pH range of 3 to 11), the results of which are shown in the Fig. 4.3. The solution with an initial pH of 5 resulted in maximum degradation of 10.25% in 60 min treatment. Based on this result, all experiments were carried out with an initial pH of 5. The other reaction parameters, viz. volume of H_2O_2, loading (or concentration) of Fe_3O_4@hollow@$mSiO_2$ particles and concentration of sodium persulfate ($Na_2S_2O_8$, a precursor for $SO_4^{\bullet-}$ radicals) were optimized using a statistical experimental design, i.e. central composite design (CCD). The levels of optimization parameters and the exact number of experiments in the CCD are given in Table 4.2, 4.3 and 4.4. The percentage of degradation of SDZ was used as the response variable. A quadratic expression was fitted to the experimental data obtained through central composite design and analyzed using response surface methodology.

$$\% \text{ Degradation} = 85.17 + 1.62\,X_1 + 10.28\,X_2 + 21.26\,X_3 - 14.15\,X_1 \cdot X_1 - 6.69\,X_2 \cdot X_2 - 15.30\,X_3 \cdot X_3 + 7.79\,X_1 \cdot X_2 - 11.01\,X_1 \cdot X_3 - 3.09\,X_2 \cdot X_3.$$

Predicted degradation = 95.10 %, Desirability = 0.99, R^2 = 0.9987; R^2 (predicted) = 0.9946; R^2 (adjusted) = 0.9975.

Optimum parameters: H_2O_2 (X_1) = 484.85 µl, Fe_3O_4@hollow@$mSiO_2$ (X_2) = 55.86 mg, Na_2SO_4 (X_3) = 57.28 mg results in 93.14 ± 1.05% (experimental) degradation of SDZ.

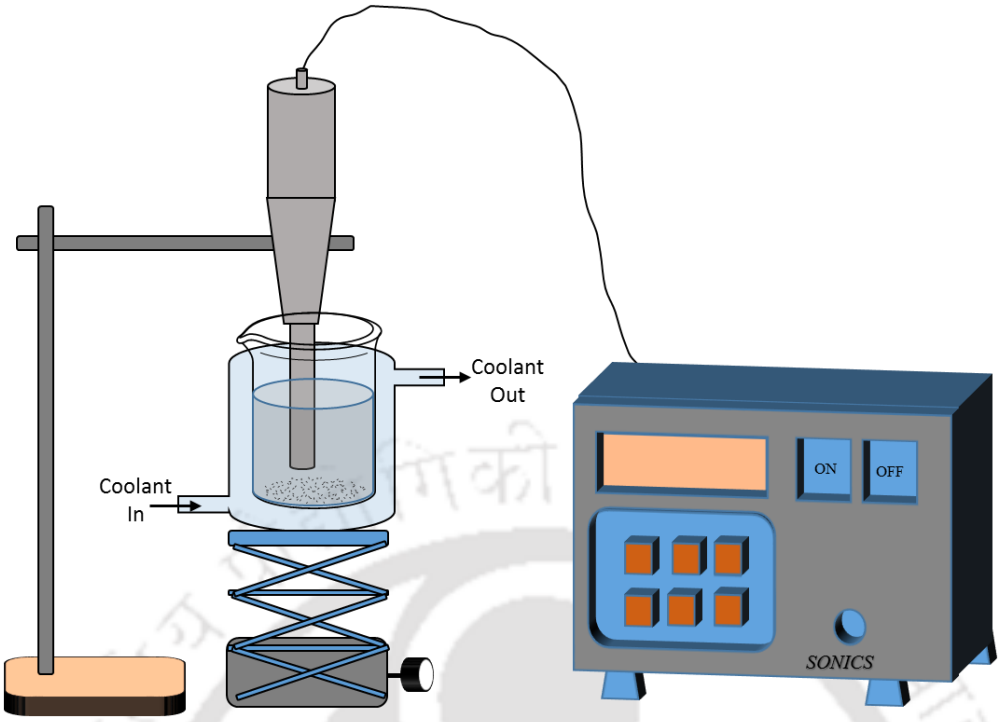

Figure 4.1: Schematic diagram of the experimental setup

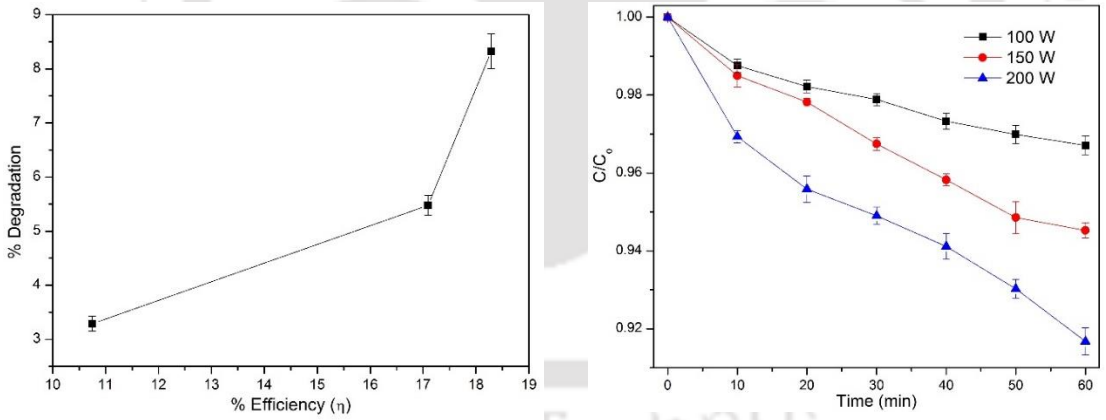

(A) (B)

Figure 4.2: (A) Total percentage SDZ degradation versus actual power input to the reaction system, (B) Degradation profiles of SDZ at various levels of theoretical power input ($[SDZ]_0$ = 20 mg L^{-1}, 25 °C)

Table 4.1: Actual power dissipation and corresponding efficiency at different intensities (Maximum power rating = 500 W)

Amplitude of horn	Theoretical Power (W)	Actual power dissipated in the given volume P (W)	Efficiency (η%)#
20%	100	10.75	10.74
30%	150	25.64	17.09
40%	200	36.58	18.29

η = (Actual power/Theoretical power) × 100

Control experiment (with mechanical agitation): The control experiment was performed with mechanical agitation of the reaction mixture at 500 rpm. All other experimental conditions, as well as procedure, was exactly the same as the test experiments.

Test experiments with inorganic anions: Test experiments were also conducted in the presence of inorganic anions to assess their scavenging effect on $^{\bullet}OH$ and $SO_4^{\bullet-}$ radicals. Four inorganic anions, commonly found in wastewater, were chosen for analysis, viz. Cl^-, NO_3^-, CO_3^{2-} and SO_4^{2-}. These ions were added in the form of their sodium salt, viz. NaCl, $NaNO_3$, Na_2CO_3 and Na_2SO_4. The exact quantities of the salts added to the reaction mixture are mentioned in Table 4.5. Other conditions and procedure of the experiments were the same as described previously.

Table 4.2: Ranges and level of catalyst's loading

Independent variable (amount of reactants per 100 mL of reaction volume)	Factors X_i	Low (-1)	Middle (0)	High (+1)
H_2O_2 (μL)	X_1	0	500	1000
Fe_3O_4@hollow@$mSiO_2$ (mg)	X_2	0	35	70
$Na_2S_2O_8$ (mg)	X_3	0	35	70

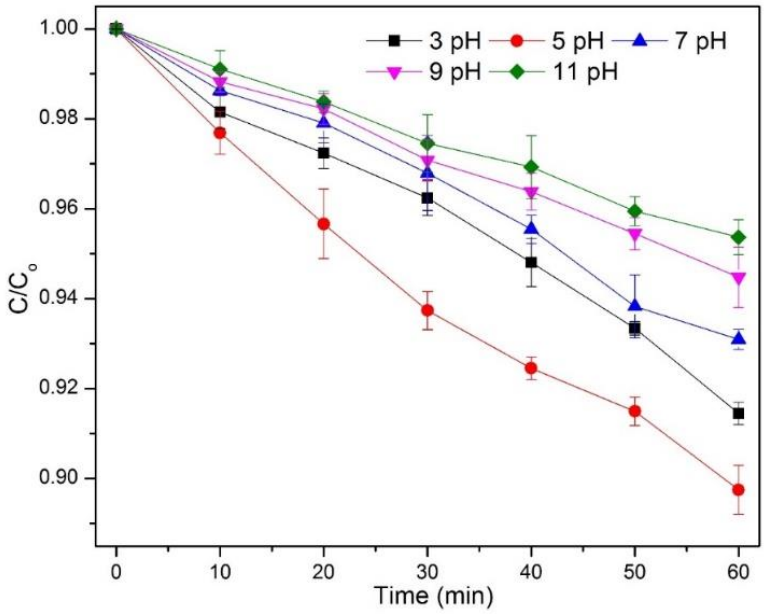

Figure 4.3: Effects of initial pH removal efficacy during US process in batch mode (Condition: $[SDZ]_o$ = 20 mg/L, US power = 200 W and 25 °C)

Table 4.3: The CCD design matrix and response of SD degradation

Run	H_2O_2 (μL)	Fe_3O_4@hollow@SiO_2 (mg)	$Na_2S_2O_8$ (mg)	% degradation (Exp)	% degradation (Predicted)
1	1000	35	35	71.71±0.91	72.64
2	500	35	0	47.29±0.84	48.61
3	0	70	70	79.28±1.57	79.08
4	1000	0	70	46.44±1.36	45.93
5	500	0	35	66.82±1.09	68.19
6	0	0	70	80.21±1.25	80.28
7	500	35	35	86.24±1.88	85.17
8	1000	70	70	75.58±1.25	75.88
9	1000	70	0	62.03±0.92	61.55
10	500	35	35	86.11±0.39	85.17
11	1000	0	0	19.42±1.17	19.22
12	500	35	35	86.11±0.77	85.17
13	0	35	35	68.64±1.25	69.41
14	500	35	35	86.57±0.28	85.17
15	500	35	35	84.68±2.54	85.17
16	500	70	35	88.45±1.25	88.76
17	500	35	70	90.76±0.86	91.14
18	500	35	35	84.68±0.97	85.17
19	0	70	0	20.64±1.04	20.74
20	0	0	0	10.26±1.48	9.55

Table 4.4: Analysis of variance (ANOVA) analysis of percentage degradation

Source	Degrees of freedom	*F*-value	*p*-Value
Regression	9	1131.06	0.00
Linear	3	1583.06	0.00
Square	3	1377.86	0.00
Interaction	3	432.25	0.00
Residual Error	10	-	-
Lack-of-Fit	5	2.43	0.176
Pure Error	5	-	-
Total	19	-	-

Table 4.5: Results of fitting pseudo n^{th} order model to degradation profiles (both experimental and simulated) of SDZ

Anions		Experimental		Experimental	Model
	C_{anion}	n	k	η (%)	η (%)
Test (no anions)	ppm (mM)	1.70	606	93.14 ± 1.24	92.12*
Control (mechanical agitation with no anions)	–	1.06	29	23.33 ± 1.12	24.88#
NO_3^-	100 (1.18)	1.57	244	87.08 ± 1.27	83.95*
	200 (2.35)	1.54	195	85.96 ± 1.04	82.72*
	500 (5.88)	1.41	83	78.33 ± 2.36	81.65*
Cl^-	100 (1.71)	1.64	365	91.67 ± 1.34	90.53*
	200 (3.42)	1.45	131	82.69 ± 1.72	89.54*
	500 (8.56)	1.33	61	74.51 ± 0.78	88.51*
CO_3^{2-}	100 (0.94)	1.49	156	85.29 ± 1.82	83.38*
	200 (1.89)	1.35	64	75.71 ± 1.13	80.45*
	500 (4.72)	1.23	35	61.51 ± 1.91	74.02*
SO_4^{2-}	100 (0.70)	1.44	119	83.28 ± 1.86	92.23*
	200 (1.41)	1.30	50	70.42 ± 1.05	91.22*
	500 (3.52)	1.26	38	65.26 ± 1.76	90.55*

Notations: n – order of reaction, k – reaction rate constant ($mol^{1-n} L^{n-1} min^{-1}$), C_{anion} – concentration of anions added externally to solution (mg/L), η – total percentage degradation of SDZ during the treatment period

* = $[Fe^{2+}]/[H_2O_2]$ ratio = 3 (SDZ degradation in presence of sonication)

= $[Fe^{2+}]/[H_2O_2]$ ratio = 0.5 (SDZ degradation in presence of mechanical agitation at 500 rpm)

Simultaneous degradation of SDZ and BA (reference compound method): The kinetic constant of SDZ degradation in Fenton + persulfate + sonication system was determined using relative rate technique with benzoic acid (BA) as the reference compound. The procedure for this technique is described in detail in our previous paper (Roy and Moholkar, 2020). For the convenience of the reader, this procedure is also reproduced in the section 4.2.6. The composition of the reaction mixture in the two sets of experiments for estimation of the kinetic constants for degradation induced by $^{\bullet}OH$ and $SO_4^{\bullet-}$ radicals, respectively, was as follows:

Set 1: SDZ = 20 ppm, BA = 20 ppm, H_2O_2 = 484.85 μL, Fe_3O_4@hollow@$mSiO_2$ = 55.86 mg, pH = 5.

Set 2: SDZ = 20 ppm, BA = 20 ppm, $Na_2S_2O_8$ = 57.28 mg, pH = 5.

4.2.5 Analytical Methods

Samples withdrawn from reaction mixture were analyzed for residual SDZ concentration by HPLC (Shimadzu, Model: SPD-20A) with C-18 reverse phase column (5 μm, 250 mm × 4.6 mm) and UV detector at 275 nm. Mobile phase comprised of 25:75 vol% mixture of acetonitrile and sodium acetate (pH 4.75, 0.02 mol/L, isocratic flow rate = 0.8 mL/min). The concentration profile of benzoic acid (BA) was also established with HPLC (mobile phase 50:50 vol% mixture of methanol and phosphoric acid, 10 mM, flow rate 1.0 mL/min, UV detector = 227 nm). We would like to categorically state that we have not identified the intermediates of SDZ degradation by Fenton + persulfate system, as previous authors have already dealt with this matter (for example, Zou et al. 2014).

4.2.6 Kinetic Analysis of SDZ Degradation

4.2.6.1 Determination of Kinetic Constants of Reactions of SDZ with Radicals

Following the reference compound method (Aschmann et al., 2011, Xie et al., 2015) the kinetic constants of SDZ degradation by $^{\bullet}OH$ and $SO_4^{\bullet-}$ radicals (viz. reactions R38 and R39 in Table 4.2 C) were determined with benzoic acid (BA) as the reference compound. Buxton et al. (1988) and Neta et al. (1988) have reported kinetic constants of benzoic acid degradation by $^{\bullet}OH$ and $SO_4^{\bullet-}$ radicals as 5.9×10^9 and 1.2×10^9 $M^{-1} \cdot s^{-1}$. The kinetic constants of SDZ and BA degradation by any of the radicals (denoted as k_{SDZ} and k_{BA}) are related as: $(C_0/C)_{SDZ} = (C_0/C)_{BA}^{(k_{SDZ}/k_{BA})}$. In other words, the kinetic constants of SDZ degradation can be determined from the slope of the plot of $\ln(C_0/C)_{SDZ}$ versus $\ln(C_0/C)_{BA}$.

As noted earlier, the degradation profiles of SDZ in all reaction system were determined using a kinetic model, which is based on a particular set of reactions for each system. These profiles were compared with the experimental profiles of SDZ in that reaction system. The basic reaction system for oxidative degradation of SDZ is Fenton + persulfate in the presence of sonication. The basic 11 chemical reaction of Fenton + persulfate system involving eight species are listed in Table 4.6.A.1 and A.2 for Fenton and persulfate system respectively. Out of these, three species are radical species, viz. [$^{\bullet}OH$], [$SO_4^{\bullet-}$], [$HO_2^{\bullet}$]. The radical's species are highly reactive and unstable. Thus, their concentration in the solution at any instance can be assumed to be negligible. Thus, we assume pseudo steady-state for these radicals. The kinetic analysis of SDZ degradation in five different systems, viz. Fenton + persulfate and Fenton + persulfate + inorganic anion (viz. Cl^-, NO_3^-, CO_3^{2-} and SO_4^{2-}) is described below.

Table 4.6 (A): The reactions and rate constants used in kinetic modelling for SDZ degradation

A.1	Fenton reaction system	k ($M^{-1}\cdot s^{-1}$)	References
R1	$Fe^{2+} + H_2O_2 \longrightarrow Fe^{3+} + {}^{\bullet}OH + OH^-$	70	Wu et al. (2010)
R2	${}^{\bullet}OH + H_2O_2 \longrightarrow H_2O + HO_2^{\bullet}$	3.3×10^7	Wu et al. (2010)
R3	$H_2O_2 + Fe^{3+} \longrightarrow Fe^{2+} + HO_2^{\bullet} + H^+$	0.01	Wu et al. (2010)
R4	$Fe^{3+} + HO_2^{\bullet} \longrightarrow Fe^{2+} + O_2 + H^+$	1.2×10^6	Wu et al. (2010)
R5	$Fe^{2+} + HO_2^{\bullet} \longrightarrow Fe^{3+} + OH^-$	1.3×10^6	Roy and Moholkar (2020)
R6	${}^{\bullet}OH + Fe^{2+} \longrightarrow Fe^{3+} + OH^-$	3.2×10^8	Roy and Moholkar (2020)
A.2	Fenton + Persulfate reaction system	k ($M^{-1}\cdot s^{-1}$)	References
R7	$S_2O_8^{2-} + Fe^{2+} \longrightarrow Fe^{3+} + SO_4^{2-} + SO_4^{\bullet-}$	27	Xu and Li (2010)
R8	$S_2O_8^{2-} + {}^{\bullet}OH \longrightarrow S_2O_8^{\bullet-} + OH^-$	1.4×10^7	Xie et al. (2015)
R9	$Fe^{2+} + SO_4^{\bullet-} \longrightarrow Fe^{3+} + SO_4^{2-}$	3×10^8	Xu and Li (2010)
R10	$Fe^{3+} + SO_4^{\bullet-} \longrightarrow Fe^{2+} + SO_4^{2-}$	4.6×10^9	Ghauch et al. (2013)
R11	$SO_4^{\bullet-} + {}^{\bullet}OH \longrightarrow HSO_5^-$	1×10^{10}	Xie et al. (2015)

Table 4.6 (B): Scavenging of radicals by inorganic anions in Fenton + persulfate system

B.1	Reactions in presence of Cl^-	k ($M^{-1}\cdot s^{-1}$)	References
R12	$Fe^{3+} + Cl^- \longrightarrow FeCl^{2+}$	6.61×10^{10}	Machulek Jr. et al. (2009)
R13	$Fe^{2+} + Cl^{\bullet} \longrightarrow Cl^- + Fe^{3+}$	5.9×10^9	Laat et al. (2004)
R14	$Fe^{2+} + Cl_2^{\bullet-} \longrightarrow Cl^- + FeCl^{2+}$	1.4×10^7	Neta et al. (1988)
R15	$Cl^- + {}^{\bullet}OH \longrightarrow [ClOH]^{\bullet-}$	4.3×10^9	Laat et al. (2004)
R16	$Cl^{\bullet} + Cl^- \longrightarrow Cl_2^{\bullet-}$	8.5×10^9	Laat et al. (2004)
R17	$Cl^{\bullet} + H_2O_2 \longrightarrow HO_2^{\bullet} + Cl^- + H^+$	1×10^9	Laat et al. (2004)
R18	$Cl_2^{\bullet-} + H_2O_2 \longrightarrow HO_2^{\bullet} + 2Cl^- + H^+$	4.1×10^4	Laat et al. (2004)
R19	$Cl_2^{\bullet-} + HO_2^{\bullet} \longrightarrow 2Cl^- + H^+ + O_2$	3.0×10^9	Neta et al. (1988)
R20	$SO_4^{\bullet-} + Cl^- \longrightarrow Cl^{\bullet} + SO_4^{2-}$	2.7×10^8	Lutze et al. (2015)

B.2	Reactions in presence of NO_3^-	k ($M^{-1}\cdot s^{-1}$)	References
R21	$NO_3^- + {}^{\bullet}OH \longrightarrow NO_3^{\bullet} + OH^-$	5×10^9	Mack & Bolton (1999)
R22	$NO_3^- + SO_4^{\bullet-} \longrightarrow NO_3^{\bullet} + SO_4^{2-}$	5.5×10^5	Zhou et al. (2016)
R23	$NO_3^{\bullet} + Fe^{2+} \longrightarrow NO_3^- + Fe^{3+}$	8×10^6	Neta et al. (1988)
R24	$NO_3^{\bullet} + NO_2^{\bullet} \longrightarrow N_2O_5$	1.0×10^9	Poskrebyshev et al. (2001)
R25	$NO_3^{\bullet} + {}^{\bullet}OH \longrightarrow NO_2^{\bullet} + HO_2^{\bullet}$	1×10^{10}	Garaix et al. (2016)
R26	$NO_3^{\bullet} + HO_2^{\bullet} \longrightarrow HNO_3 + O_2$	3×10^9	Garaix et al. (2016)
R27	$NO_3^{\bullet} + H_2O_2 \longrightarrow HNO_3 + HO_2^{\bullet}$	7.1×10^6	Garaix et al. (2016)

B.3	Reactions in presence of CO_3^{2-}	k ($M^{-1}\cdot s^{-1}$)	References
R28	$SO_4^{\bullet-} + CO_3^{2-} \longrightarrow SO_4^{2-} + CO_3^{\bullet-}$	6.1×10^6	Zhou et al. (2016)
R29	${}^{\bullet}OH + CO_3^{2-} \longrightarrow OH^- + CO_3^{\bullet-}$	3.9×10^8	Zhou et al. (2016)
R30	$SO_4^{\bullet-} + HCO_3^- \longrightarrow SO_4^{2-} + H^+ + CO_3^{\bullet-}$	9.1×10^6	Neta et al. (1988)
R31	${}^{\bullet}OH + HCO_3^- \longrightarrow CO_3^{\bullet-} + H_2O$	8.5×10^6	Merouani et al. (2010)
R32	$CO_3^{\bullet-} + H_2O_2 \longrightarrow HCO_3^- + O_2^{\bullet-} + H^+$	8.0×10^5	Beltran et al. (1998)

B.4	Reactions in presence of SO_4^{2-}	k ($M^{-1}\cdot s^{-1}$)	References
R33	$Fe^{3+} + SO_4^{2-} \longrightarrow FeSO_4^+$	2.09×10^{12}	Machulek Jr. et al. (2009)
R34	$Fe^{2+} + SO_4^{2-} \longrightarrow FeSO_4$	1.55×10^{11}	Machulek Jr. et al. (2009)
R35	$SO_4^{\bullet-} + OH^- \longrightarrow SO_4^{2-} + {}^{\bullet}OH$	1.4×10^7	Machulek Jr. et al. (2009)
R36	$SO_4^{\bullet-} + H_2O_2 \longrightarrow SO_4^{2-} + H^+ + HO_2^{\bullet}$	1.2×10^7	Machulek Jr. et al. (2009)
R37	$SO_4^{\bullet-} + HO_2^{\bullet} \longrightarrow SO_4^{2-} + H^+ + O_2$	3.5×10^9	Machulek Jr. et al. (2009)

Table 4.6 (C): Kinetic constants of simultaneous degradation of SDZ and BA (reference compound method)

C.	Degradation reactions	k ($M^{-1}\cdot s^{-1}$)	References
R38	$SDZ + {}^{\bullet}OH \longrightarrow H_2O + CO_2 + products$	2.18×10^9	This Study
R39	$SDZ + SO_4^{\bullet-} \longrightarrow H_2O + CO_2 + products$	1.34×10^9	This Study
R40	$BA + {}^{\bullet}OH \longrightarrow H_2O + CO_2 + products$	5.9×10^9	Buxton et al. (1988)
R41	$BA + SO_4^{\bullet-} \longrightarrow H_2O + CO_2 + products$	1.2×10^9	Neta et al. (1988)

System 1 (Fenton + persulfate without any additive): The differential mass balances of 8 chemical species for Fenton + persulfate system in the absence of any inorganic anion are listed in the Table 4.7A. The gross degradation kinetics of SDZ by $^{\bullet}OH$, and $SO_4^{\bullet-}$ radicals are given by reactions R38 and R39 in the Table 4.6C, while the kinetics of degradation of reference compound (BA), is represented by reactions R40 and R41. It should be noted that reaction R38 to R41 have been considered in each reaction system listed in Table 4.6C. Equating the differential mass balances of radical species (equations 2, 3 and 4 in Table 4.6A) to zero yielded the following pseudo steady-state concentrations:

$$\left[{}^{\bullet}OH\right] = \frac{k_1\left[Fe^{2+}\right]\left[H_2O_2\right]}{k_2\left[H_2O_2\right] + k_6\left[Fe^{2+}\right] + k_8\left[S_2O_8^{2-}\right] + k_{11}\left[SO_4^{\bullet-}\right] + k_{38}\left[SDZ\right]}$$

$$\left[SO_4^{\bullet-}\right] = \frac{k_7\left[S_2O_8^{2-}\right]\left[Fe^{2+}\right]}{k_9\left[Fe^{2+}\right] + k_{10}\left[Fe^{3+}\right] + k_{11}\left[{}^{\bullet}OH\right] + k_{39}\left[SDZ\right]}$$

$$\left[HO_2^{\bullet}\right] = \frac{k_2\left[{}^{\bullet}OH\right]\left[H_2O_2\right] + k_3\left[Fe^{3+}\right]\left[H_2O_2\right]}{k_4\left[Fe^{3+}\right] + k_5\left[Fe^{2+}\right]}$$

It may be noted that the experiment of SDZ degradation with Fenton + persulfate system without any additive was carried out in two protocols, viz. mechanical stirring and sonication. The experimental profiles of SDZ disappearance in these experiments were compared against the simulated profiles obtained from the kinetic model with $[Fe^{2+}]/[H_2O_2]$ ratio as the manipulation parameter. Based on the best fit between experimental and simulated profiles, the dominant ratio of concentrations of Fe^{2+} and H_2O_2 in the reaction mixture was determined. The rationale underlying this analysis is explained subsequently.

Table 4.7: Differential mass balances for chemical species in different reaction system

(A)	System 1 : Fenton + persulfate
1.	$-\frac{d[SDZ]}{dt} = k_{38}[SDZ][^{\bullet}OH] + k_{39}[SDZ][SO_4^{\bullet-}]$
2.	$\frac{d[^{\bullet}OH]}{dt} = k_1[Fe^{2+}][H_2O_2] - k_2[^{\bullet}OH][H_2O_2] - k_6[^{\bullet}OH][Fe^{2+}]$ $-k_8[S_2O_8^{2-}][^{\bullet}OH] - k_{11}[SO_4^{\bullet-}][^{\bullet}OH] - k_{38}[SDZ][^{\bullet}OH]$
3.	$\frac{d[SO_4^{\bullet-}]}{dt} = k_7[S_2O_8^{2-}][Fe^{2+}] - k_9[Fe^{2+}][SO_4^{\bullet-}] - k_{10}[Fe^{3+}][SO_4^{\bullet-}]$ $-k_{11}[SO_4^{\bullet-}][^{\bullet}OH] - k_{39}[SDZ][SO_4^{\bullet-}]$
4.	$\frac{d[HO_2^{\bullet}]}{dt} = k_2[^{\bullet}OH][H_2O_2] + k_3[Fe^{3+}][H_2O_2] - k_4[Fe^{3+}][HO_2^{\bullet}]$ $-k_5[Fe^{2+}][HO_2^{\bullet}]$
5.	$\frac{d[S_2O_8^{2-}]}{dt} = -k_7[S_2O_8^{2-}][Fe^{2+}] - k_8[S_2O_8^{2-}][^{\bullet}OH]$
6.	$\frac{d[H_2O_2]}{dt} = -k_1[Fe^{2+}][H_2O_2] - k_2[^{\bullet}OH][H_2O_2] - k_3[Fe^{3+}][H_2O_2]$
7.	$\frac{d[Fe^{2+}]}{dt} = -k_1[Fe^{2+}][H_2O_2] + k_3[Fe^{3+}][H_2O_2] + k_4[Fe^{3+}][HO_2^{\bullet}]$ $-k_5[Fe^{2+}][HO_2^{\bullet}] - k_6[Fe^{2+}][^{\bullet}OH] - k_7[Fe^{2+}][S_2O_8^{2-}] - k_9[Fe^{2+}][SO_4^{\bullet-}]$ $+k_{10}[Fe^{3+}][SO_4^{\bullet-}]$
8.	$\frac{d[Fe^{3+}]}{dt} = k_1[Fe^{2+}][H_2O_2] - k_3[Fe^{3+}][H_2O_2] - k_4[Fe^{3+}][HO_2^{\bullet}]$ $+k_5[Fe^{2+}][HO_2^{\bullet}] + k_6[Fe^{2+}][^{\bullet}OH] + k_7[Fe^{2+}][S_2O_8^{2-}] + k_9[Fe^{2+}][SO_4^{\bullet-}]$ $-k_{10}[Fe^{3+}][SO_4^{\bullet-}]$

System 2 (Fenton + persulfate + chloride Cl^- anion): The presence of Cl^- in reaction system induces additional reactions (listed in Table 4.6B.1) that result in scavenging of

$^{\bullet}OH$, and $SO_4^{\bullet-}$ radicals. The differential mass balances of 11 chemical species for Fenton + persulfate system in the presence of chloride ions are listed in Table 4.7B. Equating the differential mass balances of radical species (equations 10, 11, 12, 13 and 14 in Table 4.7B) to zero yielded the following pseudo steady-state concentrations:

$$\left[{}^{\bullet}OH\right] = \frac{k_1\left[Fe^{2+}\right]\left[H_2O_2\right]}{k_2\left[H_2O_2\right] + k_6\left[Fe^{2+}\right] + k_8\left[S_2O_8^{2-}\right] + k_{11}\left[SO_4^{\bullet-}\right] + k_{15}\left[Cl^-\right] + k_{38}\left[SDZ\right]}$$

$$\left[HO_2^{\bullet}\right] = \frac{k_2\left[{}^{\bullet}OH\right]\left[H_2O_2\right] + k_3\left[Fe^{3+}\right]\left[H_2O_2\right] + k_{17}\left[Cl^{\bullet}\right]\left[H_2O_2\right] + k_{18}\left[Cl_2^{\bullet-}\right]\left[H_2O_2\right]}{k_4\left[Fe^{3+}\right] + k_5\left[Fe^{2+}\right] + k_{19}\left[Cl_2^{\bullet-}\right]}$$

$$\left[SO_4^{\bullet-}\right] = \frac{k_7\left[S_2O_8^{2-}\right]\left[Fe^{2+}\right]}{k_9\left[Fe^{2+}\right] + k_{10}\left[Fe^{3+}\right] + k_{11}\left[{}^{\bullet}OH\right] + k_{20}\left[Cl^-\right] + k_{39}\left[SDZ\right]}$$

$$\left[Cl^{\bullet}\right] = \frac{k_{20}\left[SO_4^{\bullet-}\right]\left[Cl^-\right]}{k_{13}\left[Fe^{2+}\right] + k_{16}\left[Cl^-\right] + k_{17}\left[H_2O_2\right]}$$

$$\left[Cl_2^{\bullet-}\right] = \frac{k_{16}\left[Cl^{\bullet}\right]\left[Cl^-\right]}{k_{14}\left[Fe^{2+}\right] + k_{18}\left[H_2O_2\right] + k_{19}\left[HO_2^{\bullet}\right]}$$

Table 4.7: Differential mass balances for chemical species in different reaction system

(B)	System 2 : Fenton + persulfate + Cl^-
9.	$-\frac{d[SDZ]}{dt} = k_{38}\left[SDZ\right]\left[{}^{\bullet}OH\right] + k_{39}\left[SDZ\right]\left[SO_4^{\bullet-}\right]$
10.	$\frac{d\left[{}^{\bullet}OH\right]}{dt} = k_1\left[Fe^{2+}\right]\left[H_2O_2\right] - k_2\left[{}^{\bullet}OH\right]\left[H_2O_2\right] - k_6\left[{}^{\bullet}OH\right]\left[Fe^{2+}\right]$ $-k_8\left[S_2O_8^{2-}\right]\left[{}^{\bullet}OH\right] - k_{11}\left[SO_4^{\bullet-}\right]\left[{}^{\bullet}OH\right] - k_{15}\left[Cl^-\right]\left[{}^{\bullet}OH\right] - k_{38}\left[SDZ\right]\left[{}^{\bullet}OH\right]$

11. $$\frac{d\left[HO_2^{\bullet}\right]}{dt} = k_2\left[{}^{\bullet}OH\right]\left[H_2O_2\right] + k_3\left[Fe^{3+}\right]\left[H_2O_2\right] - k_4\left[Fe^{3+}\right]\left[HO_2^{\bullet}\right]$$
$$-k_5\left[Fe^{2+}\right]\left[HO_2^{\bullet}\right] + k_{17}\left[Cl^{\bullet}\right]\left[H_2O_2\right] + k_{18}\left[Cl_2^{\bullet-}\right]\left[H_2O_2\right] - k_{19}\left[Cl_2^{\bullet-}\right]\left[HO_2^{\bullet}\right]$$

12. $$\frac{d\left[SO_4^{\bullet-}\right]}{dt} = k_7\left[S_2O_8^{2-}\right]\left[Fe^{2+}\right] - k_9\left[Fe^{2+}\right]\left[SO_4^{\bullet-}\right] - k_{10}\left[Fe^{3+}\right]\left[SO_4^{\bullet-}\right]$$
$$-k_{11}\left[SO_4^{\bullet-}\right]\left[{}^{\bullet}OH\right] - k_{20}\left[SO_4^{\bullet-}\right]\left[Cl^{-}\right] - k_{39}\left[SDZ\right]\left[SO_4^{\bullet-}\right]$$

13. $$\frac{d\left[Cl^{\bullet}\right]}{dt} = -k_{13}\left[Fe^{2+}\right]\left[Cl^{\bullet}\right] - k_{16}\left[Cl^{\bullet}\right]\left[Cl^{-}\right] - k_{17}\left[Cl^{\bullet}\right]\left[H_2O_2\right] + k_{20}\left[SO_4^{\bullet-}\right]\left[Cl^{-}\right]$$

14. $$\frac{d\left[Cl_2^{\bullet-}\right]}{dt} = -k_{14}\left[Fe^{2+}\right]\left[Cl_2^{\bullet-}\right] + k_{16}\left[Cl^{\bullet}\right]\left[Cl^{-}\right] - k_{18}\left[Cl_2^{\bullet-}\right]\left[H_2O_2\right]$$
$$-k_{19}\left[Cl_2^{\bullet-}\right]\left[HO_2^{\bullet}\right]$$

15. $$\frac{d\left[S_2O_8^{2-}\right]}{dt} = -k_7\left[S_2O_8^{2-}\right]\left[Fe^{2+}\right] - k_8\left[S_2O_8^{2-}\right]\left[{}^{\bullet}OH\right]$$

16. $$\frac{d\left[H_2O_2\right]}{dt} = -k_1\left[Fe^{2+}\right]\left[H_2O_2\right] - k_2\left[{}^{\bullet}OH\right]\left[H_2O_2\right] - k_3\left[Fe^{3+}\right]\left[H_2O_2\right]$$
$$-k_{17}\left[Cl^{\bullet}\right]\left[H_2O_2\right] - k_{18}\left[Cl_2^{\bullet-}\right]\left[H_2O_2\right]$$

17. $$\frac{d\left[Cl^{-}\right]}{dt} = -k_{12}\left[Fe^{3+}\right]\left[Cl^{-}\right] + k_{13}\left[Fe^{2+}\right]\left[Cl^{\bullet}\right] + k_{14}\left[Fe^{2+}\right]\left[Cl_2^{\bullet-}\right]$$
$$-k_5\left[Cl^{-}\right]\left[{}^{\bullet}OH\right] - k_{16}\left[Cl^{\bullet}\right]\left[Cl^{-}\right] + k_{17}\left[Cl^{\bullet}\right]\left[H_2O_2\right] + k_{18}\left[Cl_2^{\bullet-}\right]\left[H_2O_2\right]$$
$$+k_{19}\left[Cl_2^{\bullet-}\right]\left[HO_2^{\bullet}\right] - k_{20}\left[SO_4^{\bullet-}\right]\left[Cl^{-}\right]$$

18. $$\frac{d\left[Fe^{2+}\right]}{dt} = -k_1\left[Fe^{2+}\right]\left[H_2O_2\right] + k_3\left[Fe^{3+}\right]\left[H_2O_2\right] + k_4\left[Fe^{3+}\right]\left[HO_2^{\bullet}\right]$$
$$-k_5\left[Fe^{2+}\right]\left[HO_2^{\bullet}\right] - k_6\left[Fe^{2+}\right]\left[{}^{\bullet}OH\right] - k_7\left[Fe^{2+}\right]\left[S_2O_8^{2-}\right] - k_9\left[Fe^{2+}\right]\left[SO_4^{\bullet-}\right]$$
$$+k_{10}\left[Fe^{3+}\right]\left[SO_4^{\bullet-}\right] - k_{13}\left[Fe^{2+}\right]\left[Cl^{\bullet}\right] - k_{14}\left[Fe^{2+}\right]\left[Cl_2^{\bullet-}\right]$$

19. $$\frac{d\left[Fe^{3+}\right]}{dt} = k_1\left[Fe^{2+}\right]\left[H_2O_2\right] - k_3\left[Fe^{3+}\right]\left[H_2O_2\right] - k_4\left[Fe^{3+}\right]\left[HO_2^{\bullet}\right]$$
$$+k_5\left[Fe^{2+}\right]\left[HO_2^{\bullet}\right] + k_6\left[Fe^{2+}\right]\left[{}^{\bullet}OH\right] + k_7\left[Fe^{2+}\right]\left[S_2O_8^{2-}\right] + k_9\left[Fe^{2+}\right]\left[SO_4^{\bullet-}\right]$$
$$-k_{10}\left[Fe^{3+}\right]\left[SO_4^{\bullet-}\right] - k_{12}\left[Fe^{3+}\right]\left[Cl^{-}\right] + k_{13}\left[Fe^{2+}\right]\left[Cl^{\bullet}\right]$$

System 3 (Fenton + persulfate + Nitrate NO_3^- anion): The reactions induced by NO_3^- in the system are listed along with their kinetic constants in Table 4.6B.2. The differential mass balances of 11 chemical species for Fenton + persulfate system in the presence of nitrate ions are listed in Table 4.7C. Equating the differential mass balances of radical species (equations 21, 22, 23, 24 and 25 in Table 4.7C) to zero yielded the following pseudo steady-state concentrations:

$$\left[{}^{\bullet}OH\right] = \frac{k_1\left[Fe^{2+}\right]\left[H_2O_2\right]}{k_2\left[H_2O_2\right] + k_6\left[Fe^{2+}\right] + k_8\left[S_2O_8^{2-}\right] + k_{11}\left[SO_4^{\bullet-}\right] + k_{21}\left[NO_3^-\right] + k_{25}\left[NO_3^{\bullet}\right] + k_{38}\left[SDZ\right]}$$

$$\left[HO_2^{\bullet}\right] = \frac{k_2\left[{}^{\bullet}OH\right]\left[H_2O_2\right] + k_3\left[Fe^{3+}\right]\left[H_2O_2\right] + k_{25}\left[NO_3^{\bullet}\right]\left[{}^{\bullet}OH\right] + k_{27}\left[NO_3^{\bullet}\right]\left[H_2O_2\right]}{k_4\left[Fe^{3+}\right] + k_5\left[Fe^{2+}\right] + k_{26}\left[NO_3^{\bullet}\right]}$$

$$\left[SO_4^{\bullet-}\right] = \frac{k_7\left[S_2O_8^{2-}\right]\left[Fe^{2+}\right]}{k_9\left[Fe^{2+}\right] + k_{10}\left[Fe^{3+}\right] + k_{11}\left[{}^{\bullet}OH\right] + k_{22}\left[NO_3^-\right] + k_{39}\left[SDZ\right]}$$

$$\left[NO_3^{\bullet}\right] = \frac{k_{21}\left[NO_3^-\right]\left[{}^{\bullet}OH\right] + k_{22}\left[NO_3^-\right]\left[SO_4^{\bullet-}\right]}{k_{23}\left[Fe^{2+}\right] + k_{24}\left[NO_2^{\bullet}\right] + k_{25}\left[{}^{\bullet}OH\right] + k_{26}\left[HO_2^{\bullet}\right] + k_{27}\left[H_2O_2\right]}$$

$$\left[NO_2^{\bullet}\right] = \frac{k_{25}}{k_{24}}\left[{}^{\bullet}OH\right]$$

Table 4.7: Differential mass balances for chemical species in different reaction system

(C)	System 3 : Fenton + persulfate + NO_3^-
20.	$-\frac{d[SDZ]}{dt} = k_{38}\left[SDZ\right]\left[{}^{\bullet}OH\right] + k_{39}\left[SDZ\right]\left[SO_4^{\bullet-}\right]$
21.	$\frac{d\left[{}^{\bullet}OH\right]}{dt} = k_1\left[Fe^{2+}\right]\left[H_2O_2\right] - k_2\left[{}^{\bullet}OH\right]\left[H_2O_2\right] - k_6\left[{}^{\bullet}OH\right]\left[Fe^{2+}\right]$ $-k_8\left[S_2O_8^{2-}\right]\left[{}^{\bullet}OH\right] - k_{11}\left[SO_4^{\bullet-}\right]\left[{}^{\bullet}OH\right] - k_{21}\left[NO_3^-\right]\left[{}^{\bullet}OH\right]$ $-k_{25}\left[NO_3^{\bullet}\right]\left[{}^{\bullet}OH\right] - k_{38}\left[SDZ\right]\left[{}^{\bullet}OH\right]$

22. $$\frac{d\left[HO_2^{\bullet}\right]}{dt} = k_2\left[{}^{\bullet}OH\right]\left[H_2O_2\right] + k_3\left[Fe^{3+}\right]\left[H_2O_2\right] - k_4\left[Fe^{3+}\right]\left[HO_2^{\bullet}\right]$$
$$-k_5\left[Fe^{2+}\right]\left[HO_2^{\bullet}\right] + k_{25}\left[NO_3^{\bullet}\right]\left[{}^{\bullet}OH\right] - k_{26}\left[NO_3^{\bullet}\right]\left[HO_2^{\bullet}\right] + k_{27}\left[NO_3^{\bullet}\right]\left[H_2O_2\right]$$

23. $$\frac{d\left[SO_4^{\bullet-}\right]}{dt} = k_7\left[S_2O_8^{2-}\right]\left[Fe^{2+}\right] - k_9\left[Fe^{2+}\right]\left[SO_4^{\bullet-}\right] - k_{10}\left[Fe^{3+}\right]\left[SO_4^{\bullet-}\right]$$
$$-k_{11}\left[SO_4^{\bullet-}\right]\left[{}^{\bullet}OH\right] - k_{22}\left[SO_4^{\bullet-}\right]\left[NO_3^{-}\right] - k_{39}\left[SDZ\right]\left[SO_4^{\bullet-}\right]$$

24. $$\frac{d\left[NO_3^{\bullet}\right]}{dt} = k_{21}\left[NO_3^{-}\right]\left[{}^{\bullet}OH\right] + k_{22}\left[NO_3^{-}\right]\left[SO_4^{\bullet-}\right] - k_{23}\left[NO_3^{\bullet}\right]\left[Fe^{2+}\right]$$
$$-k_{24}\left[NO_3^{\bullet}\right]\left[NO_2^{\bullet}\right] - k_{25}\left[NO_3^{\bullet}\right]\left[{}^{\bullet}OH\right] - k_{26}\left[NO_3^{\bullet}\right]\left[HO_2^{\bullet}\right] - k_{27}\left[NO_3^{\bullet}\right]\left[H_2O_2\right]$$

25. $$\frac{d\left[NO_2^{\bullet}\right]}{dt} = -k_{24}\left[NO_3^{\bullet}\right]\left[NO_2^{\bullet}\right] + k_{25}\left[NO_2^{\bullet}\right]\left[{}^{\bullet}OH\right]$$

26. $$\frac{d\left[NO_3^{-}\right]}{dt} = -k_{21}\left[NO_3^{-}\right]\left[{}^{\bullet}OH\right] - k_{22}\left[NO_3^{-}\right]\left[SO_4^{\bullet-}\right] + k_{23}\left[NO_3^{\bullet}\right]\left[Fe^{2+}\right]$$

27. $$\frac{d\left[S_2O_8^{2-}\right]}{dt} = -k_7\left[S_2O_8^{2-}\right]\left[Fe^{2+}\right] - k_8\left[S_2O_8^{2-}\right]\left[{}^{\bullet}OH\right]$$

28. $$\frac{d\left[H_2O_2\right]}{dt} = -k_1\left[Fe^{2+}\right]\left[H_2O_2\right] - k_2\left[{}^{\bullet}OH\right]\left[H_2O_2\right] - k_3\left[Fe^{3+}\right]\left[H_2O_2\right]$$
$$-k_{27}\left[NO_3^{\bullet}\right]\left[H_2O_2\right]$$

29. $$\frac{d\left[Fe^{2+}\right]}{dt} = -k_1\left[Fe^{2+}\right]\left[H_2O_2\right] + k_3\left[Fe^{3+}\right]\left[H_2O_2\right] + k_4\left[Fe^{3+}\right]\left[HO_2^{\bullet}\right]$$
$$-k_5\left[Fe^{2+}\right]\left[HO_2^{\bullet}\right] - k_6\left[Fe^{2+}\right]\left[{}^{\bullet}OH\right] - k_7\left[Fe^{2+}\right]\left[S_2O_8^{2-}\right] - k_9\left[Fe^{2+}\right]\left[SO_4^{\bullet-}\right]$$
$$+k_{10}\left[Fe^{3+}\right]\left[SO_4^{\bullet-}\right] - k_{23}\left[NO_3^{\bullet}\right]\left[Fe^{2+}\right]$$

30. $$\frac{d\left[Fe^{3+}\right]}{dt} = k_1\left[Fe^{2+}\right]\left[H_2O_2\right] - k_3\left[Fe^{3+}\right]\left[H_2O_2\right] - k_4\left[Fe^{3+}\right]\left[HO_2^{\bullet}\right]$$
$$+k_5\left[Fe^{2+}\right]\left[HO_2^{\bullet}\right] + k_6\left[Fe^{2+}\right]\left[{}^{\bullet}OH\right] + k_7\left[Fe^{2+}\right]\left[S_2O_8^{2-}\right] + k_9\left[Fe^{2+}\right]\left[SO_4^{\bullet-}\right]$$
$$-k_{10}\left[Fe^{3+}\right]\left[SO_4^{\bullet-}\right] + k_{23}\left[Fe^{2+}\right]\left[NO_3^{\bullet}\right]$$

***System 4* (*Fenton + persulfate + carbonate* CO_3^{2-} *anion*):** The presence of CO_3^{2-} in reaction system induces additional reactions (listed in Table 4.6B.3) that result in scavenging of $^{\bullet}OH$, and $SO_4^{\bullet-}$ radicals. The differential mass balances of 10 chemical species for Fenton + persulfate system in the presence of carbonate ions are listed in Table 4.7D. The pseudo steady-state concentrations of radical species were (equations 32, 33, 34, and 35 in Table 4.7D):

$$\left[{}^{\bullet}OH\right]=\frac{k_1\left[Fe^{2+}\right]\left[H_2O_2\right]}{k_2\left[H_2O_2\right]+k_6\left[Fe^{2+}\right]+k_8\left[S_2O_8^{2-}\right]+k_{11}\left[SO_4^{\bullet-}\right]+k_{29}\left[CO_3^{2-}\right]+k_{31}\left[HCO_3^{-}\right]+k_{38}\left[SDZ\right]}$$

$$\left[HO_2^{\bullet}\right]=\frac{k_2\left[{}^{\bullet}OH\right]\left[H_2O_2\right]+k_3\left[Fe^{3+}\right]\left[H_2O_2\right]}{k_4\left[Fe^{3+}\right]+k_5\left[Fe^{2+}\right]}$$

$$\left[SO_4^{\bullet-}\right]=\frac{k_7\left[S_2O_8^{2-}\right]\left[Fe^{2+}\right]}{k_9\left[Fe^{2+}\right]+k_{10}\left[Fe^{3+}\right]+k_{11}\left[{}^{\bullet}OH\right]+k_{28}\left[CO_3^{2-}\right]+k_{30}\left[HCO_3^{-}\right]+k_{39}\left[SDZ\right]}$$

$$\left[CO_3^{\bullet-}\right]=\frac{k_{28}\left[SO_4^{\bullet-}\right]\left[CO_3^{2-}\right]+k_{29}\left[{}^{\bullet}OH\right]\left[CO_3^{2-}\right]+k_{30}\left[SO_4^{\bullet-}\right]\left[HCO_3^{-}\right]+k_{31}\left[HCO_3^{-}\right]\left[{}^{\bullet}OH\right]}{k_{32}\left[H_2O_2\right]}$$

Table 4.7: Differential mass balances for chemical species in different reaction system

(D)	System 4 : Fenton + persulfate + CO_3^{2-}
31.	$-\frac{d\left[SDZ\right]}{dt}=k_{38}\left[SDZ\right]\left[{}^{\bullet}OH\right]+k_{39}\left[SDZ\right]\left[SO_4^{\bullet-}\right]$
32.	$\frac{d\left[{}^{\bullet}OH\right]}{dt}=k_1\left[Fe^{2+}\right]\left[H_2O_2\right]-k_2\left[{}^{\bullet}OH\right]\left[H_2O_2\right]-k_6\left[{}^{\bullet}OH\right]\left[Fe^{2+}\right]$ $-k_8\left[S_2O_8^{2-}\right]\left[{}^{\bullet}OH\right]-k_{11}\left[SO_4^{\bullet-}\right]\left[{}^{\bullet}OH\right]-k_{29}\left[CO_3^{2-}\right]\left[{}^{\bullet}OH\right]$ $+k_{31}\left[HCO_3^{-}\right]\left[{}^{\bullet}OH\right]-k_{38}\left[SDZ\right]\left[{}^{\bullet}OH\right]$

33. $$\frac{d[HO_2^{\bullet}]}{dt} = k_2[{}^{\bullet}OH][H_2O_2] + k_3[Fe^{3+}][H_2O_2] - k_4[Fe^{3+}][HO_2^{\bullet}] - k_5[Fe^{2+}][HO_2^{\bullet}]$$

34. $$\frac{d[SO_4^{\bullet-}]}{dt} = k_7[S_2O_8^{2-}][Fe^{2+}] - k_9[Fe^{2+}][SO_4^{\bullet-}] - k_{10}[Fe^{3+}][SO_4^{\bullet-}] - k_{11}[SO_4^{\bullet-}][{}^{\bullet}OH] - k_{28}[SO_4^{\bullet-}][CO_3^{2-}] - k_{30}[HCO_3^-][SO_4^{\bullet-}] - k_{39}[SDZ][SO_4^{\bullet-}]$$

35. $$\frac{d[CO_3^{\bullet-}]}{dt} = k_{28}[SO_4^{\bullet-}][CO_3^{2-}] + k_{29}[{}^{\bullet}OH][CO_3^{2-}] + k_{30}[SO_4^{\bullet-}][HCO_3^-] + k_{31}[HCO_3^-][{}^{\bullet}OH] - k_{32}[CO_3^{\bullet-}][H_2O_2]$$

36. $$\frac{d[CO_3^{2-}]}{dt} = -k_{28}[SO_4^{\bullet-}][CO_3^{2-}] - k_{29}[{}^{\bullet}OH][CO_3^{2-}]$$

37. $$\frac{d[S_2O_8^{2-}]}{dt} = -k_7[S_2O_8^{2-}][Fe^{2+}] - k_8[S_2O_8^{2-}][{}^{\bullet}OH]$$

38. $$\frac{d[H_2O_2]}{dt} = -k_1[Fe^{2+}][H_2O_2] - k_2[{}^{\bullet}OH][H_2O_2] - k_3[Fe^{3+}][H_2O_2] - k_{32}[CO_3^{\bullet-}][H_2O_2]$$

39. $$\frac{d[Fe^{2+}]}{dt} = -k_1[Fe^{2+}][H_2O_2] + k_3[Fe^{3+}][H_2O_2] + k_4[Fe^{3+}][HO_2^{\bullet}] - k_5[Fe^{2+}][HO_2^{\bullet}] - k_6[Fe^{2+}][{}^{\bullet}OH] - k_7[Fe^{2+}][S_2O_8^{2-}] - k_9[Fe^{2+}][SO_4^{\bullet-}] + k_{10}[Fe^{3+}][SO_4^{\bullet-}]$$

40. $$\frac{d[Fe^{3+}]}{dt} = k_1[Fe^{2+}][H_2O_2] - k_3[Fe^{3+}][H_2O_2] - k_4[Fe^{3+}][HO_2^{\bullet}] + k_5[Fe^{2+}][HO_2^{\bullet}] + k_6[Fe^{2+}][{}^{\bullet}OH] + k_7[Fe^{2+}][S_2O_8^{2-}] + k_9[Fe^{2+}][SO_4^{\bullet-}] - k_{10}[Fe^{3+}][SO_4^{\bullet-}]$$

System 5 (Fenton + persulfate + carbonate SO_4^{2-} anion): The reactions induced by SO_4^{2-} in the system are listed along with their kinetic constants in Table 4.6B.4. The

differential mass balances of 8 chemical species for Fenton + persulfate system in the presence of sulfate ions are listed in Table 4.7E. The pseudo steady-state concentrations of radicals species were (equations 42, 43, and 44) :

$$\left[{}^{\bullet}OH\right]=\frac{k_1\left[Fe^{2+}\right]\left[H_2O_2\right]+k_{35}\left[SO_4^{\bullet-}\right]\left[OH^-\right]}{k_2\left[H_2O_2\right]+k_6\left[Fe^{2+}\right]+k_8\left[S_2O_8^{2-}\right]+k_{11}\left[SO_4^{\bullet-}\right]+k_{38}\left[SDZ\right]}$$

$$\left[HO_2^{\bullet}\right]=\frac{k_2\left[{}^{\bullet}OH\right]\left[H_2O_2\right]+k_3\left[Fe^{3+}\right]\left[H_2O_2\right]+k_{36}\left[SO_4^{\bullet-}\right]\left[H_2O_2\right]}{k_4\left[Fe^{3+}\right]+k_5\left[Fe^{2+}\right]+k_{37}\left[SO_4^{\bullet-}\right]}$$

$$\left[SO_4^{\bullet-}\right]=\frac{k_7\left[S_2O_8^{2-}\right]\left[Fe^{2+}\right]}{k_9\left[Fe^{2+}\right]+k_{10}\left[Fe^{3+}\right]+k_{11}\left[{}^{\bullet}OH\right]+k_{35}\left[OH^-\right]+k_{36}\left[H_2O_2\right]+k_{37}\left[HO_2^{\bullet}\right]+k_{39}\left[SDZ\right]}$$

Table 4.7: Differential mass balances for chemical species in different reaction system

(E)	System 5 : Fenton + persulfate + SO_4^{2-}
41.	$-\frac{d\left[SDZ\right]}{dt}=k_{38}\left[SDZ\right]\left[{}^{\bullet}OH\right]+k_{39}\left[SDZ\right]\left[SO_4^{\bullet-}\right]$
42.	$\frac{d\left[{}^{\bullet}OH\right]}{dt}=k_1\left[Fe^{2+}\right]\left[H_2O_2\right]-k_2\left[{}^{\bullet}OH\right]\left[H_2O_2\right]-k_6\left[{}^{\bullet}OH\right]\left[Fe^{2+}\right]$ $-k_8\left[S_2O_8^{2-}\right]\left[{}^{\bullet}OH\right]-k_{11}\left[SO_4^{\bullet-}\right]\left[{}^{\bullet}OH\right]+k_{35}\left[SO_4^{\bullet-}\right]\left[OH^-\right]$ $-k_{38}\left[SDZ\right]\left[{}^{\bullet}OH\right]$
43.	$\frac{d\left[HO_2^{\bullet}\right]}{dt}=k_2\left[{}^{\bullet}OH\right]\left[H_2O_2\right]+k_3\left[Fe^{3+}\right]\left[H_2O_2\right]-k_4\left[Fe^{3+}\right]\left[HO_2^{\bullet}\right]$ $-k_5\left[Fe^{2+}\right]\left[HO_2^{\bullet}\right]+k_{36}\left[SO_4^{\bullet-}\right]\left[H_2O_2\right]-k_{37}\left[SO_4^{\bullet-}\right]\left[HO_2^{\bullet}\right]$
44.	$\frac{d\left[SO_4^{\bullet-}\right]}{dt}=k_7\left[S_2O_8^{2-}\right]\left[Fe^{2+}\right]-k_9\left[Fe^{2+}\right]\left[SO_4^{\bullet-}\right]-k_{10}\left[Fe^{3+}\right]\left[SO_4^{\bullet-}\right]$ $-k_{11}\left[SO_4^{\bullet-}\right]\left[{}^{\bullet}OH\right]-k_{35}\left[SO_4^{\bullet-}\right]\left[OH^-\right]-k_{36}\left[SO_4^{\bullet-}\right]\left[H_2O_2\right]-k_{37}\left[SO_4^{\bullet-}\right]\left[HO_2^{\bullet}\right]$ $-k_{39}\left[SDZ\right]\left[SO_4^{\bullet-}\right]$

45. $$\frac{d\left[SO_4^{2-}\right]}{dt} = k_7\left[S_2O_8^{2-}\right]\left[Fe^{2+}\right] + k_9\left[Fe^{2+}\right]\left[SO_4^{\bullet-}\right] + k_{10}\left[Fe^{3+}\right]\left[SO_4^{\bullet-}\right]$$
$$-k_{33}\left[Fe^{3+}\right]\left[SO_4^{2-}\right] - k_{34}\left[Fe^{2+}\right]\left[SO_4^{2-}\right] + k_{35}\left[SO_4^{\bullet-}\right]\left[OH^-\right]$$
$$+k_{36}\left[SO_4^{\bullet-}\right]\left[H_2O_2\right] + k_{37}\left[SO_4^{\bullet-}\right]\left[HO_2^{\bullet}\right]$$

46. $$\frac{d\left[S_2O_8^{2-}\right]}{dt} = -k_7\left[S_2O_8^{2-}\right]\left[Fe^{2+}\right] - k_8\left[S_2O_8^{2-}\right]\left[^{\bullet}OH\right]$$

47. $$\frac{d\left[Fe^{2+}\right]}{dt} = -k_1\left[Fe^{2+}\right]\left[H_2O_2\right] + k_3\left[Fe^{3+}\right]\left[H_2O_2\right] + k_4\left[Fe^{3+}\right]\left[HO_2^{\bullet}\right]$$
$$-k_5\left[Fe^{2+}\right]\left[HO_2^{\bullet}\right] - k_6\left[Fe^{2+}\right]\left[^{\bullet}OH\right] - k_7\left[Fe^{2+}\right]\left[S_2O_8^{2-}\right] - k_9\left[Fe^{2+}\right]\left[SO_4^{\bullet-}\right]$$
$$+k_{10}\left[Fe^{3+}\right]\left[SO_4^{\bullet-}\right] - k_{34}\left[Fe^{2+}\right]\left[SO_4^{2-}\right]$$

48. $$\frac{d\left[Fe^{3+}\right]}{dt} = k_1\left[Fe^{2+}\right]\left[H_2O_2\right] - k_3\left[Fe^{3+}\right]\left[H_2O_2\right] - k_4\left[Fe^{3+}\right]\left[HO_2^{\bullet}\right]$$
$$+k_5\left[Fe^{2+}\right]\left[HO_2^{\bullet}\right] + k_6\left[Fe^{2+}\right]\left[^{\bullet}OH\right] + k_7\left[Fe^{2+}\right]\left[S_2O_8^{2-}\right] + k_9\left[Fe^{2+}\right]\left[SO_4^{\bullet-}\right]$$
$$-k_{10}\left[Fe^{3+}\right]\left[SO_4^{\bullet-}\right] - k_{33}\left[Fe^{3+}\right]\left[SO_4^{2-}\right]$$

The methodology of the relative rate technique used in this study is based on the assumption that oxidants in the system (i.e., radicals causing degradation of pollutant and reference compound) are present in large excess so that both oxidations proceed independently without competing for kinetics. The reaction system also assumes all reactions being first order for all species.

In all systems, the set of differential equations for the mass balances of ionic and molecular species was solved as an initial value problem (IVP). The numerical solution was obtained using Runge Kutta 4th order-5th order adaptive step-size method (Cash-Karp method) (Press et al., 1992). The kinetic constants for different reactions are listed in Table 4.6, while the concentrations of radical species were obtained using pseudo steady-state expressions mentioned earlier.

4.2.6.2 Gross kinetic constants and order of SDZ degradation: The degradation profiles of SDZ were fitted to n[th] order kinetic model: $dC_A/dt = -kC_A^n$. Expressing concentrations in terms of reactant conversion, X (viz. $C_A = C_{A0}(1-X)$) and integration yields:

$$\ln(1-X) = \left\{\frac{\ln(n-1)+\ln k+(n-1)\ln C_{A0}}{1-n}\right\}+\frac{1}{(1-n)}\ln t$$

The kinetic constant of degradation k and the order of the reaction n with respect to SDZ can be determined from plot of $\ln(1-X)$ versus $\ln t$.

4.3 RESULTS AND DISCUSSION

4.3.1 Characterization of catalysts

Figs. 4.4(A) and (B) show the FE-SEM micrographs depicting surface morphology of the as-synthesized microspheres of Fe_3O_4 and Fe_3O_4@SiO_2 microspheres. The catalysts have spherical size with an average diameter ~ 250 nm and do not reveal any aggregation or clustering. Fig. 4.4(B) shows core-shell structure Fe_3O_4@SiO_2 microspheres with a smooth coating of SiO_2. TEM micrographs of final produced catalysts Fe_3O_4@hollow@mSiO_2 are shown in Figs. 4.4(C) and (D). These micrographs clearly show the structural morphology, i.e. yolk-shell structure of the particles. The metal oxide core in the particle with SiO_2 shell surrounding it is visible. The region between the core and shell is hollow and has typical width of approx. 50 nm. The total diameter of the particles is approx. 350 nm. The elemental distribution in synthesized Fe_3O_4@hollow@mSiO_2 is given in Table 4.8 while EDX spectrum is provided in Fig 4.5.

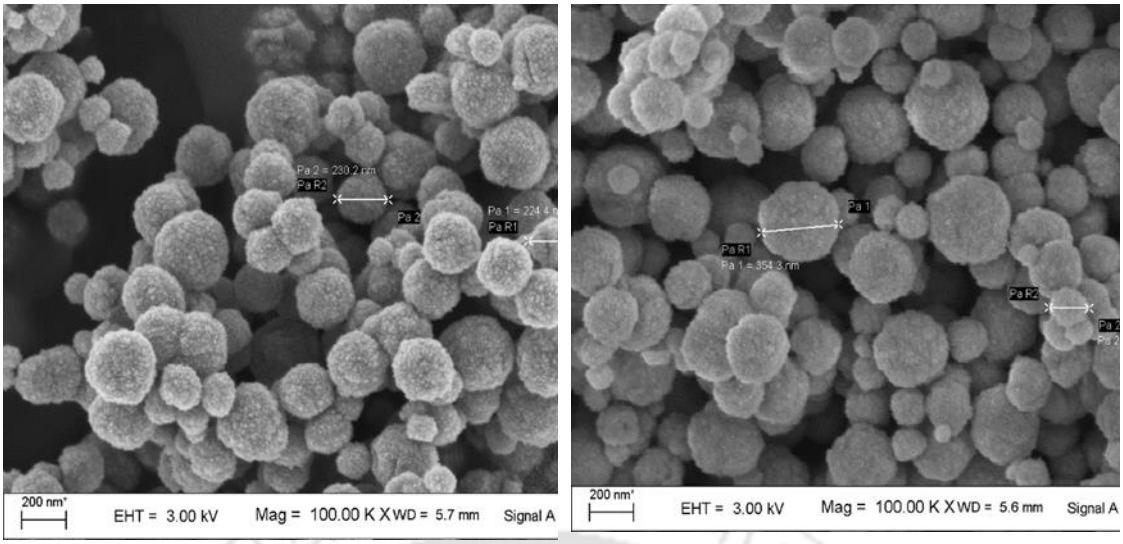

(A) (B)

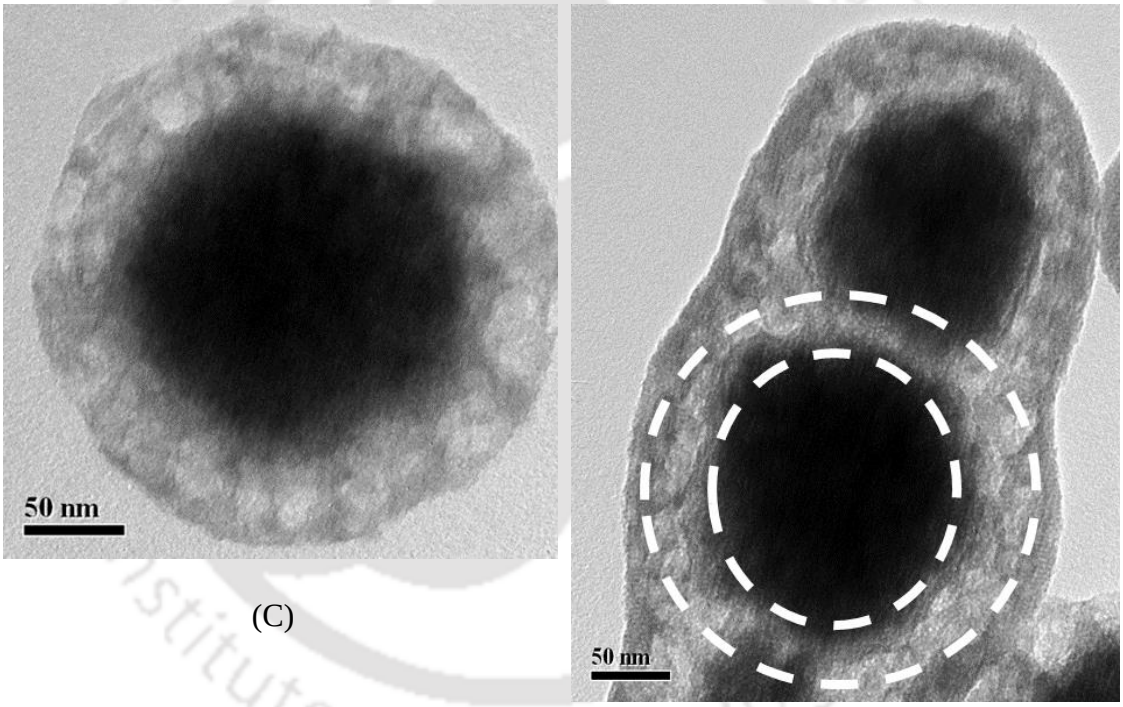

(C) (D)

Figure 4.4: FE-SEM micrographs of : (A) Fe_3O_4 microspheres, (B) Fe_3O_4@SiO_2 microspheres; TEM micrographs of Fe_3O_4@hollow@mSiO_2 particles, (C) single isolated particle, (D) a small agglomerate of two particles.

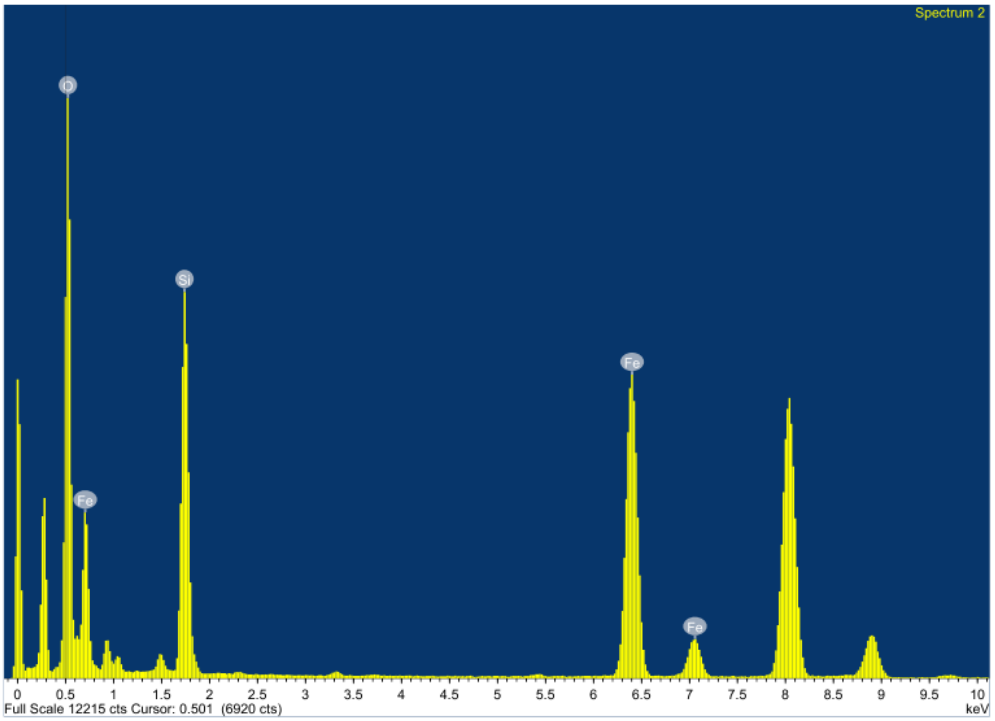

Figure 4.5: EDX spectrum of Fe_3O_4@hollow@mSiO_2 nanoparticles

Table 4.8: Elemental composition of Fe_3O_4@hollow@mSiO_2

Element	Weight (%)	Atomic (%)
O K	43.07	65.87
Si K	21.21	18.48
Fe K	35.72	15.65

Rest of the peaks appearing in Fig. 4.5 correspond to Au, Cu and C of the copper grid.

The magnetic hysteresis curves of the Fe_3O_4, Fe_3O_4@SiO_2 and Fe_3O_4@hollow@mSiO_2 microspheres in the range of -15.0 to 15.0 kOe magnetic field at room temperature are shown in Fig 4.6. The saturation magnetization (M_S) of bare Fe_3O_4 nanoparticles was 58.92 emu/g, which reduced to 52.80 and 28.71 emu/g for Fe_3O_4@nSiO_2 and Fe_3O_4@hollow@mSiO_2, respectively.

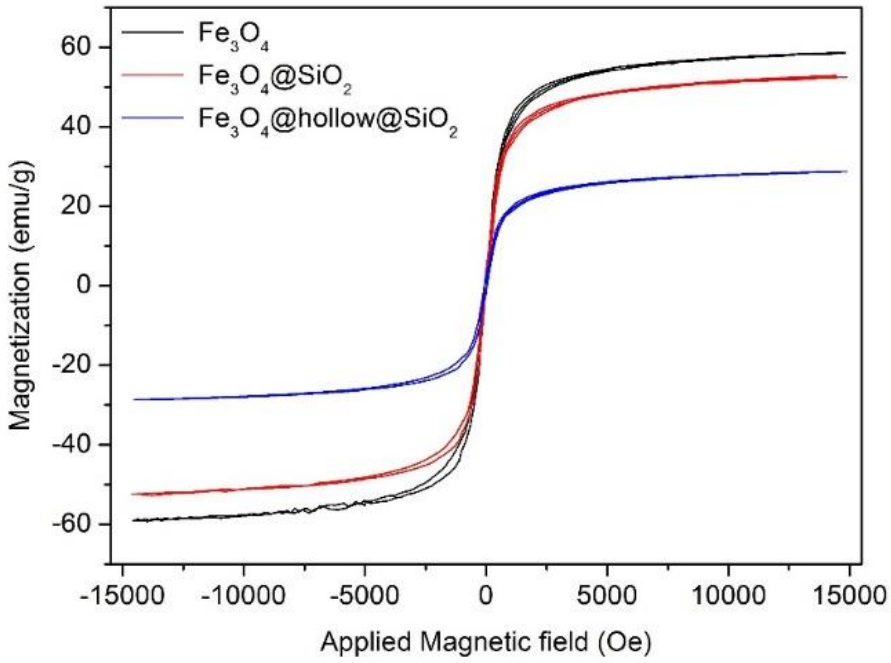

Figure 4.6: Hysteresis loop of the Fe_3O_4, Fe_3O_4@SiO_2 and Fe_3O_4@hollow@mSiO_2 microspheres

The X-ray diffractograms of Fe_3O_4 and Fe_3O_4@hollow@mSiO_2 nanoparticles are shown in Fig. 4.7. For Fe_3O_4, the characteristic diffractions at 2θ (crystal planes) = 30.1° (2 2 0), 35.5° (3 1 1), 43.1° (4 0 0), 53.5° (4 2 2), 57.0° (5 1 1) and 62.6° (4 4 0) match with JCPDS data for standard Fe_3O_4 (JCPDS 65-3107). X-ray diffractograms of Fe_3O_4@ hollow@mSiO_2 nanoparticles show the same peaks with weaker intensity, which reveal that Fe_3O_4 microspheres do not change their crystallinity after SiO_2 coating. Some weak peaks in the range of 2θ = 20°-30° correspond to amorphous silica. The X-ray diffractograms essentially confirm that Fe_3O_4@hollow@mSiO_2 nanoparticles comprise of Fe_3O_4 and SiO_2. Table 4.9 depicts the crystallite sizes (D_{hkl}) for Fe_3O_4 and Fe_3O_4@hollow@mSiO_2 calculated using the Sherrer-Debye equation.

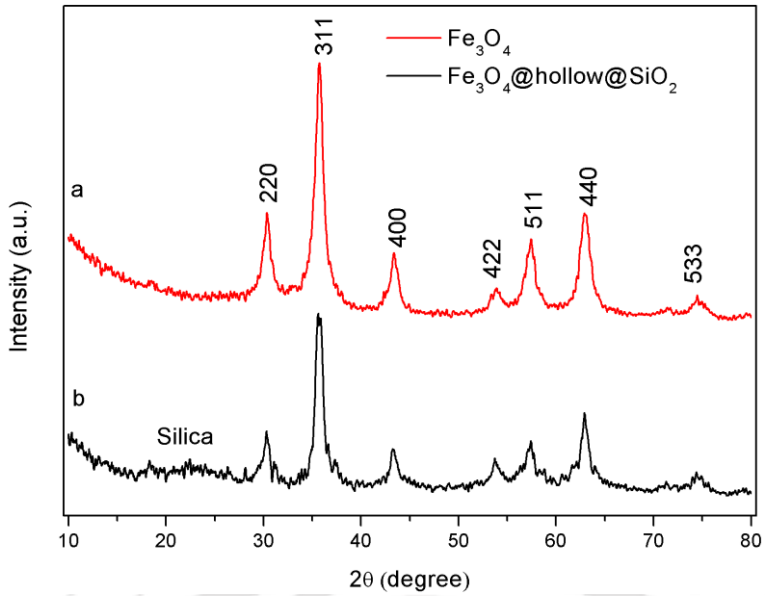

Figure 4.7: XRD patterns of (a) Fe_3O_4 microspheres, and (b) Fe_3O_4@hollow@mSiO_2

Table 4.9: Crystallite sizes for Fe_3O_4 and Fe_3O_4@hollow@mSiO_2 using Debye Sherrer equation

	Fe_3O_4		Fe_3O_4@hollow@mSiO_2		
2θ (deg)	h k l	Size (A°)	2θ (deg)	h k l	Size (A°)
30.4869	2 2 0	44.49	30.4719	2 2 0	110.34
35.7069	3 1 1	93.69	35.7359	3 1 1	79.72
43.3664	4 0 0	110.49	43.5009	4 0 0	84.91
57.3473	5 1 1	85.78	57.4568	5 1 1	58.22
63.1152	4 0 0	55.47	62.8298	4 0 0	82.09

The surface area of these porous Fe_3O_4@hollow@SiO_2 nanoparticles was measured using the Brunauer–Emmett–Teller (BET) method, as shown in Fig. 4.8. The Fe_3O_4@void@mSiO_2 nanospheres had average pore diameter of 4.67 nm, BET surface area of 335.5 m^2/g and a large pore volume of 0.24 cc/g. Avogadro (Version 1.2.0) scientific software tool was used to design and optimize SDZ molecule using steepest descent algorithm. A molecular visualization computational software, Visual Molecular Dynamics (Version 1.9.3), was used to analyse and determine the dimensions of SDZ molecule. As per the schematic of SDZ molecule shown in Fig. 4.9, the molecular length

of SDZ was 12.68 Å, which is far smaller than the average pore size of Fe_3O_4@hollow@mSiO_2 particles. Therefore, SDZ molecules, irrespective of directional orientation, can easily diffuse through surface pores of silica shell into the annular region between silica shell and metal core.

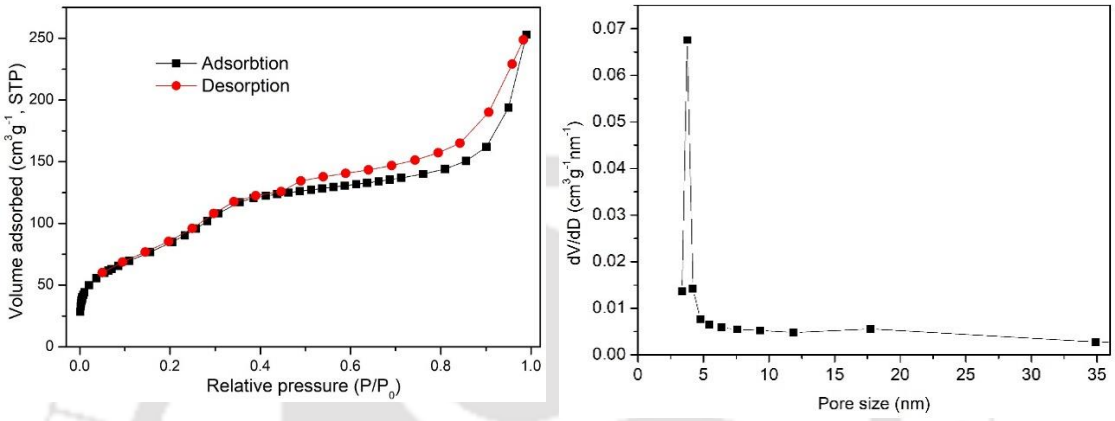

(A) (B)

Figure 4.8: BET analysis (A) N_2 adsorption–desorption isotherms (B) BJH plot of Fe_3O_4@hollow@mSiO_2

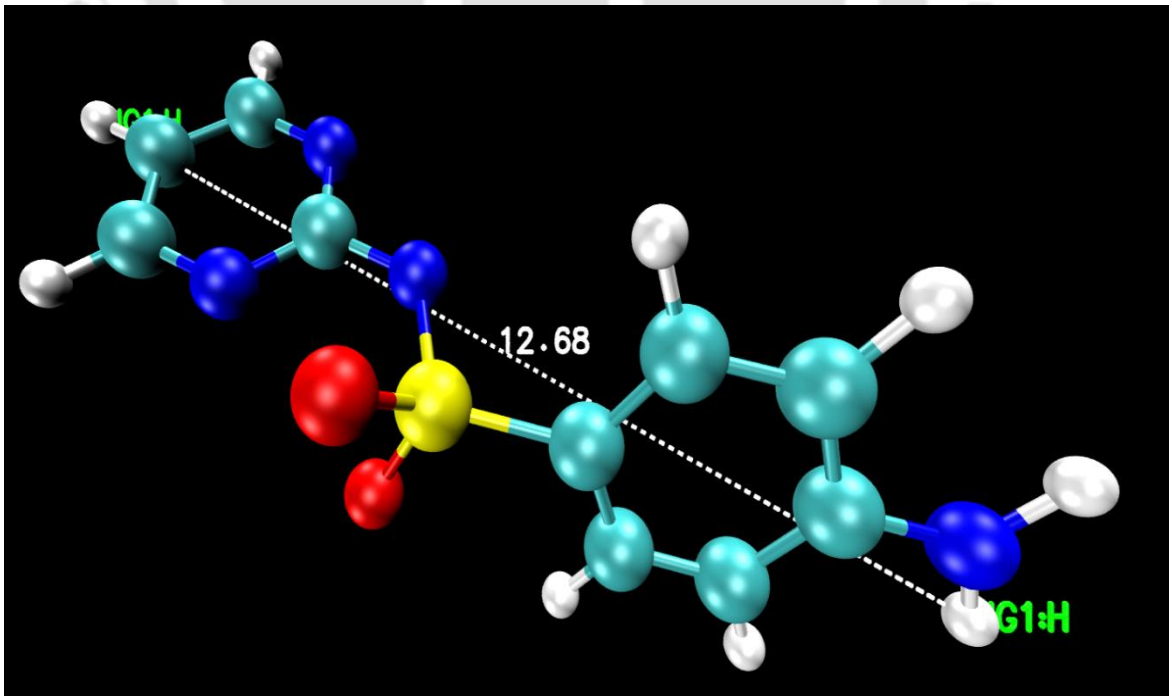

Figure 4.9: Schematic of the optimized structure of SDZ molecule

4.3.2 SDZ degradation: Experiments and simulations

4.3.2.1 Kinetic constants of SDZ reaction with radicals

As noted in section 4.2.6, the relative reference technique was used to determine kinetic constants of reaction between SDZ molecules and radicals ($^{\bullet}OH$ and $SO_4^{\bullet-}$). Fig. 4.10A shows the plot of $\ln(C_0/C)_{SDZ}$ vs. $\ln(C_0/C)_{BA}$ for simultaneous degradation of SDZ and BA by $^{\bullet}OH$ and $SO_4^{\bullet-}$ radicals. The slope of the plot for $^{\bullet}OH$ radical-induced degradation is 0.37, while the slope of the plot for $SO_4^{\bullet-}$ radicals induced degradation is 1.12. This slope is the ratio of kinetic constants k_{SDZ}/k_{BA}. Using the kinetic constants of BA degradation reported in literature (as listed in Table 4.6C), the kinetic constants of SDZ degradation by $^{\bullet}OH$ and $SO_4^{\bullet-}$ radicals have been determined as 2.18×10^9 and 1.34×10^9 $M^{-1}\cdot s^{-1}$, respectively.

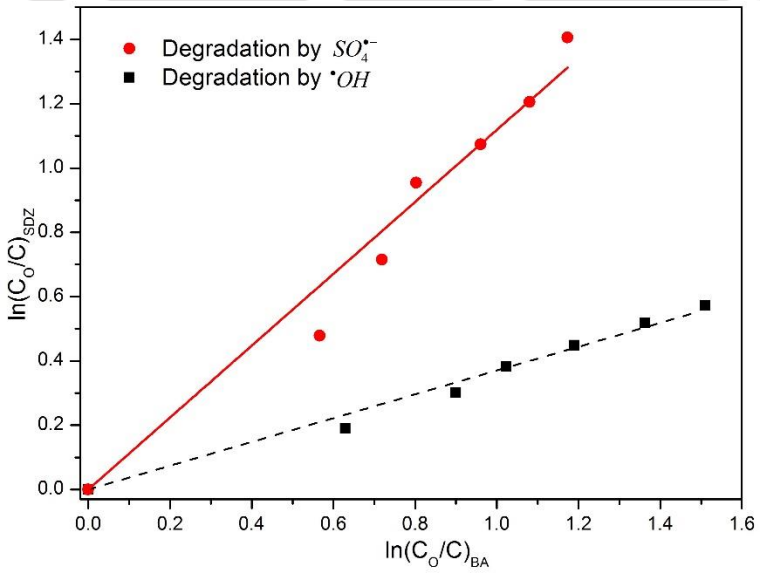

(A)

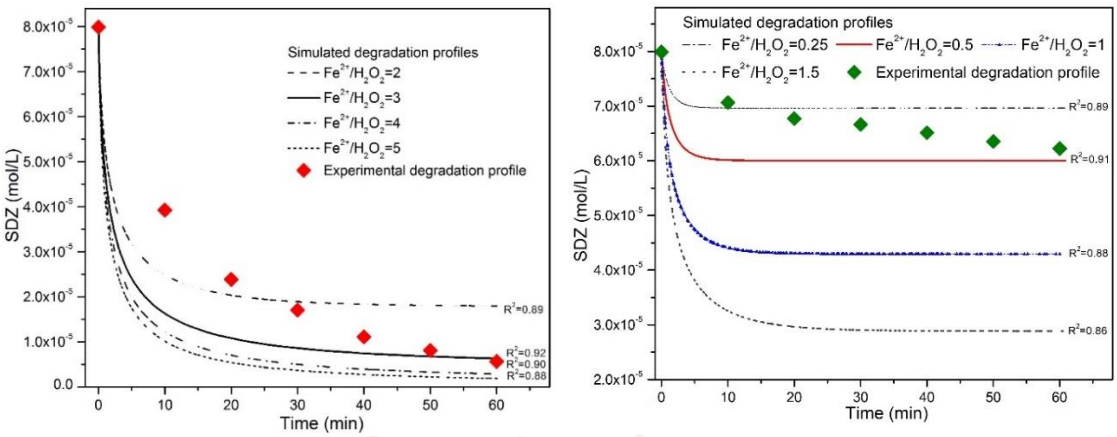

(B) (C)

Figure 4.10: (A) Kinetic constant of SDZ degradation by $^{\bullet}OH$ and $SO_4^{\bullet-}$ radicals using reference compound benzoic acid (slopes = 0.37 and 1.12 for $^{\bullet}OH$ and $SO_4^{\bullet-}$ radicals). (B) Experimental and simulated SDZ degradation profiles in test experiments. The best match (with highest R^2) is obtained for $[Fe^{2+}]/[H_2O_2] = 3$. (C) Experimental and simulated SDZ degradation profiles in control experiments. The best match (with highest R^2) is obtained for $[Fe^{2+}]/[H_2O_2] = 0.5$.

4.3.2.2 Comparative analysis of control and test experiments (without anions)

Experimental and simulated degradation profiles of SDZ in the test (sonication) and control (mechanical agitation) experiments have been depicted in Figs. 4.10B and C, respectively. As noted earlier, these experiments were carried out using Fenton + persulfate system. The simulated profiles have been calculated using the kinetic model depicted in Table 4.7A (or system 1 depicted in section 4.2.6.1). The simulated degradation profiles are based on $[Fe^{2+}]/[H_2O_2]$ ratio as the manipulation parameter. It could be seen that the best match between experimental and simulated profiles is obtained for $[Fe^{2+}]/[H_2O_2] = 3$ for the test experiment and $[Fe^{2+}]/[H_2O_2] = 0.5$ for control experiment. Table 4.5 shows the final results (or summary) for SDZ degradation. Control experiments yielded 23.33% degradation, while test experiments achieved 93.14% degradation. The gross kinetic constant (k) for test experiment was 30× higher than control, while the order of degradation reaction with respect to SDZ is also higher for the

test experiment (n = 1.70) than control (n = 1.06). The percentage degradation obtained with simulations (24.88% and 92.12%) matches well with experimental for both control and test experiments.

Markedly faster kinetics of SDZ degradation in the test experiment is attributed to the higher concentration of Fe^{2+} ions in the solution, which are leached out from the metal oxide core of Yolk-shell catalyst Fe_3O_4@hollow@mSiO_2. This enhanced leaching is essentially a result of intense micro-turbulence generated by sonication that enhances solid/liquid mass transfer. This proposition is also supported by $[Fe^{2+}]/[H_2O_2]$ ratios for the best match simulated profiles for control and test experiments. Also, the $^{\bullet}OH$ radicals generated by the transient collapse of cavitation bubbles contribute to SDZ degradation and $S_2O_8^{2-}$ activation, which synergistically enhance both kinetics and yield of SDZ degradation.

4.3.2.3 SDZ degradation in presence of inorganic anions

The degradation of SDZ by ultrasound-assisted Fenton + persulfate system was studied in the presence of 4 inorganic anions, viz. Cl^-, NO_3^-, CO_3^{2-} and SO_4^{2-}. These anions lead to scavenging of $^{\bullet}OH$ and $SO_4^{\bullet-}$ radicals as well as complexation with metal ions (Fe^{2+}/Fe^{3+}), as per reactions listed in Table 4.6B.1 to 4.6B.4.

Figs. 4.11(A) and (B) depict the simulated and experimental profiles of SDZ degradation in the presence of CO_3^{2-} ions. Figs. 4.11(C) and (D) show the same results for Cl^- ions. Figs. 4.12(A) and (B) show the simulated and experimental profiles of SDZ degradation in the presence of NO_3^- ions, while Figs. 4.12(C) and (D) show same results for SO_4^{2-} ions. The summary of the experimental and simulation results is given in Table 4.5. The concentrations of all four anions were varied in 3 levels, viz. 100, 200 and 500

ppm. The salient features and trends in SDZ degradation in the presence of inorganic anions, as evident from the results presented in Table 4.5, are listed as follows:

(1) At the lowest concentration of 100 ppm, all anions have a very marginal effect on SDZ degradation. For the Cl^- ion, the extent of degradation (91.67%) stays practically unchanged as compared to the degradation in test experiment (93.14%). For the other ions, a minor reduction of ~ 5-10% in degradation is seen.

(2) The inhibition effect on SDZ degradation increases with concentration for all anions. However, this effect is most marked for CO_3^{2-} and SO_4^{2-} ions, where the degradation reduces by 33.9 and 29.9%, respectively (as compared to test experiments) for the anion concentration of 500 ppm. For the Cl^- and NO_3^- ions, the inhibition of degradation is relatively lower, i.e. 20 and 15.9%, respectively.

(3) A close match between percentage degradation predicted by simulations and the experimental result is seen for low concentration (100 ppm) of Cl^-, NO_3^- and CO_3^{2-} ions. However, for SO_4^{2-} ions, a marginal difference of ~5% is seen between experimental degradation (83.28%) and degradation predicted by simulation (92.23%). The discrepancy between simulations results and experimental degradation rises at higher concentration of anions. Actual (or experimental) degradation is lower than the degradation predicted by simulations and a probable cause leading to this effect is the nature of interactions between different chemical species in the reaction system. The highest discrepancy of

20.3% and 38.8% between the experimental and simulation results is seen for CO_3^{2-} and SO_4^{2-} ions, respectively.

(4) Fitting of the n^{th} order kinetic model to the experimental data also reveals interesting facets of SDZ degradation. In control experiments with no additive, the order of reaction for SDZ is 1.06, which resembles pseudo 1st order behavior. In the test experiment, the kinetic constant as well as the order of reaction shows enhancement. The kinetic constants boost almost 30× to k = 606 mol^{1-n} L^{n-1} min^{-1} (from k = 29 mol^{1-n} L^{n-1} min^{-1} for the control experiments), while order of reaction increases to n = 1.7. The presence of inorganic anions, even at the lowest concentration of 100 ppm, reduces the kinetic constant as well as the order of the reaction. For example, at 100 ppm concentration, the smallest kinetic constants of 156 and 119 mol^{1-n} L^{n-1} min^{-1} with reaction orders of 1.49 and 1.44 are obtained for CO_3^{2-} and SO_4^{2-}, respectively. As the concentrations of all anions increase from 100 to 500 ppm, there is 4 to 5× reduction in kinetic constants with concurrent reduction in reaction order. At anion concentration of 500 ppm, the least kinetic constants of 35 and 38 mol^{1-n} L^{n-1} min^{-1} are obtained CO_3^{2-} and SO_4^{2-}, with reaction orders of 1.23 and 1.26, respectively. These results clearly reveal relatively stronger effect of CO_3^{2-} and SO_4^{2-} ions an inhibition of SDZ degradation, as compared to NO_3^- and Cl^- ions.

4.3.3 Analysis

In this section, we have made an attempt to give plausible explanations of the experimental and simulation results. The inhibition effect on the degradation induced by inorganic ions essentially has two origins: (1) scavenging of the $^{\bullet}OH$ and $SO_4^{\bullet-}$ radicals by the anions, and (2) complexation of anions with Fe^{2+} and Fe^{3+}, which hinders their

participation in Fenton-persulfate chemistry. The relative contribution of these effects towards inhibitions of SDZ degradation depends on two factors, viz. the concentration of the anions, and the kinetic constants of the reaction between radicals and anions (as compared to the kinetic constants of reaction between radicals and SDZ). For the highest anions uncertain of 500 ppm, the inhibition effect on SDZ degradation induced by different anions follows the trend: $NO_3^- < Cl^- < SO_4^{2-} < CO_3^{2-}$.

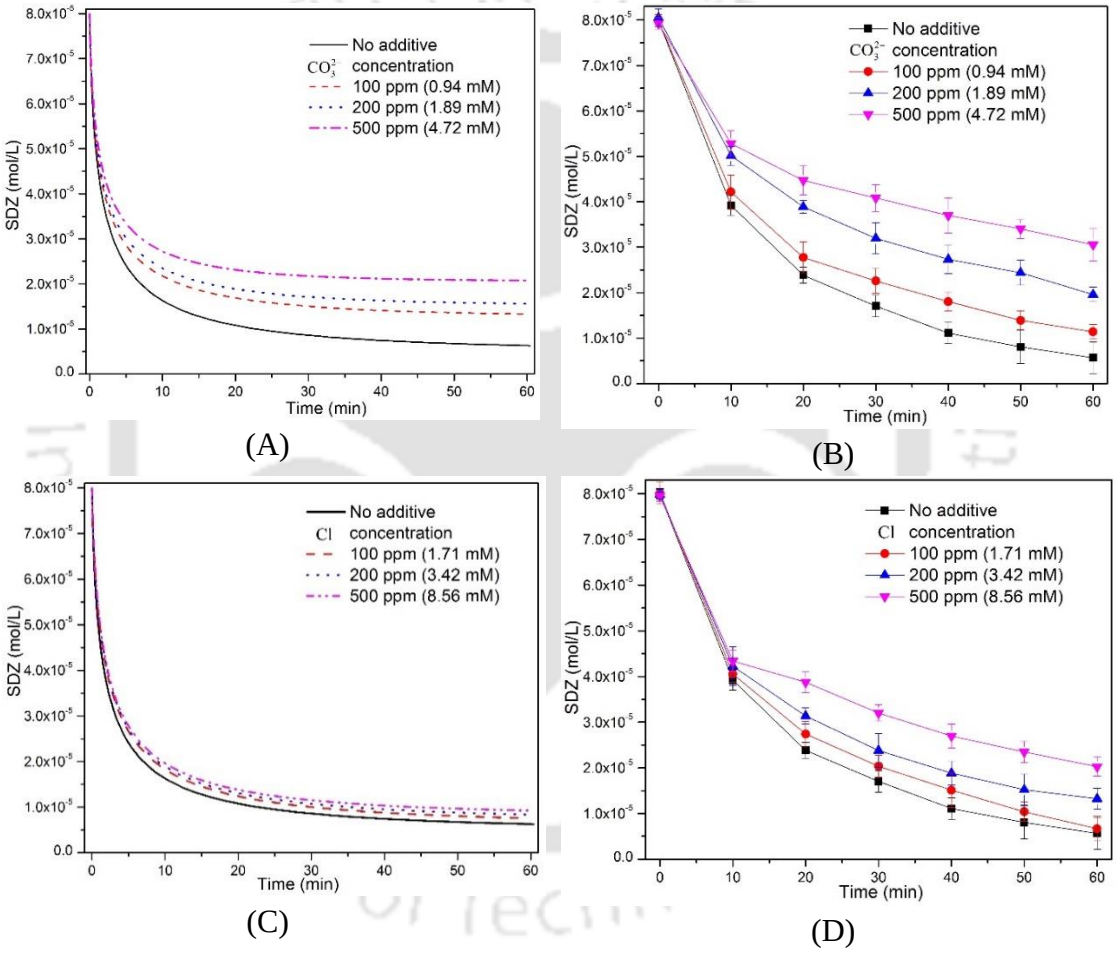

Figure 4.11: Influence of inorganic anions on sonocatalytic SDZ degradation profiles. Simulated profiles in presence of (A) CO_3^{2-} anion, (C) Cl^- anions. Experimental profiles in presence of (B) CO_3^{2-} anion, (D) Cl^- anions. Simulated and experimental profiles for only sonocatalytic degradation (in absence of any anion) are shown as reference.

The least inhibition effect on SDZ degradation is seen for NO_3^-. This result is attributed to two causes, viz. NO_3^- do not form any complex with Fe^{2+} or Fe^{3+} ions, and secondly, the scavenging of $SO_4^{\bullet-}$ radicals by NO_3^- (reaction R22) has far slower kinetics ($k = 5.5 \times 10^5$ $M^{-1} \cdot s^{-1}$) as compared to reaction between SDZ and $SO_4^{\bullet-}$ ($k = 1.34 \times 10^9$ $M^{-1} \cdot s^{-1}$). Thus, the radical scavenging effect of NO_3^- is rather limited. It may be noted that $NO_3^{\bullet}$ formed out of reaction R21 & R22 (Table 4.6B.2) has reduced reactivity due to smaller oxidation potential of 2.2 eV (Devi et al., 2011).

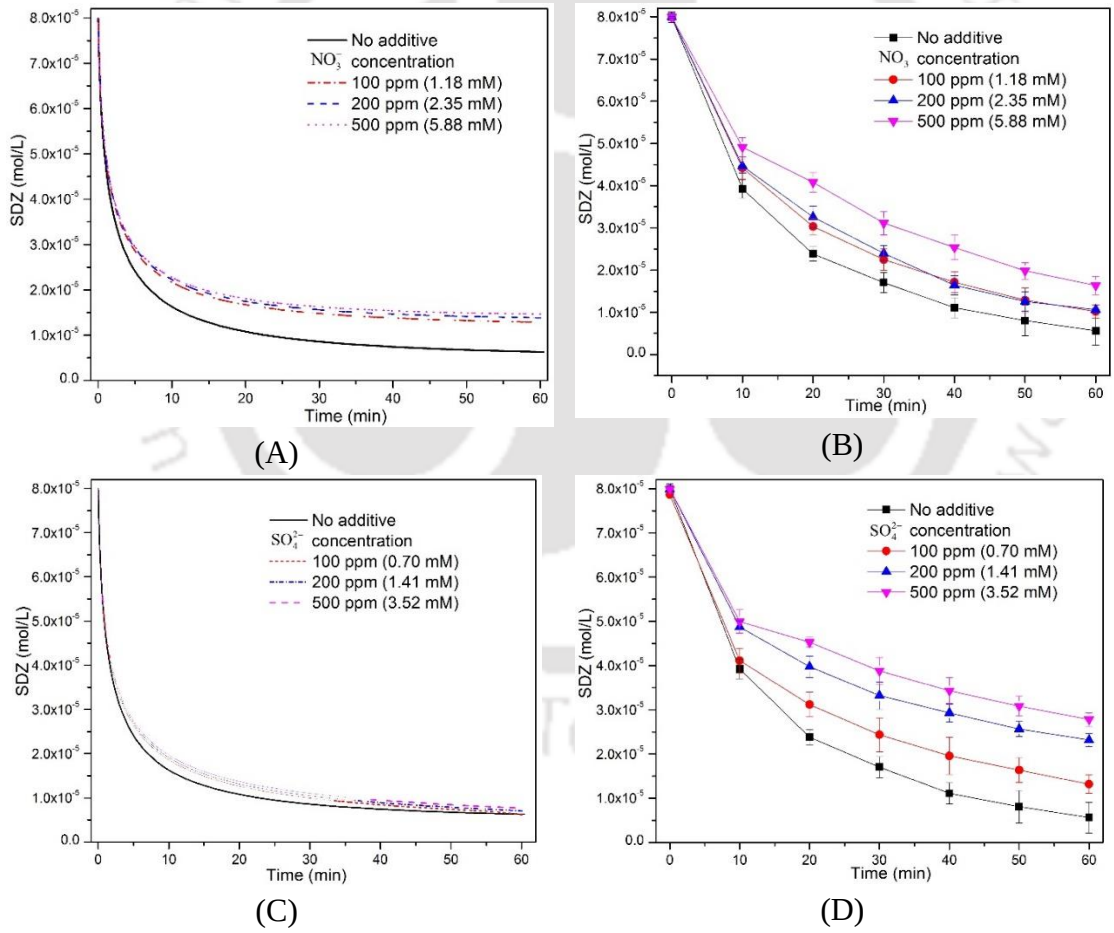

Figure 4.12: Influence of inorganic anions on sonocatalytic SDZ degradation profiles. Simulated profiles in presence of (A) NO_3^- anion, (C) SO_4^{2-} anions. Experimental profiles in presence of (B) NO_3^- anion, (D) SO_4^{2-} anions. Simulated and experimental profiles for only sonocatalytic degradation (in absence of any anion) are shown as reference.

Cl^- ions form complex with Fe^{2+} and Fe^{3+} to yield complexes $FeCl^+$, $FeCl^{2+}$, $FeCl_2^+$. However, scavenging of $^\bullet OH$ and $SO_4^{\bullet-}$ radicals by Cl^- results in the generation of species $Cl^\bullet$ and $Cl_2^{\bullet-}$ with oxidation potential of 2.4 and 2.1 eV, respectively (Armstrong et al., 2015). Degradation induced by these radicals can marginally offset the inhibition effect. At acidic pH of 5, the additional species $[ClOH]^{\bullet-}$ can also generate $Cl^\bullet$ species through intermediate $[HClOH]^\bullet$, viz.:

$Cl^- + {}^\bullet OH \longrightarrow [ClOH]^{\bullet-} + H^+ \longrightarrow [HClOH]^\bullet \longrightarrow Cl^\bullet + H_2O$ (Laat et al., 2004; Evgenidou et al., 2007; Subramanian and Madras, 2016). As a consequence of these physical/chemical phenomena, SDZ degradation in the presence of 500 ppm Cl^- is 74.51%, which is 20% reduction as compared to the test experiment without additives.

The sulfate anions can complex with Fe^{2+}/Fe^{3+} to yield complexes of $FeSO_4$ and $FeSO_4^+$ (reactions R33 and R34 in Table 4.6B.4). The kinetic constants of these reactions are several orders of magnitude higher (~ 10^{11} $M^{-1}{\cdot}s^{-1}$) than other reaction of Fe^{2+}/Fe^{3+} in Fenton-persulfate system. Moreover, at the highest SO_4^{2-} concentration of 500 ppm, another complex $Fe(SO_4)_2^-$ can form which retards participation of Fe^{2+}/Fe^{3+} in Fenton reactions and persulfate activation. The scavenging effect induced by SO_4^{2-} is more pronounced at acidic pH, where species HSO_4^- forms through reaction $H^+ + SO_4^{2-} \longleftrightarrow HSO_4^-$ with fast kinetics ($k_{forward}$ = 2.8 × 10^{11} $M^{-1}{\cdot}s^{-1}$) (Machulek Jr. et al., 2009). HSO_4^- can scavenge the $^\bullet OH$ radicals to generate $SO_4^{\bullet-}$ radicals ($HSO_4^- + HO^\bullet \longrightarrow SO_4^{\bullet-} + H_2O$, k = 3.5 × 10^5 $M^{-1}{\cdot}s^{-1}$). As the population of $SO_4^{\bullet-}$ in solution increases, it can lead to either recombination ($SO_4^{\bullet-} + SO_4^{\bullet-} \longleftrightarrow S_2O_8^{2-}$) or

neutralization with $HO_2^{\bullet}$ (reaction R37 in Table 4.6B.4). An additional factor which contributes to inhibition at high concentration of SO_4^{2-} is reduction in oxidation-reduction potential of $SO_4^{\bullet-}/SO_4^{2-}$. Wu et al. (2015) have written the oxidation induced by $SO_4^{\bullet-}$ radicals as: $SO_4^{\bullet-} + e^- \longleftrightarrow SO_4^{2-}$. Nernst equation for this reaction is written as:

$E_{(SO_4^{\bullet-}/SO_4^{2-})} = E^0_{(SO_4^{\bullet-}/SO_4^{2-})} + (RT/zF)\ln\left(\left[SO_4^{\bullet-}\right]/\left[SO_4^{2-}\right]\right)$ (R = 8.3145 J K^{-1} mol^{-1}, T = 25°C or 298 K, z = number of electrons transferred in the half-reaction = 1, Faraday constant (F) = 9.63845 × 10^4 C/mol).

Assuming that initial activation of $S_2O_8^{2-}$ by Fe^{2+} essentially goes to completion ($S_2O_8^{2-} + Fe^{2+} \longrightarrow Fe^{3+} + SO_4^{2-} + SO_4^{\bullet-}$, k = 27 M^{-1}·s^{-1}), the ratio of $\left[SO_4^{\bullet-}\right]/\left[SO_4^{2-}\right]$ in solution is ≈ 1. If this ratio increases by a factor to 10 due to external addition of SO_4^{2-} ions, it could be easily calculated that the reduction potential of $SO_4^{\bullet-}$, $E_{SO_4^{\bullet-}/SO_4^{2-}}$, will reduce by 0.05823 eV. Summarizing, as a result of above-mentioned phenomena, the SO_4^{2-} anions exert strong inhibition effect due to which the percentage degradation of SDZ reduces drastically to 65.26±1.76% (which is ~ 30% reduction as compared to 93.14±1.24% degradation in test experiment).

CO_3^{2-} ions scavenge both •OH and $SO_4^{\bullet-}$ radicals through reaction R28 and R29 listed in Table 4.6 B.3. The kinetic constants of these reactions are 6.1 × 10^6 and 3.9 × 10^8 M^{-1}·s^{-1}, which indicates stronger inhibition of •OH radical as compared to $SO_4^{\bullet-}$. Moreover, an additional species of HCO_3^- is also generated in acidic environment ($CO_3^{2-} + H^+ \longleftrightarrow HCO_3^-$), which scavenges both •OH and $SO_4^{\bullet-}$ radicals as per R30 and R31 listed in Table 4.6 B.3 (Liu et al., 2016). The kinetic constants of these reactions (9.1

$\times 10^6$ $M^{-1}\cdot s^{-1}$ and 8.5×10^6 $M^{-1}\cdot s^{-1}$, respectively) are of same order of magnitude as that of reaction R28 and R29, which shows that HCO_3^- is an efficient radical scavenger as CO_3^{2-}.

Scavenging induced by CO_3^{2-} and HCO_3^- ions leads to the generation of new radicals species viz. CO_3^{2-} and HCO_3^-. However, the oxidation potentials of these species are far lower, viz. CO_3^{2-} = 1.57 eV and HCO_3^- = 1.78 eV (Augusto and Miyamoto, 2011). Due to very low oxidation potential, CO_3^{2-} and HCO_3^- have a negligible contribution of SDZ degradation. Also, CO_3^{2-} cause precipitation of Fe^{2+} through carbonate formation: $Fe^{2+} + CO_3^{2-} \longrightarrow FeCO_3$. As a collective effect of these phenomena, CO_3^{2-} ions lead to severe inhibition of SDZ degradation (34% reduction as compared to test experiments).

4.3.4 Discrepancies between experimental and simulations results

Some interesting mechanistic facets of the influence of sonication on degradation of SDZ are evident from comparative evaluation of experimental and simulations results. The mathematical model in this work essentially considers a homogeneous Fenton persulfate system, and thus, does not account for the mass transfer effects that exist in the heterogeneous Fenton persulfate system employed in the experiments. On the other hand, sonication of a heterogeneous reaction system has major implications on the mass transfer characteristics of the system. Consequently, most discrepancies between experimental and simulations results have their origin in the mass transfer limitations in the system.

As already discussed in the previous section, intense micromixing induced by sonication enhances the leaching of Fe^{2+} and Fe^{3+} ions from metal core, which is evident from higher $[Fe^{2+}]/[H_2O_2]$ ratios corresponding to best match between experimental and simulations profiles for the test (or ultrasound-assisted) experiments. The inhibition

effect of anions on degradation is further enhanced in presence of sonication. This feature is evident from significantly lower experimental degradation than that predicted by simulations – especially for the highest concentrations (500 ppm) of the anions. The hollow core of the yolk-shell catalyst particles is essentially a nanoreactor with relatively higher concentrations of metal ions (Fe^{2+}/Fe^{3+}) than the bulk concentration. Thus, the rate of production of $^{\bullet}OH$ and $SO_4^{\bullet-}$ radicals and their instant concentration are also high in the hollow core. Under intense microconvection generated by sonication, SDZ molecules can easily diffuse through the SiO_2 shell in the hollow core, and undergo faster degradation. The inorganic anions can also diffuse to the hollow core through silica shell. At the highest concentration of 500 ppm, diffusion of anions in the hollow core is likely to outweigh the diffusion of SDZ. These anions deactivate the metal ions through complex formation. This marked reduces generation of $^{\bullet}OH$ and $SO_4^{\bullet-}$ radicals in the hollow core, as well as concentration of Fe^{2+}/Fe^{3+} in bulk solution. As a result of these physical effects, actual inhibition of SDZ degradation by anions is significantly higher than that accounted by the chemical reactions listed in Table 4.6. Among the four anions, the highest discrepancy between experimental and simulations results is seen for CO_3^{2-} and SO_4^{2-}, and it is attributed to the tendency of complexation with metal ions. This effect is relatively less marked for the Cl^- ions, due to counter production of $Cl^{\bullet}$ and $Cl_2^{\bullet-}$ radicals with high oxidation potential, as noted earlier.

CO_3^{2-} and SO_4^{2-} have been found to significantly reduce SDZ degradation, especially at the highest concentration of 500 ppm, through scavenging of radicals. Interestingly, the kinetic constants of reactions of $^{\bullet}OH$ with both CO_3^{2-} and SO_4^{2-} are at least an order of magnitude smaller than the kinetic constants of reaction with SDZ. A plausible explanation for this inconsistency is given as follows: the effective (or bulk)

rates of reactions between •OH radicals and anions/SDZ not only depends on specific kinetic constants but also the probability of interaction with •OH radical. Radicals are highly unstable and do not diffuse from their point of generation. Therefore, the probability of their interaction depends on the concentration of substrate species (i.e. SDZ or anions). In the present study, the SDZ concentration is 20 ppm, while the concentrations of anions is in the range of 100 to 500 ppm. Due to markedly higher concentration (5 to 25×), the probability of their interaction with •OH radicals is higher, leading to higher effective reaction kinetics and scavenging of •OH radicals.

4.3.4.1 Effect of pH

A peculiar result of the present study is higher degradation at acidic pH of 5. We give below brief discussion about possible rationales for this result. In a hybrid AOPs system such as heterogeneous Fenton-persulfate, in the present study, pH is an important factor that governs rate of oxidation of substrate (or pollutant).

In an extensive and state-of-the-art review, Boczkaj and Fernandes (2017) have analysed the advanced oxidation processes at basic pH conditions. The AOPs addressed by Boczkaj and Fernandes (2017) include ozone (O_3), hydrogen peroxide (H_2O_2), peroxane (H_2O_2/O_3), sulfate radical based processes and photocatalytic processes. In the context of present study, Boczkai and Fernandes (2017) have given following reaction routes for sulfate radical based processes at basic or alkaline pH conditions:

Sulfate radicals can decompose at basic pH to generate •OH radicals as:

$$SO_4^{\bullet -} + H_2O \longrightarrow {}^{\bullet}OH + HSO_4^-$$

$$SO_4^{\bullet -} + OH^- \longrightarrow {}^{\bullet}OH + SO_4^{2-}$$

The persulfate anion can be activated by a base (NaOH) as:

$$2S_2O_8^{2-} + 2H_2O \xrightarrow{OH^-} 2SO_4^{2-} + SO_4^{\bullet-} + O_2^{\bullet-} + 4H^+$$

However, at acidic pH, persulfate can be activated to produce both $SO_4^{\bullet-}$ and SO_4^{2-} as:

$$S_2O_8^{2-} + H^+ \longrightarrow SO_4^{\bullet-} + SO_4^{2-} + H^+$$

Another possibility is the scavenging of $^{\bullet}OH$ radicals by $SO_4^{\bullet-}$ radicals to form peroxy-monosulfate anion (HSO_5^-):

$$HSO_5^- \xrightarrow{\Delta} 2SO_4^{\bullet-} + {}^{\bullet}OH$$

An important influence of pH (in context of oxidative degradation of pollutant) is the prevalent ionization state of the pollutant. The ionization of pollutant is governed by the relative values of pH and pKa. For conditions of pH < pKa, the compound remains in molecular or undissociated form. As pH exceeds pKa, the compound undergoes ionization. The pKa of sulfadiazine is 6.28, and at acidic pH of 5 (corresponding to the highest degradation), it existed in molecular form. In the present context of sulfadiazine degradation with yolk-shell nanoparticles, the enhancement of degradation is a result of diffusion of SDZ in the hollow core of the catalyst, which is likely to have far higher concentration of $^{\bullet}OH$ and $SO_4^{\bullet-}$ radicals. As the pH exceeds pKa, the ionization of sulfadiazine may reduce its diffusivity in the hollow core of yolk-shell particle, due to repulsions between metal cation and pollutant cation. Thus, the rate and extent of degradation is seriously affected at basic pH.

An additional factor that enhances the degradation of sulfadiazine at acidic pH is as follows: In molecular form, the sulfadiazine has strong hydrophobic character due to which it adsorbs on the bubble interface (air/water interface or the bubble wall). This enhances the probability of interaction of the sulfadiazine molecules with $^{\bullet}OH$ radicals generated from the transient collapse of cavitation bubbles resulting in enhanced

degradation. Some $^{\bullet}OH$ radicals could be lost due to reaction with persulfate anions to produce sulfate radicals.

$$^{\bullet}OH + S_2O_8^{2-} \longleftrightarrow S_2O_8^{\bullet-} + OH^-$$

$$S_2O_8^{\bullet-} + SO_4^{2-} \longleftrightarrow SO_4^{\bullet-} + S_2O_8^{2-}$$

However, as noted earlier, sulfate radicals can cause effective degradation of sulfadiazine. Finally, the peroxymonosulfate anion (HSO_5^-) can undergo thermal dissociation to regenerate the sulfate and $^{\bullet}OH$ radicals during sonication of the bulk liquid medium. At the transient collapse of cavitation bubbles, the temperature inside the bubble reaches extreme. The thin liquid film surrounding the bubble interface also gets heated to moderate temperatures which is sufficient to cause dissociation of HSO_5^- present in the liquid in close vicinity of bubble interface to regenerate $^{\bullet}OH$ and $SO_4^{\bullet-}$ radicals.

4.4 CONCLUSIONS

With the dual approach of experiment and simulation, this study has identified mechanistic features of SDZ degradation by ultrasound-assisted Fenton-persulfate system with yolk-shell structured Fe_3O_4@hollow@$mSiO_2$ nanoparticles. Strong micro-convection generated by sonication improves leaching rate of Fe^{2+}/Fe^{3+} from metal core and their diffusion to bulk through mesoporous silica shell that boosts SDZ degradation several fold. The order of gross (or bulk) SDZ degradation was $1 < n < 2$, which resulted in faster kinetics than pseudo 1st order system. Presence of inorganic anions, viz. Cl^-, NO_3^-, CO_3^{2-} and SO_4^{2-} had inhibition effect on SDZ degradation due to radical scavenging and metal ion complexation. Inhibition by anions reduced both bulk kinetic

constant of SDZ degradation as well as order for SDZ. The inhibition effect was revealed to enhance in the presence of sonication – probably due to stronger metal ion complexation and radical scavenging in the hollow core of yolk-shell nanoparticles.

References

Armstrong, D.A., Huie, R.E., Koppenol, W.H., Lymar, S.V., Merényi, G., Neta, P., Ruscic, B., Stanbury, D.M., Steenken, S., Wardman, P., Standard electrode potentials involving radicals in aqueous solution: inorganic radicals (IUPAC Technical Report). *Pure Appl. Chem.* 87(11-12) (2015) 1139-1150.

Aschmann, S.M., Arey, J., Atkinson, R., Kinetics and products of the reaction of •OH radicals with 3-methoxy-3-methyl-1-butanol. *Environ. Sci. Technol.* 45(16) (2011) 6896-6901.

Augusto, O., Miyamoto, S., Oxygen radicals and related species. *Principles of Free Radical Biomedicine*, Nova Science Publishers, New York, (2011) 19-42.

Balaji, C., Moholkar, V.S., Pandit, A.B., Ashokkumar, M., Mechanistic investigations on sonophotocatalytic degradation of textile dyes with surface active solutes. *Ind. Eng. Chem. Res.* 50(20) (2011) 11485-11494.

Beltrán, F.J., González, M., Ribas, F.J., Alvarez, P., Fenton reagent advanced oxidation of polynuclear aromatic hydrocarbons in water. *Water Air Soil Pollut.* 105(3-4) (1998) 685-700.

Boczkaj, G., Fernandes, A., Wastewater treatment by means of advanced oxidation processes at basic pH conditions: a review. *Chem. Eng. J.* 320 (2017) 608-633.

Bokare, A. D., Choi, W., Review of iron-free Fenton-like systems for activating H_2O_2 in advanced oxidation processes. *J. Hazard. Mater.* 275 (2014) 121-135.

Buxton, G.V., Greenstock, C.L., Helman, W.P., Ross, A.B., Critical review of rate constants for reactions of hydrated electrons, hydrogen atoms and hydroxyl radicals (•OH/•O^- in aqueous solution). *J. Phys. Chem. Ref. Data* 17(2) (1988) 513-886.

Chakma, S., Moholkar, V.S., Physical mechanism of sono-Fenton process. *AIChE J.* 59(11) (2013) 4303-4313.

Chakma, S., Praneeth, S., Moholkar, V.S., Mechanistic investigations in sono-hybrid (ultrasound/Fe^{2+}/UVC) techniques of persulfate activation for degradation of Azorubine. *Ultrason. Sonochem.* 38 (2017) 652-663.

De Laat, J., Le, G.T., Legube, B., A comparative study of the effects of chloride, sulfate and nitrate ions on the rates of decomposition of H_2O_2 and organic compounds by Fe (II)/H_2O_2 and Fe (III)/H_2O_2. *Chemosphere* 55(5) (2004) 715-723.

Deng, Y., Qi, D., Deng, C., Zhang, X., Zhao, D., Superparamagnetic high-magnetization microspheres with an Fe_3O_4@SiO_2 core and perpendicularly aligned mesoporous SiO_2 shell for removal of microcystins. *J. Am. Chem. Soc.* 130(1) (2008) 28-29.

Devi, L.G., Raju, K.A., Kumar, S.G., Rajashekhar, K.E., Photo-degradation of di azo dye Bismarck Brown by advanced photo-Fenton process: Influence of inorganic anions and evaluation of recycling efficiency of iron powder. *J. Taiwan Inst. Chem. Eng.* 42(2) (2011) 341-349.

Evgenidou, E., Konstantinou, I., Fytianos, K., Poulios, I., Oxidation of two organophosphorous insecticides by the photo-assisted Fenton reaction. *Water Res.* 41(9) (2007) 2015-2027.

Feng, Y., Wu, D., Liao, C., Deng, Y., Zhang, T., Shih, K., Red mud powders as low-cost and efficient catalysts for persulfate activation: pathways and reusability of mineralizing sulfadiazine. *Sep. Purif. Technol.* 167 (2016) 136-145.

Garaix, G., Horne, G.P., Venault, L., Moisy, P., Pimblott, S.M., Marignier, J.L., Mostafavi, M., Decay mechanism of $NO_3^{\bullet}$ radical in highly concentrated nitrate and nitric acidic solutions in the absence and presence of hydrazine. *J. Phys. Chem. B* 120(22) (2016) 5008-5014.

Ghauch, A., Ayoub, G., Naim, S., Degradation of sulfamethoxazole by persulfate assisted micrometric Fe^0 in aqueous solution. *Chem. Eng. J.* 228 (2013) 1168-1181.

Grčić, I., Papić, S., Koprivanac, N., Kovačić, I., Kinetic modeling and synergy quantification in sono and photooxidative treatment of simulated dyehouse effluent. *Water Res.* 46(17) (2012) 5683-5695.

Kusic, H., Peternel, I., Ukic, S., Koprivanac, N., Bolanca, T., Papic, S., Bozic, A.L., Modeling of iron activated persulfate oxidation treating reactive azo dye in water matrix. *Chem. Eng. J.* 172(1) (2011) 109-121.

Liu, N., Ding, F., Weng, C.H., Hwang, C.C., Lin, Y.T., Minimizing the interference of carbonate ions on degradation of SRF3B dye by Fe^0-aggregate-activated persulfate process. *Sep. Purif. Technol.* 169 (2016) 230-240.

Luo, C., Ma, J., Jiang, J., Liu, Y., Song, Y., Yang, Y., Guan, Y., Wu, D., Simulation and comparative study on the oxidation kinetics of atrazine by UV/H_2O_2, UV/ HSO_5^- and UV/ $S_2O_8^{2-}$. *Water Res.* 80 (2015) 99-108.

Lutze, H.V., Kerlin, N., Schmidt, T.C., Sulfate radical-based water treatment in presence of chloride: formation of chlorate, inter-conversion of sulfate radicals into hydroxyl radicals and influence of bicarbonate. *Water Res.* 72 (2015) 349-360.

Machulek, Jr A., Moraes, J.E.F., Okano, L.T., Silvério, C.A., Quina, F.H., Photolysis of ferric ions in the presence of sulfate or chloride ions: implications for the photo-Fenton process. *Photochem Photobiol Sci.* 8(7) (2009) 985-991.

Mack, J., Bolton, J. R., Photochemistry of nitrite and nitrate in aqueous solution: a review. *J. Photochem. Photobiol., A* 128(1-3) (1999) 1-13.

Merouani, S., Hamdaoui, O., Saoudi, F., Chiha, M., Pétrier, C., Influence of bicarbonate and carbonate ions on sonochemical degradation of Rhodamine B in aqueous phase. *J. Hazard. Mater.* 175(1-3) (2010) 593-599.

Moholkar, V.S., Sable, S.P., Pandit, A.B., Mapping the cavitation intensity in an ultrasonic bath using the acoustic emission. *AIChE J.* 46(4) (2000) 684-694.

Neta, P., Huie, R.E., Ross, A.B., Rate constants for reactions of inorganic radicals in aqueous solution. *J. Phys. Chem. Ref. Data* 17(3) (1988) 1027-1284.

Poskrebyshev, G.A., Neta, P., Huie, R.E., Equilibrium constant of the reaction· OH+ HNO_3⇆ H_2O+ NO_3. in aqueous solution. *J. Geophys. Res.: Atmos.*, 106(D5), (2001) 4995-5004.

Press, W.H., Flannery, B.P., Teukolsky, S.A., Vetterling, W.T., Numerical Recipes, Cambridge University Press. New York (1992).

Purbia, R., Paria, S., Yolk/shell nanoparticles: classifications, synthesis, properties, and applications. *Nanoscale* 7(47) (2015) 19789-19873.

Qiu, P., Kang, K., Kim, K., Li, W., Cui, M., Khim, J., Facile synthesis of uniform yolk–shell structured magnetic mesoporous silica as an advanced photo-Fenton-like catalyst for degrading rhodamine B. *RSC Adv.* 5(116) (2015) 96201-96204.

Roy, K., Moholkar, V.S., Sulfadiazine degradation using hybrid AOP of heterogeneous Fenton/persulfate system coupled with hydrodynamic cavitation. *Chem. Eng. J.* 386 (2020) 121294.

Shah, Y.T., Pandit, A.B., Moholkar, V.S., Cavitation reaction engineering. Springer Science & Business Media (2012).

Sivasankar, T., Paunikar, A.W., Moholkar, V.S., Mechanistic approach to enhancement of the yield of a sonochemical reaction. *AIChE J.* 53(5) (2007) 1132-1143.

Subramanian, G., Madras, G., Introducing saccharic acid as an efficient iron chelate to enhance photo-Fenton degradation of organic contaminants. *Water Res.* 104, (2016) 168-177.

Wang, Y., Sun, D., Liu, G., Jiang, W., Synthesis of Fe_3O_4@SiO_2@ZnO core–shell structured microspheres and microwave absorption properties. *Adv. Powder Technol.* 26(6) (2015) 1537-1543.

Wang, Z., Shao, Y., Gao, N., An, N., Degradation kinetic of dibutyl phthalate (DBP) by sulfate radical-and hydroxyl radical-based advanced oxidation process in UV/persulfate system. *Sep. Purif. Technol.* 195 (2018) 92-100.

Wu, X., Gu, X., Lu, S., Qiu, Z., Sui, Q., Zang, X., Miao, Z., Xu, M., Strong enhancement of trichloroethylene degradation in ferrous ion activated persulfate system by promoting ferric and ferrous ion cycles with hydroxylamine. *Sep. Purif. Technol.* 147 (2015) 186-193.

Wu, Y., Zhou, S., Qin, F., Zheng, K., Ye, X., Modeling the oxidation kinetics of Fenton's process on the degradation of humic acid. *J. Hazard. Mater.* 179(1-3) (2010) 533-539.

Xie, P., Ma, J., Liu, W., Zou, J., Yue, S., Li, X., Wiesner, M.R., Fang, J., Removal of 2-MIB and geosmin using UV/persulfate: contributions of hydroxyl and sulfate radicals. *Water Res.* 69 (2015) 223-233.

Xu, X.R., Li, X.Z., Degradation of azo dye Orange G in aqueous solutions by persulfate with ferrous ion. *Sep. Purif. Technol.* 72(1) 2010) 105-111.

Zhou, T., Zou, X., Mao, J., Wu, X., Decomposition of sulfadiazine in a sonochemical Fe^0-catalyzed persulfate system: parameters optimizing and interferences of wastewater matrix. *Appl. Catal., B* 185 (2016) 31-41.

Zou, X., Zhou, T., Mao, J., Wu, X. Synergistic degradation of antibiotic sulfadiazine in a heterogeneous ultrasound-enhanced Fe^0/persulfate Fenton-like system. *Chem. Eng. J.* 257 (2014) 36-44.

CHAPTER 5

4-Nitrophenol Degradation using Heterogeneous Fenton-Like System in Hydrodynamic Cavitation Reactor

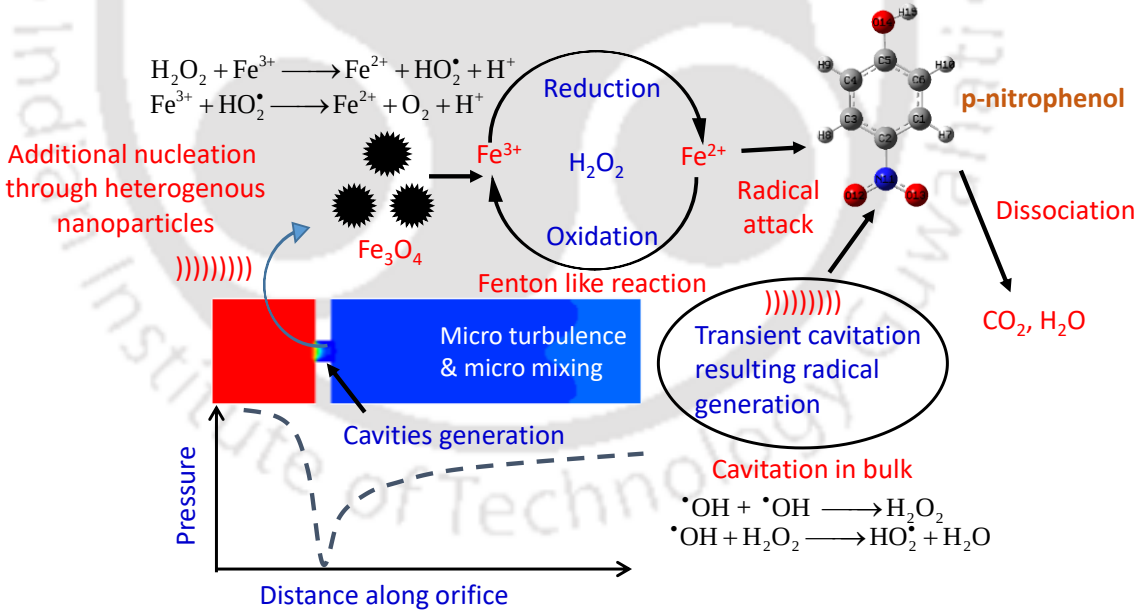

CHAPTER 5

4–NITROPHENOL DEGRADATION USING HETEROGENEOUS FENTON–LIKE SYSTEM IN HYDRODYNAMIC CAVITATION REACTOR

5.1 INTRODUCTION

In the previous chapters, we have seen the oxidative degradation of the pharmaceutical (drug) pollutant of sulfadiazine through hybrid advanced oxidation processes based on hydrodynamic and ultrasonic cavitation. The synergistic effects among the AOPs revealed through concurrent analysis of experiments and simulations were quite interesting. Hydrodynamic cavitation was able to enhance the leaching of ions at the iron oxide surface, while the yolk-shell nanoparticles with iron oxide core provided micro-reactors for degradation of the pollutant.

In order to assess the wider applicability of the techniques and underlying principles developed in previous chapters, we take ahead the theme with p-nitrophenol as the new organic compound as the biorefractory pollutant. As compared to the previous chapters, two new approaches have been adopted in this study – viz. the hydrodynamic (or flow) modelling of the cavitation phenomena to assess the cavitation intensity produced at different operating conditions and its manifestation in terms of PNP degradation, and secondly, determination of the possible reaction pathways between PNP molecule and the $^{\bullet}OH$ radical using the density functional theory (DFT) simulations. The

results of hydrodynamic flow modelling and DFT simulations have been linked to the experimental results and the reaction kinetics model (based on pseudo steady state for the radicals).

The concurrent analysis of hydrodynamic model, reaction kinetics model and experimental results have brought forth many new mechanistic features (and also the operational limitations) of the hybrid HC+Fenton system. The DFT analysis has provided insight into the chemistry of reactions between •OH radicals and PNP molecules.

5.2 MATERIAL AND METHODS

5.2.1 Experimental setup

The HC setup used for degradation of PNP has been described in the previous chapter. Among different orifice plates reported in previous chapter, the single–hole orifice plate was used for generation of cavitating flow. Fig. 5.1 shows the schematic representation of orifice plate. A computational study was performed in the same flow geometry.

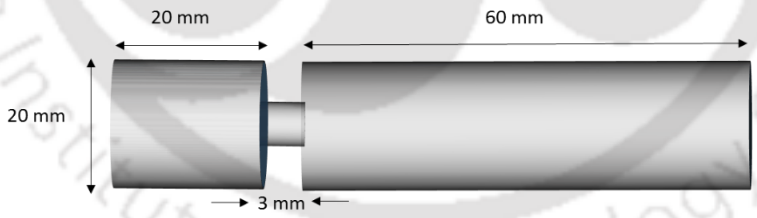

Figure 5.1: Schematic representation of orifice reactor

5.2.2 Reagent

The chemicals used in this study are: ferric chloride hexahydrate ($FeCl_3 \cdot 6H_2O$, > 99%, ACS grade), ethylene glycol (99%, LR grade), sodium acetate (CH_3COONa, 99%, AR grade), concentrated ammonia solution (30%, NH_4OH), hydrogen peroxide (30%, w/v), from Himedia and **s**odium citrate tribasic dihydrate ($Na_3Cit \cdot 2H_2O$, ≥ 99%, ACS grade)

and 4–Nitrophenol or paranitrophenol (PNP, ≥ 99%) from Sigma–Aldrich. Absolute ethanol (≥ 99%, AR Grade) was purchased from Changshu Yangyuan Chemical.

5.2.3 Synthesis of Fe_3O_4 nanoparticles

The magnetic Fe_3O_4 nanoparticles were prepared through a solvothermal method. Briefly, $FeCl_3 \cdot 6H_2O$ (2.60 g), $Na_3Cit \cdot 2H_2O$ (0.85 g) and CH_3COONa (4.80 g) were dissolved in 80 mL of ethylene glycol under magnetic stirring of 800 rpm. The mixture was stirred vigorously for 1 h at room temperature. The resulting homogeneous brown solution was transferred to a Teflon–lined stainless–steel autoclave (capacity 100 mL) and sealed to heat at 200°C for 10 h, and then allowed to cool to room temperature. The resultant precipitates were washed with deionized water several times until a neutral was attained and 3 times with ethanol. A magnet was used to separate the particles during washing. The obtained super–magnetic particle nano–particles were dried under vacuum at 60^0C overnight.

5.2.4 Analytical methods

XRD analysis of the magnetic nanoparticles (MNPs) was carried out at room temperature with X–Ray Diffractometer (Rigaku RINT 2500 TTRAX–III) equipped with Cu–Kα radiation (λ = 1.5406 Å) with nickel filter. Scans were recorded in the 2θ range = 10°–80° using step rate of 0.03° and counting time of 5°/min at 50 kV/100 mA. Surface and structural morphology of the MNPs was assessed with field emission scanning electron microscope (FE–SEM, Make: Zeiss, Model: Sigma). Brunauer–Emmett–Teller surface areas of the MNPs were obtained from nitrogen adsorption isotherms using a surface area and porosity analyser (BET, Model No.: Tristar II; Make: M/s Micromeritics, U.S.A.). Vibrating sample magnetometer (VSM) (Make: Lakeshore, Model: 7410 series) was employed to study the hysteresis loops and the magnetic properties of the magnetite

nanoparticles at 300 K. The residual concentration of PNP in reaction mixture was monitored in time step of 15 min with a UV/visible spectrophotometer (Shimadzu, Model no. UV–Vis–2600) at λ = 401 nm. Before measurement of absorption, the pH of the samples of reaction mixture was adjusted to 9 with 0.05 M of NaOH.

The concentrations of Fe^{2+} and Fe^{3+} in the samples were analysed with UV–Vis spectrophotometer (Shimadzu, Model No: UV–2600) at λ_{max} of 510 nm (Roy and Moholkar 2020, Standard methods for the examination of water and wastewater, 1915).

5.3 CFD MODEL FOR HYDRODYNAMIC CAVITATION

5.3.1 Governing equations

Given below are the governing equations for the multiphase (vapor–liquid) flow in hydrodynamic cavitation reactor. These equations in three–dimensional (3D) axisymmetric domain (single–hole orifice plate as shown in Fig. 5.1) are conservative form of Navier–Stokes equations with assumption of local equilibrium over short spatial length scales in multiphase flow (with two phases moving with different velocities).

To obtain an expression of the rate of net phase change (vaporization/ condensation), the two–phase continuity equations are written as follows (Singhal et al. 2002):

Liquid phase: $$\frac{\partial}{\partial t}\left[(1-\alpha)\rho_l\right]+\nabla.\left[(1-\alpha)\rho_l\bar{v}_l\right]=-R \quad (5.1)$$

Vapour phase: $$\frac{\partial}{\partial t}(\alpha\rho_v)+\nabla.(\alpha\rho_v\bar{v}_v)=R \quad (5.2)$$

Mixture: $$\frac{\partial}{\partial t}(\rho_m)+\nabla.(\rho_m\bar{v}_m)=0 \quad (5.3)$$

$$\rho_m=\rho_l\alpha_l+\rho_v\alpha_v,\quad \bar{v}_m=\left(\alpha_l\rho_l\bar{v}_l+\alpha_v\rho_v\bar{v}_v\right)/\rho_m$$

where, ρ_m = mixture density, $\bar{v}_m$ = mass average velocity, R (net phase change rate) = (R_e

$-R_c$), R_e = evaporation rate, R_c = condensation rate, α = volume fraction of phase. The subscripts *l* and *v* denote the liquid and vapor phases, respectively.

Summation of the momentum equations for the two individual phases yields:

$$\frac{\partial}{\partial t}\left(\rho_m \bar{v}_m\right)+\bar{v}_m.\nabla(\rho_m \bar{v}_m)=-\nabla P+\nabla.\left[\mu_m\left(\nabla \bar{v}_m+\nabla \bar{v}_m^T\right)\right]+\rho_m \bar{g} \qquad 5.4$$

μ_m is the dynamic viscosity of the two–phase mixture defined as:

$$\mu_m=\mu_l\alpha_l+\mu_v\alpha_v$$

5.3.2 Models for the turbulence and cavitation phenomena

Two–equation turbulence model in the form of realizable *k–ε* turbulence model has been used for determining the turbulent length and time scale by solving two separate transport equations. The term "realizable" means that the model satisfies certain mathematical constraints on the Reynolds stresses, consistent with the physics of turbulent flows (Mossaz et al. 2017). Compared with standard k–ε model, the realizable k–ε turbulence model provides better account of the physics of the two phase flow consisting of strong streamline curvatures and vortices. To improve the flow features such as strong streamline curvature, vortices, and rotation, Shih et al. proposed realizable k–ε model by intending new eddy–viscosity formula involving a variable C_μ and new model equation for dissipation (ε) based on the dynamic equation of the mean–square vorticity fluctuation (Bashir et al., 2011). For the liquid phase, the transport equation for the turbulent kinetic energy (*k*) is:

$$\frac{\partial}{\partial t}\left(\alpha_l\rho_l k_l\right)+\nabla.\left(\alpha_l\rho_l k_l\bar{v}_l\right)=\nabla.\left[\alpha_l\left(\mu_l+\frac{\mu_{t,l}}{\sigma_k}\right)\nabla.k_l\right]+\alpha_l G_{k,l} \qquad 5.5$$
$$+\alpha_l G_{b,l}-\alpha_l\rho_l\varepsilon_l-\alpha_l Y_M$$

and the transport equation for the turbulent dissipation rate (ε) is:

$$\frac{\partial}{\partial t}\left(\alpha_l \rho_l \varepsilon_l\right)+\nabla.\left(\alpha_l \rho_l \varepsilon_l \bar{v}_l\right)=\nabla.\left[\alpha_l\left(\mu_l+\frac{\mu_{t,l}}{\sigma_\varepsilon}\right)\nabla.\varepsilon_l\right]+\alpha_l \rho_l C_1 S_{\varepsilon l}$$

$$-\alpha_l \rho_l C_2 \frac{\varepsilon_l^2}{k_l+\sqrt{\nu_{t,l}\varepsilon_l}}+C_{1\varepsilon}\frac{\varepsilon}{k}C_{3\varepsilon}G_b \qquad 5.6$$

$$C_1=\max\left[0.43,\frac{\eta}{\eta+5}\right],\ \eta=S\frac{k}{\varepsilon}.$$

where G_k = generation of turbulence kinetic energy due to the mean velocity gradients, G_b = generation of turbulence kinetic energy due to buoyancy, Y_M = contribution of the fluctuating dilatation in compressible turbulence to the overall dissipation rate, σ_k and σ_ε are the turbulent Prandtl numbers for k and ε. The model constant are $C_{1\varepsilon}$ = 1.44, C_2 = 1.9, σ_k = 1.0, σ_ε = 1.2. Rest of the parameters, viz. $\mu_{t,l}$, $S_{\varepsilon l}$, and $G_{k,l}$ can be found in ANSYS FLUENT (ANSYS 2013).

Rayleigh–Plesset equation is a widely applied mathematical model for bubble dynamics and cavitation in liquid medium. This model has following underlying assumptions: no relative velocity (or no slip) between bubble and liquid phase, incompressible liquid, uniform bubble temperature (T_B) and pressure (P_B), uniform liquid viscosity and constant ambient temperature T_1 and pressure P_1. Rayleigh-Plesset is the 2nd order and 2nd degree ordinary differential equation given as:

$$\frac{P_B(t)-P_\infty(t)}{\rho_L}=R\frac{d^2R}{dt^2}+\frac{3}{2}\left(\frac{dR}{dt}\right)^2+\frac{4\nu_L}{R}\frac{dR}{dt}+\frac{2\sigma}{\rho_L R} \qquad 5.7$$

where $P_B(t)$ is bubble pressure and $P_\infty(t)$ is the instantaneous bulk pressure in the liquid. R is the instantaneous bubble radius. ρ_L and ν_L are liquid density and kinematic viscosity, respectively. σ is the surface tension of the liquid.

The cavitation models are based on the Rayleigh–Plesset equation, describing the growth

of a single vapour bubble in a liquid. The three cavitation models such as Singhal et al. model, Schnerr and Sauer model, Zwart–Gerber–Belamri model, have some serious concerns which are not consistent with the physics of two–phase flow. The model of Singhal et al. takes into account the noncondensable gases present in the system. It is also known as the Full Cavitation Model and is implemented in ANSYS Fluent since Version 6.1. Schnerr–Sauer cavitation model does not consider non–condensable gases and defines bubble number density in terms of total liquid volume instead of the total mixture volume. Zwart–Geber–Belamri model also does not consider non–condensable gases but following parameters viz. bubble radius, nucleation site volume fraction, evaporation and condensation coefficient has been considered (Rooze et al., 2012).

In the present work, Zwart–Geber–Belamri model was selected for the simulation of hydrodynamic cavitation reactor. In this model, total interphase mass transfer rate per unit volume (R) is calculated using the bubble density number (n). The expression of the net mass transfer is:

$$R = \frac{3\alpha\rho_v}{R_b}\sqrt{\frac{2}{3}\frac{P_v - P}{\rho_l}} \qquad 5.8$$

where R_b = bubble radius, P_v = vapour pressure. The unit volume mass transfer rate is only related to the vapor phase density (ρ_v). This equation is derived assuming bubble growth (evaporation). To apply it to the bubble collapse process (condensation), the following generalized formulation is used:

$$R_e = F\frac{3\alpha\rho_v}{R_b}\sqrt{\frac{2}{3}\frac{P_v - P}{\rho_l}}sign(P_v - P)$$

where F is empirical calibration coefficient. As the vapour volume fraction increases, the nucleation site density must decrease accordingly. To model this process, Zwart–Gerber–

Belamri proposed to replace α_v with $\alpha_{nuc}(1 - \alpha_v)$ in above equation. The final form of this cavitation model is:

$$\text{For } P \le P_v: \; R_e = F_{vap} \frac{3\alpha_{nuc}(1-\alpha_v)\rho_v}{R_b} \sqrt{\frac{2(P_v - P)}{3\rho_l}} \qquad 5.9$$

$$\text{For } P \ge P_v: \; R_c = F_{cond} \frac{3\alpha_v \rho_v}{R_b} \sqrt{\frac{2(P - P_v)}{3\rho_l}} \qquad 5.10$$

5.3.3 Numerical method

Commercial CFD tool ANSYS 14.5 is used for the numerical simulation of cavitating flow through the orifice (Fluent, 2013). These numerical approaches offer insights details of the velocity and pressure fields that cannot be analysed by the experimental method. The following assumptions are used in the CFD simulation: (1) incompressible, steady–state liquid flow; (2) fluid in continuum; (3) isothermal flow without heat transfer; (4) no slip velocity. 3D simulations were performed to assess the behaviour cavitating flow. Fine meshing was done near the throat and coarse meshing was done near the inlet and outlet boundaries. In meshing, hexahedral cells were generated in orifice plate with upto 2×10^5 cells. The enhanced wall treatment was used to account for the viscosity–affected near–wall region, taking liquid and vapour as the primary and secondary phases, respectively.

The segregated implicit pressure–based solver was used for simultaneous solutions of the governing continuity and momentum equations. SIMPLEC algorithm was utilized for pressure–velocity coupling to obtain quicker convergence using pressure–correction under–relaxation factor of 1.0 with linear pressure discretization and First Order Upwind for momentum and vapour. To achieve enhanced accuracy for stable convergence, Second Order Upwind was selected for turbulent kinetic energy and turbulent energy

dissipation rate. The convergence criteria in the present study was set to attain five orders (10^{-5}) of magnitude drop for all residuals, which are deemed sufficient for steady flow solutions (Kuldeep and Saharan, 2016).

5.4 KINETIC MODEL FOR PNP DEGRADATION

The proposed kinetic model consists of 24 reactions as listed in Table 5.1. The kinetic model is based on hypothesis that PNP degradation occurs via $^{\bullet}OH$ radicals. $^{\bullet}OH$ radicals in the reaction medium are generated through the Fenton reactions as well as transient collapse of the cavitation bubbles generated at the orifice plate in HC reactor. For the simplicity, the Fenton reaction system has been categorized into two sets of reactions, viz. bulk Fenton reaction, other bulk reaction H_2O_2.

The mass balances for all species involved in the reaction system are given below. These mass balances are based on two assumptions: (1) all reactions are 1st order with respect to the species involved in it, and (2) generated $^{\bullet}OH$ produced in large excess.

System: HC + Fenton:

$$-\frac{d[PNP]}{dt} = k_{17}[PNP][^{\bullet}OH] \tag{5.11}$$

$$\begin{aligned}\frac{d[^{\bullet}OH]}{dt} &= k_1[Fe^{2+}][H_2O_2] - k_3[Fe^{2+}][^{\bullet}OH] - k_8[^{\bullet}OH][H_2O_2] \\ &+ k_9[HO_2^{\bullet}][H_2O_2] + k_{10}[O_2^{\bullet-}][H_2O_2] - k_{12}[^{\bullet}OH][H_2O_2] \\ &- k_{13}[O_2^{\bullet-}][^{\bullet}OH] - k_{14}[HO_2^{\bullet}][^{\bullet}OH] - k_{15}[^{\bullet}OH][^{\bullet}OH] - k_{17}[PNP][^{\bullet}OH]\end{aligned} \tag{5.12}$$

$$\begin{aligned}\frac{d[HO_2^{\bullet}]}{dt} &= k_2[Fe^{3+}][H_2O_2] - k_4[Fe^{3+}][HO_2^{\bullet}] - k_5[Fe^{2+}][HO_2^{\bullet}] \\ &+ k_8[^{\bullet}OH][H_2O_2] - k_9[HO_2^{\bullet}][H_2O_2] - k_{11}[O_2^{\bullet-}][HO_2^{\bullet}] \\ &- k_{14}[HO_2^{\bullet}][^{\bullet}OH] - k_{16}[HO_2^{\bullet}][HO_2^{\bullet}]\end{aligned} \tag{5.13}$$

$$\frac{d\left[O_2^{\bullet-}\right]}{dt} = -k_6\left[Fe^{3+}\right]\left[O_2^{\bullet-}\right] - k_7\left[Fe^{2+}\right]\left[O_2^{\bullet-}\right] - k_{10}\left[O_2^{\bullet-}\right]\left[H_2O_2\right] - k_{11}\left[O_2^{\bullet-}\right]\left[HO_2^{\bullet}\right] + k_{12}\left[{}^{\bullet}OH\right]\left[H_2O_2\right] - k_{13}\left[O_2^{\bullet-}\right]\left[{}^{\bullet}OH\right] \quad 5.14$$

$$\frac{d\left[H_2O_2\right]}{dt} = -k_1\left[Fe^{2+}\right]\left[H_2O_2\right] - k_2\left[Fe^{3+}\right]\left[H_2O_2\right] - k_8\left[{}^{\bullet}OH\right]\left[H_2O_2\right] - k_9\left[HO_2^{\bullet}\right]\left[H_2O_2\right] - k_{10}\left[O_2^{\bullet-}\right]\left[H_2O_2\right] - k_{12}\left[{}^{\bullet}OH\right]\left[H_2O_2\right] + k_{15}\left[{}^{\bullet}OH\right]\left[{}^{\bullet}OH\right] + k_{16}\left[HO_2^{\bullet}\right]\left[HO_2^{\bullet}\right] \quad 5.15$$

$$\frac{d\left[Fe^{2+}\right]}{dt} = -k_1\left[Fe^{2+}\right]\left[H_2O_2\right] + k_2\left[Fe^{3+}\right]\left[H_2O_2\right] - k_3\left[Fe^{2+}\right]\left[{}^{\bullet}OH\right] + k_4\left[Fe^{3+}\right]\left[HO_2^{\bullet}\right] - k_5\left[Fe^{2+}\right]\left[HO_2^{\bullet}\right] + k_6\left[Fe^{3+}\right]\left[O_2^{\bullet-}\right] - k_7\left[Fe^{2+}\right]\left[O_2^{\bullet-}\right] \quad 5.16$$

$$\frac{d\left[Fe^{3+}\right]}{dt} = k_1\left[Fe^{2+}\right]\left[H_2O_2\right] - k_2\left[Fe^{3+}\right]\left[H_2O_2\right] + k_3\left[Fe^{2+}\right]\left[{}^{\bullet}OH\right] - k_4\left[Fe^{3+}\right]\left[HO_2^{\bullet}\right] + k_5\left[Fe^{2+}\right]\left[HO_2^{\bullet}\right] - k_6\left[Fe^{3+}\right]\left[O_2^{\bullet-}\right] + k_7\left[Fe^{2+}\right]\left[O_2^{\bullet-}\right] \quad 5.17$$

The three–radical species in the reaction system, ${}^{\bullet}OH$, $O_2^{\bullet-}$ and $HO_2^{\bullet}$ are extremely reactive and unstable. In view of this, we have assumed pseudo–steady state for these species – in which their net concentration in the reaction medium remains constant.

$$\left[{}^{\bullet}OH\right] = \frac{k_1\left[Fe^{2+}\right]\left[H_2O_2\right] + k_9\left[HO_2^{\bullet}\right]\left[H_2O_2\right] + k_{10}\left[O_2^{\bullet-}\right]\left[H_2O_2\right]}{k_3\left[Fe^{2+}\right] + k_8\left[H_2O_2\right] + k_{12}\left[H_2O_2\right] + k_{13}\left[O_2^{\bullet-}\right] + k_{14}\left[HO_2^{\bullet}\right] + k_{15}\left[{}^{\bullet}OH\right] + k_{17}\left[PNP\right]} \quad 5.18$$

$$\left[HO_2^{\bullet}\right] = \frac{k_2\left[Fe^{3+}\right]\left[H_2O_2\right] + k_8\left[{}^{\bullet}OH\right]\left[H_2O_2\right]}{k_4\left[Fe^{3+}\right] + k_5\left[Fe^{2+}\right] + k_9\left[H_2O_2\right] + k_{11}\left[O_2^{\bullet-}\right] + k_{14}\left[{}^{\bullet}OH\right] + k_{16}\left[HO_2^{\bullet}\right]} \quad 5.19$$

$$\left[O_2^{\bullet-}\right] = \frac{k_{12}\left[{}^{\bullet}OH\right]\left[H_2O_2\right]}{k_6\left[Fe^{3+}\right] + k_7\left[Fe^{2+}\right] + k_{10}\left[H_2O_2\right] + k_{11}\left[HO_2^{\bullet}\right] + k_{13}\left[{}^{\bullet}OH\right]} \quad 5.20$$

The ordinary differential was solved after substitution of pseudo–steady state expressions for radical species as: eqs. 5.18–5.20 for HC + Fenton. Runge–Kutta 4th order – 5th order method (adaptive step size) method (Press et al., 1992) was employed for numerical solution. The values of kinetic constants k_1 to k_{17} were borrowed from literature and are

listed in Table 5.1.

Table 5.1: Reaction network for kinetic modelling of p–nitrophenol degradation

Sr. No.	Reaction	k ($M^{-1}s^{-1}$)	References
	Fenton reactions		
R1	$Fe^{2+} + H_2O_2 \longrightarrow Fe^{3+} + {}^{\bullet}OH + OH^-$	70	Roy and Moholkar (2020)
R2	$Fe^{3+} + H_2O_2 \longrightarrow Fe^{2+} + H^+ + HO_2^{\bullet}$	0.02	Kusic et al. (2006)
R3	$Fe^{2+} + {}^{\bullet}OH \longrightarrow Fe^{3+} + OH^-$	3.2×10^8	Kang et al. (2002)
R4	$Fe^{3+} + HO_2^{\bullet} \longrightarrow Fe^{2+} + O_2 + H^+$	3.1×10^5	Kang et al. (2002)
R5	$Fe^{2+} + HO_2^{\bullet} \longrightarrow Fe^{3+} + HO_2^-$	1.2×10^6	Kusic et al. (2006)
R6	$Fe^{3+} + O_2^{\bullet-} \longrightarrow Fe^{2+} + O_2$	1.5×10^8	Burbano et al. (2005)
R7	$Fe^{2+} + O_2^{\bullet-} \longrightarrow Fe^{3+} + O_2$	1×10^7	Burbano et al. (2005)
	Other bulk reactions		
R8	${}^{\bullet}OH + H_2O_2 \longrightarrow HO_2^{\bullet} + H_2O$	3.3×10^7	Roy and Moholkar (2020)
R9	$HO_2^{\bullet} + H_2O_2 \longrightarrow H_2O + {}^{\bullet}OH + O_2$	3	Crittenden et al. (1999)
R10	$O_2^{\bullet-} + H_2O_2 \longrightarrow {}^{\bullet}OH + OH^- + O_2$	0.13	Crittenden et al. (1999)
R11	$O_2^{\bullet-} + HO_2^{\bullet} \longrightarrow HO_2^- + O_2$	9.7×10^7	Kusic et al. (2011)
R12	${}^{\bullet}OH + H_2O_2 \longrightarrow O_2^{\bullet-} + H_2O$	2.7×10^7	Kusic et al. (2011)
R13	$O_2^{\bullet-} + {}^{\bullet}OH \longrightarrow HO^- + O_2$	1.01×10^{10}	Gallard and Laat (2000)
R14	$HO_2^{\bullet} + {}^{\bullet}OH \longrightarrow H_2O + O_2$	0.71×10^{10}	Gallard and Laat (2000)
R15	${}^{\bullet}OH + {}^{\bullet}OH \longrightarrow H_2O_2$	5.3×10^9	Burbano et al. (2005)
R16	$HO_2^{\bullet} + HO_2^{\bullet} \longrightarrow H_2O_2 + O_2$	8.5×10^5	Burbano et al. (2005)
	Gross degradation of SDZ		
R17	$PNP + {}^{\bullet}OH \longrightarrow H_2O + CO_2 + products$	1.08×10^9	Mei et al. (2020)

5.5 DFT SIMULATIONS FOR PNP DEGRADATION

Gaussian 09 software was used to study the possible reaction pathways of oxidative degradation of 4–nitrophenol induced by hydroxyl radicals. The geometry optimizations were carried out using the exchange–correlation functional B3LYP (Becke's three–parameter Lee–Yang–Parr) with 6–31g(d) level of theory. The optimizations were followed by frequency computations at the same level of theory to confirm that the stationary points are minima (no imaginary frequencies) and each of the transition state

(TS) structures has only one imaginary frequency. The reaction pathways were subjected to intrinsic reaction coordinate (IRC) analysis in order to trace their paths and to confirm the optimized TS connects the correct reactant and product.

5.6 RESULT AND DISCUSSION

5.6.1 Characterization of catalysts

Fig. 5.2 (A) shows the surface morphology of the as–synthesized Fe_3O_4 microspheres. The FE–SEM image of the synthesized catalysts depicts the spherical size and the average diameter is around 250 nm without any aggregation of particle. The surface area of Fe_3O_4 nanoparticle was measured using the Brunauer–Emmett–Teller (BET) method and the typical N_2 adsorption–desorption isotherm at 77 K and the pore size distribution by the Barrett–Joyner–Halenda (BJH) method as shown in Fig. 5.2 (B). The resultant Fe_3O_4 nanospheres possess a high BET surface area of 90.10 m^2/g with a pore diameter of 3.55 nm and large pore volume 0.039 cm^3/g. Moreover, the catalyst can work in a wide pH range (3–10) and exhibit an excellent reusability.

Fig. 5.2(C) shows the XRD powder diffraction patterns of Fe_3O_4 MNPs. For Fe_3O_4, the characteristic diffractions at 2θ (crystal face) = 30.1° (2 2 0), 35.5° (3 1 1), 43.1° (4 0 0), 53.5° (4 2 2), 57.0° (5 1 1) and 62.6° (4 4 0) suggest face centered cubic (FCC) structure, which matched well with the database of magnetite in the Joint Committee on Powder Diffraction Standards (JCPDS 65–3107) file. The magnetic properties of the as–synthesized products, i.e. magnetic hysteresis curves of nanoparticles measured in the range of –15.0 to 15.0 kOe magnetic field at room temperature are shown in Fig. 5.2 (D). The saturation magnetization (M_S) of Fe_3O_4 nanoparticles is 58.92 emu/g.

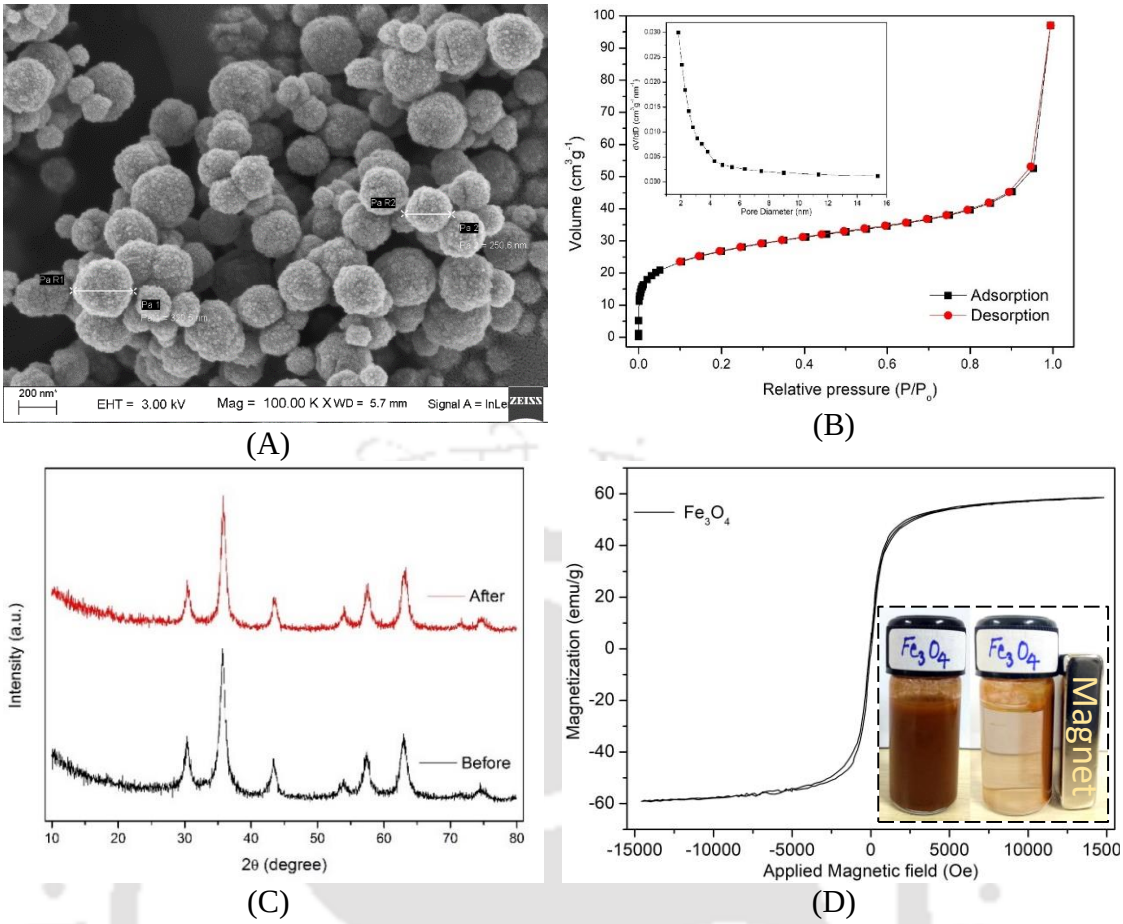

Figure 5.2: (A) FE–SEM images (B) BET surface area (C) XRD (D) VSM of Fe_3O_4 nanoparticles

5.6.2 Computational fluid dynamics (CFD) study of HC reactor

The ability of HC in the degradation of PNP depends on the cavitation intensity produced in the reactor, which in turn depends on the operating parameters like inlet pressure and cavitation number. The intensity of the collapse of individual cavitation bubble depends upon the rate of pressure recovery in the downstream region of the orifice where flow expansion occurs. The increase in the pressure upstream of the orifice (or the inlet pressure) increases both pressure head loss and final recovery pressure. This in turn increases the peak temperature and pressure conditions reached during the transient collapse of cavitation bubble. It also should be noted that the increase in inlet pressure, if operated with constant flow rate increases the cavitation number (Ebrahimi et al., 2017).

This gives an interesting relationship between the cavitation number and the generated collapse pressure. A rise in inlet pressure beyond a threshold may lead to the generation of very large number of cavitation bubbles and coalescence among them leading to bubble cloud formation in the downstream region (Moholkar and Pandit, 1997). This phenomenon is called choked cavitation. Once choking occurs, a thick vaporous cavity cloud is generated throughout the downstream section of orifice that reduces the length of the cavitation zone. This essentially means that there is an optimum inlet pressure corresponding to maximum cavitation intensity at constant flow rate (Moholkar and Pandit, 2001).

Contour plot shown in Fig. 5.3(A) depicts that increase in the inlet pressure from 2 to 10 atm resulted in rise of length of cavitation zone, followed by reduction at even higher pressures. This result was attributed to collapse of the cavitation bubble with the highest intensity at inlet pressure of 10 atm. Fig. 5.3 (C) also shows sudden drop of bulk liquid pressure near the throat of orifice plate, with further recovery to 1 atm in downstream region. Similarly, the vapour volume fraction (VVF) shown in Fig. 5.3 (B) also reveals proportionate variation with inlet pressure. For 2 atm inlet pressure, no VVF was observed near throat. The inception of cavitation zone in the downstream region was seen from inlet pressure of 3 atm. Pressure contours around the orifice plate for different inlet pressures shown in Fig. 5.3(A) also confirm the above trend in the cavitation zone.

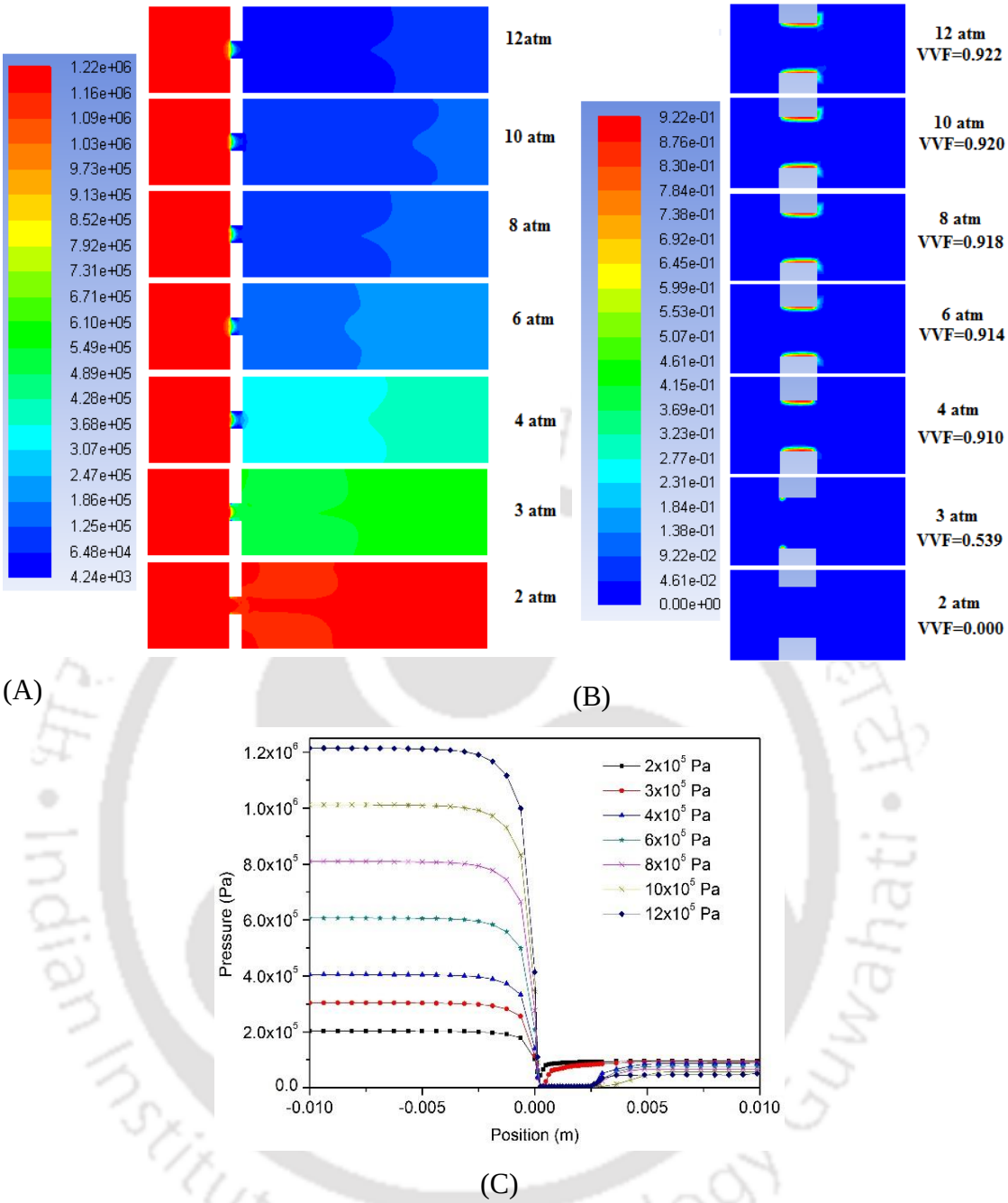

Figure 5.3: (A) Pressure contours (B) Vapour Volume Fraction (VVF) contours (C) Pressure plot at different inlet pressures across the orifice plate

5.6.3 Degradation of PNP

5.6.3.1 Effect of inlet pressure

The effect of inlet pressure on PNP degradation was assessed in the range 2 – 12 atm. A maximum degradation of 43.03% was obtained at inlet pressure of 8 atm. Thereafter, reduction in the degradation was seen due to the coalescence of bubbles resulting in the

formation of bubble clouds. The intensity of the cavitation bubble collapse increased proportionately with inlet pressure, which in turn enhanced the production of radicals through dissociation of water molecules.

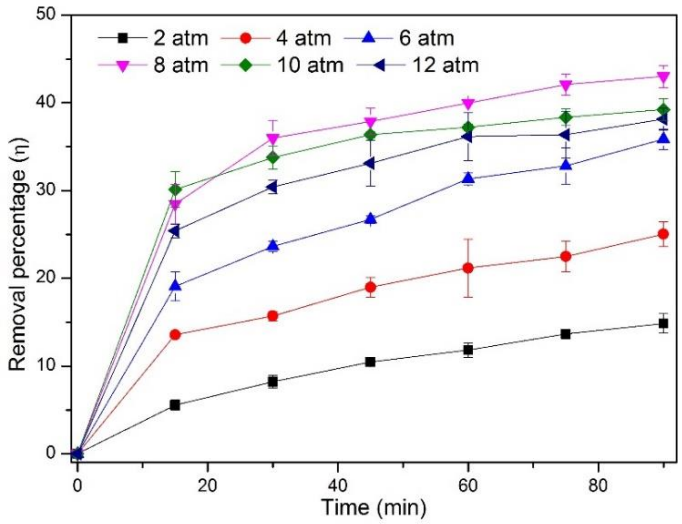

Figure 5.4: Effect of inlet pressure on the rate of degradation of PNP using hydrodynamic cavitation (initial concentration of PNP = 25 ppm, temperature = 35°C)

5.6.3.2 Effect of initial concentration

The effect of initial concentration of PNP on the extent of degradation has been investigated with hydrodynamic cavitation as individual process without any other supporting AOP. The experiments were performed at four different initial concentrations of 20, 25, 30 and 35 ppm. Fig. 5.5 depicts the variation of extent of degradation with the initial concentration. It can be seen that the extent of degradation decreases with an increase in the initial concentration of PNP. The extent of degradation decreased from 46.58% to 32.26% with increasing initial concentration from 20 to 35 ppm. The absolute degradation for 20 and 35 ppm initial concentration was 9.11 and 11.29 ppm, respectively. Rise in extent of degradation with initial concentration is probably a consequence of enhanced interaction among radicals and the pollutant molecules at higher initial concentration of the substrate, which results in greater utilization of the

oxidizing radicals towards the degradation of the pollutant (Sivasankar and Moholkar 2009, Sun and Lemley, 2011, Zhang et al., 2003, Capocelli et al., 2014).

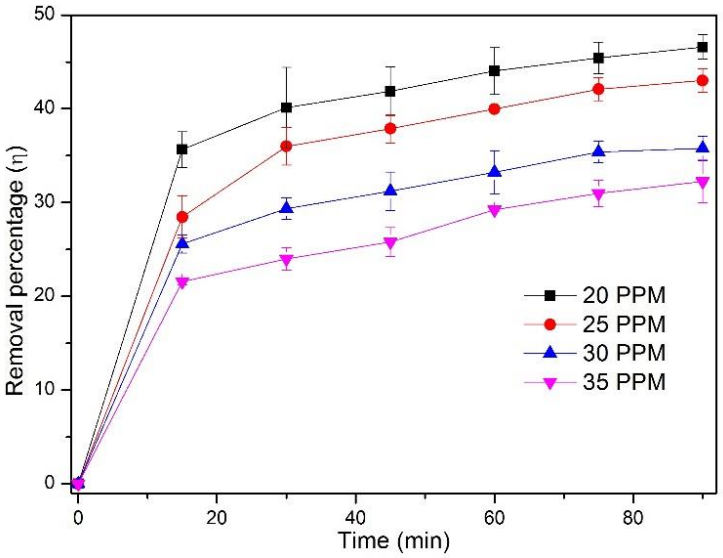

Figure 5.5: Effect of initial concentration on PNP degradation (inlet pressure = 8 atm, temperature = 35 °C)

5.6.3.3 PNP Degradation with H_2O_2 + hydrodynamic cavitation

In order to enhance production of •OH radicals, hydrogen peroxide was added to the reaction mixture. The quantity of H_2O_2 was varied in proportion of the molar concentration of PNP ranging from 1:0 to 1:350 (PNP: H_2O_2). The results depicted in Fig. 5.6 reveal that rate of PNP degradation was enhanced with addition of H_2O_2 to system. This is due to the decomposition of hydrogen peroxide into hydroxyl radicals causing higher degradation of PNP. The highest degradation of 65.03% was observed for molar ratio of PNP:H_2O_2 = 1:300. With further rise in H_2O_2 concentration, however, the degradation reduced. A plausible reason for this effect is the scavenging of •OH radicals by excessive quantity of H_2O_2, which reduces the utilization of the radicals for degradation of PNP (Arrojo and Benito, 2008; Capocelli et al., 2014a; Capocelli et al., 2014b; Capocelli et al., 2015).

To avoid scavenging of oxidizing radicals, H_2O_2 addition was carried out in stepwise manner (0, 30 and 60 min) with total quantity of H_2O_2 addition remaining the same. This protocol resulted in minor rise in degradation from 60.27% to 68.26% - which is probably a consequence of reduced scavenging effect due to relatively smaller instantaneous concentration of H_2O_2 in the reaction mixture.

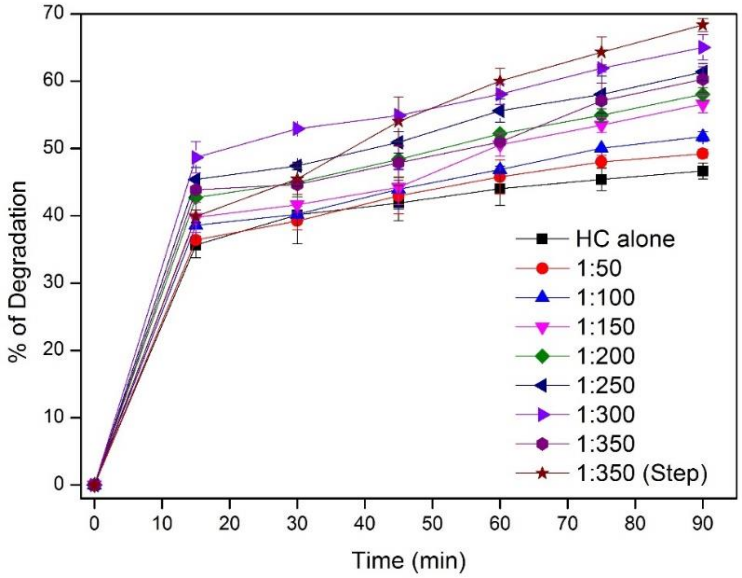

Figure 5.6: Effect of H_2O_2 loading on PNP degradation (temperature = 35 °C, inlet pressure = 8 atm, initial concentration = 20 ppm)

5.6.3.4 PNP degradation with Fenton + hydrodynamic cavitation

Efficacy of hybrid AOP HC + Fenton for degradation of PNP has been investigated by addition of Fenton's reagents (heterogeneous) to the reaction solution, viz. solid Fe_3O_4 nanoparticles and H_2O_2 at molar ratio (Fe_3O_4:H_2O_2) ranging from 1:25 to 1:125 with quantity of Fe_3O_4 fixed at 100 mg/L. Fig. 5.7 depicts the degradation patterns of PNP for this system. The highest 76.48% degradation of PNP was obtained for molar ratio of Fe_3O_4:H_2O_2 as 1:100. The combination of HC + Fenton enhanced the generation of reactive oxygen species (ROS) due to the conversion of Fe^{3+} to Fe^{2+} or vice versa into the aqueous solution. Reduced PNP degradation for Fe_3O_4:H_2O_2 molar ratio of 1:125

results in reduced degradation due to the scavenging of radicals by H_2O_2. Enhanced concentration of H_2O_2 in solution (at fix loading of Fe_3O_4) could promote the rate of surface leaching of iron oxides particles, which results in enhanced production of •OH radicals. However, this effect is offset by the scavenging of radicals, which results in reduced degradation.

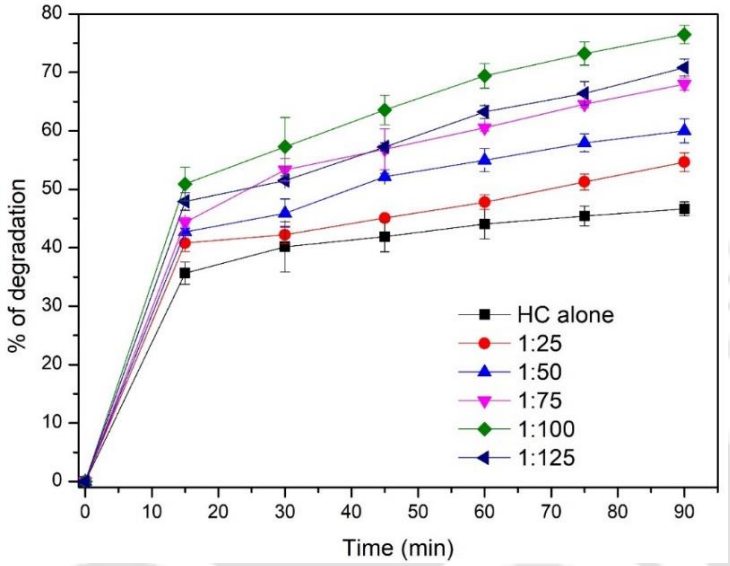

Figure 5.7: Effect of different loadings of Fenton reagent on PNP degradation (temperature = 35 °C, inlet pressure = 8 atm, initial concentration = 20 ppm)

5.6.3.5 Effect of pH on PNP degradation

Removal of PNP was investigated at three pH levels of 3, 7 and 10 at optimum loading of Fenton catalysts. As evident from degradation profiles shown in Fig 5.8, the apparent degradation reduces with increasing pH as 78.78%, 72.57% and 66.09% for pH 3, 7 and 11, respectively. Under strong alkaline conditions, the CO_2 generated during degradation will be converted into CO_3^{2-} and HCO_3^-, which have high reactivity with •OH with rate constants as 3.9×10^8 $M^{-1}s^{-1}$ and 8.5×10^8 $M^{-1}s^{-1}$, respectively (Zhou et al. 2016, Daneshvar et al. 2007, Krishnan et al., 2006). Another plausible reason for this effect could be the dissociation of H_2O_2 to form HO_2^- under the alkali conditions. The HO_2^-

ions have higher reactivity with •OH than H_2O_2, which again reduces the utilization of •OH radicals for PNP degradation. This essentially explains as why the hybrid AOP of HC+Fenton is more effective in the degradation of PNP in acidic pH conditions than the alkaline conditions.

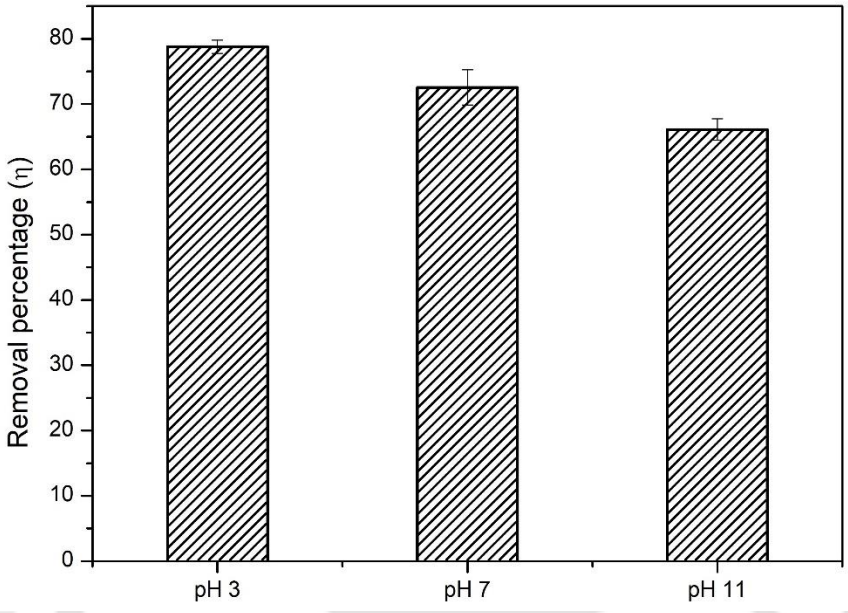

Figure 5.8: Effect of pH on degradation of PNP (temperature=35 °C, inlet pressure=8 atm, initial concentration=20 ppm, Fe_3O_4:H_2O_2=1:100)

5.6.3.6 Regeneration, reuse and stability of the Fe_3O_4 catalysts

The regeneration and stability of the catalyst is one of the important issues in practical operation. In order to assess the potential regeneration and reuse of the Fe_3O_4 magnetic nanoparticles (MNPs) as heterogeneous Fenton catalysts, these particles were separated from the reaction solution at the end of the experiment using a normal magnet and reused for next experiment. The stability of Fe^{3+} species on catalyst surface is crucial for its leaching into the solution and reduction to Fe^{2+}. As compared to the fresh Fe_3O_4 particles, >75% degradation was retained after five cycles of experiments, which suggested stable activity of MNPs. Marginal reduction in PNP removal efficiency with recycled catalyst might be a result of agglomeration of particles during treatment that leads to reduction in

surface area or permanent deposits of certain contaminants/products of degradation on the catalyst surface – which also hampers the rate of leaching at catalyst surface.

Number of recycle	1st	2nd	3rd	4th	5th
% degradation	77.98	78.57	76.41	75.89	75.37

The concentration of iron species viz. Fe^{3+}, Fe^{2+} and total dissolved iron were quantified in reaction solution using standard methods as shown in Fig. 5.9. As noted previously, leaching of Fe^{3+} ions at the surface of Fe_3O_4 particles occurs due to which concentration of soluble iron species increases. Some of these Fe^{3+} ions undergo Fenton reactions to convert into the Fe^{2+} ions. Nonetheless, the concentration of Fe^{3+} species in the solution at any instance was at least 2× larger than the Fe^{2+} concentration.

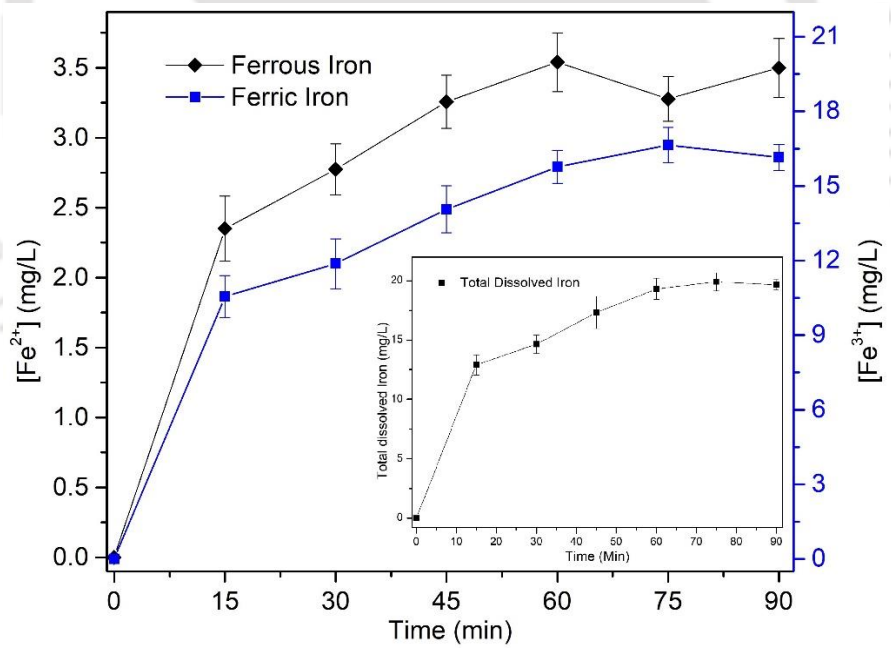

Figure 5.9: Concentrations of Fe^{3+}, Fe^{2+} and total dissolved iron oxide

5.6.3.7 Validation of CFD results with experimental

In this section, we correlate the results of CFD simulations with experimental results of PNP degradation. The intensity of cavitation produced in the system at different inlet

pressures can be quantified using dimensionless parameter of cavitation number. Theoretically, cavitation inception occurs at $C_v = 1$. However, in practical situations, cavitation can occur for condition of $C_v > 1$ due to release of dissolved gases in the throat region downstream of orifice or presence of particulate matters in the system (such as the iron oxide nanoparticles in the present study). Fig. 5.10 shows a plot of variation in cavitation number – both experimentally observed and determined with CFD simulations – with inlet pressure. It could be seen that there is some discrepancy between the experimentally observed cavitation number and the one calculated with CFD simulations. This could be a consequence of additional pressure head loss in the flow loop due to which actual inlet pressure at the orifice is somewhat reduced than pressure indicated in the pressure gauge. The percentage degradation of PNP obtained at these operating conditions is also plotted in Fig. 5.10. It could be seen that the percentage degradation of PNP varies inversely with C_v and reaches a maxima till inlet pressure of 8 atm. This is very much in consistence with the arguments presented earlier that the cavitational intensity produced in the hydrodynamic cavitation reactor and the degradation of PNP varies proportionately with the inlet pressure. The reduction in degradation beyond inlet pressure of 8 atm is attributed to chocked cavitation that results in formation of cavitation bubble clouds. This feature is not accounted for the in the CFD model which still predicted reduction in C_v indication of higher cavitation intensity.

5.6.3.8 Validation of kinetic model vis-à-vis experimental results

Prior to comparison and experimental profiles, we would like to point out that the kinetic model used in this work applies for the Fenton reactions in homogeneous phase – while in reality the AOP system used in experiments comprises of heterogeneous Fenton reagents with iron oxide nanoparticles. The concentration of the Fe^{2+}/Fe^{3+} ions in the

reaction solution depends on rate of leaching at the surface of the solids. Fig. 5.11 compares the simulated profiles of PNP degradation against the experimental profiles of degradation. As the rate of leaching of Fe^{2+}/Fe^{3+} ions at surface of solids is not known precisely, we have carried out simulations with initial $[Fe^{2+}]/[H_2O_2]$ ratio in the solution as manipulation parameter with all other parameters held at their optimum values. It could be seen that the closest match between experimental and simulated profiles of degradation (with $R^2 = 0.92$) was obtained for initial $[Fe^{2+}]/[H_2O_2]$ ratio = 5. Despite this, the PNP degradation of 61.26% predicted by simulations smaller than the experimental degradation of 78.78%. A possible and plausible explanation for this discrepancy can be given as follows: In the initial phase of PNP degradation, i.e. the first 30 min of treatment, the reactions occur very fast due to high concentration of oxidizing radicals resulting in rapid fall of PNP concentration. This trend is evident from both experimental and simulations profiles of PNP for initial 30 min of treatment. The simulated profile of PNP, however, does not show any significant reduction in concentration beyond 30 min. A probable cause for this result could be in reduction in the H_2O_2 concentration in the solution that reduces rate of Fenton reactions and $^{\bullet}OH$ radical production, which is manifested in terms of nearly constant PNP concentration in the solution beyond 30 min of treatment, as predicted by simulations. This conjecture also indicates that PNP degradation beyond 30 min is affected by the hydrodynamic cavitation alone.

On the contrary, the experimental profile of PNP shows continuous fall in concentration (although at reduced rate) till end of the treatment (i.e. 90 min), and thus the final concentration of PNP in solution is much smaller than that predicted by simulations. The degradation of PNP beyond 30 min is essentially attributed to $^{\bullet}OH$ radicals produced through hydrodynamic cavitation. However, the extent of production and population of these radicals in the system is expected to be lower than that in hybrid

AOP of HC + Fenton (prevalent in first 30 min of treatment), due to which the rate of degradation is reduced.

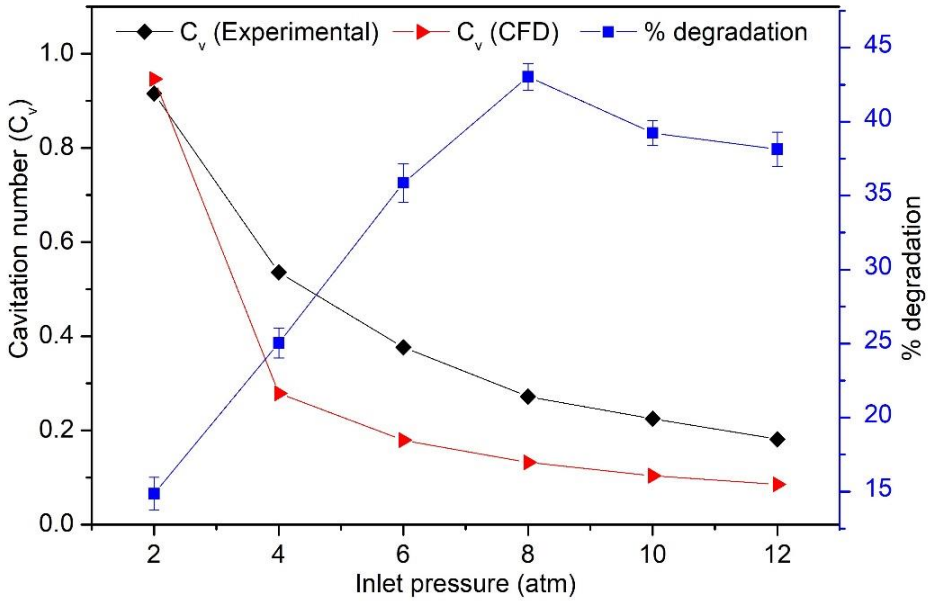

Figure 5.10: Experimental validation of CFD results – variation of percentage degradation with inlet pressure and cavitation number

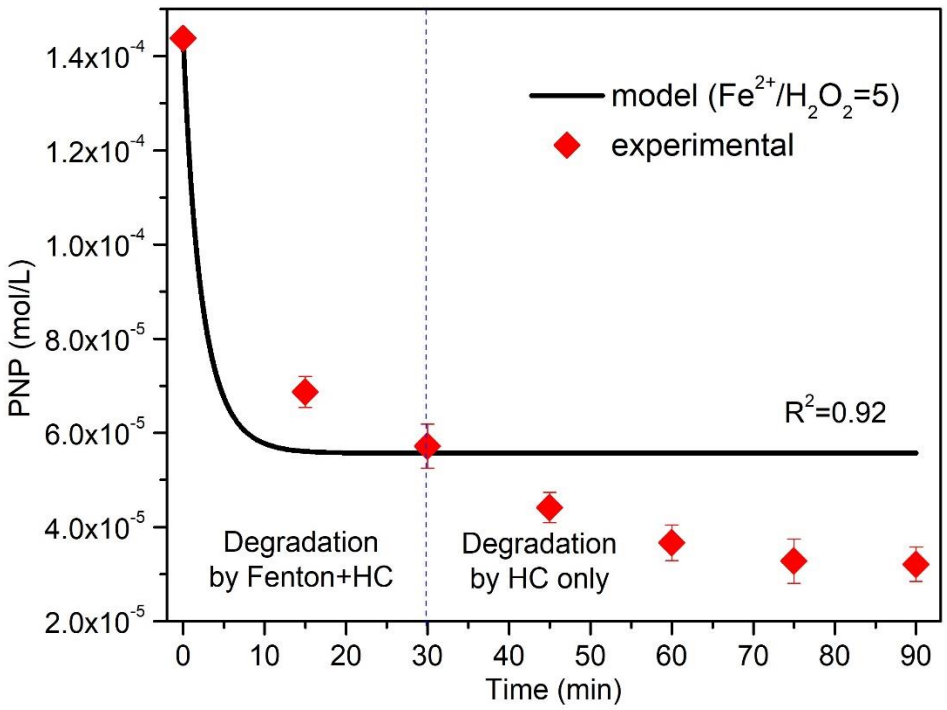

Figure 5.11: Validation of reaction kinetic modelling of PNP degradation

5.6.3.9 DFT simulation for degradation pathway of PNP

DFT simulations were performed for the reactions of •OH mediated oxidative degradation of PNP. In a relatively simple approach, two possible pathways can be identified for the reaction of PNP with •OH radicals: (1) addition of •OH radical on benzene ring, and (2) H–abstraction reactions (•OH radicals abstracting the H atoms form PNP) (Mei et al., 2020; Li et al., 2015). The addition of •OH radicals to the benzene ring may take place at three sites (*ortho*, *meta*, *para* carbon) due to the symmetrical structure of PNP. Fig. 5.12 represents the bond properties and Mulliken charges of optimized structure of PNP. The vulnerable site for the oxidation can be identified from bond lengths and atomic charges. Two bonds, viz. C5-O14 and C2-N11 have relatively higher lengths of 1.359 and 1.462 Å, respectively, which also simultaneously corresponds to larger negative charge on O12, O13, and O14 atoms. Due to higher negative charge on carbon atom, *ortho* and *meta* positions on PNP molecule can also be the vulnerable sites for the attack of •OH radicals (Wang et al., 2011). For further justification of this hypothesis, free activation energies were calculated for all possible reaction sites. The detailed mechanisms of the above reactions are represented in Fig. 5.13 with forward and backward activation energies.

Hydroxyl addition reactions: Pathways 1–3 (Fig. 5.13) represent the addition of •OH radicals to benzene ring. Initially, paths 1, 2 and 3 will form the pre–complexes, viz. IM1_1, IM1_2, IM2_1, IM2_2, IM3. Each pathway generates corresponding •OH·– adduct intermediates containing a free electron, and destroys the aromaticity of PNP. In the oxidation of PNP with •OH radical, three major products were formed as 4–nitrocatechol, 4–nitroresorcinol and hydroquinone. The DFT simulations show that the energy barrier of pre-reactive complexes was lower than the energy of reactant, which

would influence the energy barriers for the reaction. This observation was also reported in previous literature (Alvarez-Idaboy et al., 2001; Uc et al., 2006; Wu et al., 2017). The position of the •OH radical in the pre-reactive complex was very far from the carbon atom (distance between C6 to •OH radical = 2.577 Å) of *ortho* position. Further reaction will adduct the stable compound as P1_1 with forward activation energy 2.46 Kcal/mol. Figs. 5.14, 5.15 and 5.16 represent the pre–reactive complexes, transition state and adduct complex during the oxidation, respectively. Product P1_1 will further react with dissolved oxygen present in reaction system. This pathway proceeds to generate 4-nitrocatechol (forward activation energy = 9.87 Kcal/mol) compound during oxidation of PNP. Similar reaction pathway will be followed for the production of 4-nitroresorcinol on the attack of •OH radical on meta position. Attack of •OH radical on the para position results in formation of the adduct compound hydroquinone. Relatively low activation energy of 2.46 Kcal/mol made path 1 more favourable for reaction. The nitro group of PNP is electron–withdrawing while hydroxyl group is electron–donating, which essentially renders the ortho–position as favourable site for attack. Fig. 5.17 (A) shows the relative energy of reaction pathways involving the •OH radical. Fig. 5.17 (C) shows the intrinsic reaction coordinate (IRC) to confirm the optimized structure of TS1_1 that connects the reactant and product.

Hydrogen abstraction reactions: Three hydrogen abstraction reactions, viz. paths 4, 5 and 6 as shown in Fig. 5.13, are considered as possible mechanisms of oxidation. For path 4, the position of the •OH radical in the pre-reactive complex (IM4) was far from the carbon atom (distance between H15 to •OH radical = 1.589 Å). The H atom abstraction by •OH radical via TS4 (distance between H15 to •OH radical = 1.446 Å) is quite easy because the reaction is a barrier–less process. Further reaction will form the stable compound P4,

where H_2O molecule was very far from O14 atom. Similar abstraction of H bond was found in the *ortho* and *meta* positions with activation energies of 6.32 and 9.71 kcal/mol, respectively. Comparing the three H–abstraction paths, path 4 was barrier–less step for the hydrogen abstraction (Wang et al., 2021). This means that abstraction of H atom from carbon atoms of the benzene ring was relatively easy, and thus, it played an important role in the PNP degradation. Fig. 5.18 (D) shows the intrinsic reaction coordinate (IRC) to confirm the optimised structure of TS4 which connects the reactant and product. Fig 5.18 (B) shows the relative energies of reaction pathways involving the hydrogen abstraction.

Mei et al. (2020) studied the possible pathways of PNP degradation with DFT simulation. Eleven possible pathways were explained for the oxidation of PNP. Based on transition state theory and Collins–Kimball theory, overall rate constant of PNP degradation by $^{\bullet}OH$ radicals was quantified as 1.08×10^9 $M^{-1}s^{-1}$ at 298 K, 1 atm. For the simulation of heterogenous Fenton system, rate constant of 1.08×10^9 $M^{-1}s^{-1}$ was adopted to predict the degradation profile of PNP as discussed in earlier section.

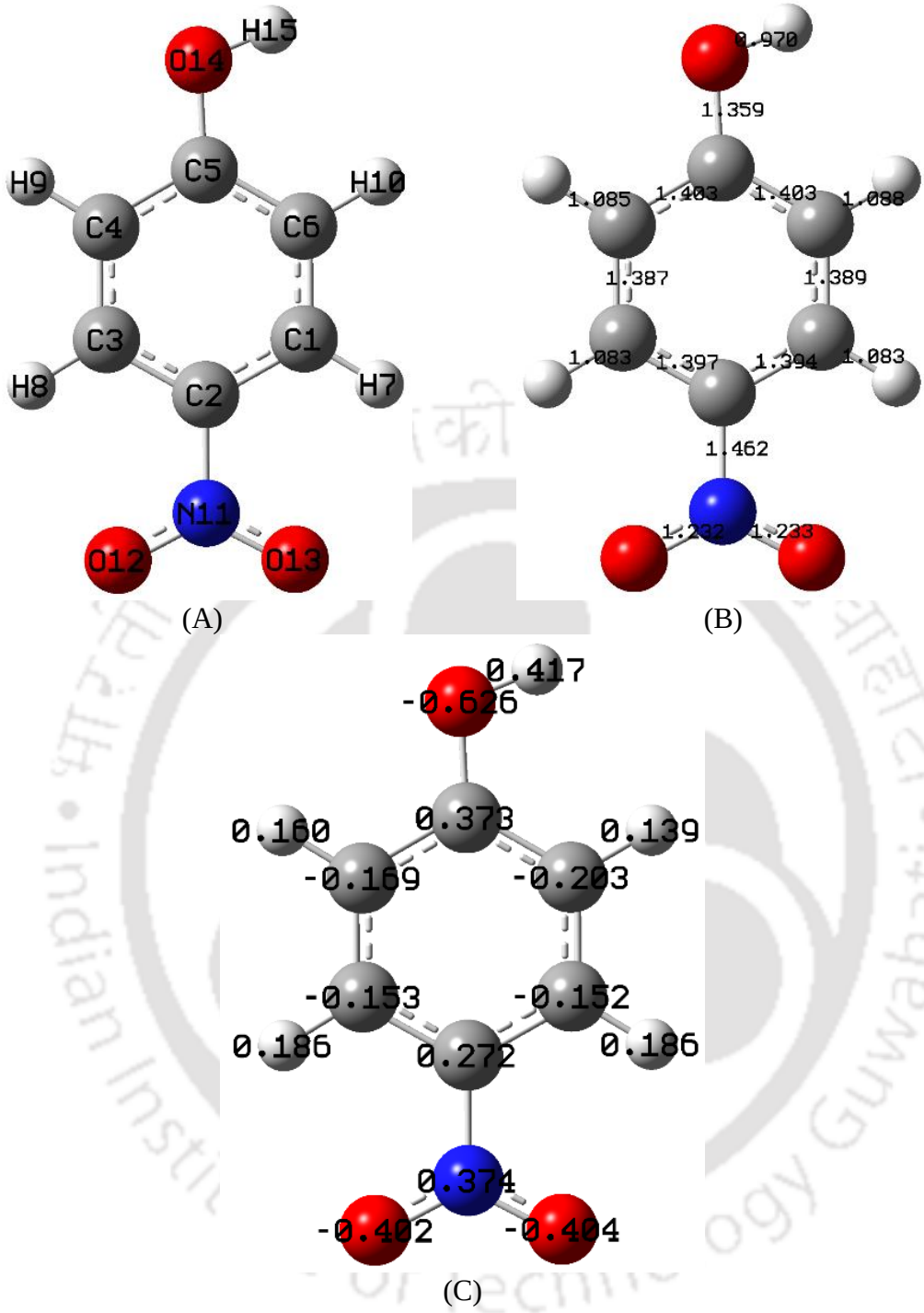

Figure 5.12: (A) Optimized structure, (B) Bond properties, and (C) Mulliken charges of p– nitrophenol (PNP)

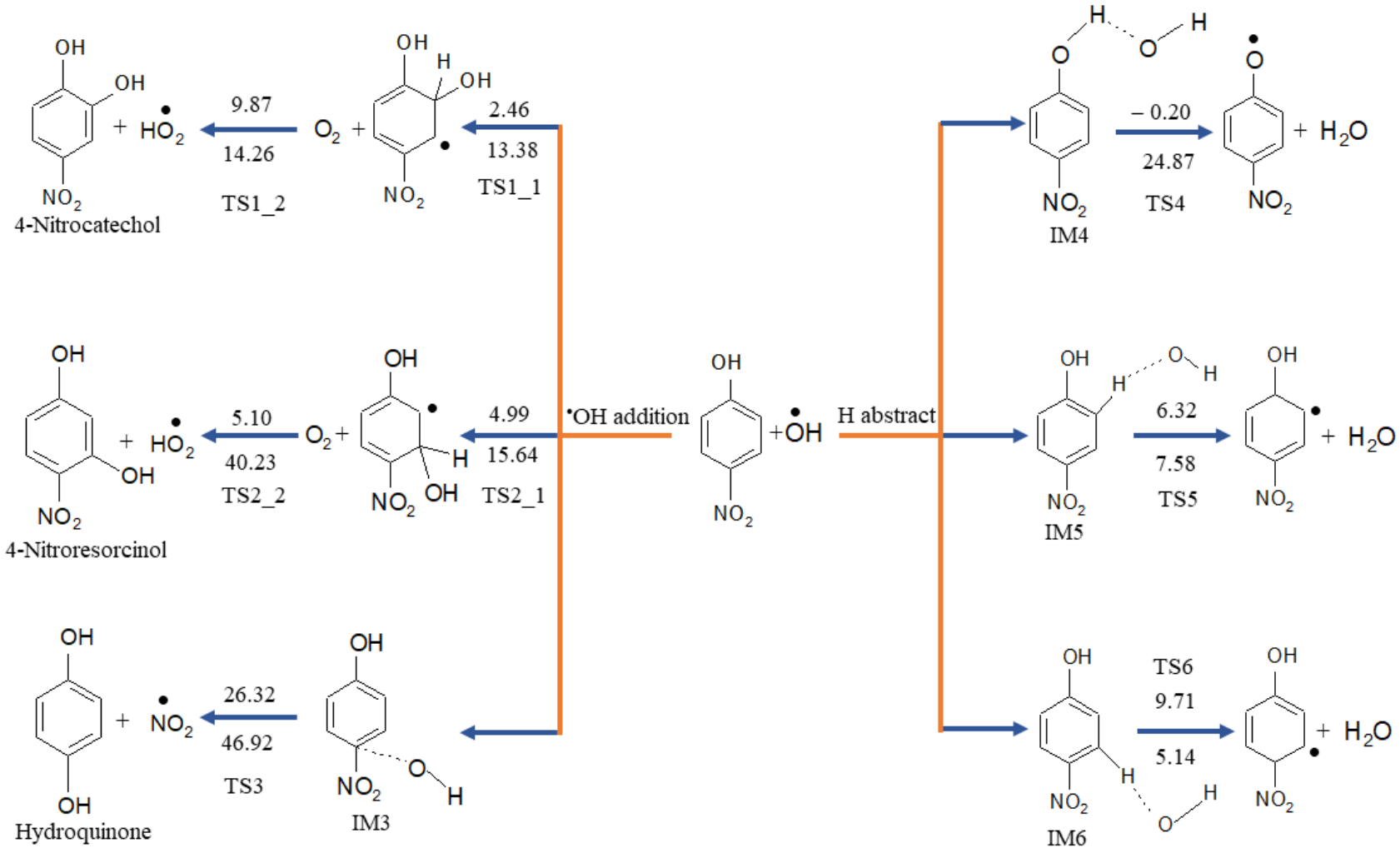

Figure 5.13: Oxidative degradation reaction pathways for the hydroxyl attack and hydrogen abstraction on 4–nitrophenol (the numbers on arrows indicate activation energies for the forward and backward reactions in kcal/mol)

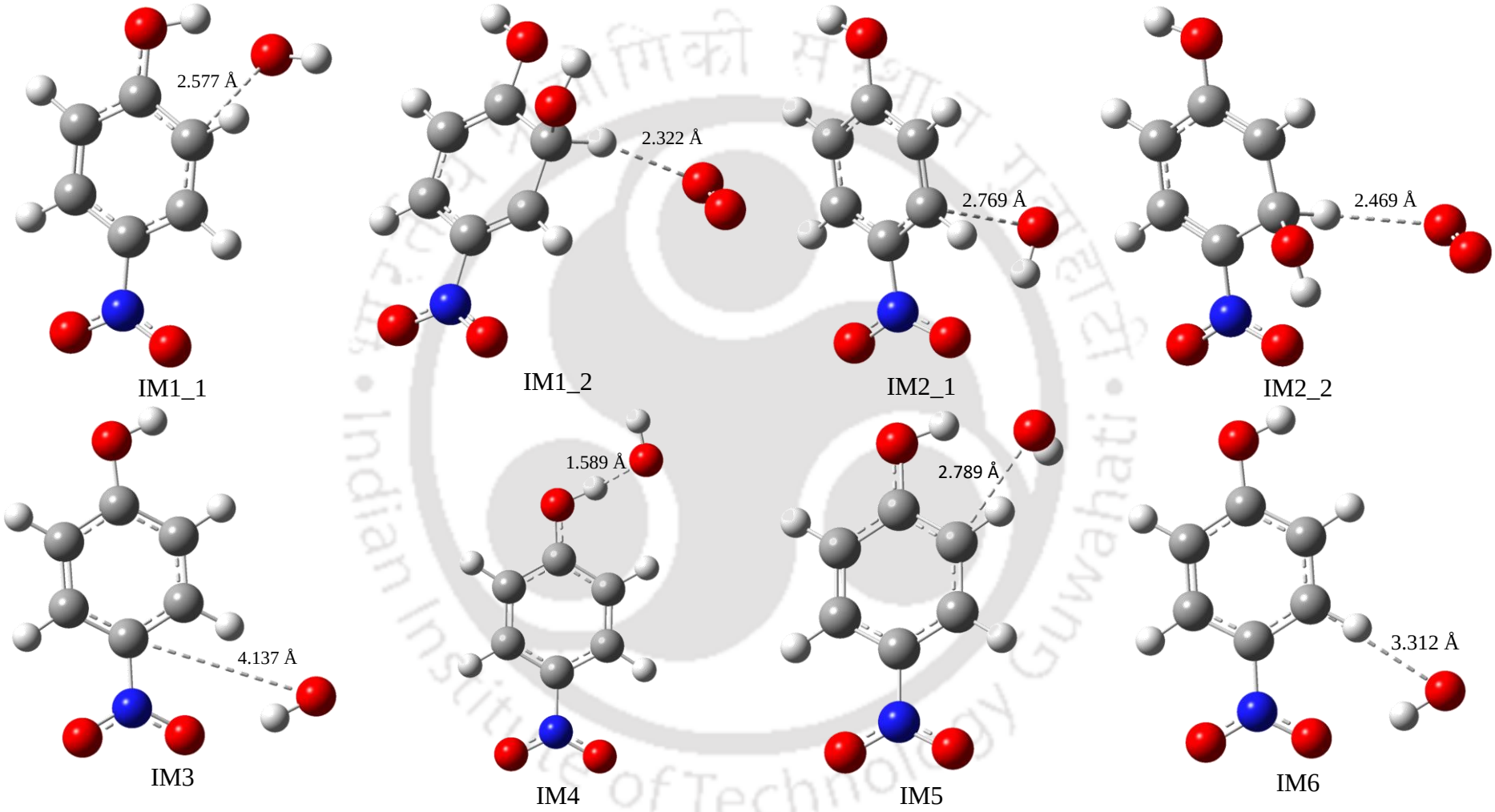

Figure 5.14: Pre–reactive complexes of •OH radical induced PNP degradation

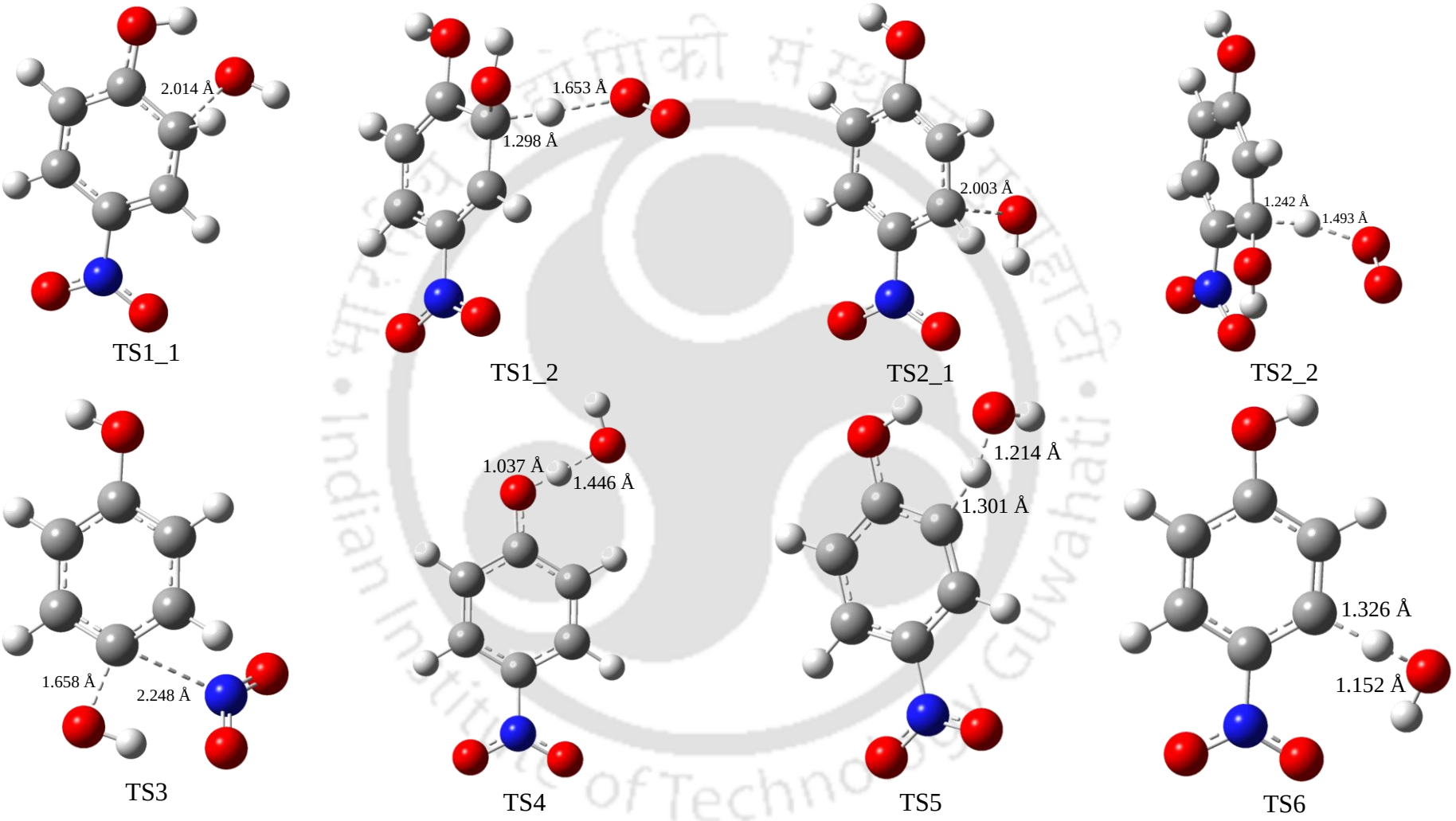

Figure 5.15: Transitions states of •OH radical induced PNP degradation

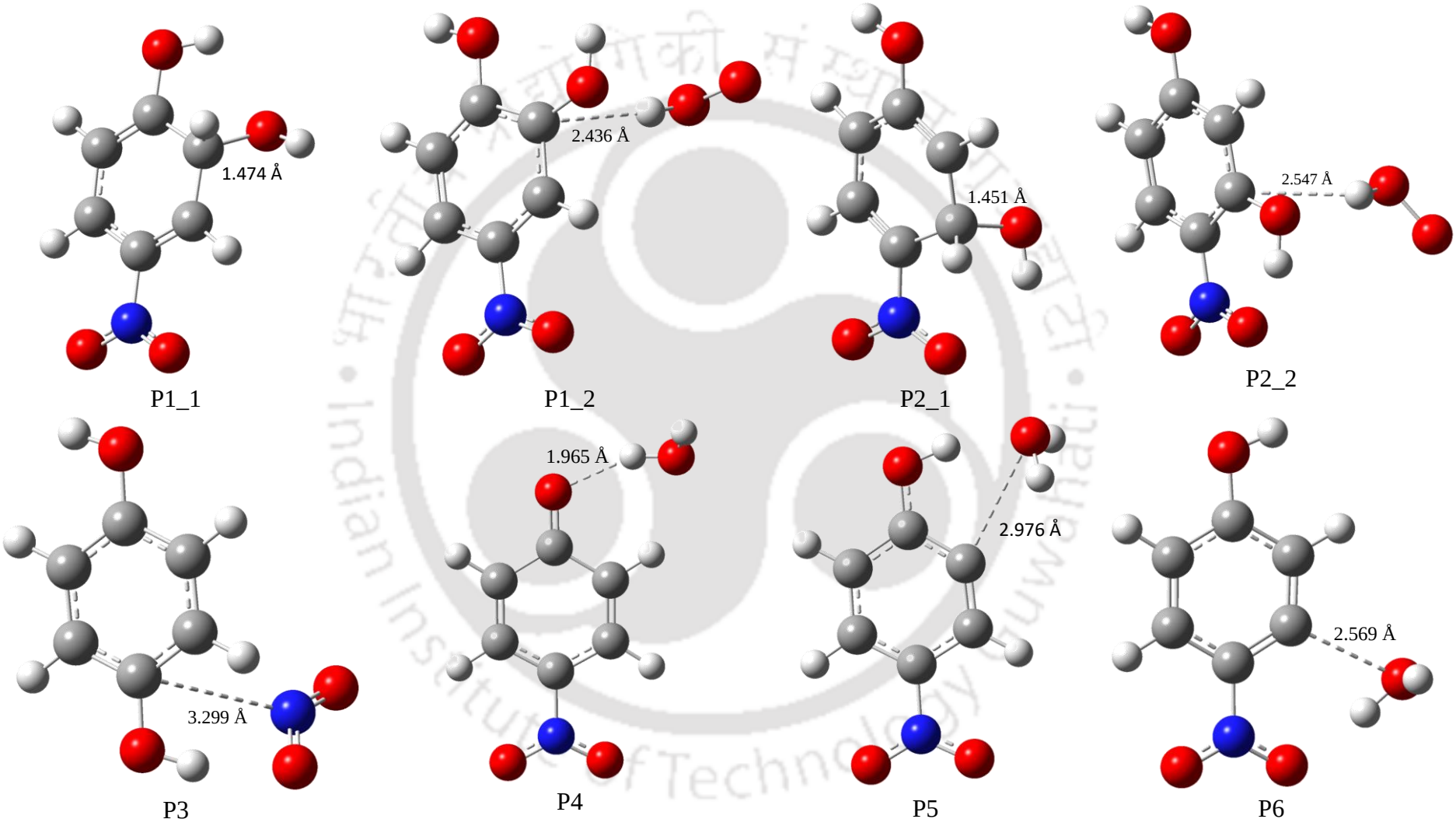

Figure 5.16: Adduct complex of •OH radical induced PNP degradation

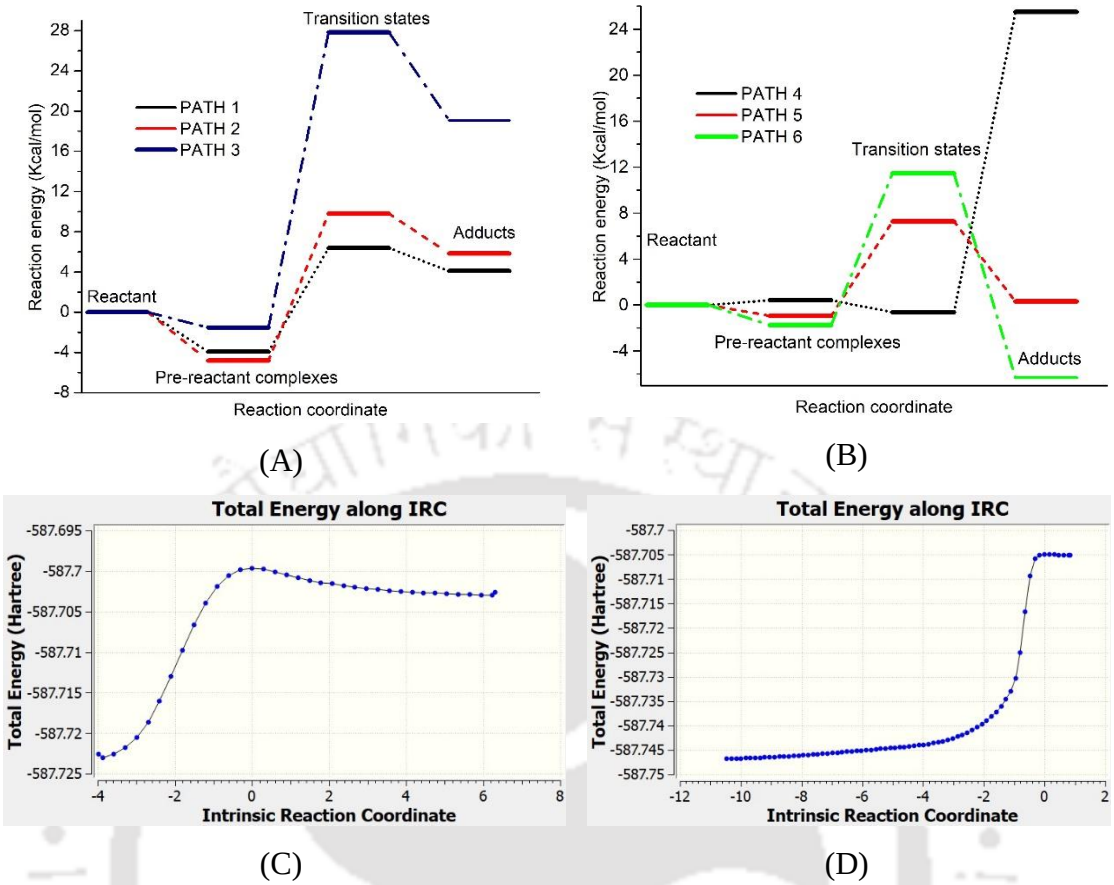

Figure 5.17: (A) Relative energy of reaction pathways involving hydroxyl radical addition; (B) Relative energy of reaction pathways involving hydrogen abstraction; (C) IRC path 1 for TS1_1; (D) IRC path 4 for TS4.

5.7 CONCLUSIONS

The combination of hydrodynamic cavitation and the heterogeneous Fenton oxidation can be effectively used for the treatment of PNP. In this study, spherical shaped Fe_3O_4 magnetic nanoparticles (mean dia. 250 nm) were synthesized and used as heterogeneous Fenton reagent. The catalytic activity Fe_3O_4 nanoparticles as heterogeneous Fenton catalyst was evaluated at different process conditions. The process parameters of initial concentration of PNP, pH, catalyst loading, H_2O_2 concentration were also optimized. Experimental results showed that 78% PNP degradation could be achieved under

optimized operating conditions. Fe_3O_4 nanoparticles had good stability and reusability (with retention of activity till 5 experimental cycles). Moreover, these particles could be separated from the solution with the application of an external magnetic field.

The experimental results were explained with three approaches: (1) hydrodynamic model for the cavitating flow, (2) kinetic model for PNP degradation and (3) DFT simulations for identification of the intermediates of the PNP degradation and possible pathways. The hydrodynamic model revealed the influence of the design and operational parameters of the reactor on degradation. The inlet pressure played a major role in degradation – however, a maxima was seen in degradation with this parameter. The kinetic model revealed significant leaching of the Fe^{3+}/Fe^{2+} ions at the surface of magnetic nanoparticles. This model also brought forth the relative contributions of hybrid (HC+Fenton) and sole (HC) process in PNP degradation. DFT simulations assessed different possible intermediates that can form due to attack of •OH radicals on PNP molecules. The vulnerable sites for attack were identified and a reaction pathway was proposed. Two distinct pathways for PNP degradation were identified, viz. •OH addition and H-abstraction. For the former route, the *ortho*-C of benzene ring was the most favourable site, while H atom of phenolic hydroxyl group was more susceptible (or more reactive) for H-atom abstraction route.

References

Alvarez-Idaboy, J.R., Mora-Diez, N., Boyd, R.J., Vivier-Bunge, A., On the importance of pre-reactive complexes in molecule− radical reactions: hydrogen abstraction from aldehydes by •OH. *J. Am. Chem. Soc.* 123(9) (2001) 2018-2024.

American Public Health Association, American Water Works Association, Water Pollution Control Federation, & Water Environment Federation. (1915). Standard

methods for the examination of water and wastewater (Vol. 2). American Public Health Association.

ANSYS FLUENT (2013). ANSYS FLUENT Theory Guide (release 15.0), Canonsburg, PA.

Arrojo, S., Benito, Y., A theoretical study of hydrodynamic cavitation. *Ultrason. Sonochem.* 15(3) (2008) 203–211.

Bashir, T.A., Soni, A.G., Mahulkar, A.V., Pandit, A.B., The CFD driven optimisation of a modified venturi for cavitational activity. *Can. J. Chem. Eng.* 89(6) (2011) 1366–1375.

Capocelli, M., Musmarra, D., Prisciandaro, M., Lancia, A., Chemical effect of hydrodynamic cavitation: simulation and experimental comparison. *AIChE J.* 60(7) (2014a) 2566–2572.

Capocelli, M., Prisciandaro, M., Lancia, A., Musmarra, D., Cavitational reactor for advanced treatment of contaminated water: the effect of recovery pressure. *Desalin. Water Treat.* 55(12) (2015) 3172–3177.

Capocelli, M., Prisciandaro, M., Lancia, A., Musmarra, D., Hydrodynamic cavitation of p–nitrophenol: a theoretical and experimental insight. *Chem. Eng. J.* 254 (2014b) 1–8.

Daneshvar, N., Behnajady, M.A., Asghar, Y.Z., Photooxidative degradation of 4–nitrophenol (4–NP) in UV/H_2O_2 process: Influence of operational parameters and reaction mechanism. *J. Hazard. Mater.* 139(2) (2007) 275–279.

Ebrahimi, B., He, G., Tang, Y., Franchek, M., Liu, D., Pickett, J., Springett, F., Franklin, D., Characterization of high–pressure cavitating flow through a thick orifice plate in a pipe of constant cross section. *Int. J. Therm. Sci.* 114, (2017) 229–240.

Gogate, P.R., Pandit, A.B., Hydrodynamic cavitation reactors: a state-of-the-art review. *Rev. Chem. Eng.* 17(1) (2001)1–85.

Krishnan, J.S., Dwivedi, P., Moholkar, V.S., Numerical investigation into the chemistry induced by hydrodynamic cavitation. *Ind. Eng. Chem. Res.* 45(4) (2006) 1493–1504.

Kuldeep, Saharan, V.K., Computational study of different venturi and orifice type hydrodynamic cavitating devices. *J. Hydrodyn. Ser. B* 28(2) (2016) 293–305.

Kumar, K.S., Moholkar, V.S., Conceptual design of a novel hydrodynamic cavitation reactor. *Chem. Eng. Sci.* 62(10) (2007) 2698–2711.

Lai, B., Chen, Z., Zhou, Y., Yang, P., Wang, J., Chen, Z., Removal of high concentration

p–nitrophenol in aqueous solution by zero valent iron with ultrasonic irradiation (US–ZVI). *J. Hazard. Mater.* 250 (2013) 220–228.

Li, M., Cao, H., Han, D., Li, X., He, M., Kinetics and mechanism of the reactions of •OH radicals with p-nitroaniline in gas-phase and aqueous solution. *Comput. Theor. Chem.* 1055 (2015) 68-77.

Mei, Q., Cao, H., Han, D., Li, M., Yao, S., Xie, J., Zhan, J., Zhang, Q., Wang, W. He, M., Theoretical insight into the degradation of p-nitrophenol by •OH radicals synergized with other active oxidants in aqueous solution. *J. Hazard. Mater.* 389 (2020) 121901.

Merouani, S., Hamdaoui, O., Saoudi, F., Chiha, M., Pétrier, C., Influence of bicarbonate and carbonate ions on sonochemical degradation of Rhodamine B in aqueous phase. *J. Hazard. Mater.* 175(1) (2010) 593–599.

Moholkar, V.S., Pandit, A.B., Bubble behavior in hydrodynamic cavitation: effect of turbulence. *AIChE J*. 43(6) (1997).1641–1648.

Moholkar, V.S., Pandit, A.B., Numerical investigations in the behaviour of one–dimensional bubbly flow in hydrodynamic cavitation. *Chem. Eng. Sci.* 56(4) (2001) 1411–1418.

Mossaz, S., Colombet, D., Ayela, F., Hydrodynamic cavitation of binary liquid mixtures in laminar and turbulent flow regimes. *Exp. Therm Fluid Sci.* 80, (2017) 337–347.

Pradhan, A.A., Gogate, P.R., Degradation of p–nitrophenol using acoustic cavitation and Fenton chemistry. *J. Hazard. Mater.* 173(1) (2010) 517–522.

Pradhan, A.A., Gogate, P.R., Removal of p–nitrophenol using hydrodynamic cavitation and Fenton chemistry at pilot scale operation. *Chem. Eng. J.* 156(1) (2010) 77–82.

Rooze, J., André, M., van der Gulik, G.J.S., Fernández–Rivas, D., Gardeniers, J.G., Rebrov, E.V. Keurentjes, J.T., Hydrodynamic cavitation in micro channels with channel sizes of 100 and 750 micrometers. *Microfluid. Nanofluid.* 12(1–4) (2012) 499–508.

Roy, K., Moholkar, V.S., Sulfadiazine degradation using hybrid AOP of heterogeneous Fenton/persulfate system coupled with hydrodynamic cavitation. *Chem. Eng. J.* 386 (2020) 121294.

Saharan, V.K., Badve, M.P., Pandit, A.B., Degradation of Reactive Red 120 dye using hydrodynamic cavitation. *Chem. Eng. J.* 178, (2011) 100–107.

Shah, Y.T., Pandit, A.B., Moholkar, V.S., Cavitation reaction engineering, New York: Plenum Press/Kluwer Academic (1999).

Singhal, A.K., Athavale, M.M., Li, H., Jiang, Y., Mathematical basis and validation of the full cavitation model. *J. Fluids Eng.* 124(3) (2002) 617–624.

Sivasankar, T., Moholkar, V.S., Physical insights into the sonochemical degradation of recalcitrant organic pollutants with cavitation bubble dynamics. *Ultrason. Sonochem.* 16(6) (2009) 769–781.

Sun, S.P., Lemley, A.T., p–Nitrophenol degradation by a heterogeneous Fenton–like reaction on nano–magnetite: process optimization, kinetics, and degradation pathways. *J. Mol. Catal. A: Chem.* 349(1) (2011) 71–79.

Uc, V.H., Alvarez-Idaboy, J.R., Galano, A., García-Cruz, I., Vivier-Bunge, A., Theoretical determination of the rate constant for •OH hydrogen abstraction from toluene. *J. Phys. Chem. A* 110(33) (2006) 10155-10162.

Wang, T., Lu, N., Li, J., Wu, Y., Su, Y., Enhanced degradation of p-nitrophenol in soil in a pulsed discharge plasma-catalytic system. *J. Hazard. Mater.* 195 (2011) 276-280.

Wang, Y., He, L., Lv, G., Sun, X., Experimental and theoretical insights into the RCS-Involved electro-catalytic transformation of 4-nitrophenol. *Chemosphere*, 262 (2021) 128015.

Wu, C., De Visscher, A., Gates, I.D., Reactions of hydroxyl radicals with benzoic acid and benzoate. *RSC Adv.* 7(57) (2017) 35776-35785.

Zhang, W., Xiao, X., An, T., Song, Z., Fu, J., Sheng, G., Cui, M., Kinetics, degradation pathway and reaction mechanism of advanced oxidation of 4-nitrophenol in water by a UV/H_2O_2 process. *J. Chem. Technol. Biotechnol.* 78(7) (2003) 788–794.

CHAPTER 6

Degradation of Carbamazepine by Hybrid Hydrodynamic Cavitation + Photo–Fenton System

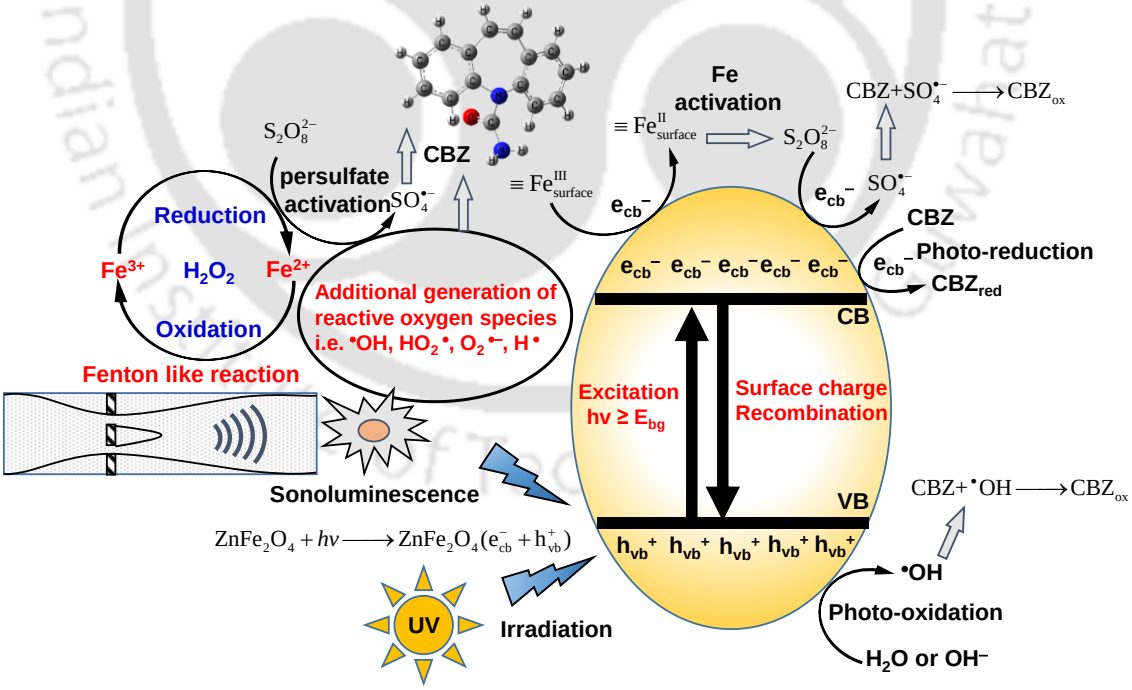

CHAPTER 6

DEGRADATION OF CARBAMAZEPINE BY HYBRID HYDRODYNAMIC CAVITATION + PHOTO–FENTON SYSTEM

6.1 INTRODUCTION

So far in this thesis, studies on the degradation of two organic pollutants (originating from pharmaceutical industries) using hybrid cavitation–assisted advanced oxidation processes have been presented. These studies – based on concurrent analysis of experimental results and simulations – have yielded interesting results that reveal relative influence and inter–relation between various design and operating parameters – as well as the synergistic interactions between the different AOPs in the hybrid system.

In this chapter, we take ahead this theme with a new ubiquitous pollutant Carbamazepine and the hybrid AOP of hydrodynamic cavitation + photo–Fenton system. Carbamazepine (CBZ) is a typical compound used for the treatment of seizure disorders, relief of neuralgia, and a wide variety of psychiatric disorders. The worldwide consumption of CBZ is estimated to be 1014 tons per year and its annual usage ranks the second among all the antiepileptic drugs in China (Rao et al., 2014). CBZ is also sometimes used to treat mental illnesses, depression, post–traumatic stress disorder, drug

and alcohol withdrawal, restless leg syndrome, diabetes insipidus, certain pain syndromes, and a disease in children called chorea (Mohapatra et al., 2014). Due to the high production level and pharmacokinetic behaviour of CBZ during normal therapeutic use (e.g. half–life, urinary and fecal excretion, and metabolism), the presence of CBZ and its metabolites have been detected in WWTPs and they were considered to be a major source of discharge of CBZ into the environment. Spreading wastewater (WW) on soil during reuse may result in the transfer of some pharmaceutical active compounds (PhACs) including CBZ and their metabolites. Recent studies have revealed that CBZ was present in wastewater–irrigated soil with concentration ranging from 0.02 to 15 ng g^{-1} dry matter. CBZ is one of the most frequently detected pharmaceuticals in various waters due to its low biodegradability and persistent nature in wastewater. CBZ has been detected in WWTP effluents at concentration up to 6.3 µg/L (Heberer 2002). The CBZ concentration was found to be 3.09 µg/L, 610 ng/L, and 30 ng/L in surface water, groundwater, and drinking water, respectively (Rao et al., 2014). CBZ has been evaluated as toxic to aquatic life, including bacteria, algae, invertebrates, and fish. Therefore, it is necessary to treat the effluents containing pharmaceutical compounds including CBZ adequately before discharging or treating the water for drinking purposes.

This study has essentially compared the efficacy of individual process of hydrodynamic cavitation (HC) and hybrid systems of HC+UV, HC + $Na_2S_2O_8$, HC+ $ZnO/ZnFe_2O_4$, UV+ $Na_2S_2O_8$, UV + $ZnO/ZnFe_2O_4$, $Na_2S_2O_8$ + $ZnO/ZnFe_2O_4$, HC + UV + $ZnO/ZnFe_2O_4$, HC + UV + $ZnO/ZnFe_2O_4$ + $Na_2S_2O_8$ for the degradation of carbamazepine. The principal distinction of the Fenton process used in the present study compared to earlier chapters is that the heterogeneous Fenton reagent in this study is a composite oxide/ferrite, i.e. zinc oxide/zinc ferrite ($ZnO/ZnFe_2O_4$) and not iron oxides as used in previous studies. Non–linear regression analysis was used to develop an empirical kinetic model

considering the effect of the main operational parameters on k_{app}, including inlet pressure, pH, initial concentration, power UV and catalyst dosage.

6.2 MATERIALS AND METHODS

6.2.1 Materials

Carbamazepine (99%, AR grade) was purchased form Sigma–Aldrich. Zinc chloride ($ZnCl_2$, AR grade), ferric chloride hexahydrate ($FeCl_3 \cdot 6H_2O$, >99%, ACS grade), sodium acetate (CH_3COONa, 99%, AR grade), ethylene glycol (99%, LR grade) were purchased from Himedia (India). Absolute ethanol (≥99%, AR Grade) was purchased from Changshu Yangyuan Chemicals, China. All chemicals and reagents were used as received without any pretreatment. Deionized water was used as the medium in all experiments.

6.2.2 Synthesis of ZnO/$ZnFe_2O_4$

The precursor was synthesized by a solvothermal method (Liu et al., 2016). In a typical synthesis, $FeCl_3 \cdot 6H_2O$ (1.2 g) and $ZnCl_2$ (2.42 g) were dissolved in 70 mL of ethylene glycol (EG). CH_3COONa (3.2 g) was added to the mixture with vigorous stirring. The homogeneous mixture was transferred into a 100 mL Teflon–lined autoclave, which was then tightly sealed and heated at 200°C for 12 h. The autoclave was allowed to cool down to room temperature. Precipitates obtained in the reaction were washed with deionized water several times until a neutral pH was attained – followed by 3× wash with ethanol. A magnet was used to separate the particles after washing. The resultant solid nanoparticles were dried under vacuum at 60°C overnight.

6.2.3 Experimental Setup

Fig. 6.1 shows the schematic diagram of the hydrodynamic cavitation reactor (same as used in previous chapters) with included facility for UV irradiation. A water cooling

jacket around the feed tank was used to control the temperature (30 ± 5 °C) of the treated solution. The inner diameter of both mainline and bypass line was 21 mm and holding tank was having the maximum capacity of 30 L. For degradation studies with hybrid HC/UV advanced oxidation systems, UV–C tube (TUV, 6W/G6T5, Philips) was placed inside the feed tank of HC reactor. The UV tube was placed above the water surface in the holding tank at a distance of approx. 10 cm. All experiments were conducted using 5 L solutions of CBZ.

Table 6.1: Power calculation for UV tubes

Number of Tubes	Theoretical Power of UV tube (W)	UV intensity (W/cm^2)	Average light intensity per volume (I_0) (Einstein L^{-1} s^{-1}) ∗
1	6 (500 Lx)	2.5×10^{-3}	2.03×10^{-6}
2	12 (1100 Lx)	5.5×10^{-3}	4.48×10^{-6}
3	18 (1800 Lx)	9.0×10^{-3}	7.32×10^{-6}

∗ Unit conversion as per the procedure of Xiao et al. (2016)

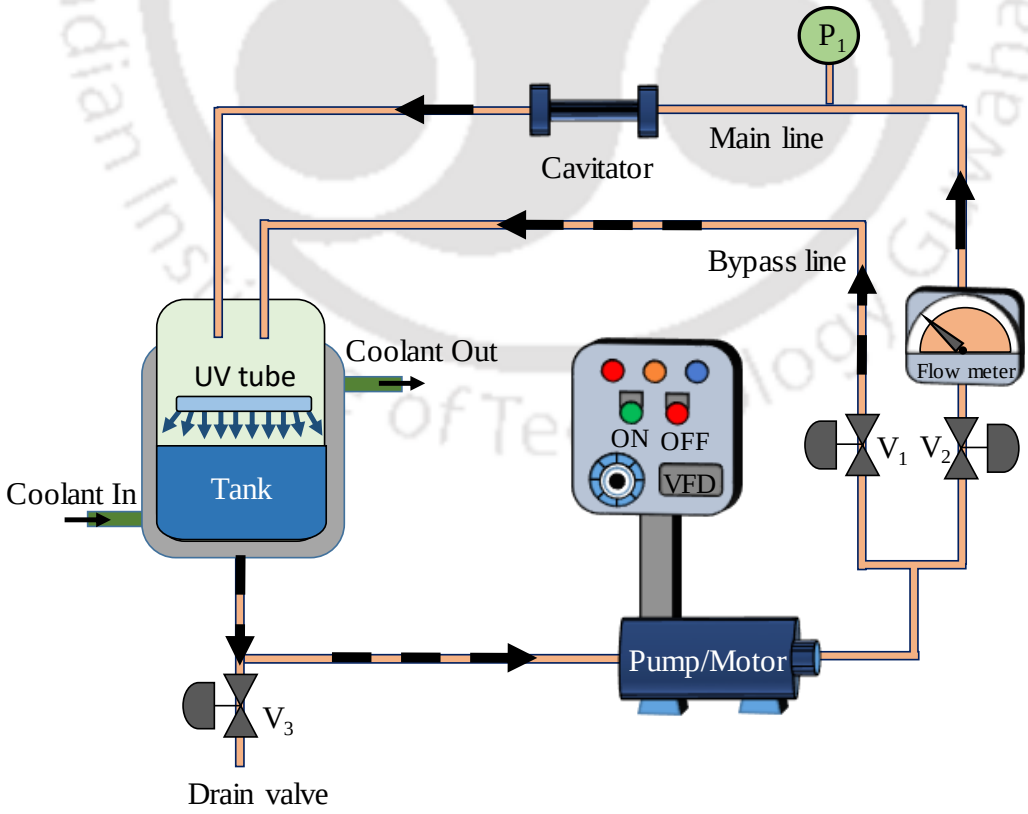

(A)

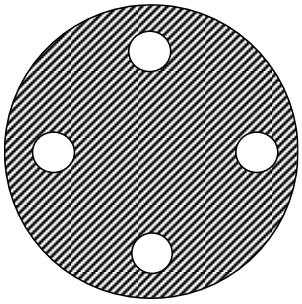

Diameter of each hole (d_h) = 2 mm

Number of holes (N_h) = 4

Flow area = 12.56 mm^2

Perimeter of holes = 25.12 mm

α = 2.00 mm^{-1}, β_o = 0.036

(B)

Figure 6.1: (A) Schematic of hydrodynamic cavitation reactor coupled with a UV source (for the photochemical system); (B) Geometric specifications of 4–hole orifice plate used as a cavitator

6.2.4 Analytical methods

Aliquots of reaction mixture were analyzed for residual CBZ concentration by HPLC (Shimadzu, Model: SPD–20A) with C–18 reverse phase column (5 µm particle size, 250 mm × 4.6 mm) and UV detector at the wavelength λ_{max} = 210 nm. The mobile phase was the mixture of acetonitrile (60 vol %) and milli–Q water (40 vol %) with a flow rate of 0.8 mL/min. Concentration of benzoic acid (BA) as reference compounds was also quantified in HPLC with mobile phase 50:50 vol% mixture of methanol and phosphoric acid (10 mM) (flow rate = 1.0 mL/min, UV detector = 227 nm). The absorption spectra measurements of persulfate and CBZ solutions were performed on a UV–Vis spectrophotometer (Model No.: UV–2600, Make: Shimadzu, Singapore) at a path length of 1 cm. Surface morphology of the nanocomposites was analyzed with the Field emission transmission electron microscope (FE–TEM, Make: JEOL, Model: 2100F) and field emission scanning electron microscope (FE–SEM, Make: Zeiss, Model: Sigma). Brunauer–Emmett–Teller (BET) surface area of the nanoparticles was determined from nitrogen adsorption isotherms using a surface area and porosity analyzer (BET, Make: Quantachrome, Model: Autosorb–IQ MP). Vibrating sample magnetometer (VSM)

(Make: Lakeshore, Model: 7410 series) was used to study the hysteresis loops and the magnetic properties of the nanoparticles at 300 K under applied field ranging from − 15 kOe to 15 kOe. The mass spectrometric analysis was performed using Q–Tof Premier Mass Spectrometer (Make: Waters, LC–MS/MS) equipped with Electro Spray ionization (ESI)/Time of flight (Tof) source in MS mode without any purification to identify the intermediate products. The ESI–MS was performed in selected ion monitoring modes with positive electrospray ionization (ESI+) ion source with a full scan.

6.2.5 Kinetic model

The experimental profiles of degradation have been analyzed on the basis of a kinetic model. In the present case, the degradation of CBZ is contributed by three mechanisms, viz. direct photolysis, oxidation induced by •OH radicals and oxidation induced by SO4 radicals. CBZ degradation through direct UV photolysis was considered to be independent of (or un–influenced by) the degradation through oxidative radicals. Accordingly, the degradation of CBZ by direct UV photolysis and by oxidizing radicals can be written as:

$$r_{[CBZ],Total} = r_{[CBZ],UV} + r_{[CBZ],^{\bullet}OH} + r_{[CBZ],SO_4^{\bullet-}} \quad 6.1$$

Notation: $r_{[CBZ],UV}$ = rate of direct photolytic degradation of CBZ, $r_{[CBZ],^{\bullet}OH}$ = rate of CBZ degradation induced by •OH radicals, $r_{[CBZ],SO_4^{\bullet-}}$ = rate of CBZ degradation induced by $SO_4^{\bullet-}$. The kinetic modelling of CBZ degradation proceeded in three steps: (1) determination of direct degradation rate through UV alone, (2) reaction network for degradation through oxidizing radicals, (3) species mass balance. All degradation reactions of CBZ were fitted the first–order kinetic model (assuming that the order of all

species in the reaction network as one). The procedure for determination of $r_{[CBZ],UV}$, $r_{[CBZ],\bullet OH}$ and $r_{[CBZ],SO_4^{\bullet-}}$ is given below.

Determination of direct degradation rate: The rate of degradation of CBZ through direct photolysis (254 nm wavelength) is determined by the following expression (Crittenden et al. 1999; Luo et al., 2015, Su et al., 2018):

$$r_{[CBZ],UV} = I_0 \cdot \phi_{[CBZ]} \cdot f_{[CBZ]} \cdot (1 - e^{-A_0}) \quad 6.2$$

$$A_0 = 2.303 \cdot b \cdot \left(\varepsilon_{CBZ}[CBZ] + \varepsilon_{oxidant}[oxidant]\right) \quad 6.3$$

$$f_{[CBZ]} = \frac{2.303\ \varepsilon_{[CBZ]}\ b\ [CBZ]}{A_0} \quad 6.4$$

Notation: I_o = average photonic light intensity per volume of UV, $\phi_{[CBZ]}$ = quantum yield of CBZ at 254 nm, $f_{[CBZ]}$ = fraction of UV irradiation absorbed CBZ, A_o = empirical constant, b = the optical path length (10 cm), ε_{CBZ} = the molar extinction coefficient of CBZ, $\varepsilon_{oxidant}$ = the molar extinction coefficient of the oxidant at 254 nm. I_0 was determined as 7.32×10^{-6} Einstein L^{-1} s^{-1} (which corresponds to a power output of 9 mW cm^{-2} for a set of 3 UV tubes). For the calculation of I_0, the intensity of irradiation (in Lux) was measured and a typical value of the luminous efficiency of the UV–C tube was taken as 20 lumen/W. The cross–sectional area of the tank over which the UV–C source was placed was calculated as 0.0688 m^2.

The capacity of a compound for absorbing photons of the incident light is an important factor governing its photochemical reactivity. The decadic molar extinction coefficient (ε) represents the ability of the compound to absorb light at a certain wavelength (λ). ε

can be calculated by measuring the absorbance (A) of the solute (either CBZ or $Na_2S_2O_8$) as: $A = \varepsilon\,[C_i]\,z$.

CBZ and $Na_2S_2O_8$ solutions with initial concentrations of 15 ppm (6.35×10^{-5} M) and 500 mg/L (2.1×10^{-3} M), respectively, were used for the experiments. The absorbance was measured using a quartz cuvette with 1 cm path length (z). It may be noted that initial concentrations of 15 ppm and 500 mg/L for CBZ and persulfate mentioned above are optimized values.

Fig. 6.2 illustrates the variation of decadic molar extinction coefficients for CBZ and persulfate in the range 200–300 nm. For 254 nm, ε value of CBZ was 5760.7 $M^{-1}cm^{-1}$, which is in a good agreement with previous studies (Gerrity et al., 2016, Wols et al., 2014). A similar analysis was also done for persulfate, and the value of $\varepsilon_{[SO_4^{\bullet-}]}$ was determined as 21.38 $M^{-1}cm^{-1}$.

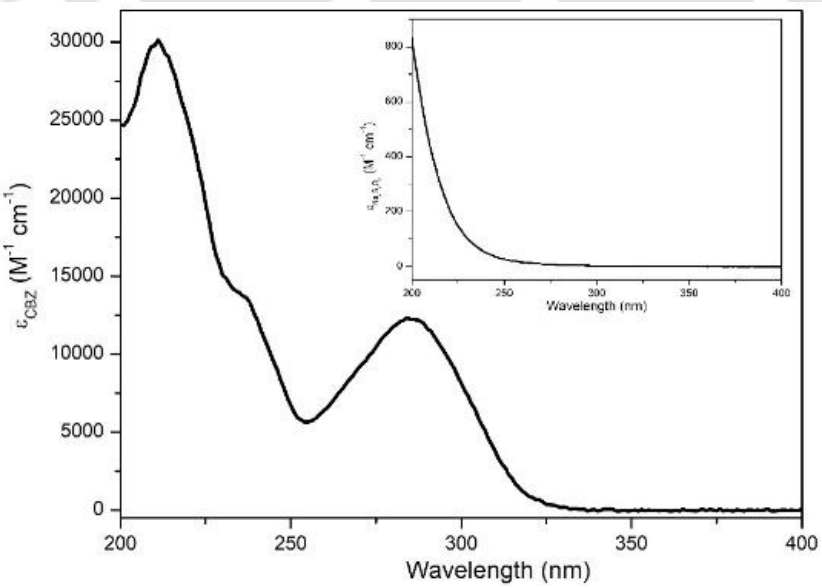

Figure 6.2: Decadic molar absorption coefficient (ε) of CBZ. Inset figures are the decadic molar absorption coefficient of persulfate

The quantum yield describes the ratio of the total numbers of molecules of the compound destroyed to the total numbers of photons absorbed by the system. The quantum yield (φ) of CBZ can be calculated from equation (a) as follows:

The values of different variables were deduced as: $r_{[CBZ],\,UV} = 1.589 \times 10^{-9}$ M s^{-1}, $f_{[CBZ]} = 0.89$, $I_o = 7.32 \times 10^{-6}$ Einstein L^{-1} s^{-1}, $A_o = 9.458$. Substituting these values, the quantum yield $\phi_{[CBZ]}$ was calculated to be 2.4×10^{-4} mol Einstein^{-1}. A typical value of $\phi_{[CBZ]}$ reported in previous literature (Shu et al., 2013; Pereira et al., 2007) for CBZ is 6×10^{-4} mol Einstein^{-1}, which is of similar order of magnitude.

Determination of kinetic constants (*k*)*:* In order to measure the kinetic rate constants k_{25} and k_{26}, for reactions of $^{\bullet}OH$ and $SO_4^{\bullet-}$ with CBZ, we have adopted the competing kinetic method (relative rate technique). Benzoic acid (BA) was applied as a reference compound for determining kinetic rate contacts. The kinetic constants of benzoic acid by $^{\bullet}OH$ and $SO_4^{\bullet-}$ radicals have been reported by Buxton et al., 1988 and Neta et al., 1988 as 5.9×10^9 and 1.2×10^9 M^{-1} s^{-1}, respectively. The *k* values of CBZ reacting with $^{\bullet}OH$ / $SO_4^{\bullet-}$ were calculated as: $\frac{k_{[CBZ]}}{k_{[BA]}} = \frac{\ln\left([CBZ]_0/[CBZ]_t\right)}{\ln\left([BA]_0/[BA]_t\right)}$. A plot of $\ln([CBZ]_0/[CBZ]_t)$ vs. $\ln([BA]_0/[BA]_t)$ yields a straight line with slope k_{SDZ}/k_{BA} and zero intercept. From the value of k_{BA} (for the two oxidizing radicals) reported in literature and numerical value of slope, k_{SDZ} can be determined (Ling et al., 2017).

From Fig. 6.3, the slopes of the plots (i.e. the ratio k_{CBZ}/k_{BA}) corresponding to reactions with $^{\bullet}OH$ and $SO_4^{\bullet-}$ radicals are 0.61 and 1.85, respectively. The values of the kinetic constants for CBZ degradation by the two radicals ($k_{[CBZ],\,^{\bullet}OH}$ and $k_{[CBZ],\,SO_4^{\bullet-}}$) are determined as 3.6×10^9 and 2.2×10^9, respectively.

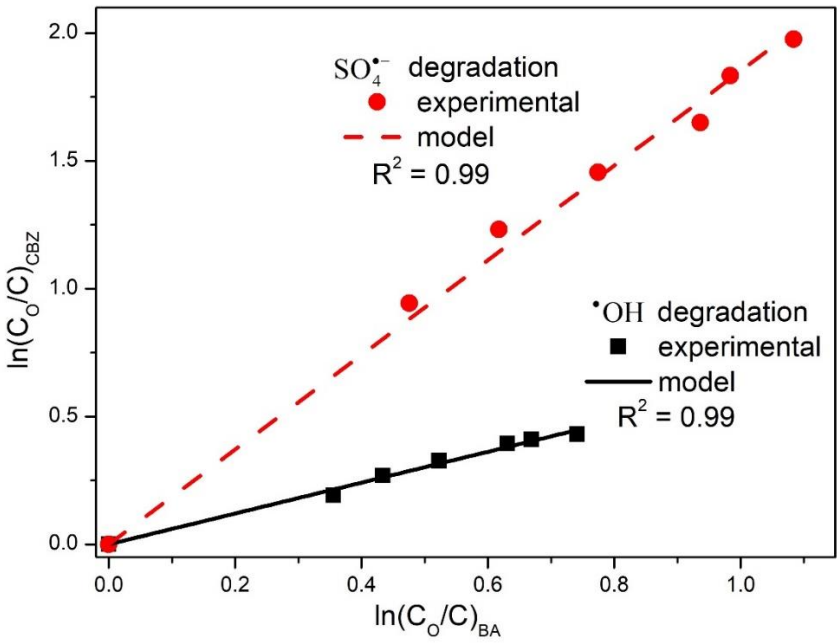

Figure 6.3: Determination of kinetic constants of CBZ degradation by •OH and $SO_4^{\bullet-}$ radicals using relative reference technique

Mass balance equations : Pseudo steady–state approximation was also used to calculate the kinetics of CBZ oxidation by reactive radicals like •OH and $SO_4^{\bullet-}$. Various reactions in the photo Fenton/persulfate system along with their kinetic constants, as reported in literature, are listed in Table 6.2. For the simplicity, the kinetic modelling was categorized into different sections, viz. photo–induced reactions, inorganic bulk reactions with $S_2O_8^{2-}$, bulk Fenton reactions with iron oxides and oxygen species, inorganic bulk reactions with H_2O_2 and main CBZ degradation reactions. Here, sulfate radicals are produced by the activation of persulfate through hydrodynamic cavitation, UV, $ZnO/ZnFe_2O_4$.

Table 6.2: The reactions and rate constants used in kinetic modelling for Carbamazepine (CBZ) degradation

Sr. No.	Reaction	k ($M^{-1}s^{-1}$)	Reference
		Photo induced reactions	
R1	$S_2O_8^{2-} \xrightarrow{UV} 2SO_4^{\bullet-}$	$r_{S_2O_8^{2-},UV} = -r_{SO_4^{\bullet-},UV}/2 = -I_0\phi_{S_2O_8^{2-}} f_{S_2O_8^{2-}}(1-e^{-A_0})$, s^{-1} $A_0 = 2.303 \cdot b \cdot \left(\sum_i \varepsilon_i C_i\right)$ $f_{[S_2O_8^{2-}]} = 2.303 \cdot b \cdot \varepsilon_{[S_2O_8^{2-}]} \cdot [S_2O_8^{2-}]/A_0$ $\phi_{S_2O_8^{2-}}$ = 0.567 mole/Einstein (Heidt et al., 1948) ε = 21.379 M^{-1} cm^{-1}	Crittenden et al. (1999), Luo et al. (2015)
		Inorganic bulk reactions with $S_2O_8^{2-}$	
R2	$S_2O_8^{2-} + Fe^{2+} \longrightarrow Fe^{3+} + SO_4^{2-} + SO_4^{\bullet-}$	27	Roy and Moholkar (2020a)
R3	$S_2O_8^{2-} + {}^{\bullet}OH \longrightarrow S_2O_8^{\bullet-} + OH^-$	1.4×10^7	Roy and Moholkar (2020a)
R4	$Fe^{2+} + SO_4^{\bullet-} \longrightarrow Fe^{3+} + SO_4^{2-}$	3×10^8	Roy and Moholkar (2020b)
R5	$Fe^{3+} + SO_4^{\bullet-} \longrightarrow Fe^{2+} + SO_4^{2-}$	4.6×10^9	Roy and Moholkar (2020b)
R6	$SO_4^{\bullet-} + S_2O_8^{2-} \longrightarrow SO_4^{2-} + S_2O_8^{\bullet-}$	6.1×10^5	Hanci et al. (2013)
R7	$SO_4^{\bullet-} + SO_4^{\bullet-} \longrightarrow S_2O_8^{2-}$	4.0×10^8	Hanci et al. (2013)

	Reaction	k ($M^{-1}s^{-1}$)	Reference
	Bulk Fenton reactions with iron oxides and oxygen species		
R8	$Fe^{2+} + H_2O_2 \longrightarrow Fe^{3+} + {}^{\bullet}OH + OH^-$	70	Roy and Moholkar (2020a)
R9	$Fe^{2+} + {}^{\bullet}OH \longrightarrow Fe^{3+} + OH^-$	3.2×10^8	Kang et al. (2002)
R10	$Fe^{2+} + HO_2^{\bullet} \longrightarrow Fe^{3+} + HO_2^-$	1.2×10^6	Kušić et al. (2006)
R11	$Fe^{2+} + O_2^{\bullet-} \longrightarrow Fe^{3+} + O_2$	1×10^7	Burbano et al. (2005)
R12	$Fe^{3+} + H_2O_2 \longrightarrow Fe^{2+} + H^+ + HO_2^{\bullet}$	0.02	Kušić et al. (2006)
R13	$Fe^{3+} + HO_2^{\bullet} \longrightarrow Fe^{2+} + O_2 + H^+$	3.1×10^5	Kang et al. (2002)
R14	$Fe^{3+} + O_2^{\bullet-} \longrightarrow Fe^{2+} + O_2$	1.5×10^8	Burbano et al. (2005)
	Inorganic bulk reactions with H_2O_2		
R15	${}^{\bullet}OH + H_2O_2 \longrightarrow HO_2^{\bullet} + H_2O$	3.3×10^7	Roy and Moholkar (2020b)
R16	${}^{\bullet}OH + H_2O_2 \longrightarrow O_2^{\bullet-} + H_2O$	2.7×10^7	Kušić et al. (2011)
R17	$HO_2^{\bullet} + H_2O_2 \longrightarrow H_2O + {}^{\bullet}OH + O_2$	3	Crittenden et al. (1999)
R18	$O_2^{\bullet-} + HO_2^{\bullet} \longrightarrow HO_2^- + O_2$	9.7×10^7	Kušić et al. (2011)
R19	$HO_2^{\bullet} + {}^{\bullet}OH \longrightarrow H_2O + O_2$	0.71×10^{10}	Gallard and Laat (2000)
R20	${}^{\bullet}OH + {}^{\bullet}OH \longrightarrow H_2O_2$	5.3×10^9	Burbano et al. (2005)
R21	$HO_2^{\bullet} + HO_2^{\bullet} \longrightarrow H_2O_2 + O_2$	8.5×10^5	Burbano et al. (2005)
	CBZ degradation reactions		
R22	$CBZ + UV \longrightarrow H_2O + CO_2 + products$	$r_{[CBZ],\,UV} = I_0 \cdot \phi_{[CBZ]} \cdot f_{[CBZ]} \cdot (1 - e^{-A_0})$ $A_0 = 2.303 \cdot b \cdot \left(\sum_i \varepsilon_i C_i \right)$ $f_{[CBZ]} = 2.303 \cdot \varepsilon_{[CBZ]} \cdot b \cdot [CBZ] / A_0$	This Study
R23	$CBZ + {}^{\bullet}OH \longrightarrow H_2O + CO_2 + products$	3.6×10^9	This Study
R24	$CBZ + SO_4^{\bullet-} \longrightarrow H_2O + CO_2 + products$	2.2×10^9	This Study

Mass balances for different species can be written as follows:

$$\frac{d[CBZ]}{dt} = -r_{[CBZ],UV} - k_{23}[CBZ][^{\bullet}OH] - k_{24}[CBZ][SO_4^{\bullet-}] \quad 6.5$$

$$\frac{d[SO_4^{\bullet-}]}{dt} = r_{SO_4^{\bullet-},UV} + k_2[S_2O_8^{2-}][Fe^{2+}] - k_4[Fe^{2+}][SO_4^{\bullet-}] - k_5[Fe^{3+}][SO_4^{\bullet-}] - k_6[SO_4^{\bullet-}][S_2O_8^{2-}] - k_7[SO_4^{\bullet-}][SO_4^{\bullet-}] - k_{24}[CBZ][SO_4^{\bullet-}] \quad 6.6$$

$$\frac{d[^{\bullet}OH]}{dt} = -k_3[S_2O_8^{2-}][^{\bullet}OH] + k_8[Fe^{2+}][H_2O_2] - k_9[Fe^{2+}][^{\bullet}OH] - k_{15}[^{\bullet}OH][H_2O_2] - k_{16}[^{\bullet}OH][H_2O_2] + k_{17}[HO_2^{\bullet}][H_2O_2] - k_{19}[HO_2^{\bullet}][^{\bullet}OH] - k_{20}[^{\bullet}OH][^{\bullet}OH] - k_{23}[CBZ][^{\bullet}OH] \quad 6.7$$

$$\frac{d[O_2^{\bullet-}]}{dt} = -k_{11}[Fe^{2+}][O_2^{\bullet-}] - k_{14}[Fe^{3+}][O_2^{\bullet-}] + k_{16}[^{\bullet}OH][H_2O_2] - k_{18}[O_2^{\bullet-}][HO_2^{\bullet}] \quad 6.8$$

$$\frac{d[HO_2^{\bullet}]}{dt} = -k_{10}[Fe^{2+}][HO_2^{\bullet}] + k_{12}[Fe^{3+}][H_2O_2] - k_{13}[Fe^{3+}][HO_2^{\bullet}] + k_{15}[^{\bullet}OH][H_2O_2] - k_{17}[HO_2^{\bullet}][H_2O_2] - k_{18}[O_2^{\bullet-}][HO_2^{\bullet}] - k_{19}[HO_2^{\bullet}][^{\bullet}OH] - k_{21}[HO_2^{\bullet}][HO_2^{\bullet}] \quad 6.9$$

$$\frac{d[H_2O_2]}{dt} = -k_8[Fe^{2+}][H_2O_2] - k_{12}[Fe^{3+}][H_2O_2] - k_{15}[^{\bullet}OH][H_2O_2] - k_{16}[^{\bullet}OH][H_2O_2] - k_{17}[HO_2^{\bullet}][H_2O_2] + k_{20}[^{\bullet}OH][^{\bullet}OH] + k_{21}[HO_2^{\bullet}][HO_2^{\bullet}] \quad 6.10$$

$$\frac{d[S_2O_8^{2-}]}{dt} = -r_{S_2O_8^{2-},UV} - k_2[S_2O_8^{2-}][Fe^{2+}] - k_3[S_2O_8^{2-}][^{\bullet}OH] - k_6[S_2O_8^{2-}][SO_4^{\bullet-}] + k_7[SO_4^{\bullet-}][SO_4^{\bullet-}] \quad 6.11$$

$$\frac{d[Fe^{2+}]}{dt} = -k_2[Fe^{2+}][S_2O_8^{2-}] - k_4[Fe^{2+}][SO_4^{\bullet-}] + k_5[Fe^{3+}][SO_4^{\bullet-}] - k_8[Fe^{2+}][H_2O_2] - k_9[Fe^{2+}][^{\bullet}OH] - k_{10}[Fe^{2+}][HO_2^{\bullet}] - k_{11}[Fe^{2+}][O_2^{\bullet-}] + k_{12}[Fe^{3+}][H_2O_2] + k_{13}[Fe^{3+}][HO_2^{\bullet}] + k_{14}[Fe^{3+}][O_2^{\bullet-}] \quad 6.12$$

$$\frac{d\left[Fe^{3+}\right]}{dt} = k_2\left[Fe^{2+}\right]\left[S_2O_8^{2-}\right] + k_4\left[Fe^{2+}\right]\left[SO_4^{\bullet-}\right] - k_5\left[Fe^{3+}\right]\left[SO_4^{\bullet-}\right]$$
$$+k_8\left[Fe^{2+}\right]\left[H_2O_2\right] + k_9\left[Fe^{2+}\right]\left[^{\bullet}OH\right] + k_{10}\left[Fe^{2+}\right]\left[HO_2^{\bullet}\right] \qquad 6.13$$
$$+k_{11}\left[Fe^{2+}\right]\left[O_2^{\bullet-}\right] - k_{12}\left[Fe^{3+}\right]\left[H_2O_2\right] - k_{13}\left[Fe^{3+}\right]\left[HO_2^{\bullet}\right] - k_{14}\left[Fe^{3+}\right]\left[O_2^{\bullet-}\right]$$

The four radical species in the reaction system, $SO_4^{\bullet-}$, $^{\bullet}OH$, $HO_2^{\bullet}$ and $O_2^{\bullet-}$ are extremely reactive and unstable. We have made the assumption of pseudo steady state for these unstable species. Thus, the time derivatives (or mass balance equations) for these species can be set to zero. This yields their pseudo steady state concentration as:

$$\left[SO_4^{\bullet-}\right] = \frac{r_{SO_4^{\bullet-},UV} + k_2\left[S_2O_8^{2-}\right]\left[Fe^{2+}\right]}{k_4\left[Fe^{2+}\right] + k_5\left[Fe^{3+}\right] + k_6\left[S_2O_8^{2-}\right] + k_7\left[SO_4^{\bullet-}\right] + k_{24}\left[CBZ\right]} \qquad 6.14$$

$$\left[^{\bullet}OH\right] = \frac{k_8\left[Fe^{2+}\right]\left[H_2O_2\right] + k_{17}\left[HO_2^{\bullet}\right]\left[H_2O_2\right]}{k_3\left[S_2O_8^{2-}\right] + k_9\left[Fe^{2+}\right] + k_{15}\left[H_2O_2\right] + k_{16}\left[H_2O_2\right] + k_{19}\left[HO_2^{\bullet}\right]} \qquad 6.15$$
$$+k_{20}\left[^{\bullet}OH\right] + k_{23}\left[CBZ\right]$$

$$\left[O_2^{\bullet-}\right] = \frac{k_{16}\left[^{\bullet}OH\right]\left[H_2O_2\right]}{k_{11}\left[Fe^{2+}\right] + k_{14}\left[Fe^{3+}\right] + k_{18}\left[HO_2^{\bullet}\right]} \qquad 6.16$$

$$\left[HO_2^{\bullet}\right] = \frac{k_{12}\left[Fe^{3+}\right]\left[H_2O_2\right] + k_{15}\left[^{\bullet}OH\right]\left[H_2O_2\right]}{k_{10}\left[Fe^{2+}\right] + k_{13}\left[Fe^{3+}\right] + k_{17}\left[H_2O_2\right] + k_{18}\left[O_2^{\bullet-}\right] + k_{19}\left[^{\bullet}OH\right]} \qquad 6.17$$
$$+k_{21}\left[HO_2^{\bullet}\right]$$

The ordinary differential eqs. for the other species, viz. CBZ, $S_2O_8^{2-}$, Fe^{2+}, Fe^{3+} and H_2O_2 were solved after substitution of pseudo–steady state expressions for radical species. Runge–Kutta 4th order – 5th order method (adaptive step size) method was employed for numerical solution.

6.3 RESULTS AND DISCUSSION

6.3.1 Characterization of octahedral ZnO/$ZnFe_2O_4$

The XRD pattern (Fig. 6.4) of the ZnO/$ZnFe_2O_4$ nanocomposite displays sharp diffraction peaks indexed to (1 1 1), (2 2 0), (3 1 1), (2 2 2), (4 0 0), (4 2 2), (5 1 1), (4 4 0), (6 2 0) and (5 3 3) crystal planes of $ZnFe_2O_4$ (JCPDS Card No. 22–1012) as well as (1 0 0), (0 0 2), (1 0 1), (1 0 2), (1 1 0), (1 0 3), (1 1 2) and (2 0 1) planes of ZnO (JCPDS Card No.36–1451). The narrow and sharp diffraction peaks reveal that ZnO and $ZnFe_2O_4$ are highly crystallized. No other phases can be found in the ZnO/$ZnFe_2O_4$ nanocomposite, suggesting that no impurity species were formed between ZnO and $ZnFe_2O_4$. The crystallite sizes of ZnO/$ZnFe_2O_4$ estimated from the peak broadening using Scherer's equation as shown in Table 6.3.

Representative field-emission scanning electron microscope (FE–SEM) and transmission electron microscopy (TEM) images of the synthesized nanocomposite are shown in Figs. 6.5(A) and (B). Well-defined uniform octahedra nanoparticles were obtained with uniform edges of particles using hydrothermal method. From the HR–TEM micrograph (Fig. 6.5D), clear lattice fringes can be observed. The lattice fringes with the spacings of 2.47 Å and 2.8 Å can be indexed to the (2 2 2) plane in $ZnFe_2O_4$ and the (1 0 0) plane in ZnO, respectively, which essentially support the formation of ZnO/$ZnFe_2O_4$ composite phase. The selected area electron diffraction (SAED) pattern (Fig. 6.5C) with a series of concentric rings reveals the polycrystallinity of ZnO/$ZnFe_2O_4$ composite which matches well with (0 0 2), (1 0 2), (1 1 0), (1 0 3) planes for ZnO, and (2 2 2), (5 1 1), (4 4 0) planes for $ZnFe_2O_4$, respectively. Moreover, the SAED pattern reveals the clearly discrete diffraction cycles, suggesting the crystalline nature of octahedral shaped ZnO/$ZnFe_2O_4$ particles. The EDX spectra (Fig. 6.6) of the selected individual ZnO/$ZnFe_2O_4$ particle

shows that the elements of Zn, Fe and O are uniformly dispersed throughout the composite. In addition, Table 6.4 shows the elemental composition of $ZnO/ZnFe_2O_4$.

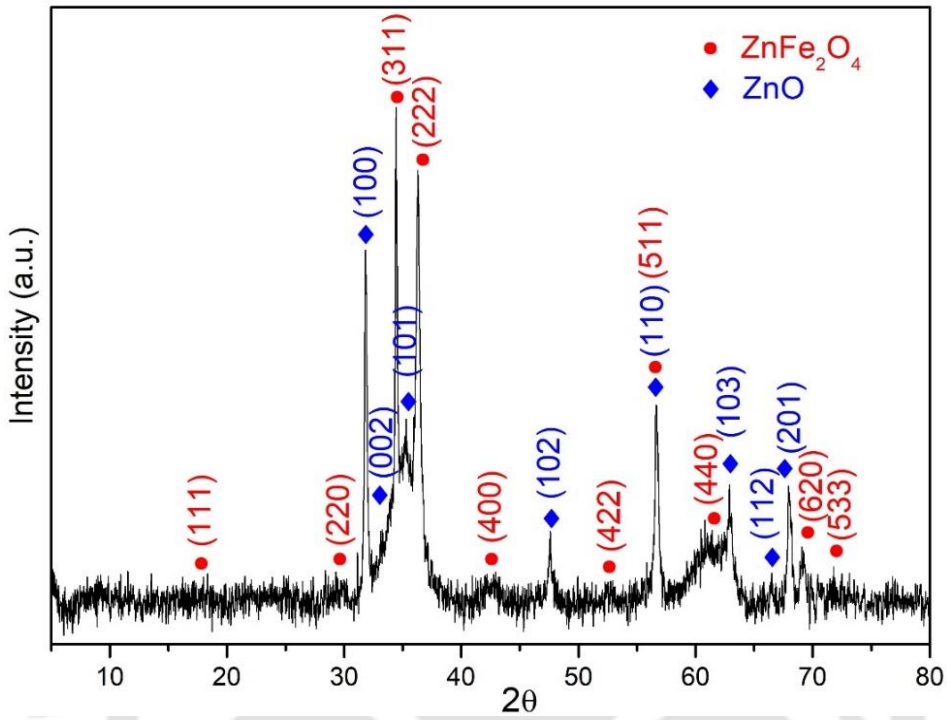

Figure 6.4: XRD pattern for the as prepared nanocomposite

Table 6.3: 2θ values with crystallites size (D_{hkl}) for octahedral $ZnO/ZnFe_2O_4$

2θ (deg)	h k l	Size (Å)
31.8316	1 0 0	380.2
33.8887	0 0 2	76.76
34.4351	3 1 1	750.96
35.2409	1 0 1	75.65
36.3018	2 2 2	230.97
47.621	1 0 2	272.5
56.6446	1 1 0 or 5 1 1	393.32
61.3275	4 4 0	29.84
62.9023	1 0 3	322.53
67.9517	2 0 1	384.57
69.0717	6 2 0	252.19

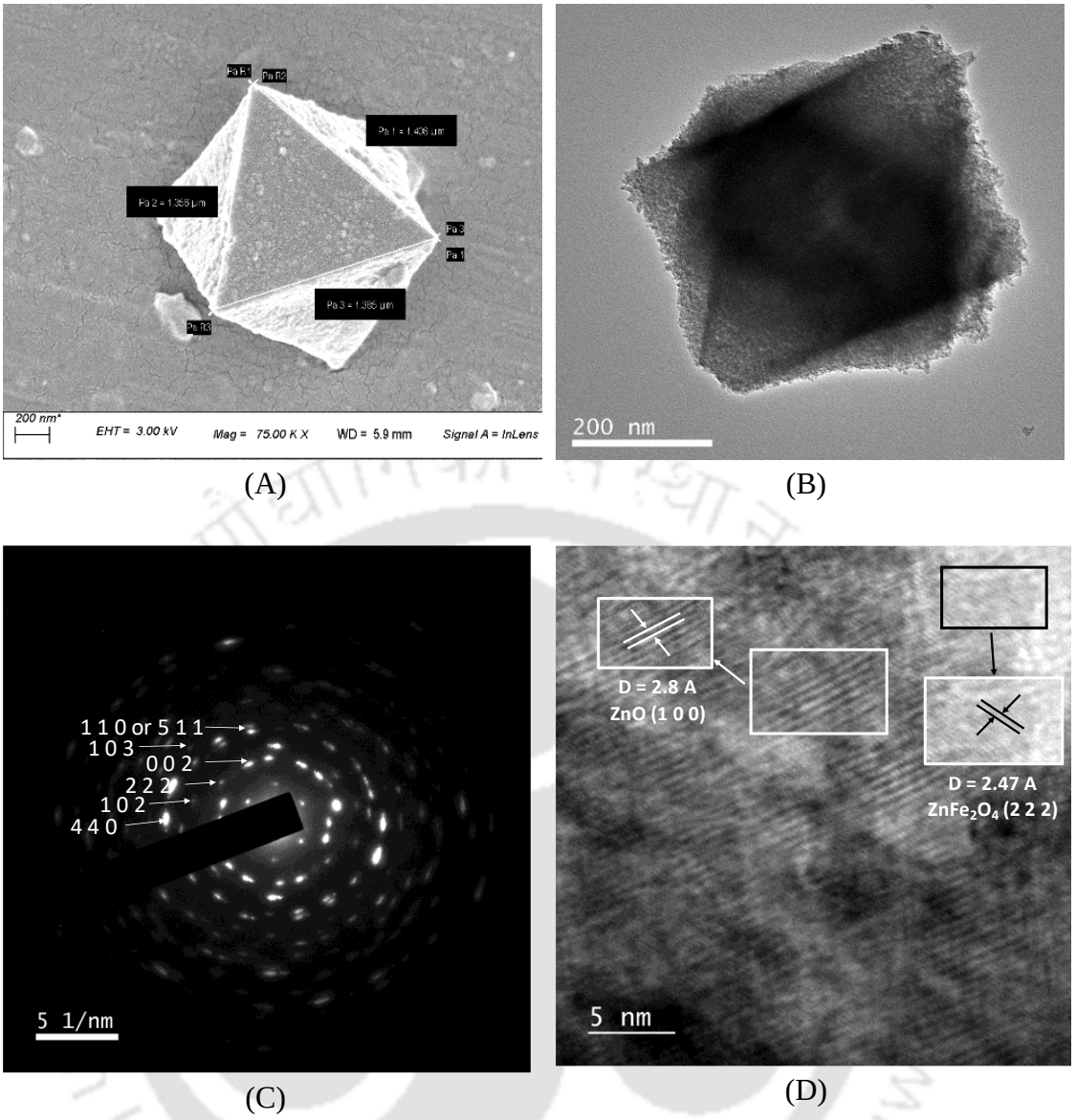

Figure 6.5: (A) FE–SEM micrograph, (B) TEM micrograph, (C) SAED pattern (D) HR–TEM images of ZnO/$ZnFe_2O_4$ nanocomposite.

Table 6.4: Elemental composition of ZnO/$ZnFe_2O_4$

Element	Weight (%)	Atomic (%)
O K	32.88	65.36
Fe K	23.92	13.63
Zn K	43.20	21.02

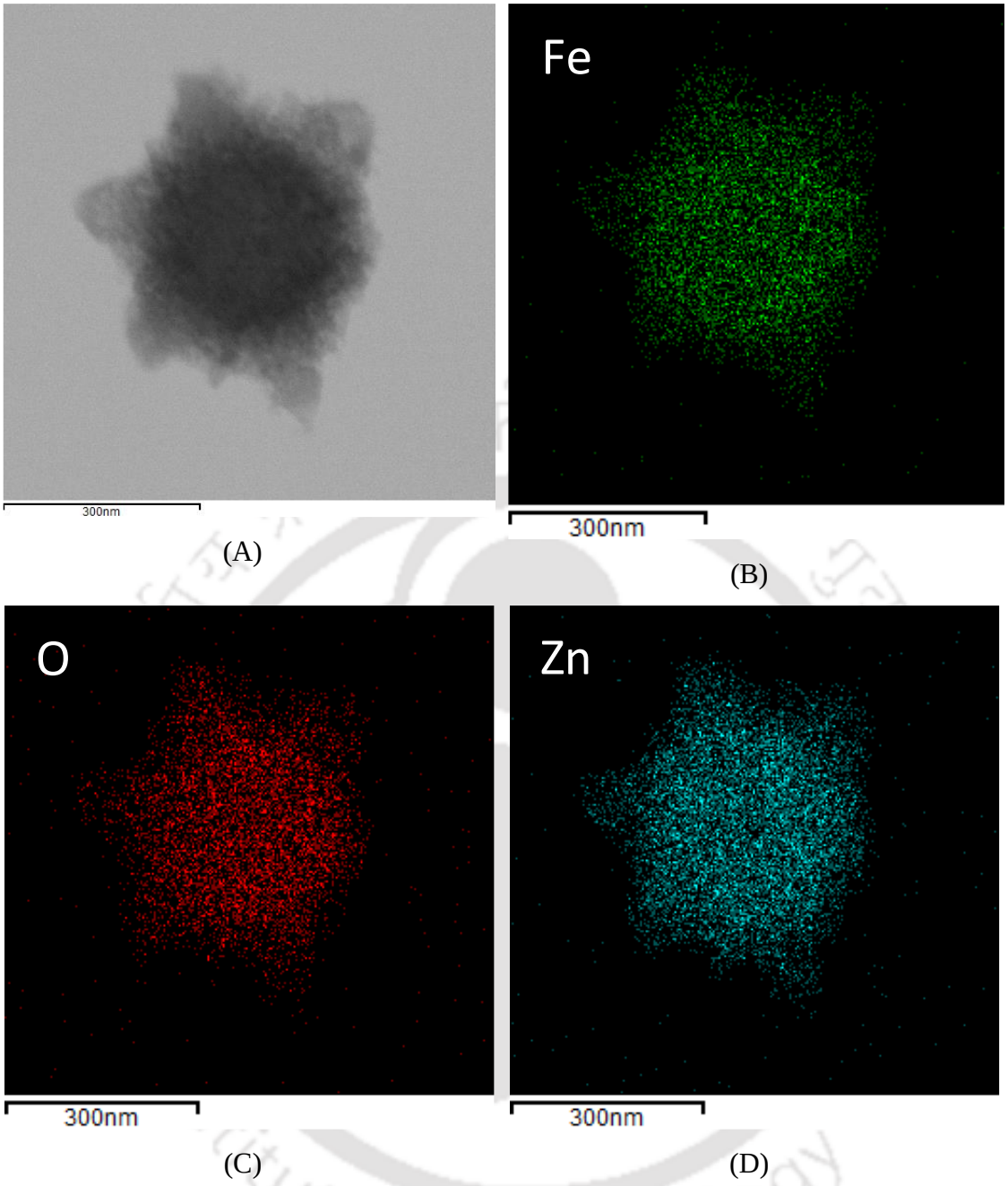

Figure 6.6: EDX elemental mapping images to the corresponding area of $ZnO/ZnFe_2O_4$

The Brunauer–Emmett–Teller (BET) surface area and specific pore structure of the $ZnO/ZnFe_2O_4$ composite were analyzed with N_2 adsorption-desorption isotherm measurements at a temperature of 77 K. A large surface area can provide more active sites for oxidative degradation. The BET measurements show that the as–synthesized

$ZnO/ZnFe_2O_4$ particles possess a BET specific surface area of 224.83 m^2/g and average pore size of 5.88 nm by BJH method (as shown in Fig. 6.7(A)).

The magnetization–magnetic field (M–H) hysteresis loops of the $ZnO/ZnFe_2O_4$ particles are shown in Fig. 6.7(B). The results indicate that the composites are magnetic, and the saturation magnetization (Ms) of $ZnO/ZnFe_2O_4$ is 4.84 emu/g, which is large enough for magnetic separation in practical applications.

The bandgap energy of $ZnO/ZnFe_2O_4$ particles was determined through Touc' plot method based on direct transition using UV–Vis spectrophotometer, expressed as: $(\alpha hv)^n = A(hv - E_g)$, E_g = the optical band gap energy of samples, α = absorbance coefficient, hv = incident light intensity, A = constant, and n = 2 (direct transition). From Fig. 6.7(C), the band gaps of ZnO and $ZnO/ZnFe_2O_4$ are calculated to be 3.06 and 2.69 eV, respectively. Lower bandgap energy of nanocomposite $ZnO/ZnFe_2O_4$ could easily excite the electron/hole pair from the surface of photocatalyst.

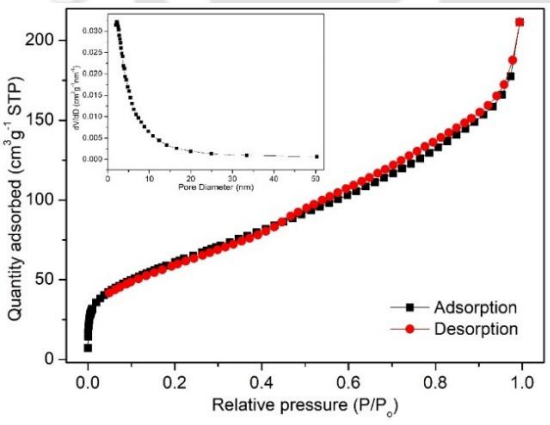

(A)

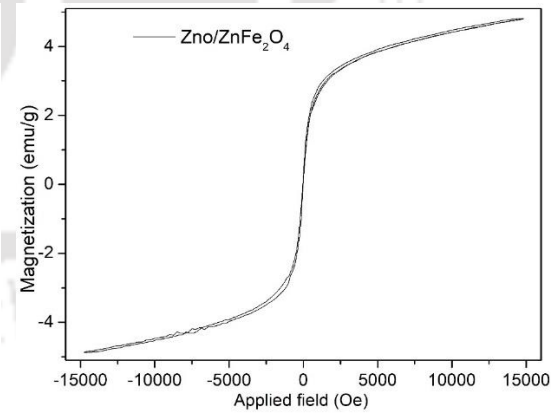

(B)

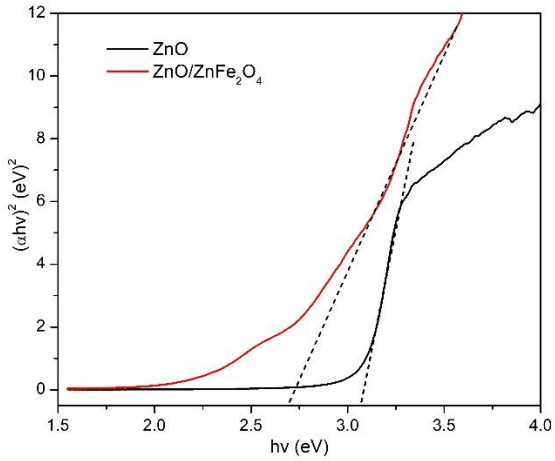

(C)

Figure 6.7: (A) N_2 adsorption–desorption isotherms and pore–size distribution (inset: the pore size of $ZnO/ZnFe_2O_4$ by BJH method), (B) Magnetic hysteresis loop of $ZnO/ZnFe_2O_4$ at room temperature (C) Optical bandgap energy (E_g) for ZnO and $ZnO/ZnFe_2O_4$

6.3.2 Optimization of process parameters for CBZ degradation

The kinetics and extent of degradation of CBZ depend on the experimental conditions. To assess this dependence, extensive experimentation was conducted with varying operating parameters, as listed in Table 6.5.

Table 6.5: The operational conditions of CBZ degradation

Parameter	Range
Inlet pressure	4–10 atm
pH	4–10
Initial concentration of CBZ	15–25 ppm
UV power	6–18 W
$ZnO/ZnFe_2O_4$ loading	100 – 700 ppm
$Na_2S_2O_8$ loading	100 – 700 ppm

The effect of inlet pressure on the extent of degradation of CBZ in the range 4–10 atm has been studied, and the results are shown in Table 6.6. It can be observed that the extent of degradation increases with inlet pressure till 9 atm. Further rise in inlet pressure

resulted in only marginal increase in the extent of degradation. The cavitation intensity rises proportionately with inlet pressure (as cavitation number is lowered). However, further increase in pressure beyond optimum value leads to the formation of cavity cloud which in turn reduces cavitational intensity resulting in a decrease in the extent of degradation. The inlet pressure of the cavitation pump was maintained at 9 atm in all experiments (Thanekar et al., 2018).

The effect of pH on the extent of degradation was assessed at varying pH, viz. acidic (pH = 4), neutral (pH = 7) and basic (pH = 10). The results of the extent of degradation are shown in Table 6.6. The minimum degradation was 31.64% at pH 10, whereas maximum degradation of 41.33 % was achieved at pH 4. Under the acidic conditions, generation of $^{\bullet}OH$ radical is favoured as its oxidation potential is higher (Ghauch et al., 2011).

A plausible explanation for hybrid system could be given as follows: (A) CBZ is a nonvolatile organics compound and it exists in molecular form at acidic condition. Hydrophobic nature of CBZ molecules accelerated the degradation under acidic condition in which CBZ would be in molecular form (Rao et al., 2016). CBZ molecules adhere on the gas-liquid interface of cavitation bubble and dissociated at the time of bubble collapse. On the other hand, CBZ exist in ionized state at pH neutral and basic condition. Its hydrophilicity nature limit CBZ molecules to reach at interface of the cavitational bubbles. (B) At acid conditions, a rapid transformation of persulfate into $SO_4^{\bullet-}$ was favoured due to formation of $HS_2O_8^-$ ($S_2O_8^{2-} + H^+ \longrightarrow HS_2O_8^-$) and further dissociation of $HS_2O_8^-$ into $SO_4^{\bullet-}$ and SO_4^{2-} ($HS_2O_8^- \longrightarrow SO_4^{\bullet-} + SO_4^{2-} + H^+$). However, additional generated $SO_4^{\bullet-}$ may cause quenching with persulfate ions ($S_2O_8^{2-} + SO_4^{\bullet-} \longrightarrow SO_4^{2-} + S_2O_8^{\bullet-}$) or self-quenching ($SO_4^{\bullet-} + SO_4^{\bullet-} \longrightarrow S_2O_8^{2-}$) in the bulk reaction medium (Al Hakim et al., 2020). Thus, the presence of CBZ in an acidic

medium allows the persulfate–induced radicals to be partially quenched. At higher pH, hydroxide ions (OH^-) quench the $SO_4^{\bullet-}$ radicals to generate sulfate anions (SO_4^{2-}) and the generated hydroxyl radical was less potent at alkaline condition. $SO_4^{\bullet-} + OH^- \longrightarrow SO_4^{2-} + OH^\bullet$ $k = 6.5 \times 10^7$ M^{-1} s^{-1}. (C) CBZ has two pKa values: pka_1 = 2.3 (protonation of the NH_2 group) and pka_2 = 13.9 (deprotonation of the amino group) [17]. Under acid conditions, the CBZ molecule protonated at carbon atom in heterocyclic benzene rings which enhanced the electrostatic attraction of $SO_4^{\bullet-}$. Similar observation was discussed in the degradation path of CBZ molecules where Single electron transfer (SET) was the initial step for the degradation. Higher pH solution ripples the electrostatic force of attraction between CBZ and radical. Leached ions like Fe^{2+}/Fe^{3+} ions generated complexes ($Fe(OH)_3$) at basic medium and reduced the regeneration of Fe^{2+} which ultimately inhibit the formation of $^\bullet OH$. It lead to decrease the activity of catalysts and consequently the degradation of CBZ.

Effect of initial concentration of CBZ on the extent of degradation was investigated by varying initial concentration as 15, 20 and 25. The results of experiment are shown in Table 6.6. It can be seen that percent degradation of CBZ decreases from 41.33 – 25.45% with an increase in initial concentration from 15 to 25 ppm. However, the absolute quantity of CBZ degraded (6.19 and 6.36 ppm for initial concentrations of 15 and 25 ppm) essentially remain constant. This indicates that the degradation of CBZ follows zero order kinetics. This also indicates that CBZ is an excess reactant and the degradation is governed by generation and fruitful consumption (i.e. with interaction with CBZ molecules without recombining) of $^\bullet OH$ radicals (Deng et al., 2013, Wang et al., 2016).

In order to study the efficacy of UV power, degradation of CBZ was studied by inserting a bank of UV tubes inside the feed tank. The UV tube holder could accommodate

maximum of 3 tubes – each with capacity of 6 W. Thus, the UV power could be varied in steps of 6, 12 and 18 W. The maximum extent of degradation (52.9%) was obtained using UV lamps of power 18 W (3 UV tubes) and the least degradation (41.33%) was obtained at 6 W. The UV radiation intensity determines the amount of photons absorbed by the catalysts, viz. $ZnO/ZnFe_2O_4$, and $Na_2S_2O_8$ loading. With increase of UV power, the solid catalysts absorb more photon energy to generate large number of electron–hole pairs on the catalytic surfaces. Generated electron–hole pairs increase the concentration of radicals, viz. $^{\bullet}OH$ and $SO_4^{\bullet-}$ and consequently increases the degradation rate (Zuo et al., 2020).

The influence of $ZnO/ZnFe_2O_4$ loading on CBZ degradation was studied in the range 100 – 500 ppm (with $Na_2S_2O_8$ concentration fixed at 100 ppm). The lowest CBZ degradation was obtained for $[ZnO/ZnFe_2O_4]$:$[Na_2S_2O_8]$ ratio of 1:1. Increasing the quantum of $ZnO/ZnFe_2O_4$ from 1:1 to 7:1 accelerated the CBZ degradation. Higher dosage of $ZnO/ZnFe_2O_4$ particles could improve the generation rate of $^{\bullet}OH$ and $SO_4^{\bullet-}$ radicals, which accelerated the decomposition of CBZ. The highest degradation (73.55%) was obtained for $[ZnO/ZnFe_2O_4]/[Na_2S_2O_8]$ ratio of 5:1. Further increase in $[ZnO/ZnFe_2O_4]/[Na_2S_2O_8]$ ratio leads to reduction in the extent of degradation. A plausible explanation for this reduction is given as follows: the increase in photocatalysts loading may limit the generation and sufficient separation of electron–hole pairs (avoiding recombination) that results in marginal increment in degradation.

$Na_2S_2O_8$ concentration is a critical parameter as the source of sulfate radicals in HC + UV + $ZnO/ZnFe_2O_4$ + $Na_2S_2O_8$ process. A increase in ratio of $[Na_2S_2O_8]/ [ZnO/ZnFe_2O_4]$ form 1:5 to 5:5 lead to an enhancement in CBZ removal efficiency from 71.92 % to 98.13% in 60 min. Approx. complete degradation might be explained by the larger

amount of persulfate that generates larger concentration of $SO_4^{\bullet-}$ radicals. Further increase of persulfate dosage does not result in significant rise in CBZ degradation.

Table 6.6: Apparent pseudo–first–order rate constants of the sonocatalytic process at different operational conditions

Inlet pressure (atm)	pH	$[CBZ]_0$ (ppm)	UV power (W)	ZnO/ $ZnFe_2O_4$ (ppm)	$Na_2S_2O_8$ (ppm)	η (exp)	η (model)
4	6	15	6	100	100	15.93	17.24
5	6	15	6	100	100	23.16	21.18
6	6	15	6	100	100	27.17	25.06
7	6	15	6	100	100	30.78	28.89
8	6	15	6	100	100	33.97	32.68
9	6	15	6	100	100	36.14	36.44
10	6	15	6	100	100	36.79	40.16
9	4	15	6	100	100	41.33	38.57
9	7	15	6	100	100	36.08	35.66
9	10	15	6	100	100	31.64	33.92
9	4	15	6	100	100	41.33	38.57
9	4	20	6	100	100	34.16	33.22
9	4	25	6	100	100	25.45	29.59
9	4	15	6	100	100	41.33	38.57
9	4	15	12	100	100	45.79	46.98
9	4	15	18	100	100	52.09	52.72
9	4	15	18	100	100	52.09	52.72
9	4	15	18	200	100	59.22	59.83
9	4	15	18	300	100	63.85	64.42
9	4	15	18	400	100	68.19	67.89
9	4	15	18	500	100	71.92	70.71
9	4	15	18	600	100	72.66	73.11
9	4	15	18	700	100	73.55	75.19
9	4	15	18	500	100	71.92	70.71
9	4	15	18	500	200	83.92	82.30
9	4	15	18	500	300	91.33	89.94
9	4	15	18	500	400	96.91	95.78
9	4	15	18	500	500	98.13	100.57

6.3.3 Development of empirical correlation and validation

In order to characterize the performance of the reactor in terms of its operational parameters, we relate the percentage degradation obtained in different experiments to the operational parameters in the form of empirical correlation as (Devi et al., 2009; Devi

and Rajashekhar 2011; Marandi et al., 2012, Khataee et al., 2014, 2016, 2018; Daneshvar et al., 2004):

$$\eta = \alpha \cdot (\text{inlet pressure})^{a} \cdot (pH)^{b} \cdot [\text{initial concentration}]^{c} \cdot (\text{UV power})^{d} \times [\text{ZnO/ZnFe}_2\text{O}_4]^{e} \cdot [\text{Na}_2\text{S}_2\text{O}_8]^{f}$$

Non–linear regression analysis was used to estimate the constants *a*, *b*, *c*, *d*, *e* and *f* using the data listed in Table 6.6. To determine the global minimum, the model parameters, viz. *a*, *b*, *c*, *d*, *e* and *f* were calculated with nonlinear programming (NLP) using Microsoft Excel (2016) solver. Generalized reduced gradient (GRG) method, as a deterministic optimization approach, was also used in concurrent analysis of experiment data with proper R^2. The following expression was obtained:

$$\eta = 2.38 \frac{(\text{inlet pressure})^{0.92} (\text{UV power})^{0.28} [\text{ZnO/ZnFe}_2\text{O}_4]^{0.18} [\text{Na}_2\text{S}_2\text{O}_8]^{0.22}}{(\text{pH})^{0.14} [\text{initial concentration}]^{0.52}}$$

For the validation of the empirical model, the experimental and calculated values were compared in Table 6.6. It could be seen that the experimental and simulated values of percentage degradation match very closely that essentially validates the above expression. The best match of the empirical expression obtained using regression analysis is also evident from parity plot shown in Fig. 6.8 with regression coefficient of $R^2 = 0.99$.

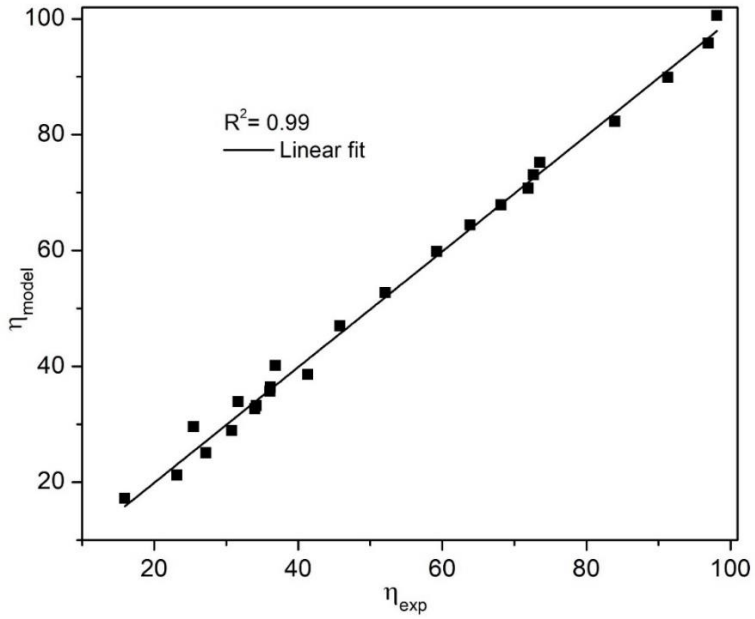

Figure 6.8: Plot of empirical model calculated degradation versus experimental degradation for HC + UV + $ZnO/ZnFe_2O_4$ + $Na_2S_2O_8$ process

6.3.4 Validation of the new photo–Fenton kinetic model

The validation of photo–Fenton processes was performed on the basis of experiments conducted at established optimal operating parameters. With the aim to develop mechanistic model describing that can be used to predict persulfate oxidation activated by either iron oxides, UV or by microturbulence generated though cavitation, the reactions describing the behaviour of heterogeneous processes using $ZnO/ZnFe_2O_4$ as a catalyst in the photo–Fenton reactions are included. Accordingly, previously described methodology for the homogeneous process, the characteristic reactions and rate constants for this heterogeneous process were taken from literature.

Fig. 6.9 (A) compares the simulated degradation profiles of CBZ degradation against the experimental profile of degradation through initial guesses value for ratios of initial $[Fe^{2+}]/[H_2O_2]$ at optimum set of parameters. It could be seen that the best match between experimental and simulated profiles (R^2 = 0.96) is obtained for initial $[Fe^{2+}]/[H_2O_2]$ ratio = 20. Predicted degradation was 94.5% through mechanistic

modelling which is close to experimental degradation as 98%. This result is essentially attributed to high rate of leaching at the surface of $ZnO/ZnFe_2O_4$ particles. The rapid depletion of generated H_2O_2 form HC and regeneration of iron oxides is often observed with Fenton's reagents is probably due to combined reactions R8–R14. However, reactions R8 and R12 are the rate limiting steps of the redox reactions of iron oxides with oxygen species. Ratios of reactive oxygen species (ROS) such as $^{\bullet}OH$, H_2O_2, $O_2^{\bullet-}$, HO_2 with iron oxides signifies the reactivity with CBZ in the bulk solution. High concentration of H_2O_2 is prevalent in the reaction medium due to occurrence of transient cavitation in the medium during 60 min treatment. H_2O_2 generated through transient cavitation can either undergo photolysis under UV irradiation or it can undergo Fenton reaction with Fe^{2+} ions leached out from $ZnO/ZnFe_2O_4$ particles – resulting in generation of $^{\bullet}OH$ radicals that degrade the CBZ molecules. Fig. 6.9 (B) shows the rapid utilization of $S_2O_8^{2-}$ ions in the initial period of treatment. Fe^{2+} ions leached out from $ZnO/ZnFe_2O_4$ particles are predominantly utilized for Fenton reactions due to their high kinetic constants.

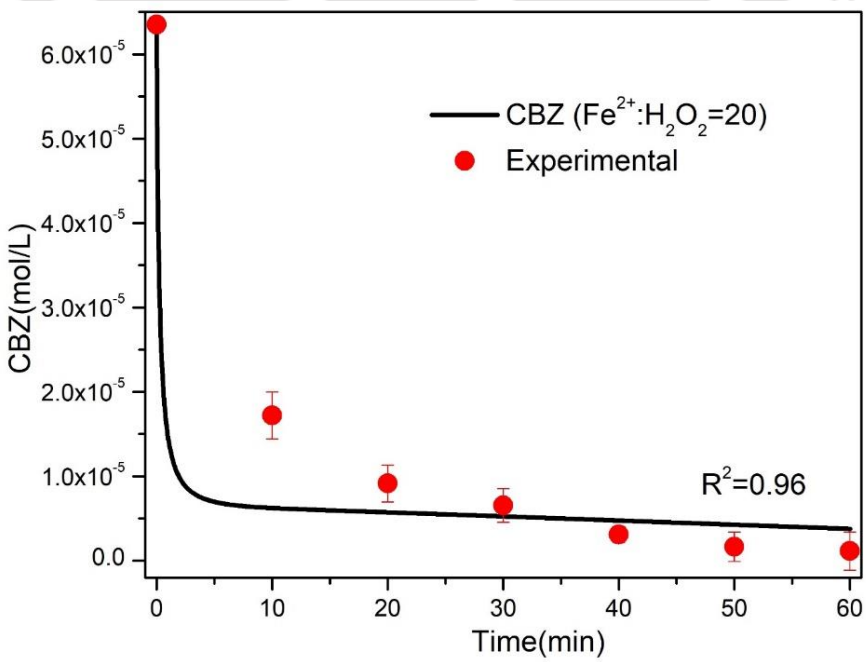

(A)

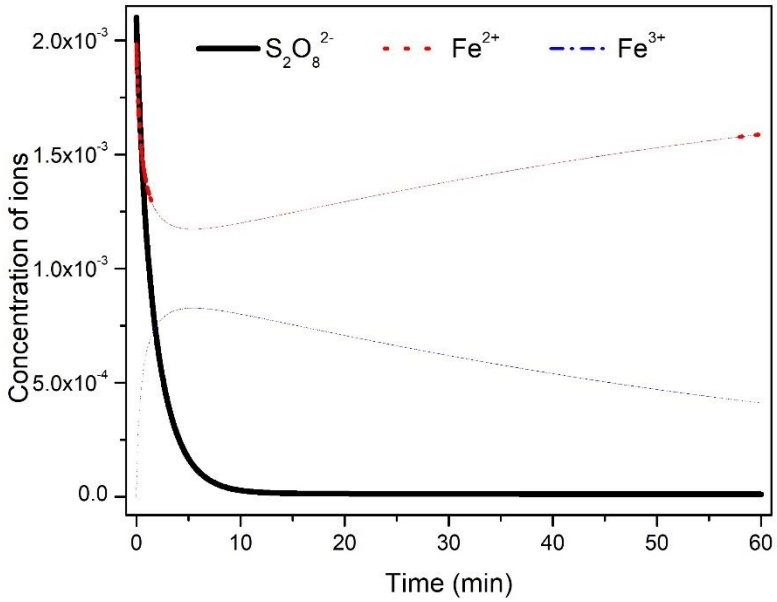

(B)

Figure 6.9: (A) Experimental profile of CBZ degradation in a hybrid AOP of HC/UV/ $ZnO/ZnFe_2O_4/S_2O_8^{2-}$ vis–à–vis simulated profiles of CBZ degradation. (B) time profiles of ions viz. $S_2O_8^{2-}$, Fe^{2+}, Fe^{3+}

6.3.5 Identification of intermediates and degradation pathways of CBZ

Density functional theory (DFT) calculations: DFT calculations were performed to predict the vulnerable sites of CBZ molecules for reactions with either $^{\bullet}OH$ or $SO_4^{\bullet-}$ radicals, and the probable intermediates resulting from the reactions. The global minimum structure of CBZ molecule was optimized using Gaussian 09 at B3LYP/6–31g(d) level of theory. Tables 6.7 and 6.8 show the bond lengths and charge distributions of the optimized structure of CBZ molecule. The atoms with negative charges, viz. 1C, 2C, 5C, 6C, 12C, 13C, 14C, 15C, 21C, 22C for heterocyclic and bilateral benzene ring, and 23N, 27O, 28N, can be vulnerable sites for reactions with radicals. The bonds C3–N23, N23–C11, C16–C22, C21–C4 have higher lengths of 1.431, 1.432, 1.462, 1.462 Å, respectively. Xiao et al. (2020) have demonstrated the probable reaction sites for both $^{\bullet}OH$ and $SO_4^{\bullet-}$ radicals with CBZ molecules on the basis of enthalpy change, Gibbs free energy change and the activation free energy. $^{\bullet}OH$ and $SO_4^{\bullet-}$ radicals have the lowest

activation free energy for the radical addition at position of C22 (Fig. 6.10). The olefinic double bond on the central heterocyclic ring exhibits high degree of reactivity. Similar observation was also made during LC–MS/MS analysis, where C22 was activated through electron transfer before hydroxylation and oxidation.

For $^{\bullet}OH$, it was found that all reactions were thermodynamically favourable except for the two addition sites C16–C11 and C3–C4 due to larger bond length as 1.410 and 1.413 Å, respectively. The addition reactions of C14, C16, C4 and C6 sites by $SO_4^{\bullet-}$ are thermodynamically unfavourable. The single electron transfer (SET) pathway of $SO_4^{\bullet-}$ oxidizing CBZ should be the most favourable site for oxidation.

Table 6.7: Bond lengths (Å) between atoms in optimized structure of CBZ molecule

Bond	Length	Bond	Length	Bond	Length
C1–C2	1.393	N23–C11	1.432	N28–H30	1.011
C2–C3	1.400	C11–C16	1.410	C16–C15	1.40
C3–C4	1.413	C16–C22	1.462	C15–C14	1.390
C4–C5	1.409	C22–C21	1.352	C14–C13	1.398
C5–C6	1.390	C21–C4	1.462	C12–C13	1.392
C6–C1	1.398	C22–H24	1.089	C12–C11	1.397
C1–H7	1.086	C21–H25	1.089	C15–H20	1.087
C2–H8	1.085	N23–C26	1.401	C14–H19	1.086
C5–H9	1.087	C26–O27	1.222	C13–H18	1.086
C6–H10	1.086	C26–N28	1.385	C12–H17	1.084
C3–N23	1.431	N28–H29	1.011		

Table 6.8: Charge of atoms in optimized structure of CBZ molecule

Atom	Charges	Atom	Charges	Atom	Charges	Atom	Charges
1C	–0.148	9H	0.136	17H	0.146	25H	0.134
2C	–0.126	10H	0.135	18H	0.135	26C	0.710
3C	0.135	11C	0.207	19H	0.131	27O	–0.518
4C	0.195	12C	–0.109	20H	0.131	28N	–0.765
5C	–0.212	13C	–0.148	21C	–0.200	29H	0.336
6C	–0.120	14C	–0.118	22C	–0.185	30H	0.341
7H	0.138	15C	–0.211	23N	–0.627		
8H	0.150	16C	0.189	24H	0.138		

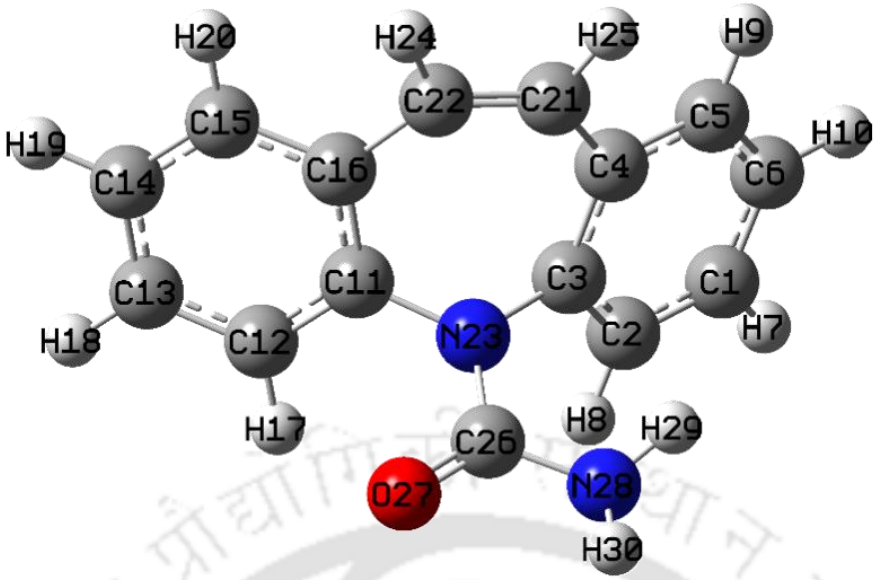

Figure 6.10: Optimized structure of CBZ molecule at B3LYP/6–31g(d) level of theory.

Identification of Intermediates: The identification of the intermediates formed during degradation of CBZ was done using LC–MS/MS for the hybrid AOP of HC + UV + $ZnO/ZnFe_2O_4$ + $Na_2S_2O_8$. Seven intermediates with m/z values 237, 283, 267, 253, 224, 196, 180, 149 were detected, and the possible chemical structures of these species are listed in Table 6.9. Based on these intermediates, a possible pathway of CBZ degradation in the hybrid AOP is shown in scheme 1. Radicals such as $SO_4^{\bullet-}$ and $^{\bullet}OH$ generated in the system can attack at positions 10 and 11 (CH=CH bond) resulting in ionization of the CBZ molecule. Consequently, CBZ undergoes oxidation through one electron transfer (or single electron transfer) oxidation process during reaction with $SO_4^{\bullet-}$, followed by hydroxylation of the CBZ aromatic rings through reaction with $^{\bullet}OH$. Similar observation of ionization of C22 prior to oxidation has also been reported in literature (Xiao et al., 2020) employing the DFT simulations.

A plausible mechanism is one electron transfer oxidation leading to formation of a C–centred radical cation, which is stabilized by resonance. This step might be followed by

hydration, which results in simultaneous formation of intermediates II, III, IV. Ahmed and Chiron (2014) have identified three isobaric species with m/z = 253 (empirical formula $C_{15}H_{13}N_2O_2$) for the degradation of CBZ with hybrid AOP of persulfate/Fe^{2+}/ UV. The intermediate III probably forms from the CBZ molecule through hydroxylation ring contraction. The structure of intermediate IV was assigned to oxcarbazepine resulting from hydroxylation at position 10. The addition of •OH radical to the olefinic double bond (10–11 position) of CBZ could generate an epoxide intermediate of 10,11–epoxycarbamazepine (m/z = 253) (Kosjek et al., 2009; Rao et al. 2014). With addition of •OH radical, the intermediate II (10, 11–epoxycarbamazepine) undergoes hydrolysis to produce glycol, intermediate A (10, 11–dihydro–10, 11–dihydroxycarbamazepine). Intermediate II could oxidize to generate intermediate V, or could undergo ring contraction reaction to form intermediate IV. Hydroxyl radical is also capable of reacting with olefinic double bond by breaking the double bond and generating aldehydes or ketones, such as compound B. A detailed mechanism of ring closure of compound B to quinazoline moiety (VII) is provided elsewhere (McDowell et al., 2005). Intermediate VII could get further oxidized to intermediate XII. Further, intermediates III and VIII could oxidize into intermediate IX (acridine, m/z = 180) and X (acridone, m/z = 196). Further reactions in the pathway can lead to dissociation of these intermediates into smaller molecular weight species like H_2O, CO_2, NO_2 etc.

Table 6.9: Intermediates and products detected by LC–MS/MS during CBZ degradation by HC assisted UV/ $Na_2S_2O_8$/ $ZnO/ZnFe_2O_4$ process

Product ID	ESI(+) MS m/z	Formula	Proposed structure	References
I.	237	$C_{15}H_{12}N_2O$	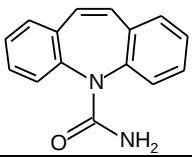	

II.	253	$C_{15}H_{13}N_2O_2$	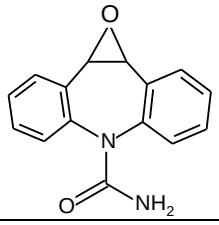	Ahmed and Chiron (2014), Kosjek et al. (2009), Franz et al. (2020)
III.	253	$C_{15}H_{13}N_2O_2$	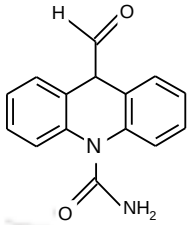	Ahmed and Chiron (2014)
IV.	253	$C_{15}H_{13}N_2O_2$	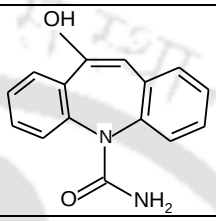	Ahmed and Chiron (2014)
V.	267	$C_{15}H_{10}N_2O_3$	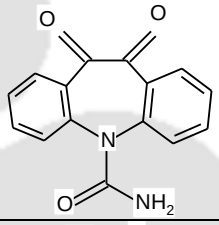	Ahmed and Chiron (2014)
VI.	267	$C_{15}H_{10}N_2O_3$	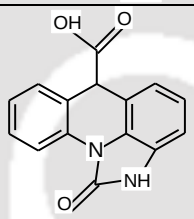	Ahmed and Chiron (2014)
VII.	267	$C_{15}H_{10}N_2O_3$	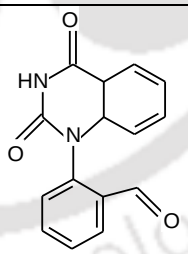	Ahmed and Chiron (2014)
VIII.	224	$C_{14}H_9NO_2$	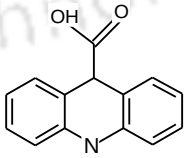	Franz et al. (2020)
IX.	180	$C_{13}H_9N$	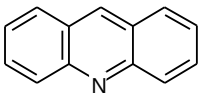	Kosjek et al. (2009), Ahmed and Chiron (2014)
X.	196	$C_{13}H_9NO$	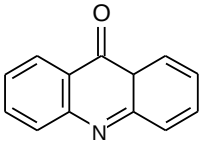	Kosjek et al. (2009), Ahmed and Chiron (2014)

XI.	224	$C_{14}H_9NO_2$	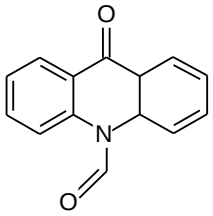	Kosjek et al. (2009)
XII.	283	$C_{15}H_{10}N_2O_4$	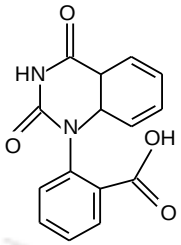	Ahmed and Chiron (2014)
XIII.	149	$C_4H_4O_6$	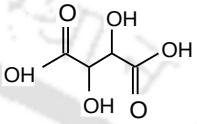	Zhu et al. (2019)

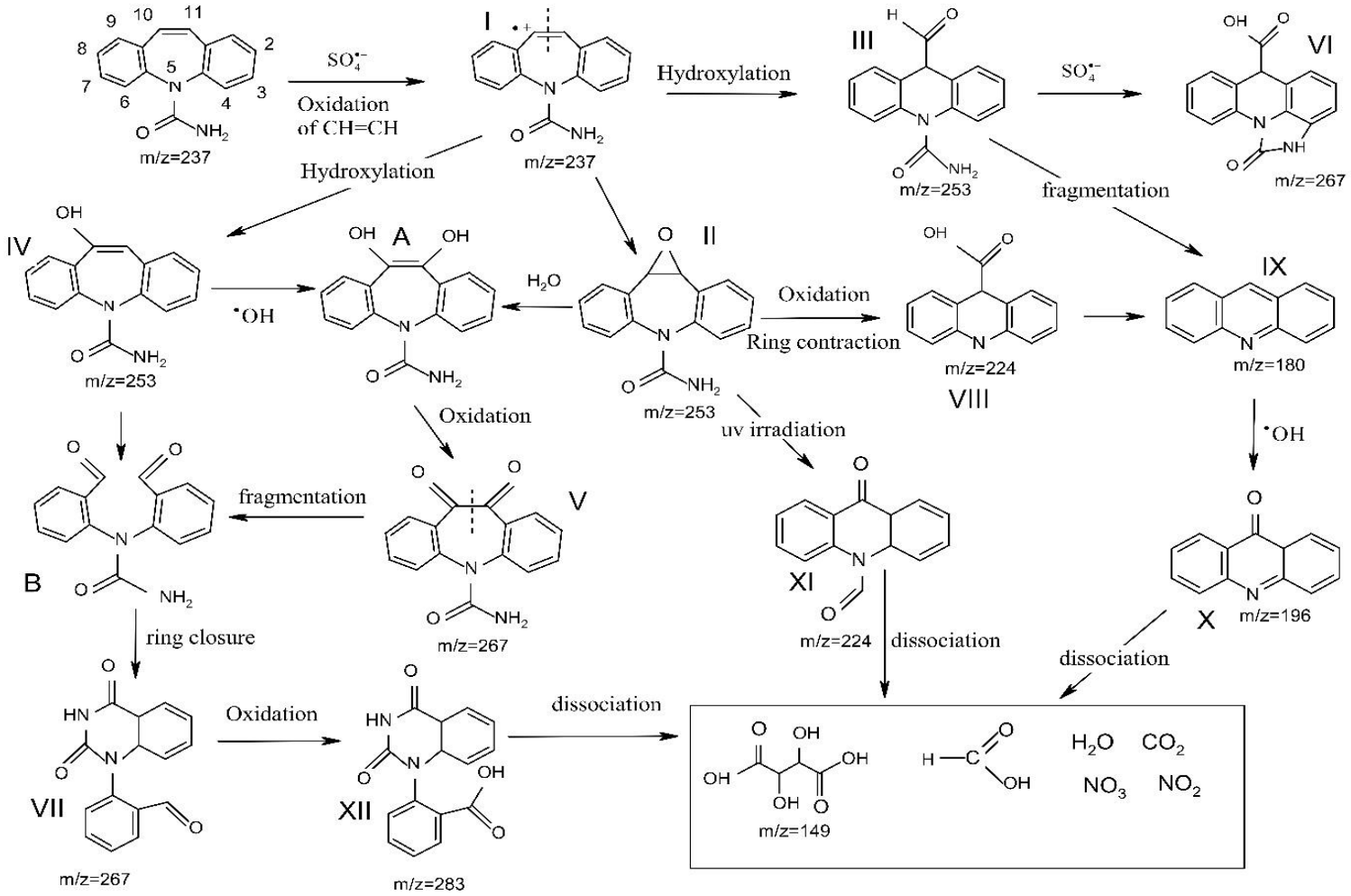

Scheme 1: Proposed CBZ transformation pathways under HC assisted UV + ZnO/ $ZnFe_2O_4$ + $Na_2S_2O_8$ oxidation system

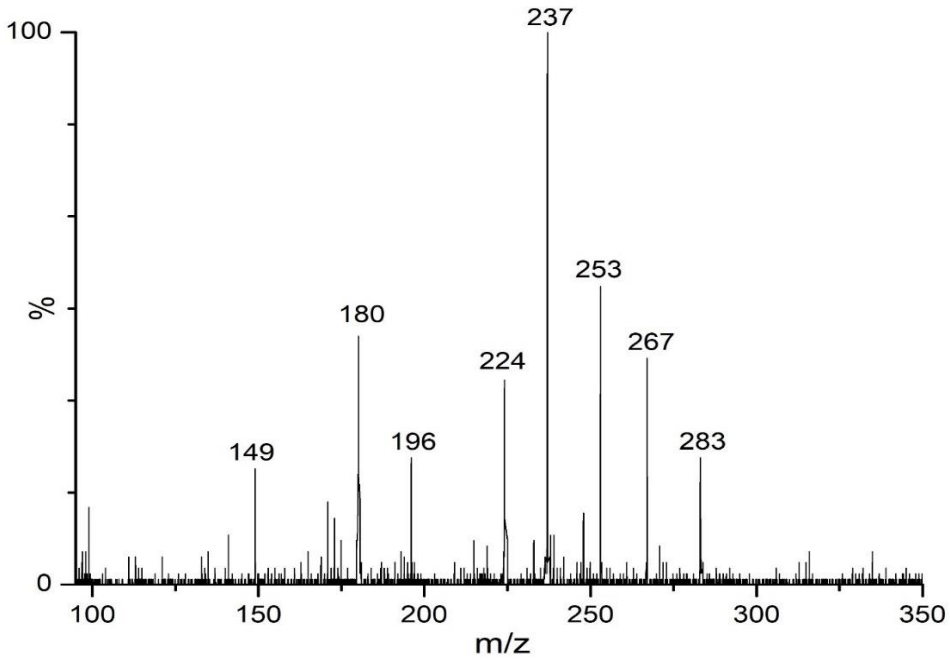

Figure 6.11: ESI–Mass spectra of intermediate metabolites formed during CBZ degradation recorded at 20 min of reaction time.

Table 6.10: Degradation performances of HC based hybrid advanced oxidation process

Hybrid AOP	Extent of degradation (η) %
HC	7.70
HC + UV	22.27
HC + $Na_2S_2O_8$	65.73
HC + $ZnO/ZnFe_2O_4$	18.29
HC + UV + $ZnO/ZnFe_2O_4$	53.26
HC + UV + $ZnO/ZnFe_2O_4$ + $Na_2S_2O_8$	98.13

Degradation performance: In hydrodynamic cavitation–based hybrid advanced oxidation processes, intense shear layer turbulence and *in-situ* generation of •OH radicals causes activation of persulfate ions resulting in generation of $SO_4^{\bullet-}$ radicals that cause maximum degradation of CBZ. Table 6.10 compares the CBZ degradation with HC-based hybrid oxidation processes. In binary AOPs, viz. HC+UV, HC+$Na_2S_2O_8$ and HC+$ZnO/ZnFe_2O_4$, the highest rise in degradation (> 9×) was obtained for HC+$Na_2S_2O_8$

system. Relatively much smaller rise in degradation was obtained for other two systems, viz. HC + UV and HC + $ZnO/ZnFe_2O_4$. The degradation obtained with ternary system of HC+UV+$ZnO/ZnFe_2O_4$ was still smaller than the binary system of HC+$Na_2S_2O_8$. This result is interesting because the ternary system would be mostly dominated with the OH radicals – produced both by hydrodynamic cavitation and photocatalysis of UV and $ZnO/ZnFe_2O_4$. Higher degradation obtained with HC+$Na_2S_2O_8$ signifies greater contribution to CBZ degradation by $SO_4^{\bullet-}$ radicals, as compared to $^{\bullet}OH$ radicals.

In the quaternary system of HC + UV + $Na_2S_2O_8$ + $ZnO/ZnFe_2O_4$, the CBZ degradation is contributed by three possible mechanisms: $^{\bullet}OH$ radicals generated by HC, $SO_4^{\bullet-}$ radicals generated through persulfate activation by both HC and UV, and the $^{\bullet}OH$ radicals generated through photocatalytic mechanism of UV+$ZnO/ZnFe_2O_4$. The population of oxidizing radicals in reaction system is expected to be much higher in case of quaternary systems that results in almost complete degradation of CBZ. As previously discussed in section 6.3.5, higher degradation in presence of $SO_4^{\bullet-}$ radicals is essentially a consequence of ionization of the CBZ molecules through C22 site. The ionized form of CBZ molecule is more susceptible for the degradation by both $SO_4^{\bullet-}$ and $^{\bullet}OH$ radicals.

6.4 CONCLUSIONS

In this chapter, investigations on degradation of carbamazepine have been presented using hydrodynamic cavitation-based hybrid advanced oxidation systems. Hydrodynamic cavitation has been coupled with persulfate system ($Na_2S_2O_8$) and photocatalytic system employing $ZnO/ZnFe_2O_4$ particles. Among several binary, ternary and quaternary hybrid AOPs, the binary system of HC and persulfate (HC+$Na_2S_2O_8$) seemed most effective in boosting the CBZ degradation, as compared to HC alone.

Although the CBZ degradation is contributed by both $^{\bullet}OH$ and $SO_4^{\bullet-}$ radicals, the latter are more effective in degradation. An analysis of the intermediates of CBZ degradation was done with LC–MS/MS analysis. Seven intermediates with m/z values 237, 283, 267, 253, 224, 196, 180, 149 were detected during the oxidation in quaternary hybrid AOP. The analysis of the CBZ molecule using DFT helped in identification of several vulnerable sites for the attack of $^{\bullet}OH$ and $SO_4^{\bullet-}$ radicals. The ionization of CBZ molecule through carbon atoms in heterocyclic and bilateral benzene rings is the key step in the degradation pathway. Thus, hybrid AOPs involving the persulfate system resulted in higher degradation of CBZ – as compared to systems involving only $^{\bullet}OH$ radicals. The empirical correlation relating degradation to the operational parameters revealed inverse relationship with pH and initial concentration. The inlet pressure of hydrodynamic cavitation was the most effective operational parameter governing the degradation. The optimum operational conditions for almost complete CBZ degradation were: inlet pressure = 9 atm, pH = 4, initial concentration of CBZ = 15 ppm, UV power = 18W, $Na_2S_2O_8$ = 500 mg/L, $ZnO/ZnFe_2O_4$ = 500 mg/L.

References

Ahmed, M.M., Chiron, S., Solar photo–Fenton like using persulphate for carbamazepine removal from domestic wastewater. *Water Res.* 48 (2014) 229–236.

Al Hakim, S., Jaber, S., Eddine, N.Z., Baalbaki, A., Ghauch, A., Degradation of theophylline in a UV254/PS system: matrix effect and application to a factory effluent. *Chem. Eng. J.* 380 (2020) 122478.

Daneshvar, N., Rabbani, M., Modirshahla, N., Behnajady, M.A., Kinetic modeling of photocatalytic degradation of Acid Red 27 in UV/TiO_2 process. *J. Photochem. Photobiol. A: Chem.* 168(1–2) (2004) 39–45.

Deng, J., Shao, Y., Gao, N., Xia, S., Tan, C., Zhou, S., Hu, X., Degradation of the antiepileptic drug carbamazepine upon different UV–based advanced oxidation processes in water. *Chem. Eng. J.* 222 (2013) 150–158.

Devi, L.G., Rajashekhar, K.E., A kinetic model based on non–linear regression analysis is proposed for the degradation of phenol under UV/solar light using nitrogen doped TiO2. *J. Mol. Catal. A: Chem.* 334(1–2) 2011 65–76.

Devi, L.G., Rajashekhar, K.E., Raju, K.A., Kumar, S.G., Kinetic modeling based on the non–linear regression analysis for the degradation of Alizarin Red S by advanced photo Fenton process using zero valent metallic iron as the catalyst. *J. Mol. Catal. A: Chem.* 314(1–2) (2009) 88–94.

Gerrity, D., Lee, Y., Gamage, S., Lee, M., Pisarenko, A.N., Trenholm, R.A., Gunten, U., Snyder, S.A., Emerging investigators series: prediction of trace organic contaminant abatement with UV/H_2O_2: development and validation of semi–empirical models for municipal wastewater effluents. *Environ. Sci. Water Res. Technol.* 2(3), (2016) 460–473.

Ghauch, A., Baydoun, H., Dermesropian, P., Degradation of aqueous carbamazepine in ultrasonic/Fe^0/H_2O_2 systems. *Chem. Eng. J.* 172(1) (2011) 18–27.

Heberer, T., Tracking persistent pharmaceutical residues from municipal sewage to drinking water. J. Hydrol. 266(3–4) (2002) 175–189.

Khataee, A., Mohamadi, F.T., Rad, T.S., Vahid, B., Heterogeneous sonocatalytic degradation of anazolene sodium by synthesized dysprosium doped CdSe nanostructures. *Ultrason. Sonochem.* 40 (2018) 361–372.

Khataee, A., Vahid, B., Behjati, B., Safarpour, M., Joo, S.W., Kinetic modeling of a triarylmethane dye decolorization by photoelectro–Fenton process in a recirculating system: nonlinear regression analysis. *Chem. Eng. Res. Des.* 92(2) (2014) 362–367.

Khataee, A., Vahid, B., Saadi, S., Joo, S.W., Development of an empirical kinetic model for sonocatalytic process using neodymium doped zinc oxide nanoparticles. *Ultrason. Sonochem.* 29 (2016) 146–155.

Kosjek, T., Andersen, H.R., Kompare, B., Ledin, A., Heath, E., Fate of carbamazepine during water treatment. *Environ. Sci. Technol.* 43(16) (2009) 6256–6261.

Kušić, H., Koprivanac, N., Božić, A.L., Selanec, I., Photo–assisted Fenton type processes for the degradation of phenol: a kinetic study. *J. Hazard. Mater.* 136(3) (2006) 632–644.

Kušić, H., Peternel, I., Ukic, S., Koprivanac, N., Bolanca, T., Papic, S., Božić, A.L., Modeling of iron activated persulfate oxidation treating reactive azo dye in water matrix. *Chem. Eng. J.* 172(1) (2011) 109–121.

Ling, L., Zhang, D., Fan, C., Shang, C., A Fe (II)/citrate/UV/PMS process for carbamazepine degradation at a very low Fe (II)/PMS ratio and neutral pH: The mechanisms. *Water Res.* 124 (2017) 446–453.

Liu, J., Zeng, M., Yu, R., Surfactant-free synthesis of octahedral $ZnO/ZnFe_2O_4$ heterostructure with ultrahigh and selective adsorption capacity of malachite green. *Sci. Rep.* 6(1) (2016) 1-10.

Marandi, R., Olya, M.E., Vahid, B., Khosravi, M., Hatami, M., Kinetic modeling of photocatalytic degradation of an azo dye using nano–TiO_2/polyester. *Environ. Eng. Sci.* 29(10), (2012) 957–963.

Mcdowell, D.C., Huber, M.M., Wagner, M., von Gunten, U., Ternes, T.A., Ozonation of carbamazepine in drinking water: identification and kinetic study of major oxidation products. *Environ. Sci. Technol.* 39(20) (2005) 8014–8022.

Mohapatra, D.P., Brar, S.K., Daghrir, R., Tyagi, R.D., Picard, P., Surampalli, R.Y., Drogui, P., Photocatalytic degradation of carbamazepine in wastewater by using a new class of whey–stabilized nanocrystalline TiO_2 and ZnO. *Sci. Total Environ.* 485 (2014) 263–269.

Rao, Y., Yang, H., Xue, D., Guo, Y., Qi, F., Ma, J., Sonolytic and sonophotolytic degradation of Carbamazepine: Kinetic and mechanisms. *Ultrason. Sonochem.* 32 (2016) 371-379.

Rao, Y.F., Qu, L., Yang, H., Chu, W., Degradation of carbamazepine by Fe (II)–activated persulfate process. *J. Hazard. Mater.* 268 (2014) 23–32.

Roy, K., Agarkoti, C., Malani, R.S., Thokchom, B., Moholkar, V.S., Mechanistic Study of Sulfadiazine Degradation by Ultrasound–Assisted Fenton–persulfate System using Yolk–shell Fe_3O_4@hollow@mSiO_2 Nanoparticles. *Chem. Eng. Sci.* 217 (2020b) 115522.

Roy, K., Moholkar, V.S., Sulfadiazine degradation using hybrid AOP of heterogeneous Fenton/persulfate system coupled with hydrodynamic cavitation. *Chem. Eng. J.* 386 (2020a) 121294.

Shu, Z., Bolton, J.R., Belosevic, M., El Din, M.G., Photodegradation of emerging micropollutants using the medium–pressure UV/H_2O_2 advanced oxidation process. *Water Res.* 47(8) (2013) 2881–2889.

Thanekar, P., Panda, M., Gogate, P.R., Degradation of carbamazepine using hydrodynamic cavitation combined with advanced oxidation processes. *Ultrason. Sonochem.* 40, (2018) 567–576.

Wang, S., Zhou, N., Removal of carbamazepine from aqueous solution using sono–activated persulfate process. *Ultrason. Sonochem.* 29 (2016) 156–162.

Wols, B.A., Harmsen, D.J.H., Beerendonk, E.F., Hofman–Caris, C.H.M., Predicting pharmaceutical degradation by UV (LP)/H_2O_2 processes: a kinetic model. *Chem. Eng. J.* 255 (2014) 334–343.

Xiao, R., Ma, J., Luo, Z., Zeng, W., Wei, Z., Spinney, R., Hu, W.P., Dionysiou, D.D., Experimental and theoretical insight into hydroxyl and sulfate radicals–mediated degradation of carbamazepine. *Environ. Pollut.* 257 (2020) 113498.

Zuo, S., Li, D., Xu, H., Xia, D., An integrated microwave–ultraviolet catalysis process of four peroxides for wastewater treatment: Free radical generation rate and mechanism. *Chem. Eng. J.* 380 (2020) 122434.

CHAPTER 7

Overview and Suggestions for Future Work

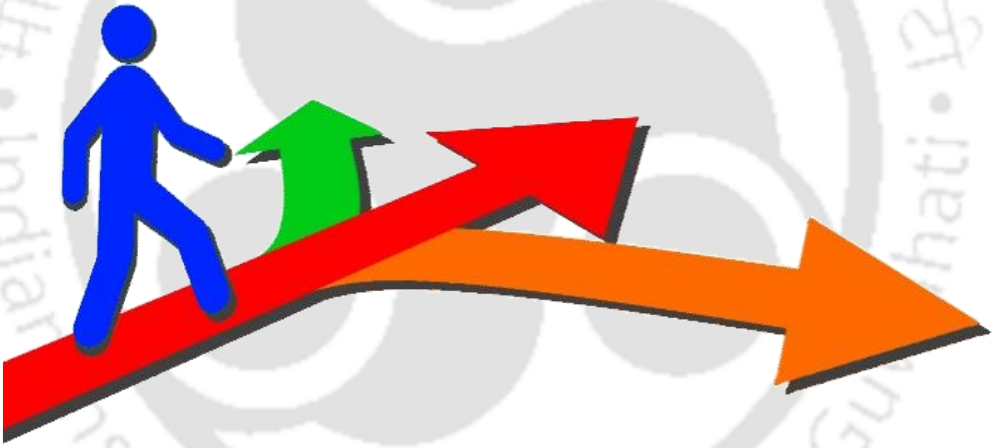

CHAPTER 7

OVERVIEW AND SUGGESTIONS FOR FUTURE WORK

7.1 OVERVIEW

As we come to the end of this thesis, we recapitulate the contributions and major results of the research presented in the previous chapters. Prior to the presentation of the summary of various chapters of the thesis, we briefly outline the background of the subject (or theme) addressed in this work, and the rationale of the present research. The first thesis on sonochemical degradation organic pollutants in our group was by Sivasankar (2008), who adopted the approach of correlating the experimental results to simulations of cavitation bubble dynamics. This novel approach provided important links between the physics of ultrasound and cavitation and the chemistry of sonochemical degradation of organic pollutants with widely different physical properties. Sivasankar (2008) adopted simple techniques such as additives in the solution or gas sparging through the solution, which had marked impact on the cavitation phenomena occurring in the system – which was manifested in terms of enhanced degradation of pollutants.

The second thesis in this topic was by Sankar Chakma (2015) in which the concept of hybrid advanced oxidation processes was presented with a similar approach of concurrent analysis of experimental results and simulations of cavitation bubble dynamics. This

work provided crucial mechanistic insights into the functioning of the hybrid AOPs - especially the synergistic effects between the different AOPs applied together that lead to enhanced degradation of pollutants as against the individual AOPs. The techniques adopted by Sankar Chakma (2015) were able to discriminate between the physical and chemical effects of sonication, and helped identify their individual contributions to the enhancement of the degradation process.

Both Sivasankar (2008) and Sankar Chakma (2015) adopted ultrasonic cavitation-based hybrid AOPs. A relatively new technique of producing controlled cavitation to be applied for enhancement (or intensification) of physical/chemical processes is hydrodynamic cavitation. Hydrodynamic cavitation has been widely investigated for the treatment of wastewater with biorefractory pollutants. However, research in hybrid AOPs based on hydrodynamic cavitation is relatively small. The synergistic interactions among hydrodynamic cavitation and other AOPs like Fenton or persulfate have not been explored. This thesis has addressed this important issue and has attempted to give mechanistic insights in hydrodynamic cavitation-based hybrid AOPs. This thesis has also adopted the approach of coupling experimental results with simulations. However, unlike the previous thesis by Sivasankar (2008) and Sankar Chakma (2015), a new approach of reaction kinetics model has been presented in this taking into account various basic reactions that occur between pollutant molecules and various radical/molecular species that degrade the pollutants. An attempt is also made to deduce the degradation pathway of pollutants using the Density Functional Theory. Another novel feature of this thesis has been in terms of the type of pollutants. A large fraction of previous literature in cavitation-aided wastewater treatment has dealt with organic pollutants emerging from petrochemical and textile industries. In this work, we have dealt with the pollutants from pharmaceuticals and pesticide industries such as sulfadiazine (SDZ), carbamazepine

(CBZ) and p-nitrophenol (PNP).

We now present an overview of the main results of the preceding chapters. These results of individual studies, when viewed at a glance, give an interesting account of the efficacy of the cavitation-based hybrid AOPs for the enhanced degradation of recalcitrant pollutants.

Chapter 2 has dealt with SDZ degradation with hybrid AOP coupling hydrodynamic cavitation and heterogeneous Fenton + persulfate. Two solid Fenton catalysts (α-Fe_2O_3 and Fe_3O_4) in the form of nanoparticles were synthesized. Optimization of degradation process resulted in the highest degradation of 81% for the conditions: $[SDZ]_o$ = 20 ppm, pH = 4, inlet pressure = 10 atm, $Na_2S_2O_8$ = 348.5 mg/L, H_2O_2 = 0.95 mL/L and α-Fe_2O_3 loading = 181.8 mg/L. A kinetic model for SDZ degradation was proposed based on homogeneous Fenton/persulfate system, and experimental degradation profiles were analyzed vis-à-vis simulated profiles. Kinetic model analysis showed best match between experimental and simulated profiles for $[Fe^{2+}]/[H_2O_2]$ initial ratio = 4. This indicated efficient catalytic activity of α-Fe_2O_3 nanoparticles – close to that of homogeneous catalyst. This is a consequence of high rate of mass transfer at surface of α-Fe_2O_3 particles due to intense turbulence and shear generated in cavitating flow in hydrodynamic cavitation reactor.

In **Chapter 3**, we have attempted to get physical insight into the relationship between hydraulic characteristics of hydrodynamic cavitation and the SDZ degradation with heterogeneous Fenton + persulfate system. The turbulent pressure fluctuations could enhance the cavitational yield through altering the flow geometry. Optimum turbulence can be achieved by manipulating the flow conditions and geometry of the cavitation device. At optimum operating conditions determined in Chapter 2, SDZ degradation was carried out with different flow geometries, viz. the number and size of holes on orifice

place. Three orifice plates were employed, viz. Plate 1 (d_h = 4 mm, N_h = 2), Plate 2 (d_h = 3 mm, N_h = 3) and Plate 3 (d_h = 2 mm, N_h = 4). Maximum degradation of SDZ (93.07 ± 1.67%) was achieved with plate 3 (d_h = 2 mm, N_h = 4) with conditions: $[SDZ]_o$ = 20 ppm, pH = 4, α-Fe_2O_3 = 181.8 mg/L, $Na_2S_2O_8$ = 348.5 mg/L, H_2O_2= 0.95 mL/L. The plate with a smaller hole size achieved relatively larger area of the shear layer that resulted in higher degradation. On the contrary, for larger hole sizes on orifice plates reduced the intensity of turbulence that resulted in lower collapse intensity. Eight intermediates of degradation, viz. m/z – 251, 233, 219, 187, 158, 109, 96, 95, were detected through LC-MS/MS analysis. DFT calculations were also performed to identify the vulnerable sites for the oxidation of SDZ molecule. Concurrent analysis of LC-MS/MS results and DFT simulations revealed the probable chemical mechanism of degradation in the hybrid AOP system.

In **Chapter 4**, we have addressed ultrasound-assisted sulfadiazine (SDZ) degradation in heterogeneous Fenton-persulfate system and attempted to reveal mechanistic features. The Fenton reagent (Fe^{2+} + H_2O_2) was added in the form of yolk-shell nanoparticles Fe_3O_4@hollow@mSiO_2. A three factor central composite design (CCD) coupled with response surface methodology (RSM) was applied to optimize the catalysts loading viz. H_2O_2, Fe_3O_4@hollow@mSiO_2 and $Na_2S_2O_8$. Control experiments yielded 23.33% degradation, while test experiments (ultrasound) achieved 93.14% degradation at optimized conditions: SDZ = 20 ppm, H_2O_2 = 484.85 μL, Fe_3O_4@hollow@mSiO_2 = 55.86 mg, $Na_2S_2O_8$ = 57.28 mg, pH = 5. A kinetic model for SDZ degradation was formulated using reactions of Fenton-persulfate system. Concurrent analysis of experiments and simulations revealed faster leaching of Fe^{2+}/Fe^{3+} ions from the metal core of Fe_3O_4@hollow@mSiO_2 nanoparticles due to micro-convection generated by sonication, which enhanced SDZ degradation four times. Inhibition effect of inorganic

anions (Cl^-, NO_3^-, CO_3^{2-}, SO_4^{2-}) on SDZ degradation was also studied with experiments and an extended kinetic model. CO_3^{2-} and SO_4^{2-} had the strongest inhibition effect due to both metal ion complexation and radical scavenging. Significant discrepancy between experimental and simulations results in the presence of anions were explained in terms of enhanced metal ion complexation with Fe^{2+} and Fe^{3+} and radical scavenging of $^{\bullet}OH$ than $SO_4^{\bullet-}$ in the hollow core of yolk-shell particles. For the highest anions uncertain of 500 ppm, the inhibition effect on SDZ degradation induced by different anions follows the trend: $NO_3^- < Cl^- < SO_4^{2-} < CO_3^{2-}$.

Chapter 5 has dealt with PNP degradation using the hybrid AOP of heterogeneous Fenton (magnetite, Fe_3O_4) and hydrodynamic cavitation. One variable at a time (OVAT) approach has been adopted for the determination of maximum PNP degradation. 78% degradation was achieved at optimized conditions: temperature = 35 °C, inlet pressure = 8 atm, $[PNP]_o$ = 20 ppm, Fe_3O_4:H_2O_2 = 1:100 and pH = 3. The results demonstrated that the degradation of PNP was induced by the hydroxyl radicals ($^{\bullet}OH$) generated by both Fenton reactions of the Fe^{2+}/Fe^{3+} ions leached from Fe_3O_4 surface as well as direct oxidation from hydrodynamic cavitation. The experimental results were explained with three approaches: (1) CFD modeling of the cavitating flow that predicted the length (or extent) of cavitation zone, (2) reaction kinetics model, and (3) DFT simulations for identification of the intermediates of the PNP degradation and possible pathways. The CFD model revealed influence of design and operational parameters of the hydrodynamic cavitation reactor on PNP degradation. The inlet pressure played a major role in degradation. The reaction kinetic model revealed significant leaching of the Fe^{3+}/Fe^{2+} ions at the surface of magnetic nanoparticles. Concurrent analysis of the experimental and simulations result reveals the mechanistic features of individual radicals and ions

behaviour in hybrid (HC+Fenton). DFT simulations assessed different possible intermediates that can form due to attack of •OH radicals on PNP molecules. The vulnerable sites for attack were identified and a reaction pathway was proposed. Two distinct pathways for PNP degradation were identified, viz. •OH addition and H-abstraction. For the former route, the *ortho*-C of benzene ring was the most favourable site, while H atom of phenolic hydroxyl group was more susceptible (or more reactive) for H-atom abstraction route.

Chapter 6 reports degradation of pharmaceutical compound carbamazepine (CBZ) in hydrodynamic cavitation reactor using octahedral shaped $ZnO/ZnFe_2O_4$ as a heterogeneous photo Fenton-like reaction system. Process parameters, viz. inlet pressure, pH, initial CBZ concentration, UV power, $ZnO/ZnFe_2O_4$ and $Na_2S_2O_8$ were optimized using one variable at a time (OVAT) approach. Maximum CBZ degradation of 98.13% was obtained at conditions: inlet pressure = 9 atm, pH = 4, initial CBZ concentration = 15 ppm, UV power = 18 W, $Na_2S_2O_8$ = 500 mg/L, $ZnO/ZnFe_2O_4$ = 500 mg/L. An empirical correlation that related percentage degradation to the process parameters was obtained as: $\eta = 2.38\frac{(\text{inlet pressure})^{0.92}(\text{UV power})^{0.28}[ZnO/ZnFe_2O_4]^{0.18}[Na_2S_2O_8]^{0.22}}{(\text{pH})^{0.14}[\text{initial concentration}]^{0.52}}$.

The kinetic model was developed by quantifying total rate expression ($r_{[CBZ],Total}$) by combining the rate constant of individual processes, viz. $r_{[CBZ],UV}$, $r_{[CBZ],^{\bullet}OH}$, $r_{[CBZ],SO_4^{\bullet-}}$. For the validation of the kinetic model, the experimental and simulated profiles of CBZ degradation were matched with $[Fe^{2+}]/[H_2O_2]$ ratio as the manipulation parameter – which was a measure of leaching of Fe^{2+}/Fe^{3+} ions at the surface of iron oxide nanoparticles. The closest match between experimental and simulated profiles was obtained for initial $[Fe^{2+}]/[H_2O_2]$ ratio = 20. Seven intermediate with m/z – 237, 283, 267, 253, 224, 196, 180, 149 were detected though LC-MS/MS analysis and tentatively

identified elemental compositions.

On a whole, this thesis has demonstrated the efficacy of the cavitation (both ultrasonic and hydrodynamic) based advanced oxidation processes for enhanced degradation of organic pollutants, and has also brought forth the mechanistic features of these processes in terms of the synergistic interactions. A peculiar feature of degradation systems used in this study is that Fenton reagent has been added in heterogeneous phase. The synergy between hydrodynamic cavitation and other AOPs is mostly of physical nature, i.e. enhanced leaching at the catalyst surface. The turbulence generated by hydrodynamic cavitation is equally effective as the microconvection generated by ultrasound. However, it has the advantage of handling much larger volumes as compared to ultrasonic systems. The interaction between radicals and substrate (or pollutant) molecules is again found to be the governing factor of the AOPs. The yolk-shell particles essentially enhanced this factor that resulted in faster and higher degradation. The influence of flow geometry in hydrodynamic cavitation reactor is also evident from this work. Higher pressure head loss in the flow intensifies the transient cavitation events and results in faster degradation. Finally, in all cases almost complete degradation of all pollutants was achieved.

7.2 SUGGESTIONS FOR FUTURE WORK

The work presented in this thesis can be taken ahead with aim of translating the ideas and knowhow gained in this work into a full-scale workable process applicable in industry. We give herewith three specific suggestions for further work.

1. More detailed studies on quantification of total mineralization of the pollutants with parameters such as COD and total organic carbon (TOC). The present study has treated a single pollutant in all cases. More studies with actual wastewater from

industry containing multiple pollutants is necessary. This will give an idea of interactions between the pollutants as they undergo simultaneous degradation.

2. Extensive characterization of the intermediates of degradation. Total mineralization may not be achieved with hybrid AOP alone. Characterization of the intermediates will give an idea as how the original biorecalcitrant pollutant has been degraded or broken down into fragments that can be further treated with conventional technique of anaerobic digestion.

3. In case of hydrodynamic cavitation, venturi flow configuration can be tried instead of orifice configurations used in this study. Venturi configurations are likely to give higher cavitation intensities at relatively lower power inputs (or the inlet pressures). In more novel approach, the biological treatments can be coupled with hydrodynamic cavitation by inoculating the solution in the tank with microbial cultures. This approach has already been demonstrated for ultrasonic cavitation. It has been shown that sonication of the fermentation broth results in marked augmentation of both kinetics and yield of the process. Similar protocols may be attempted with hydrodynamic cavitation.

PUBLISHED IN PEER REVIEWED INTERNATIONAL JOURNALS

Research Outputs form the Thesis

- **Kuldeep Roy**, Chandrodai Agarkoti, Ritesh S. Malani, Binota Thokchom, and Vijayanand S. Moholkar. "Mechanistic study of sulfadiazine degradation by ultrasound-assisted Fenton-persulfate system using yolk-shell Fe_3O_4@hollow@ $mSiO_2$ nanoparticles" *Chemical Engineering Science,* 217 115522 (2020).
- **Kuldeep Roy**, Vijayanand S. Moholkar. "Sulfadiazine Degradation using Hybrid AOP of Heterogeneous Fenton/Persulfate System Coupled with Hydrodynamic Cavitation" *Chemical Engineering Journal* 386 121294 (2020).

Manuscript Under Preparation/Submitted

- **Kuldeep Roy**, Vijayanand S. Moholkar. "Mechanistic Analysis of Carbamazepine Degradation in Hybrid Advanced Oxidation Process of Hydrodynamic Cavitation/UV/persulfate in the presence of $ZnO/ZnFe_2O_4$" (under review).
- **Kuldeep Roy**, Vijayanand S. Moholkar. "Optimization of Hydrodynamic Cavitation Rector For Sulfadiazine Degradation" (under preparation).
- **Kuldeep Roy**, Vijayanand S. Moholkar. "4–Nitrophenol Degradation Using Heterogeneous Fenton–Like System in Hydrodynamic Cavitation Reactor" (under preparation).

Other Research Outputs

- Niharika Kashyap, **Kuldeep Roy**, Vijayanand S. Moholkar. "Mechanistic Investigation in Co-biodegradation of Phenanthrene and Pyrene by Candida tropicalis MTCC 184." *Chemical Engineering Journal*, 399, 125659 (2020).
- Amit H. Batghare, **Kuldeep Roy**, Vijayanand S. Moholkar. "Investigations in physical mechanism of ultrasound-assisted antisolvent batch crystallization of lactose monohydrate from aqueous solutions." *Ultrasonics Sonochemistry,* 67, 105127 (2020).
- Niharika Kashyap, **Kuldeep Roy** and Vijayanand S. Moholkar "Mechanistic investigations in ultrasound-assisted biodegradation of phenanthrene" *Ultrasonics Sonochemistry*, 104890 (2020).

- Amit H. Batghare, **Kuldeep Roy**, Kaustubh C. Khaire, and Vijayanand S. Moholkar. "Mechanistic investigations in ultrasound-induced intensification of fermentative riboflavin production." *Bioresource Technology Reports*, 100380 (2020).
- Neha Singh, **Kuldeep Roy**, Arun Goyal, and Vijayanand S. Moholkar. "Investigations in ultrasonic enhancement of β-carotene production by isolated microalgal strain Tetradesmus obliquus SGM19" *Ultrasonics sonochemistry*, 58, 104697 (2019).
- Arup J. Borah, **Kuldeep Roy**, Arun Goyal, Vijayanand S. Moholkar. "Mechanistic investigations in biobutanol synthesis via ultrasound-assisted ABE fermentation using mixed feedstock of invasive weeds" *Bioresource Technology*, 272, 389-397 (2019) **(Featured Cover).**
- Amit H. Batghare, Saiprasad Pati, **Kuldeep Roy**, Vijayanand S. Moholkar. "Mechanistic investigations in ultrasound-assisted extraction of astaxanthin from Phaffia rhodozyma MTCC 7536" *Bioresource Technology Reports*, 4, 166-173 (2018).
- Belachew Z. Tizazu, **Kuldeep Roy**, Vijayanand S. Moholkar. "Ultrasonic enhancement of xylitol production from sugarcane bagasse using immobilized Candida tropicalis MTCC 184" *Bioresource Technology*, 268, 247-258 (2018).
- Belachew Z. Tizazu, **Kuldeep Roy**, Vijayanand S. Moholkar. "Mechanistic Investigations in Ultrasound-Assisted Xylitol Fermentation" *Ultrasonics Sonochemistry*, 48, 321-328 (2018).
- Gazliya Nazimudheen, **Kuldeep Roy**, Thirugnanasambandam Sivasankar and Vijayanand S. Moholkar. "Mechanistic investigations in ultrasonic pretreatment and anaerobic digestion of landfill leachates" *Journal of Environmental Chemical Engineering*, 6(2), 1690-1701 (2018).
- Sandip K. Pawar, Amit V. Mahulkar, Aniruddha B. Pandit, **Kuldeep Roy**, Vijayanand S. Moholkar. "Sonochemical Effect Induced by Hydrodynamic Cavitation: Comparison of Venturi/Orifice Flow Geometries" *AIChE Journal*, 63(10), 4705–4716 (2017).
- Ritesh S. Malani, Shubham Patil, **Kuldeep Roy**, Sankar Chakma, Arun Goyal, Vijayanand S. Moholkar. "Mechanistic analysis of ultrasound-assisted biodiesel synthesis with Cu_2O catalyst and mixed oil feedstock using continuous (packed bed) and batch (slurry) reactors" *Chemical Engineering Science*, 170, 743-755 (2017).

Conference Presented

- **Kuldeep Roy** and Vijayanand S. Moholkar, Degradation of Sulfadiazine in Hydrodynamic Cavitation Assisted Fenton/Persulfate System: A Kinetic Modelling Approach. *Fourth International Conference on Sustainable Energy & Environmental Challenges (IV SEEC)*, 27-29th November 2019, CSIR-National Environmental Engineering Research Institute, Nagpur, Maharashtra, India. **(Best Oral Presentation, ACS Sustainable Chemistry & Engineering)**
- **Kuldeep Roy** and Vijayanand S. Moholkar, Comparative Study of Acoustic and Hydrodynamic Cavitation for the Degradation of Nile Blue Sulphate Dye: A Kinetic Modelling Approach. *Annual Symposium of Chemical Engineering (Reflux 7.0)*, 28-29th September 2019, Indian Institute of Technology Guwahati, Assam, India. **(Best Oral Presentation)**
- **Kuldeep Roy** and Vijayanand S. Moholkar, Mechanistic investigation in sulfadiazine degradation using heterogeneous catalyst and hydrodynamic cavitation. Proceeding of *14th International Conference on Gas-Liquid and Gas-Liquid-Solid Reactor Engineering (GLS-14)*, 30th May-03rd June 2019, Grand Link Hotel, Guilin, **China**.
- **Kuldeep Roy** and Vijayanand S. Moholkar, Intensified degradation of 4-nitrophenol using hydrodynamic cavitation in the presence of heterogeneous Fenton-like catalyst. Proceeding of *Indo-Japan Bilateral Symposium (IJBS)*, 01-04th February 2018, Indian Institute of Technology Guwahati, Assam, India.
- Arup Jyoti Borah, Mriganka Saha, Prachi Arya, **Kuldeep Roy**, Arun Goyal, Vijayanand S. Moholkar, Immobilization of cellulase on Magnetic Nano particles for cost effective hydrolysis of lignocellulosic biomass. *5th International Conference on Advanced Nanomaterials and Nanotechnology (ICANN)*, 18-21th December 2017, Indian Institute of Technology Guwahati, Assam, India (**Best Poster**).
- **Kuldeep Roy**, Ritesh S. Malani, Binota Thokchom, and Vijayanand S. Moholkar, Ultrasound-Assisted Degradation of Sulfadiazine Using Rattles-Type/Yolk Shell Structured Magnetic Particles: A Mechanistic Investigation. Proceeding of *3rd Asia-Oceania Sonochemical Society Conference (AOSS-3)*, 14-16th September 2017, SRM Research Institute, SRM University, Kattankulathur, Chennai, Tamil Nadu, India.